

AD-A281 980



IMENTATION PAGE

Form Approved
OMB No 0704-01

This document contains neither recommendations nor conclusions of the Defense Technical Information Center. It has been cleared for release under the Defense Technical Information Center's discretion. Reproduction of this document by other than the Defense Technical Information Center is subject to certain restrictions.

1. REPORT DATE

3. REPORT TYPE AND DATES COVERED

THESIS/DISSERTATION

4. TITLE AND SUBTITLE

THERMAL CHARACTERISTICS AND HEAT TRANSFER
IN AN ELECTROTHERMAL LIGHT GAS GUN

5. FUNDING NUMBERS

6. AUTHOR(S)

Joseph James R. TEGTMEYER

7. PERFORMING ORGANIZATION NAME(S) AND ADDRESS(ES)

AFIT Student Attending:

OHIO STATE UNIVERSITY

8. PERFORMING ORGANIZATION
REPORT NUMBER

AFIT/C1/CIA-

94-086

9. SPONSORING/MONITORING AGENCY NAME(S) AND ADDRESS(ES)

DEPARTMENT OF THE AIR FORCE

AFIT/C1

2950 P STREET

WRIGHT-PATTERSON AFB OH 45433-7765

10. SPONSORING/MONITORING
AGENCY REPORT NUMBER

11. SUPPLEMENTARY NOTES

12a. DISTRIBUTION/AVAILABILITY STATEMENT

Approved for Public Release IAW 190-1

Distribution Unlimited

MICHAEL M. BRICKER, SMSgt, USAF

Chief Administration

12b. DISTRIBUTION CODE

13. ABSTRACT (Maximum 200 words)

DTIC
ELECTE
JUL 21 1994
S B D

215P
94-22787

94 27 20 020

DTIC EDITION NUMBER 1

14. SUBJECT TERMS

15. NUMBER OF PAGES

160

16. PRICE CODE

17. SECURITY CLASSIFICATION
OF REPORT18. SECURITY CLASSIFICATION
OF THIS PAGE19. SECURITY CLASSIFICATION
OF ABSTRACT

20. LIMITATION OF ABSTRACT

94-086

THESIS ABSTRACT

THE OHIO STATE UNIVERSITY GRADUATE SCHOOL

NAME: Tegtmeyer, R. Joseph James **QUARTER/YEAR:** Spring, 1994

DEPARTMENT: Aeronautical and Astronautical
Engineering **DEGREE:** M.S.

ADVISER'S NAME: Turchi, Peter J.

TITLE OF THESIS: Thermal Characteristics and Heat Transfer in an
Electrothermal Light Gas Gun

In the electrothermal gun concept, the high enthalpy, low molecular weight, and high relative sound speed of a hot hydrogen plasma is used to impart high velocities to projectiles. While the plasma accelerates the projectile out of the gun barrel, it also transfers heat energy to the barrel walls and suffers from viscous dissipation.

This thesis calculates the radiative, convective and conductive heat transfer processes and viscous effects. A study of plasma opacity is also presented, showing the gas in the barrel to be optically thick in most operating regimes, thus allowing the use of Rosseland diffusion theory. Finally, the overall energy loss is determined and a comparison of results to MACH2 computer code presented.



Adviser's Signature

Nothing in the world can take the place of persistence. Talent will not; nothing is more common than unsuccessful men with talent. Genius will not; unrewarded genius is almost a proverb. Education alone will not; the world is full of educated derelicts. Persistence and determination alone are omnipotent.

Accession For	
NTIS GRA&I	<input checked="" type="checkbox"/>
DTIC TAB	<input type="checkbox"/>
Unannounced	<input type="checkbox"/>
Justification _____	
By _____	
Distribution/_____ Availability Codes	
Avail and/or Dist	Special
A-1	

**THERMAL CHARACTERISTICS AND
HEAT TRANSFER IN AN ELECTROTHERMAL
LIGHT GAS GUN**

A Thesis

**Presented in Partial Fulfillment of the Requirements for the Degree
Master of Science in the Graduate School of The Ohio State University**

by

R. Joseph James Tegtmeyer, B.S. Astronautical Engineering

* * * * *

The Ohio State University

1994

Master's Examination Committee:

Dr. P. J. Turchi

Dr. T. M. York

Approved by


Adviser

**Department of Aeronautical
and Astronautical Engineering**

ACKNOWLEDGMENTS

Without a doubt, I would never have come to Ohio State and earn my Master of Science degree had it not been the faith that Major Keith Briem and Colonel William Welser, III had in me. Before I met them, my future seemed quite dim indeed. Major Briem acted not only as my friend, but as an excellent role model, and I am forever grateful for his leadership. I cannot forget to mention Cliff and Michelle Ozmun and Ray Mijares for keeping me sane while I completed my tour in Altus.

The support of AFROTC Detachment 645, especially Anne, was instrumental in creating the right environment for my studies. I am also grateful for my selection by the Air Force Institute of Technology to attend graduate school and earn my degree. They provided much needed assistance and advice throughout my stay here, and I must thank Captain Payne for helping me with all my crazy questions.

Chuck Finley must be given credit for suggesting that I spend the summer of 1993 at the Air Force Phillips Laboratories in Albuquerque, New Mexico. This time proved to be the most informative, insightful, and ultimately productive time I spent while at this university. I wish to also thank the people at the Phillips Laboratories for their help and assistance while I was out there. Thanks also go to my adviser, Dr. Peter Turchi for helping me secure the trip to New Mexico, and for working hard to help me finish this program. His patience with me was beyond extraordinary.

A very special thank you and admiration goes to the people of the Air Force Technical Library at Kirtland Air Force Base. They have without a doubt the best library I have ever seen. Bobbie was my savior, never too busy to take the time and help me get the references, sources, or journals I needed, and always with a smile. Thanks again!

Wes Hallman, Chris Bjorkman, Margo Willoughby, Brett and Jeanett Pauer, Stew and Beth Devilbiss, and Sabrina Taijeron were great friends to have and helped me keep my perspective on what I was trying to do here. I cannot adequately express my appreciation for what they did for me. Yangos and Pavlos Mikiledes deserve a lot of credit with helping me finish this thesis, and getting the cantankerous MACH2 code working.

Finally, I must never forget to thank the "Gang". Kurt Mallory, Mark Peters, Anne Chinnery and of course, Ben Culp. Your presence is always with me regardless of where the Air Force puts us. Thanks for your support and continual encouragement.

VITA

July 8, 1964	Born - London, England
1988	B.S., United States Air Force Academy, Colorado Springs, Colorado
1988-1989	Euro-NATO Joint Jet Pilot Training, Sheppard Air Force Base, Texas
1989-1991	Squadron Section Commander, Fuels Management Officer, and LGSC Branch Chief, 443 rd Supply Squadron, Altus Air Force Base, Oklahoma
1991-1992	Euro-NATO Joint Jet Pilot Training, Sheppard Air Force Base, Texas
1993	Aeronautical and Astronautical Engineer, Air Force Phillips Laboratory, Albuquerque, New Mexico

FIELD OF STUDY

Major Field: Aeronautical and Astronautical Engineering
Studies in Quantum Mechanics, Orbital Dynamics,
Mathematics, and Plasma Dynamics

TABLE OF CONTENTS

	PAGE
DEDICATION	ii
ACKNOWLEDGMENTS	iii
VITA	v
LIST OF TABLES	ix
LIST OF FIGURES	xi
CHAPTER	PAGE
I. INTRODUCTION	1
1.1 Problem Statement	3
1.2 Preliminary Discussion	4
II. BACKGROUND	7
2.1 History and Configurations of Electrothermal Guns	8
2.2 Hydrogen Plasma as a Working Fluid	17
2.3 Power Source for the Electrothermal Light Gas Gun	21
III. APPROACH FOR HEAT TRANSFER	23
3.1 Description of the Plasma State	23
3.2 Description of Energy Loss Mechanisms	25
3.3 Development of Model	27
3.4 Viscous Effects Model	31
3.5 Conductive and Radiative Heat Transfer Model	37

3.6 Conductive and Convective Heat Transfer	39
3.6.1 Boundary Layer Discussion	40
3.6.2 Boundary Layer Development in a Pipe	41
3.6.3 Pipe Flow	42
3.6.4 Heat Flow Equation	45
3.6.5 Forced Convection in Turbulent Flow	48
3.6.6 Turbulent Flow in a Tube	50
3.7 Radiative Heat Transfer Processes and Hydrogen Opacity	52
3.8 MACH2 Operation and Test	63
 IV. ANALYSIS OF HEAT TRANSFER	65
4.1 Determination of Degree of Ionization and Working Fluid Composition	65
4.2 Conductive Heat Transfer Analysis	75
4.3 Analysis of Viscous Effects	79
4.4 Analysis of Convection	84
4.5 Analysis of Radiation	89
4.6 Comparative Analysis	93
 V. ANALYSIS OF MACH2 COMPUTATIONS	107
 V. CONCLUSION	113
 APPENDICES	
A. Degree of Hydrogen Ionization Calculations	118
B. SESAME Plots	121
C. Opacity and Blackbody Radiation Plots	124
D. Hydrogen Composition and Data	130
E. Rosseland Diffusion Approximation Calculations	139
F. Calculation Results for Conduction Model	142

G.	Calculation Results for Radiation Models	147
H.	Calculation Results for Viscous Effects.	155
I.	Calculation Results for Convection Model	160
J.	Calculation Results for Barrel Theoretical Length	165
K.	MACH2 Test Results	170
L.	MACH2 Calculation Results and Charts	176
LIST OF REFERENCES		190

LIST OF TABLES

TABLE		PAGE
2.1	Comparison of three different types of guns	15
2.2	Impetus calculations for various propellants	19
4.1	Calculation of relaxation times at various velocities, temperatures and constant pressure of 1,000 atm	71
4.2	Translational relaxation times	74
4.3	Conduction data for heat transfer and percent power available at exit	78
4.4	Viscous effects with varying input data and friction factors with constant velocity of 4,500 m/sec	80
4.5	Viscous effects with varying input data and friction factors with constant velocity of 13,500 m/sec	80
4.6	Effect of friction factor on convection heat transfer	85
4.7	Effect on convection heat transfer using various inlet conditions	86
4.8	Convection parameters at varying inlet conditions	88
4.9	Conductive heat transfer data	97
4.10	Radiative heat transfer data	98
4.11	Convective heat transfer data	98
4.12	Energy liberated during recombination (1,000 atm)	104

4.13	Transport energy loss at 1,000 atm	105
4.14	Hydrogen internal energy data	106
5.1	Full model results for MACH2 computations	108
5.2	Argon internal energy data	112
F.1	Mathcad conduction data	145
F.2	Mathcad conduction data	146
G.1	Mathcad rosseland radiation data	150
G.2	Mathcad planck radiation data	153
G.3	Mathcad rosseland radiation data	154
G.4	Mathcad planck radiation data	154
H.1	Mathcad viscous data	158
H.2	Mathcad viscous data	159
I.1	Mathcad convection data	163
I.2	Mathcad convection data	164
J.1	Theoretical length calculations from Mathcad	169

LIST OF FIGURES

FIGURE		PAGE
2.1	CAP Gun basic configuration	9
2.2	Electrothermal Light Gas Gun configuration	12
2.3	Correlation of main parameters	14
3.1	First Law of Thermodynamics model of Electrothermal Gun	25
3.2	Flow through control volume	27
3.3	Effect of friction factor on theoretical length of pipe	35
3.4	Growth of boundary layers in a pipe	42
3.5	Developed region of flow	43
3.6	Regimes of energy transport	52
3.7	Test case for rosseland and planck evaluations	60
3.8	Results of Mathcad rosseland and planck mean free path versus temperature calculations	61
3.9	Results of Mathcad rosseland and planck mean free path versus temperature calculations	62
4.1	Ionization at 100 atm	67
4.2	Ionization at 1,000 atm	67
4.3	Number densities of hydrogen at 1,000 atm	73
4.4	Heat transfer per unit mass for conduction only	76

4.5	Ratio of stagnation pressures verses velocity with a friction factor of .003	82
4.6	Ratio of stagnation pressures verses velocity at different friction factors	83
4.7	Heat transfer per unit mass for convection at a friction factor of .003	89
4.8	Rosseland radiation heat transfer per unit mass	90
4.9	Planck radiation heat transfer per unit mass	91
4.10	Comparison between planck and rosselnad radiation heat transfer at 1,000 atm and 10,000K	91
4.11	Representation of transport processes in the regime of less than 1 eV	100
4.12	Representation of transport processes in the regime from 1 eV to 2 eV	100
4.13	Representation of transport processes in the regime from 2 eV to 3 eV	101
5.1	Full model computations	109
A.1	Ionization potential lowering as a function of temperature (Rankine)	120
B.1	SESAME rosseland opacity for hydrogen	122
B.2	SESAME opacity comparison for hydrogen	123
C.1	Hydrogen rosseland mean free path based on data by Patch ⁷⁸	125
C.2	Hydrogen planck mean free path based on data by Patci ⁷⁹	126
C.3	Comparison of hydrogen mean free paths based on data by Patch ⁷⁸	127
C.4	Planck mean opacity for hydrogen	128

C.5	Posseland mean opacity for hydrogen	129
D.1	Hydrogen viscosity as a function of temperature	131
D.2	Hydrogen enthalpy as a function of temperature	131
D.3	Hydrogen specific heats as a function of temperature	132
D.4	Hydrogen γ as a function of temperature	132
D.5	Hydrogen thermal conductivity as a function of temperature	133
D.6	Hydrogen sound velocity as a function of temperature	133
D.7	Hydrogen density as a function of temperature	134
D.8	Hydrogen composition at 10 atmospheres	135
D.9	Hydrogen composition at 100 atmospheres	136
D.10	Hydrogen species number densities at 100 atmospheres	137
D.11	Hydrogen number densities at 1,000 atmospheres	138
D.12	Calculated number densities of hydrogen at 1,000 atm	138
E.1	Radiative heat transfer to wall at 100 atmospheres	141
E.2	Radiative heat transfer to wall at 500 atmospheres	141
J.1	Theoretical length calculations with γ 1.31	167
J.2	Theoretical length calculations with γ 1.41	167
J.3	Theoretical length calculations with γ 1.51	168
J.4	Theoretical length calculations with γ 1.61	168
K.1	MACH2 Calculation mesh cycle 1.	172

K.2	MACH2 Velocity calculation cycle 1	172
K.3	MACH2 Density calculation cycle 1.	172
K.4	MACH2 Temperature calculation cycle 1	172
K.5	MACH2 Pressure calculation cycle 1	173
K.6	MACH2 Velocity calculation cycle 5000	173
K.7	MACH2 Density calculation cycle 5000	173
K.8	MACH2 Temperature calculation cycle 5000	173
K.9	MACH2 Pressure calculation cycle 5000	174
K.10	MACH2 Density calculation cycle 33210	174
K.11	MACH2 Temperature calculation cycle 33210	174
K.12	MACH2 Pressure calculation cycle 33210	174
K.13	MACH2 sample run data	175
L.1	Calculation mesh for MACH2 calculations	178
L.2	MACH2 planck full model velocity cycle 1000	178
L.3	MACH2 planck full model velocity cycle 5000	178
L.4	MACH2 planck full model velocity cycle 10895.	179
L.5	MACH2 planck full model vorticity cycle 1000	179
L.6	MACH2 planck full model vorticity cycle 5000	179
L.7	MACH2 planck full model vorticity cycle 10895	180
L.8	MACH2 planck full model temperature cycle 1000	180
L.9	MACH2 planck full model temperature cycle 5000	180
L.10	MACH2 planck full model temperature cycle 10895	181

L.11	MACH2 planck full model pressure cycle 1000	181
L.12	MACH2 planck full model pressure cycle 5000	181
L.13	MACH2 planck full model pressure cycle 10895	182
L.14	MACH2 planck full model density cycle 1000	182
L.15	MACH2 planck full model density cycle 5000	182
L.16	MACH2 planck full model density cycle 10895	183
L.17	MACH2 planck full model velocity cycle 1000	185
L.18	MACH2 planck full model velocity cycle 5000	185
L.19	MACH2 planck full model velocity cycle 10895	185
L.20	MACH2 planck full model vorticity cycle 1000	186
L.21	MACH2 planck full model vorticity cycle 5000	186
L.22	MACH2 planck full model vorticity cycle 10895	186
L.23	MACH2 planck full model temperature cycle 1000	187
L.24	MACH2 planck full model temperature cycle 5000	187
L.25	MACH2 planck full model temperature cycle 10895	187
L.26	MACH2 planck full model pressure cycle 1000	188
L.27	MACH2 planck full model pressure cycle 5000	188
L.28	MACH2 planck full model pressure cycle 10895	188
L.29	MACH2 planck full model density cycle 1000	189
L.30	MACH2 planck full model density cycle 5000	189
L.31	MACH2 planck full model density cycle 10895	189

CHAPTER I

INTRODUCTION

The concept of the electrothermal gun was first developed in the hopes of increasing the muzzle velocity of a projectile for use in a wide variety of tasks. Most notably, the use of this concept has applications in the area of both space-based hypervelocity "kinetic-kill" type weaponry as well as more conventional tank and artillery uses. An electrothermal gun is designed to utilize the interaction of an electrically-generated plasma or working fluid to create the high temperatures and high pressures necessary for projectile motion. "The deposition of electrical energy into the gun represents a way of increasing the work potential of the driver gases as compared to conventional propellants."¹ By using electricity as the source of energy, instead of the conventional chemical reactions in an ordinary propellant, the working fluid may be chosen for its low molecular weight, high sound speed, favorable base pressure-to-breech pressure ratios, and other beneficial thermal characteristics without regard to the chemical reactions required to form the working fluid. The "tailoring" of the amount of energy and type of working fluid represents a significant advancement over that of conventional propellant commonly used in projectile devices.

Typically, electrothermal guns offer a substantial increase in muzzle velocity over that attained through the use of conventional propellants. As an example, most conventional

type propellants can impart velocities to projectiles on the order of 2 to 3 km/sec, whereas electrothermal guns have been demonstrated to attain projectile muzzle velocities in excess of 6 to 7 km/sec. In fact, under ideal circumstances, it is theoretically possible to extend these velocities for small mass projectiles to over 9 km/sec.²

In the attempt to harness these advantages, several classes of electrothermal gun have been developed over the last few decades. These include Combustion-Augmented Plasma, or "CAP", guns, Thermal-Electric (ET) guns, and the Electrically Powered Light Gas Gun (ELGG). Each of these devices use slightly different working characteristics, but are, in reality, variations on the same theme.

This thesis examines a new variation on the ELGG concept, that differs in both the initial configuration of the device, as well as the development of the working fluid or plasma within the "propellant chamber". The "propellant chamber" is synonymous with the breech of the gun. The "propellant chamber" in the case of the ELGG has temperatures of up to several electron volts and pressures ranging from 850 to 1,150 atmospheres.

The extremely high velocities and subsequent high operating temperatures and pressures attained by electrothermal guns suggest that a great deal of heat transfer from the plasma to the gun barrel must take place and that this heat transfer is likely to be much greater than that in a conventionally powered device. However, much of the previous research into electrothermal guns has not adequately addressed this concern, and in fact many of the published documents simply assume that the heat transfer is of the

same order of magnitude as that in conventional guns with radiation assumed to be negligible. Little, if any, further study on this subject has been conducted.

It is the aim of this thesis to examine the new class of electrothermal gun and to study its operation. Specifically, the heat transfer mechanisms in the electrothermal gun barrel environment are examined in detail. MACH2, a 2 1/2 dimensional magnetohydrodynamic simulation code developed at the Phillips Laboratories (Kirtland AFB, New Mexico) running on an Ohio State Cray supercomputer will be utilized in order to provide highly accurate and insightful computer simulated data for various heat transfer modes and viscous effects within the barrel section of the ELGG. The combination of first principle model development and MACH2 data will yield a substantial understanding of the ELGG operational and heat transfer characteristics.

1.1 -- PROBLEM STATEMENT

The basic configuration and operation of the EL GG will be discussed with the future application of a 2,100 capacitor bank located at the Ohio State University , known as "Godzilla", to the ELGG in mind. Additionally, this thesis will study the three main heat transfer mechanisms: thermal radiation, forced convection and thermal conduction from the high temperature plasma "working fluid" to the walls of the electrothermal gun barrel. Since various theoretical heat transfer radiation models are available, the determination of which model is appropriate to the conditions within the ELGG barrel will be made, and the comparison between the various heat transfer modes will be derived and their regions

of influence described. Viscous effects will be taken into account, and the combined energy loss due to the main transfer mechanisms and the viscous effects will be discussed.

The impact of the heat transfer mechanisms and viscous losses will be discussed and demonstrated from predicted data obtained with models developed in this thesis. Consideration will be given to the degree of ionization and dissociation created by the changing temperature and pressure profiles throughout the length of the barrel. Finally, this thesis will discuss the applicability and useability of the magnetohydrodynamic simulation code, MACH2, to the problem of high heat transfer and viscous effects within the barrel region of an ELGG.

1.2 – PRELIMINARY DISCUSSION

The system described in this thesis uses hydrogen gas as the working fluid, unless specified otherwise, and avoids the use of chemical reactions as the source of energy by introducing an arc discharge in the breech chamber. The region prior to the beginning of the ELGG barrel is not studied in this thesis, but it is assumed that hydrogen gas at a specific stagnation pressure and temperature, as well as inlet velocity, is provided as initial conditions. The analysis deals with a hydrogen plasma at initial stagnation temperatures ranging from one to three electron volts (eV) and at stagnation pressures from 850 to 1,150 atmospheres. These initial parameters, in addition to a set of assumed velocity profiles at the inlet are consistent with the flow exiting the chamber. The initial conditions pose extreme heat transfer problems within the barrel region of the gun, as

well as the necessity to contain the force on the barrel walls caused by the high pressures.

The actual heating of the working fluid by an electric arc is not discussed.

Hydrogen gas was chosen as the working fluid for several important reasons. The low molecular weight of the gas is one of the keys to attaining very high projectile velocities, and the corresponding high sound speed of hydrogen aids in the interaction of the hot plasma gas and the projectile by decreasing the wave transit time throughout the working fluid, further increasing the possible projectile velocity. Because of the choice to use hydrogen gas, the thermal characteristics, opacities, and thermodynamic properties of hydrogen need to be well understood.

In addition to gaining a good understanding of the properties of hydrogen at the conditions necessary for electrothermal gun operation, the main modes of heat transfer need to be well understood. The nature of these modes is vital to the understanding of the overall heat transfer, and governs the exit kinetic energy the projectile may acquire from interaction with the plasma.

The importance of studying the heat transfer mechanisms is dramatically illustrated by the results of an experiment by Tidman and Massey.³ They developed a similar ELGG with a barrel length of 5.0 m, bore diameter of 1.6 cm, and chamber volume of 244 cm³ in which a projectile with a mass of 10 grams was accelerated to speeds of about 7 km/sec with an efficiency (defined as the transfer of the energy contained within the propellant gas to kinetic energy of the projectile) of 32%. This indicates that fully 68% of the energy initially stored in the plasma is lost due to a variety of sources. Most of these are in the form of heat convection out of the barrel walls, heat transfer to the projectile,

conversion of energy into internal energy modes, energy of ionization, and dissociation energy. This represents a considerable amount of energy which must be accounted for.³

The main problem with describing the heat transfer mechanisms stems from the large pressure, hence density gradients throughout the length of the barrel, as well as the large temperature gradients between the plasma and the surrounding barrel walls, especially near the wall surface within a thermal boundary layer. In addition, the effects of each of the heat transfer modes is difficult, if not impossible to uncouple from each other. As the plasma travels down the barrel, the movement of the projectile changes the volume the plasma must occupy, thus further decreasing the pressure and temperature in the plasma itself, resulting in larger gradients in the direction of the flow and less plasma energy available to be imparted to the projectile.

Electrothermal guns operate in regions of temperature and pressure where more conventional artillery guns do not function. As a consequence of this, very little data for thermodynamic and opacity properties of hydrogen has been collected with guns in mind. However, much of the data used in this thesis was obtained from studies of stellar surfaces, which in many ways, has similar environmental factors to those in an electrothermal gun barrel.

In addition to losses due to heat transfer, viscous effects are also important and are studied. Problems associated with viscous effects include loss of flow energy and possible choking of the flow within the barrel region of the ELGG. Regimes of operation in which choking becomes a problem will be discussed and will be correlated with heat transfer studies as well.

CHAPTER II

BACKGROUND

In order to have a good understanding of what the system physically looks like, and what regions of the gun the considerations of heat transport are important, it is necessary to understand the operational characteristics of an electrothermal gun. There have been several concepts of electrothermal guns, and what differentiates one design from another is also important to understand. To begin with, an electrothermal gun is an advanced concept which involves addition of electrical energy via a plasma working fluid to a projectile. A working fluid is merely a gas or plasma which imparts energy, in this case, to a projectile.

The working fluid maintains the high temperatures and pressures necessary for the acceleration of a projectile down a gun barrel. The separation of the tasks of power generation and gas generation (both accomplished by one propellant source in a conventional gun approach) is inherently more flexible, allowing the tailoring of the working fluid to products with low molecular weight. In the case of the ELGG studied in this thesis, hydrogen is the propellant selected due to its very low molecular weight of 2.016×10^{-3} Kg/Kmol. The use of a low molecular weight propellant helps to minimize the pressure losses along the gun barrel.

A major advantage of the ELGG is that by separating the sources of thermal energy and working fluid, it is possible to select a working fluid based on its physical and thermodynamic characteristics without worry as to the energy-producing chemical reactions taking place. In addition, if the assumption that the rate of production of the working fluid is "directly related to the rate of deposition of electrical energy into the system, pressure time traces can be much more readily optimized in terms of producing maximum muzzle velocity for a fixed maximum allowable breech pressure."⁴

2.1 -- HISTORY AND CONFIGURATIONS OF ELECTROTHERMAL GUNS

"Thermal-electric, or ET propulsion as it is known today, has its origins in the 1950's and 60's when researchers attempted various means of utilizing electrical energy in the interior of a gun tube. Primarily, these experiments involved the conversion of electrical energy to thermal energy of the propelling gases in the breech or barrel."⁴³ During the 1970's, electromagnetic propulsion (EM) devices were studied and developed . Several key technologies were developed which were then adapted for use in ET devices, most notably the advanced power supplies required by both types of systems.

The 1980's saw increased interest in ET devices, and the development of the Combustion-Augmented Plasma (CAP) gun provided renewed study of this technology. The CAP gun is "typically a hybrid system combining the attributes of electrothermal and liquid propellant systems. Electrical energy stored in a capacitor bank is discharged through a breech mounted cartridge. A capillary section within the cartridge consists of

the anode/cathode terminals, consumable liner, and a solid fuel source. The electrical discharge strikes a plasma arc within the capillary which ablates the liner material and vaporizes the fuel source. A plasma jet is formed and accelerated through a nozzle and into the combustion chamber. Through the interaction of the rich plasma jet and liquid liner, thermal energy is transferred.¹⁵ A schematic of a typical CAP gun demonstrates its basic configuration:

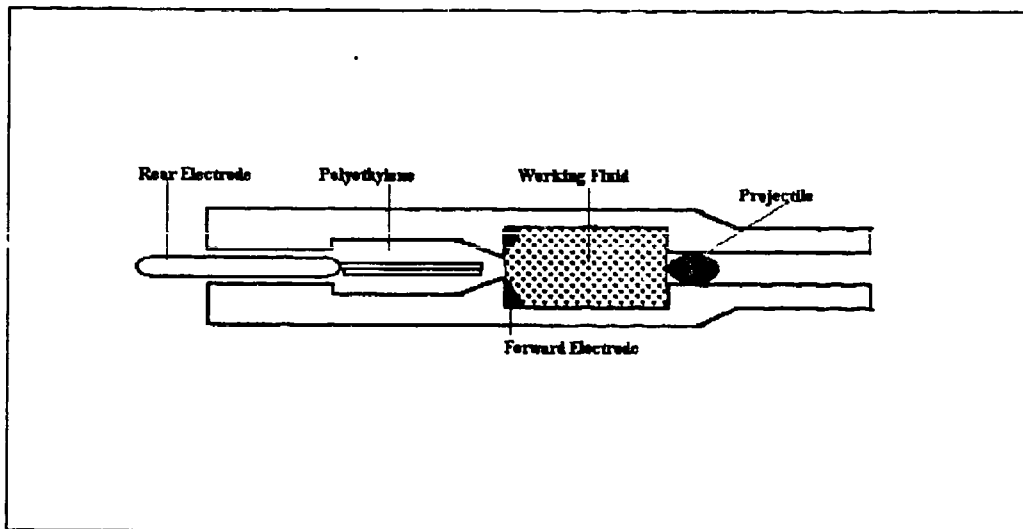


Figure 2.1 CAP Gun basic configuration¹⁶

The above description demonstrates that this type of electrothermal gun, although using a plasma as part of the gas used for projectile motion, is really a different type of chemical propellant device and is not too far removed from conventional artillery guns. Indeed, it has been discussed that the main fraction of energy within the accelerating gas is formed from chemical reactions, and the plasma has little if any effect on the energy

content of the gas. Juhsz notes that, "one strong specific concern [of the electrothermal community] was that with a large percentage of the propulsion energy coming from the chemical source (a common figure was a 75/25 chemical to electrical energy ratio) the electrothermal [CAP] gun could reduce to a modern version of the ill-fated bulk loaded liquid propellant gun concept."⁷

The system described in detail in this thesis uses hydrogen gas as the sole working fluid, unless noted otherwise, and does not rely on any chemical reactions for the development of the plasma. Typically the hydrogen is at stagnation pressures of 850 to 1,150 atmospheres and stagnation temperatures initially between one eV and three eV. This system is generally configured as a chamber separated from a tube (the muzzle) by a diaphragm designed to break at a given pressure.

Hydrogen gas is introduced into the "combustion chamber" (or capillary, or breech), at some initial pressure and temperature, and then hydrogen plasma is created by the interaction of the initial hydrogen "charge" with an electric arc created between an annular anode casing, or nozzle, and a cathode probe. A wire connects the anode and cathode to facilitate the start of the arc discharge. This wire explodes with the application of electrical current (usually within the first few microseconds), but its short life span is sufficient to create the path for the arc to develop. It is assumed in this thesis that the mass of the exploding wire atoms does not significantly impact the propellant mass, and therefore does not alter the molecular weight of the working fluid, nor does it impact the thermal characteristics and the ratio of specific heats of the hydrogen gas.

Once initiated, the arc is self sustaining as long as electrical energy is provided. "The actual thermal conversion takes place when electrons which are driven from one end of the capillary [or breech] to the other collide with ions or atoms in the plasma. This increases the energy of the plasma constituents which is directly related to the plasma temperature. The collision rate and the number of electrons available define the electrical resistance of the discharge so that the usual relation for ohmic heating holds."¹ It is assumed that the electrical energy is uniformly distributed throughout the working fluid.

At a specified pressure (usually between 850 and 1,150 atmospheres), the diaphragm breaks, allowing the energetic plasma to expand either directly into the ELGG barrel or through a convergent-divergent nozzle and into the barrel where the fluid interacts with the projectile. This interaction takes place as long as the projectile remains in the muzzle, and the effects of muzzle wall interactions, as well as the increasing volume due to projectile motion and heat transfer, must be taken into account. The main components of the ELGG are the electric power source (capacitor bank), an electrical switch, the "combustion or arc chamber" with anode casing and cathode probe, diaphragm, muzzle or barrel, and the projectile. The following figure graphically illustrates a schematic a typical ELGG. Note that this figure does not illustrate a convergent-divergent nozzle section prior to the barrel inlet.

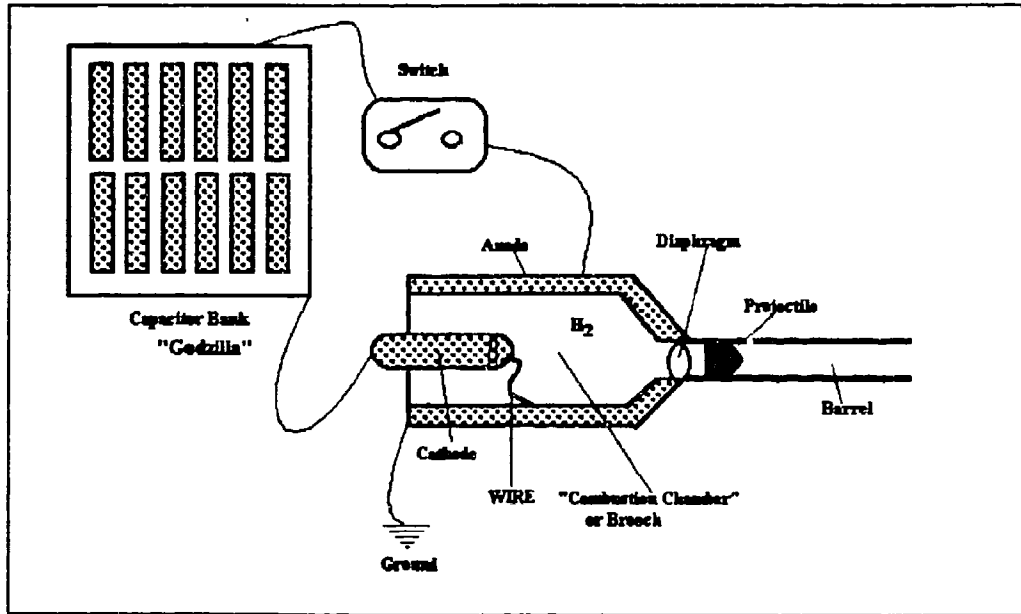


Figure 2.2 Electrothermal Light Gas Gun configuration

The kinetic energy transferred to the projectile is a function of the velocity attained throughout the muzzle. "It is generally accepted that the practical velocity limit of chemical propulsion is on the order of two kilometers per second. It is also thought [by the requirements for higher velocity weaponry] that this may not be adequate. Three factors, propellant energy density, progressivity, and the partitioning of kinetic energy between the propellant gases and projectile are seen as potential contributors to this velocity limit."¹

"The first parameter, propellant energy, is determined by the heats of formation and the relative amounts of propellant constituents. Given the mature state of the art in energetic materials, extending the energy limits of new formulations significantly may not

energetic materials, extending the energy limits of new formulations significantly may not be practical. While formulations with higher energies are certainly possible, their potentially increased hazard properties may not be acceptable."¹

The second parameter, progressivity, "i.e. the increase in gas generation rate as burning progresses concerns the ceiling on the amount of propellant which may be profitably burned in the gun."¹ Since progressivity is governed by the chemistry or the granulation of the propellant, there is an optimum limit to which a chemical propellant can impart kinetic energy to the projectile. The energy limitations inherent in the propellant chemistry are thereby avoided by the use of the electrothermal gun.

"The third parameter, partitioning of kinetic energy between the propellant gases and the projectile becomes important due to the high propellant mass (charge) to projectile mass ratios (C/M) required to attain high velocities. In interior ballistics it is generally estimated that for C/M approxir. ately 1, the kinetic energy of the propellant gases is about one third the projectile kinetic energy. Above a C/M of three, the kinetic energy of the propellant gases begins to exceed the kinetic energy of the projectile, making high velocity systems increasingly less efficient."¹

The following figure graphically illustrates the effects of changing any combination of the propellant molecular mass, C, the sound speed of the working fluid, A, the projectile mass ,M , and the projectile muzzle velocity, V, has on the gas expansion ratio, E.²

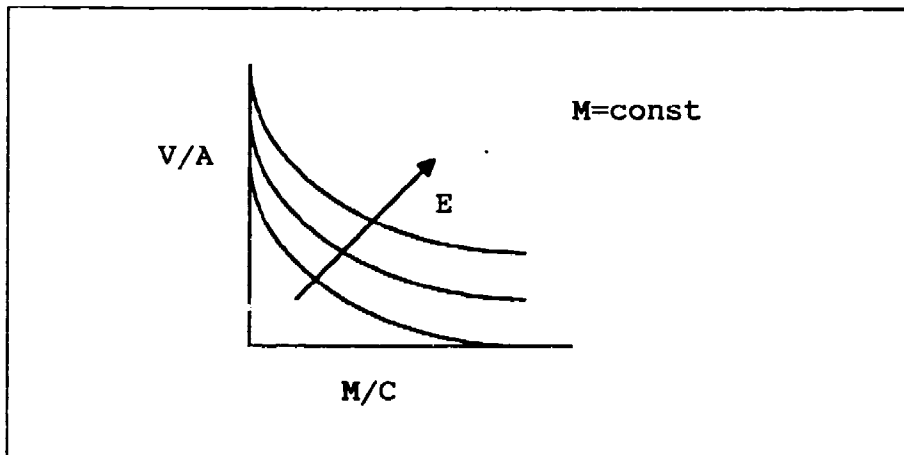


Figure 2.3 Correlation of main parameters²

"The degree of expansion, E, is a parameter. Sound speed, A, in electric-discharge gun appears to be much more than powder [conventional propellant] gun mainly because of mass of light gases is considerably less, and to be considerably higher than in piston light-gas gun due to rather high temperature. Therefore, at other equal (sic.) conditions, the higher muzzle velocity is obtained."² The following table illustrates the advantages of the ELGG over conventional powder (i.e. chemical reaction dependent) guns and piston light gas guns.

Table 2.1 Comparison of three different types of guns. (Note conventional propellant has a relative number of 1 for comparison.)²

Parameter	Conventional powder gun	Piston light gas gun	ELGG
Minimum molecular mass of gas	1	0.06	0.06
Maximum temperature of gas	1	0.3 - 0.8	1.5 - 2.0
Chamber speed of sound, A	1	2	4 - 5
Relative mass of projectile, M/C	1	2 - 3	5 - 6
Maximum projectile muzzle velocity at the same expansion ratio, E	1	1.5 - 2	2 - 3
Weight of barrel	1	2	1

The electrothermal gun concept is a way of avoiding the disadvantages of conventional propellant and offer the ability to achieve higher velocity projectiles. Since electrothermal guns use gas pressure to impart motion to the projectile, it has been speculated that conventional barrel technologies and materials could be used. However, this is a discussion which needs to be analyzed by considering the heat transfer from the hot

plasma, which will be accomplished in chapters three and four. Typical electrothermal plasma temperatures can range from 10,000K (about 1 eV) to 34,000K (about 3 eV), whereas typical conventional gun flame temperatures are in the 4,000K to 5,000K regime.

"For a conventional solid propellant gun the constraining factors on performance in terms of muzzle velocity are gun strength, chamber volume and tube length as well as the combustion characteristics of the propellant. The gun chamber volume limits the pressures at which the gun can operate. Burning characteristics of the propellant determine the pressure distribution throughout the gun. An electrothermal gun is also limited by similar constraints. Gun strength again limits operational pressures. The rate and magnitude of the electrical input in combination with properties of the working fluid determine the pressure profiles in the gun. The [ELGG] differs from the solid propellant gun, however, since there is no limitation, at least in theory, on the total available energy for the system."⁸

"Although the amount of electrical energy input is theoretically unlimited, from the practical point of view, the maximum operating gun temperature limits the amount of which can be introduced into the system. In fact, thermal management for an [ELGG] gun is much more difficult than for conventional systems. In the conventional gun, the overall temperature is essentially limited by propellant flame temperature. Even if the rate of energy input increases by increasing the burning rate of the propellant, the gun temperature is still limited by the flame temperature which is independent of the burning rate. For the [ELGG] gun, on the other hand, there is no such upper limit. The temperature of the gases resulting from the ... electrically heated plasma ... is an

increasing function of the amount of electrical energy being transmitted to a unit mass of working fluid. Thus, temperature limitation results only through controlling the magnitude and rate of electrical energy input in combination with the mass and properties of the working fluid."⁸ From this discussion, it is apparent that the magnitude and the rate of electrical energy input, and the properties of the working fluid are the controlling factors in the gun pressure profiles which determine projectile velocity and overall gun temperature.

2.2 – HYDROGEN PLASMA AS A WORKING FLUID

The question of why choose hydrogen gas as the main working fluid is easily answered by considering what the ideal working fluid would be. "It is particularly desirable that gun propellants have low molecular weight since such products result in minimization of the amount of product mass which has to be accelerated through the gun barrel along with the projectile. Accordingly, low molecular weight products result in reduction of the amount of energy "wasted" as propellant product kinetic energy for a given imparted projectile kinetic energy. Looked at another way, low molecular weight products result in reduced pressure differential from the gun breech to the base of the projectile in the gun barrel. Since maximum allowable breech pressure is an important gun design parameter, this reduction in pressure gradient results in increased application of force to the projectile base for a given gun design."⁴

The superiority to conventional chemical propulsion goes beyond simply reducing the molecular weight and pressure gradients of the plasma. Higher propellant gas energies, improved ballistic pressure-time profile tailoring, higher sound speeds and lower gas temperatures are all benefits of using hydrogen. A way to measure the effectiveness of projectile acceleration with various propellants is to compute the impetus. The impetus is defined as "an index generally used by ballisticians to describe the potential of a propellant to do work."¹ It is defined as:

$$I = RT/m \quad (2.1)$$

R is the universal gas constant, T is the adiabatic flame temperature and m is the molecular weight of the propellant gas. By considering this equation, it is apparent that to maximize the impetus, either the temperature can be increased, or the molecular weight can be decreased. "For conventional propellants, T and M are determined by the propellant chemistry. In the ELGG, however, the temperature can be increased by introducing more electrical energy into the working fluid. This is an enormous potential advantage."¹ The following table demonstrates the differences in the impetus for JA2 (an Army artillery chemical gun propellant), hydrogen gas, water, and carbon dioxide. All are calculated at a temperature of 3,450K.¹

Table 2.2 Impetus calculations for various propellants¹

Material (Species)	Molecular Weight of Species	Impetus (J/g)
JA 2	24.9	1,142
H ₂	2	14,342
H ₂ O	18	1,594
CO ₂	44	652

At the flame temperature of 3,450K, the impetus of pure hydrogen would be nine times greater than pure water, and more interestingly, it is over twelve times greater than that available from JA 2. Clearly, lowering of the molecular weight of propulsion gases has a significant beneficial effect on impetus. "To the extent that ELGG can take advantage of lower molecular weight propelling gases, therefore, it could offer significant increases in ballistic performance.¹ The the ELGG could favorably increase the kinetic energy distribution between the projectile and the propellant. This is accomplished by increasing the impetus with a low molecular weight working fluid. The kinetic energy budget in a gun may be described as:

$$KE_{tot} = KE_{projectile} + KE_{gas} \quad (2.2)$$

$$KE_{tot} = 1/2(M V^2 (1 + C/3M)) \quad (2.3)$$

M is the projectile mass, V is the projectile velocity, and C is the propellant charge mass. "With higher impetus gasses (working fluids) the value of C decreases for equivalent performance, altering the kinetic energy distribution in favor of the projectile.

For example, in conventional propellants, C/M ratios of approximately 3 are required to obtain velocities of 2 km/sec. This means that in conventional ballistics there is more kinetic energy in the propellant gases than the projectile once a velocity of 2 km/sec is exceeded. Lower molecular weight ELGG working fluids leading to reduced C, therefore, could present a significant advantage at high muzzle velocities.¹ Clearly from this discussion, hydrogen is the propellant of choice for these considerations.

Unfortunately, it is not a simple matter of simply choosing a particular gas to use as the working fluid based solely on a high sound speed and low molecular mass. The interior of the ELGG barrel experiences rapid changes in working fluid temperature, pressure and density due to the various heat loss mechanisms and the viscous effects. This changing environment causes drastic changes in the thermodynamic properties of the working fluid, as well as the optical thickness associated with radiation heat transport. For example, the ratio of specific heats for hydrogen can vary by an order of magnitude simply from a temperature change from 10,000 K to 7,000K. This magnitude (or larger) of temperature decrease can be expected throughout the length of the ELGG barrel.

Additionally, the changes in the thermodynamic properties of the working fluid greatly affect the flow characteristics within the barrel region, allowing for the possibility of shock development and thus choked flow prior to the exit of the barrel. The boundary layer growth and development within the tube is highly dependent on the initial conditions of the fluid entering the barrel, as well as the conditions existing at any point in the flow up to the barrel exit.

2.3 – POWER SOURCE FOR THE ELECTROTHERMAL LIGHT GAS GUN

At the Aeronautical and Astronautical Research Laboratory of The Ohio State University a gigawatt-level, quasi-steady, high speed flow capacitor bank and facility commonly referred to as "Godzilla" has been constructed. "A flexible arrangement has been adopted involving 2,100, 43 microfarad capacitors, at 6 kilovolts, that allows giga-watt power levels (into a matched load) at 333 kilo-amperes and 3,000 volts, for 1.63 milliseconds, and various lower current, longer pulsetime combinations, (e.g., 111 kilo-amperes for 4.9 milliseconds)." ⁹

Aluminum support racks were obtained and assembled (each rack or bank is 28 feet long, 14 feet high, and 4 feet deep) into three equal sections. "Construction of the racks allowed seven equal horizontal rows on each side of a rack. These rows are in turn separated into five sections supporting ten capacitors each." ⁹

The capacitance per section is calculated to be approximately 3 micro-faradays. The charging voltage of 6 kilovolts and power input using a matched load of 10^9 Watts, the total transmission line impedance is 9 milliohms. ⁹ "The two-way transit time in the line is 1.625 milliseconds, which corresponds to the release of 1.625 Mega Joules (MJ) at 1 Giga-watt. The total current is 333 Kilo-amperes or 111 Kilo-amperes per line." ⁹

By disconnecting two banks from the system, 111 Kilo-amperes can be provided into a 27 milliohm load for 4.875 milliseconds. With two banks connected, an intermediate 222 Kilo-amperes can be provided for 3.25 milliseconds. ⁹ The technical specifications of "Godzilla" are well within the energy requirements for the electrothermal gun, and make

it an obvious choice for electrical energy, at least for short duration testing. For development of the heat transfer studies in following chapters, the technical specifications of "Godzilla" will be used.

CHAPTER III

APPROACH

3.1 – DESCRIPTION OF PLASMA STATE

Before continuing the study of the plasma contained within the electrothermal gun, the static and equilibrium properties of the plasma must be established. For example, the population of ions and electrons that exist at any specified total pressure and temperature must be calculated. This can be accomplished by beginning with the assumption that the gas is in thermodynamic equilibrium, and then move on to conditions that do not satisfy this assumption.

Using the Saha equation which determines the fraction of particles that have been ionized in thermal equilibrium, we can determine the degree of ionization of the plasma. If the ionization is high, then a significant amount of energy is used for this process and represents a loss that could otherwise have been used for projectile motion. The following is a variation of the familiar Saha equation:¹⁰

$$X = \sqrt{\frac{K_H}{1+K_H}} \quad (3.1)$$

$$K_H = \frac{u_1}{u_0} \frac{2}{P_{\text{gas}}} \frac{(2\pi m_e)^{\frac{3}{2}}}{h^3} (kT)^{\frac{5}{2}} \exp\left[-\frac{\chi_H}{kT}\right] \quad (3.2)$$

where:

- u_1 = Partition function for ionized hydrogen ($= 1$)
- u_0 = Partition function for ground state hydrogen ($= 2$)
- χ_H = Ionization energy for hydrogen ($= 13.6 \text{ eV}$)
- P_{gas} = Total pressure of the gas (in Pascal)
- m_e = Rest mass of electron ($= 9.11 \times 10^{-31} \text{ Kg}$)
- k = Planck's Constant ($= 1.38 \times 10^{-23} \text{ J/K}$)
- h = Boltzmann Constant ($= 6.63 \times 10^{-34} \text{ J sec}$)
- T = Total single temperature (in K)
- X = Degree of ionization

"In order to compute the degree of ionization, the partition function has to be known.

For this we need the statistical weights of the different states of excitation, which are given by quantum mechanics. Since the higher states contribute little to the partition function, we may approximate it by the weight of the ground state, $u_0 g_{0,0} = 2$, while for ionized hydrogen, $u_1 = 1$.¹⁰ Since K_H increases with temperature and decreases with pressure, we can see from the above equations that the degree of ionization increases with temperature and decreases with the gas pressure. This can be easily understood: with increasing temperature the collisions become more violent, and the process of "kicking off" the electrons from the atoms more frequent. If, on the other hand, the temperature is kept constant but the pressure increases, then the probability grows that the ion meets an electron and recombines.¹⁰

3.2 – DESCRIPTION OF ENERGY LOSS MECHANISMS

As a starting point to understanding the heat transfer process within the electrothermal gun, it is helpful to model the gun as a control volume and illustrate the first law of thermodynamics. The following is an illustration of the model:

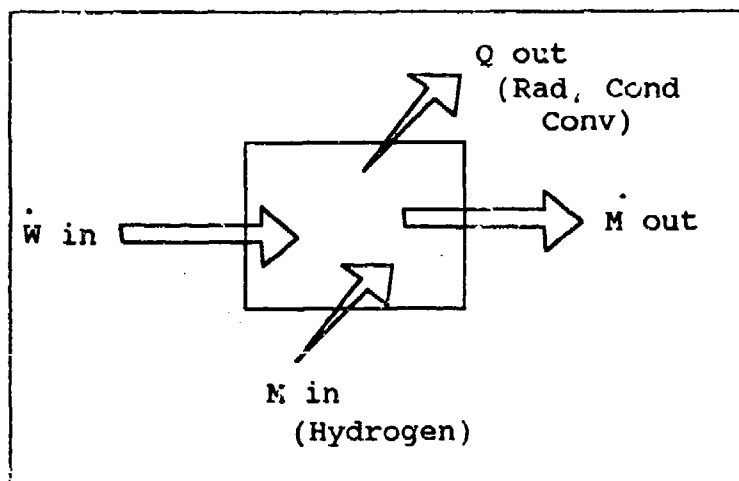


Figure 3.1 First Law of Thermodynamics model of Electrothermal Gun

The study of heat transfer concerns the rate term Q_{out} in the above figure. There are three general types of heat transfer mechanisms operating within the electrothermal gun barrel region. These are 1) thermal radiation from the plasma to the walls and projectile, 2) thermal conduction from the plasma to the walls and projectile, and 3) forced convection due to the motion of the plasma.

Conduction is caused by the fact that molecules in higher temperature regions have higher kinetic energies than molecules in adjacent, but cooler temperature. These higher energy molecules transmit some of their energy to the cooler adjacent molecules through

collisions. Conduction can occur both internally (among particles making up the fluid), or by contact with another substance, such as a ELGG barrel wall.

In convection, heat is carried from a higher to a lower temperature region within a moving fluid. This is a macroscopic effect, and occurs in one of two main ways. The first is natural convection, which is caused simply because of density differences caused by temperature gradients. The second is forced convection, which is caused by some external mechanism, such as an electric arc heating a fluid to high temperatures, then expanding rapidly down the barrel.

In contrast to conduction and convection which rely on collisions or bulk movement of the fluid, radiation allows heat energy to travel over distances without the aid of contact. Radiation operates by the expelling and recapturing photons.

In addition to the loss of energy due to the various heat transfer mechanisms detailed above, viscous effects represent another form of energy loss. The forces of friction act as a shear stress between the walls and the moving fluid, which in essence drags the fluid velocity near the wall from the freestream value in the mid-line of the tube to zero at the face of the wall. This velocity gradient forms a boundary layer in which heat transfer by conduction takes place, as well as serves to decrease the available area for the freestream to travel along the interior of the tube.

3.3 -- DEVELOPMENT OF MODEL

Development of a model for the heat loss in a fluid traversing a gun barrel requires the adoption of several assumptions in order to make the equations of motion and equation of state tractable. The purpose of this model is, in effect, to provide insight into the actual processes occurring in the barrel region of an ELGG. These equations and the model to be developed will be used in order to verify and compare results given in MACH2, a 2 1/2 dimensional magnetohydrodynamic simulation code for problems with complex shapes and areas of operation.

To develop this model, the method of a one dimensional compressible flow through a constant area duct will be used. Thus, it will be assumed that the flow variables such as pressure or temperature vary in the flow direction only. Consider the flow through a one dimensional control volume as shown in the following figure:

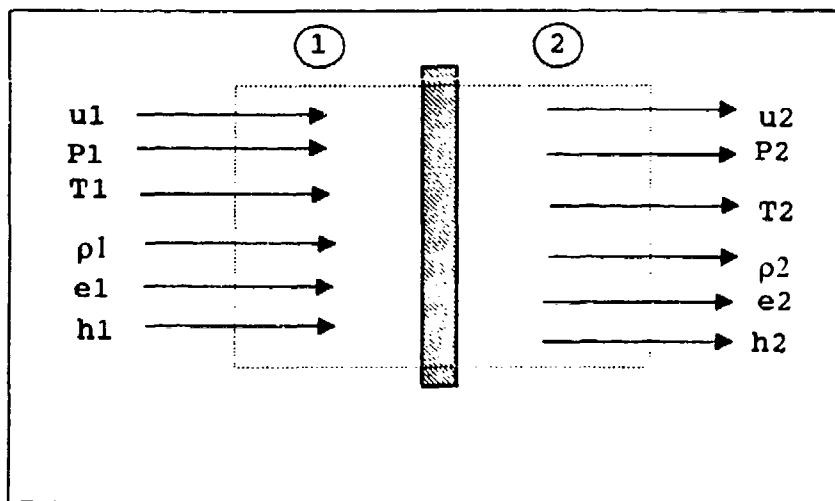


Figure 3.2 Flow through control volume.¹¹

Consider this region as one of heat addition or, in this case, heat extraction. What this is suggesting is that flow properties change as a function of the position along the flow direction. Since the flow is assumed to be one dimensional, the flow properties are constant on either side of the region of heat loss bounded by the control volume. The areas are equal since we are dealing with a constant area barrel. It will be assumed that the flow is steady, requiring all time derivatives to be zero.

With these assumptions, the following equations of motion result.¹¹

$$\text{CONTINUITY: } \rho_1 A_1 u_1 = \rho_2 A_2 u_2 \quad (3.3)$$

$$\text{MOMENTUM: } P_1 + \rho_1 u_1^2 = P_2 + \rho_2 u_2^2 \quad (3.4)$$

$$\text{ENERGY: } h_1 + \frac{u_1^2}{2} + q = h_2 + \frac{u_2^2}{2} \quad (3.5)$$

In addition to the equations of motion, it will be assumed that the fluids used are calorically perfect and are represented by the following equation of state.¹¹

$$\text{EQUATION OF STATE: } P = \rho R T \quad (3.6)$$

In order to complete the development of the one dimensional model, the first and second laws of thermodynamics must be discussed. Consider a system which has a fixed amount of heat added for an incremental amount of work done on the system by the

surroundings. It is assumed that the processes within this model are isentropic unless otherwise specified. The change in specific internal energy is thus written as, using v , to be the specific volume:¹¹

$$de = dq - pdv \quad (3.7)$$

The second law of thermodynamics is important in that it describes the direction a process will proceed. This directed movement of a process is termed entropy, and is defined as:

$$ds = \frac{\delta q}{T} + ds_{(irrev)} \quad (3.8)$$

From this equation, δq is an incremental amount of heat added reversibly to the system, and $ds_{(unrev)}$ is a dissipative loss which is not reversible, such as friction. This suggests that any dissipative process increases the entropy, and we can see that at best, entropy merely remains constant. For an adiabatic process, δq is equal to zero.

Using relations for thermally perfect gasses in place of de and dh , we find:¹¹

$$s_2 - s_1 = C_p \ln\left(\frac{T_2}{T_1}\right) - R \ln\left(\frac{P_2}{P_1}\right) \quad (3.9)$$

or

$$s_2 - s_1 = C_v \ln\left(\frac{T_2}{T_1}\right) + R \ln\left(\frac{V_2}{V_1}\right) \quad (3.10)$$

These two equations allow the calculation of the change in entropy between two states of a calorically perfect gas in terms of either pressure or volume and temperature. For an isentropic process (by definition, $ds=0$), the entropy is constant throughout the system. From this, important and useful relations are developed and are:¹¹

$$\frac{P_2}{P_1} = \left(\frac{\rho_2}{\rho_1}\right)^\gamma = \left(\frac{T_2}{T_1}\right)^{\frac{\gamma}{\gamma-1}} \quad (3.11)$$

This set of relations is valuable in that it relates the flow properties of pressure, temperature, and density at different locations in the flow. Using the stagnation conditions, we can relate the stagnation enthalpy to the static flow properties.¹¹

$$h_o = C_p T_o \quad (3.12)$$

$$C_p T + \frac{u^2}{2} = C_p T_o \quad (3.13)$$

In this equation, T_o is the stagnation temperature and would exist if we were able to adiabatically bring the fluid element to rest. The following useful relations can be obtained by using combinations of previous equations.¹¹

$$\frac{T_o}{T} = 1 + \frac{\gamma-1}{2} M^2 \quad (3.14)$$

$$\frac{P_o}{P} = \left(1 + \frac{\gamma-1}{2} M^2\right)^{\frac{\gamma}{\gamma-1}} \quad (3.15)$$

$$\frac{\rho_o}{\rho} = \left(1 + \frac{\gamma-1}{2} M^2\right)^{\frac{1}{\gamma-1}} \quad (3.16)$$

These relations do not require that the flow be adiabatic or isentropic, which allows them to be used throughout the muzzle section of the ELGG and for various conditions of the flow. However, if the general flow field is isentropic throughout, then T_o , P_o , and ρ_o are constant at all locations in the flow. The change in entropy is related to the change in stagnation pressure from the following equation:¹¹

$$s_2 - s_1 = -R \ln\left(\frac{P_{o2}}{P_{o1}}\right) \quad (3.17)$$

The change in specific energy is given by the Hugoniot equation as follows:¹¹

$$e_2 - e_1 = \frac{P_1 + P_2}{2} \left(\frac{1}{\rho_1} - \frac{1}{\rho_2} \right) \quad (3.18)$$

From these equations of motion, the equation of state, thermodynamic relations, and derived fluid flow relations, the model is now capable of being tailored for use in calculation of the various heat transfer modes, and can be adapted for viscous effects.

3.4 – VISCOUS EFFECTS MODEL

In order to develop a model to account for the frictional effects of flow through a gun barrel, assumptions need to be made which will make the equations analytically solvable.

Consider a one dimensional flow of a compressible fluid in a pipe. It is assumed that the flow is steady, adiabatic, and shockless. The assumption of shockless flow is important and will be discussed shortly. If this fluid is viscous, the friction acting between the moving fluid and barrel will cause the flow properties to vary as they travel down the tube.

If this frictional effect is modeled as shear stress at the wall acting on the fluid with an assumed uniform set of properties across the cross section, then the following set of equations of motion may be used:¹¹

$$\text{CONTINUITY: } \rho_1 u_1 A_1 = \rho_2 u_2 A_2 \quad (3.19)$$

$$\text{MOMENTUM: } P_1 + \rho_1 u_1^2 = P_2 + \rho_2 u_2^2 + \frac{4}{D} \int \tau_w dx \quad (3.20)$$

where: $\frac{4}{D} \int \tau_w dx$ is evaluated from 0 to L and accounts for frictional losses.

$$\text{ENERGY: } h_1 + \frac{u_1^2}{2} = h_2 + \frac{u_2^2}{2} \quad (3.21)$$

$$\text{EQUATION OF STATE: } P = \rho R T \quad (3.22)$$

The modification of the momentum equation is due to the shear stress, τ_w , acting on the surface of the gun barrel, thus imparting a surface force in the integral formation of the momentum equation. The frictional effect added to the momentum equation can be rewritten by considering the total pressure drop over a distance dx:

$$dp = -4f \frac{\rho V^2}{2D} dx - \rho V dV \quad (3.23)$$

where:
 dp = total pressure change
 f = friction factor (dimensionless)
 ρ = density
 V = velocity
 D = hydraulic diameter
 dx = length of tube
 dV = incremental velocity change

By definition, the friction factor, f , is:¹¹

$$f = \frac{\tau}{\frac{\rho V^2}{2}} \quad (3.24)$$

Using the constant area duct assumption, and the perfect gas equation, it can be shown that:¹¹

$$\frac{4fL_{max}}{D} = \int \frac{2(1-M^2)}{M^3 \left\{ \left[\frac{(\gamma-1)}{2} \right] M^2 + 1 \right\} \gamma} \quad (3.25)$$

The frictional factor depends greatly on the flow Reynolds number as well as the Mach number and surface roughness, among others. The effect the Reynolds number has is to determine whether the flow is laminar or turbulent. The surface roughness is a measure of the hydraulic smoothness of the interior of the gun barrel. For this thesis, it will be assumed that the surface is hydraulically smooth, meaning that the surface roughness is less than .001 times the interior diameter of the tube.¹¹

If the inlet flow is supersonic, friction will tend to drive the Mach number to 1. If the flow is subsonic, the friction will tend to bring the mach number up to 1. "Whether or not [the Mach number] will become unity depends on the extent of the friction, which is actually dependent on the length of the pipe."¹²

If the actual pipe or barrel length exceeds the theoretical length necessary for the inlet Mach number to be driven to Mach 1, choking will occur, and if the inlet flow is supersonic, then shock phenomena will develop and may progress upstream within the barrel. When choking occurs, the flow must readjust itself since the mass flow has reached a maximum and cannot be increased further. There are two main ways in which this can be eliminated. For supersonic flow, the shock wave formation can be accepted, and allow it to "correct" the flow inlet conditions, suffering a loss in efficiency, or the inlet conditions can be adjusted in advance, allowing the Mach number to at most become sonic at the exit of the barrel. This would represent the maximum mass flow possible without shock formation (supersonic flow) and thus provide the maximum gas enthalpy which would theoretically be able to provide the best possible projectile acceleration. Note that Mach one can be approached from either supersonic or subsonic inlet conditions.

The following figure shows a graphical analysis of the effect of various frictional factors on the theoretical maximum length of pipe for various inlet Mach numbers. The full theoretical length analysis and calculated data is located in appendix J.

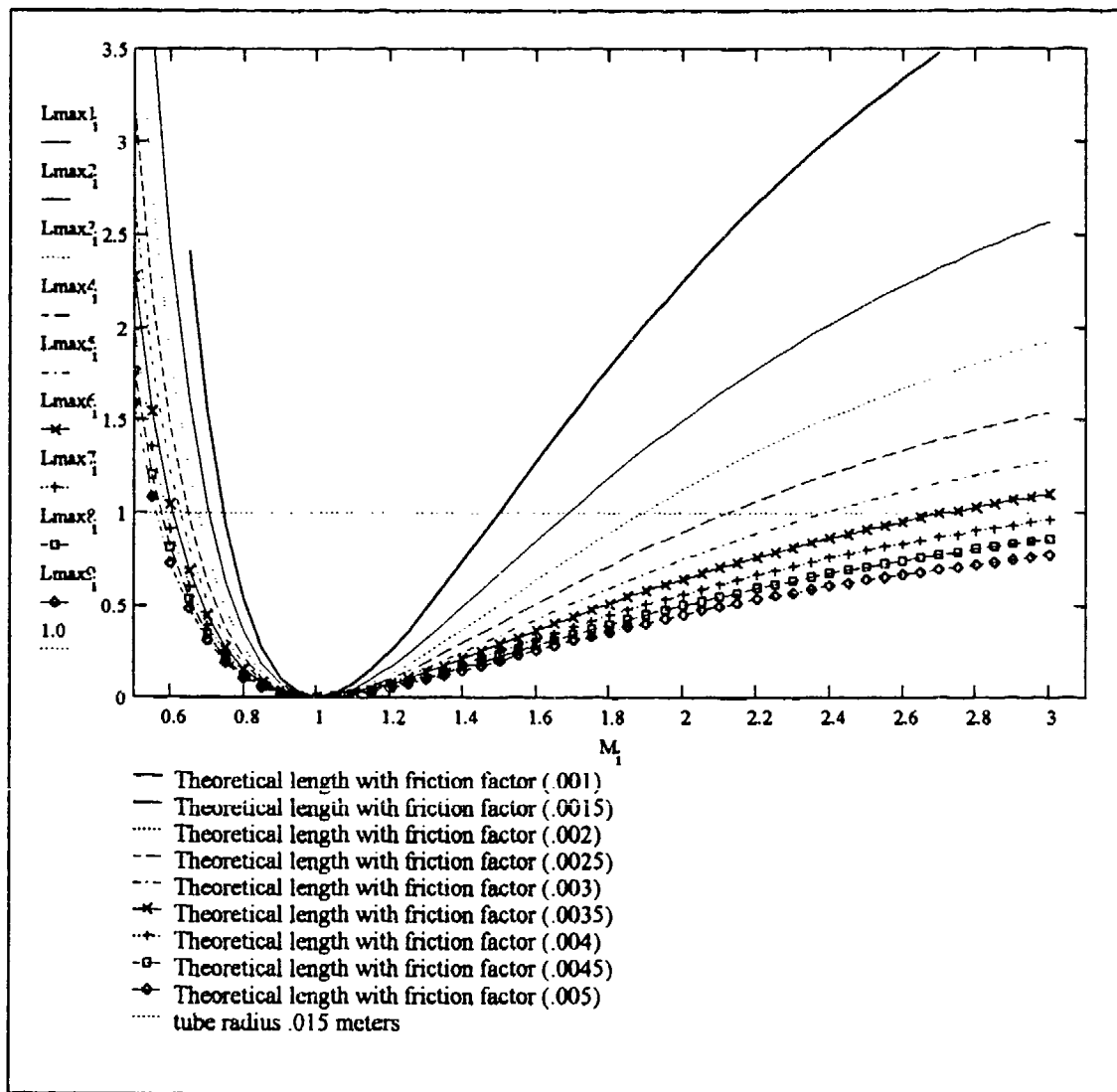


Figure 3.3 Effect of friction factor on theoretical length of pipe

The final consideration is the selection of the average friction factor which depends on whether the flow is laminar or turbulent. "In almost all practical cases, the flow is turbulent, and the variation of f must be obtained empirically. Anderson further suggests that for our purposes, it is reasonable to assume an approximate constant value of .005"¹³

Experiments by Keenan and Neumann were undertaken in the hopes of determining the turbulent friction factor for flow in pipes. "They report that for supersonic flow of air in a tube, the friction coefficient is influenced as usual by the Reynolds number and a dimensionless parameter L/D, in which L is the length of the test section and D is the inside diameter of the tube."¹² They also discovered that at high velocities, the Mach number is also an influencing factor. "Keenan and Neumann studied frictional phenomena in smooth pipes for Mach numbers from 0.22 to 3.87 and for Reynolds numbers from 1×10^5 to 8.7×10^5 . They found that at supersonic speeds, the results were influenced greatly by the presence of shock waves."¹²

"They concluded further that, when the ratio L/D was greater than 50.0, the friction factor was approximately equal to the friction factor for incompressible flow for the same Reynolds number. They found also that supersonic flow can rarely be maintained if the L/D ratio is greater than 50.0."¹² Thus it is determined that Mach number acts as a limitation to the possible range of L/D values.

Keenan and Neumann conclude that the coefficient of friction is not well understood for turbulent flow, mostly due to the fact that the friction effects can vary from place to place in turbulent flow. This necessitates the consideration of an apparent or average friction factor rather than a local one. They suggest that for most supersonic flow, a value for the friction factor between .002 and .003 in hydraulically smooth pipes is consistent with their experimental data.¹² In fact, values of the friction factor for similar systems have been shown to range from .002 to .005, so this is the range of values that will be used for this thesis.

3.5 – CONDUCTIVE AND RADIATIVE HEAT TRANSFER MODEL

These two different heat transfer modes have been grouped together for an important reason. The basic model to be discussed is based on a bulk fluid flow assumption, which is equally valid for conduction and radiation, except where noted. The heat dissipation term, q , to be introduced into the energy equation can be either from conduction, radiation, or a combination of both.

In a similar manner to that used in the development of the viscous effects model, a model is developed for the loss of heat energy from the bulk working fluid. For heat transfer calculations, note that inside the control volume illustrated in figure 3.2, something is happening which causes the flow properties in region 2 to be different to those in region 1. This is caused by the loss of heat energy due to the high temperature in this region in relation to the barrel wall, which is assumed to be at a constant temperature of 300K. By losing heat energy by conduction or radiation (or a combination of both), the enthalpy and specific internal energy are decreased and an increase in entropy results.

The following one dimensional flow equations are similar to those for friction, except there is not an extra term in the momentum equation (viscous effects are neglected) and the energy equation now contains the quantity, q . This is the heat loss per unit mass.

$$\text{CONTINUITY} \quad \rho_1 u_1 A_1 = \rho_2 u_2 A_2 \quad (3.26)$$

$$\text{MOMENTUM} \quad P_1 + \rho_1 u_1^2 = P_2 + \rho_2 u_2^2 \quad (3.27)$$

ENERGY

$$h_1 + \frac{u_1^2}{2} + q = h_2 + \frac{u_2^2}{2} \quad (3.28)$$

For a calorically perfect gas, it is possible to achieve an analytical solution which in many ways is similar to that described for friction. However, there are some important differences. Unlike friction, heat can be lost or gained, and the process can be reversed whereas friction only results in a loss of energy. For heat loss, which will be the nature of the flow through the barrel, the Mach number diverges away from a Mach = 1 condition. Thus, unlike the effects caused by friction, choking of the flow will not occur because of heat loss.¹¹

3.6 – CONDUCTIVE AND CONVECTIVE HEAT TRANSFER

The heat exchange between a wall and a fluid whose motion has been caused by external forces is called forced convection heat transfer. The resistance to heat transfer is concentrated primarily in a thin layer immediately adjacent to the surface of the boundary. The heat transfer is determined by the intensity of the conductive and convective transport within this boundary layer. Thus, the heat transfer coefficient is determined essentially by the thickness of the boundary layer. The boundary layer thickness is dependent on the type of fluid flow which occurs along the surface. With forced convection, the differential equations which describes the fluid and heat flow processes yield the result that the flow field and hence the development of the boundary layer are independent of the heat transfer if the properties of the fluid are temperature independent. However, in general, all properties of the fluid are temperature dependent, but as long as the internal temperature differences are not extreme, the temperature dependence of the property values can be neglected. For this investigation, it will be assumed that the temperature dependence can be accounted for by use of tabulated thermodynamic data provided in appendix D.

For the development of a simplified model to describe the convective and conductive heat transfer within the ELGG, many fluid properties, such as mass, viscosity, and specific heats, have been taken into account and actual experimental data is used whenever possible. Density is also included as a property in these calculations. For a gas, density is highly pressure dependent, especially at high velocities. Generally, the

limit for which density becomes highly pressure dependent is approximately one third of the sonic velocity.

3.6.1 – BOUNDARY LAYER DISCUSSION

There are two concepts in fluid flow theory which are essential for understanding heat transfer. These are the concept of the boundary layer and the concept of turbulence. Due to viscosity effects, fluids suffer frictional forces while in motion. However, real situations can be approximated by assuming a frictionless fluid. Later, the effects of viscosity will be added.

There are two kinds of forces that will be considered in the development of the model. These are forces of inertia and forces of pressure. Gravity, centrifugal force and electrical forces will be neglected. Additional forces exist in real fluids which are caused by viscosity. These are shear stresses between individual stream lines which move at different velocities. The stress, τ , can be described by Newton's equation:

$$\tau = \nu \frac{\partial u}{\partial y} \quad \nu = \frac{\mu}{\rho} \quad (3.29)$$

The factor, μ , is the dynamic viscosity, ρ is the fluid density, ν is the kinematic viscosity, and the shear stress is seen to be directly proportional to the velocity gradient normal to the wall. The kinematic viscosity of gasses is, by the ideal gas law, inversely proportional to pressure. Since numerical values of the viscosity are comparatively small,

high shear stresses in the flow, according to Newton's equation, will exist only where large velocity gradients exist.

There are basically two different forms of flow within the ELGG barrel region: laminar and turbulent. In laminar flow, the individual streamlines are orderly and parallel, while the turbulent case sees the streamlines intermingled in an irregular way. Convective heat exchange from the working fluid to the barrel walls is enhanced by the fluctuation and turmoil in the turbulent region. This, of course, makes the convective heat transfer in a turbulent flow considerably higher than it would otherwise be in a laminar flow.

Turbulent flow may also exist within the boundary layer.

If fluids of different viscosity's are considered , the laminar-turbulent transition occurs at $U_c X_c / v$, which has been known for a long time as the Reynolds number, R_c . Typically, it can be expected that the boundary layer will become turbulent when the Reynolds number exceeds approximately 500,000.

3.6.2 - BOUNDARY LAYER DEVELOPMENT IN A PIPE

The flow conditions in a pipe in the vicinity of the inlet are similar to those on a flat plate in parallel flow. The thickness at the inlet is zero and increases rapidly as the flow travels down the pipe (or barrel). It will be assumed that the inlet geometry is such that the flow into the ELGG barrel for the arc chamber or convergent-divergent nozzle proceeds without separation.

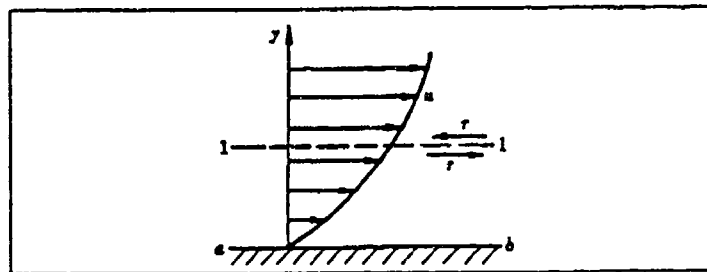


Figure 3.4 Growth of boundary layers in a pipe

At a certain distance, L_c , from the inlet, the boundary layers expand to fill the entire pipe. The velocity profile downstream from this point has the form of a parabola (laminar flow) or an arched curve (turbulent flow). Further downstream the velocity profile does not change shape. The developed flow region will be turbulent if the Reynolds number is greater than a critical value. By defining the Reynolds number as the mean velocity over the cross section of the pipe, U_m , and the tube diameter, d , the critical value under normal conditions is:¹⁵

$$R_{ecr} = \frac{U_m d}{v} \approx 3,000 \quad (3.30)$$

"In general, transition point calculations is the weakest link in the convective heat transfer calculations."¹³

3.6.3 -- PIPE FLOW

Consider flow in a pipe. For two dimensional flow in the entrance of a channel or a tube, with circular cross section, the equation for axisymmetric flow are used. The

following figure shows how flow develops in the pipe from inlet down stream:

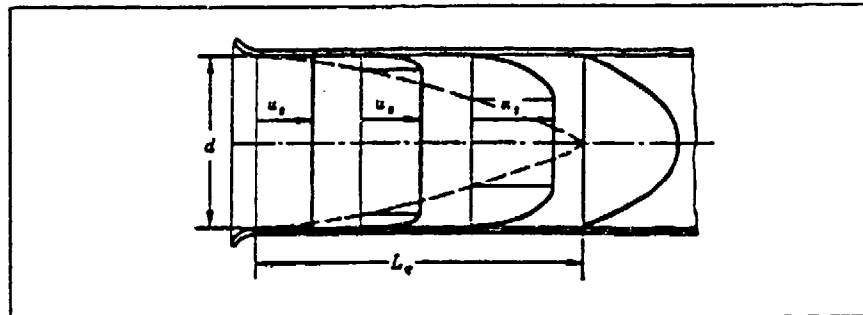


Figure 3.5 Developed region of flow

The flow enters from the left and progresses to the right. The velocity in the core of the flow outside the boundary layers increases with increasing distance from the entrance because the fluid mass flowing through any cross section must be constant and the boundary layer thickens as it moves downstream. For laminar flow, the ratio of the entrance length, L_e , to the diameter, d , of the tube is a function of the Reynolds number:

$$\frac{L_e}{d} = 0.0288 R_{ed} \quad (3.31)$$

R_{ed} is calculated by using the mean velocity, U_m , of the flow in the tube and the tube diameter, d . The laminar/turbulent transition point moves toward the entrance of the tube as the Reynolds number increases. Since the turbulent boundary layer grows more quickly than the laminar one, the entrance length, L_e , becomes shorter as the transition point moves upstream. "At the critical Reynolds number (R_{ed} approximately 3000) it can be assumed that the flow in the entrance region is laminar."¹⁴ The equation above yields

at this Reynolds number an entrance length of approximately $100d$. If the Reynolds number increases, then the transition occurs in the entrance region. The results of numerical analysis show that L_e at first decreases to between $10d$ and $40d$, depending on the Reynolds number, and then starts to slowly increase.

The velocity profile in the fully developed turbulent flow, up to Reynolds numbers of about 100,000 can be represented by Prandtl's equation (previously discussed) with the boundary layer thickness replaced by the radius of the tube. The velocity, U_s , is now the velocity of the flow at the axis. "Integration over the tube cross sectional area yields $U_m = 0.82 U_s$."⁵ Thus the following equations may be used to describe tube flow:⁵

$$\tau_w = \frac{0.0384}{(R_{ed})^{\frac{1}{4}}} \rho U_m^2 \quad (3.32)$$

$$\frac{U_b}{U_m} = \frac{2.44}{(R_{ed})^{\frac{1}{8}}} \quad (3.33)$$

$$\frac{\delta_b}{d} = \frac{63.5}{(R_{ed})^{\frac{7}{8}}} \quad (3.34)$$

Prandtl has proposed, for Reynolds numbers greater than 100,000, a general equation for the friction factor, f , which should be used.⁵ This equation appears as follows:

$$\frac{1}{f} = 2.0 \log\left(\frac{V_y}{V}\right) + 5.5 \quad (3.35)$$

$$V^* = \sqrt{\frac{\tau_w}{l}} \quad (3.36)$$

Here, V^* , is called the shear stress or friction velocity. Due to the complicated nature of this equation, solving for the friction factor has been discussed previously, and based on the work of Keenan and Neumann, a friction factor between .002 and .005 should be used.

The previous development of a turbulent model in a tube is for smooth walls only. For this thesis, the tube is considered to be hydraulically smooth.

3.6.4 -- HEAT FLOW EQUATION

When a body submerged in a flow is heated or cooled, a temperature field is built up in the surrounding medium and a temperature boundary layer is formed. Within this layer, the temperature varies from the value at the wall to the free stream temperature. At a distance δ_t from the wall, the temperature reaches the free stream temperature, t_s .

$$\frac{\partial}{\partial x} \int (t_s - t) U \partial y = \alpha \left(\frac{\partial t}{\partial y} \right)_w \quad (3.37)$$

This is the heat flow equation for the thermal boundary layer. By using tabulated and experimental data, included in the appendices, the temperature and pressure dependence of the specific heat, C_p , the thermal conductivity, k , and the viscosity, μ , is accounted for

at each region of differing pressure. "The equation of state may be used to determine the pressure values for gasses."⁵

The ratio ν/α is a dimensionless property which is used a lot in heat transfer equations. This is termed the Prandtl number, Pr :

$$Pr = \frac{\nu}{\alpha} = \frac{c_p \mu}{k} \quad (3.38)$$

"In general, the Prandtl number is a function of temperature only. The temperature dependence for gasses is rather small."⁵ Using this fact and solving for L yields:¹³

$$L = \frac{\left\{1 - \left(\frac{x_0}{x}\right)^{75}\right\}^{\frac{1}{2}}}{1.026\{Pr\}^{\frac{1}{3}}} \quad \text{where } L = \delta_t / \delta_\beta \quad (3.39)$$

"Gases typically have Prandtl numbers somewhat smaller than 1".⁵ In this case, the assumption that $L < 1$ made previously would be in error. "However, since the smallest value for gaseous Prandtl number is about 0.6, the largest value of L is equal to 1.18. The error introduced in using the above equation for such values of L is very small."¹³

From this discussion, flow through a tube can now be considered. If the wall of a tube through which a fluid flows is heated, relative to the fluid flowing within the tube, a thermal boundary layer builds up along the walls. This layer grows in the downstream direction and meets at the axis of the tube at some distance from the entrance. This is where the thermal starting region ends. The heat flux is assumed to be independent of r.

"The heat transfer coefficient for the flow in a tube is usually calculated on the basis of the difference between the average temperature of the fluid and the wall temperature of the tube."¹⁵ The average temperature is, by convention, defined as that temperature which the fluid would assume if it were instantly and adiabatically mixed after leaving the cross section of the tube and is called the bulk temperature, t_b .

Note that the bulk temperature change $\Delta t_b/L$ per unit length is constant. This means that the bulk temperature changes linearly in the axial direction. Since the heat transfer coefficient is constant in the thermally developed region, it follows that the tube wall temperature also varies linearly in this region.¹⁶

Heat transfer to the barrel walls for thermally developing conditions can now be discussed when the velocity profile is already fully developed. Graetz and Nusselt developed the calculations for the developing conditions. Their findings show two important facts. First, the temperature profile is rectangular in shape in the section where heat transfer starts, changes in the flow direction because of thermal boundary layer formation and growth along the wall. The point where the boundary layers meet at the axis of the tube defines the end of the starting region. From this point on, the temperature profile does not change, it only decreases in size gradually in the direction of flow. Second, the Nusselt number is infinitely large at the beginning of the tube and decreases until it reaches the value 3.65. The thermal starting length is calculated from:

$$\frac{L_s}{d} = 0.05 R_{ed} P_r \quad (3.40)$$

This equation gives, with good approximation, the entrance length for the case of simultaneous flow and thermal development. "H. Hausen has developed a formula which represents the results of the theory of both Graetz and Nusselt."⁵ This is as follows:

$$NU_d = 3.65 + \frac{0.068(\frac{d}{x})R_{ed}Pr}{1+0.04\{(\frac{d}{x})R_{ed}Pr\}^{\frac{2}{3}}} \quad (3.41)$$

The influence of variable viscosity is taken into account by multiplying the right hand side of the equation by the ratio $(\mu_b / \mu_w)^{0.14}$, where μ_b is the viscosity evaluated at the bulk temperature and μ_w is the viscosity at the wall temperature. The properties in the dimensionless parameters of the equation are then based on bulk temperature.

3.6.5 – FORCED CONVECTION IN TURBULENT FLOW

In turbulent flow, heat is transferred by the turbulent mixing motions in addition to the heat flow by conduction and by bulk convection due to the motion of the fluid. The turbulent fluctuations become smaller as a solid wall is approached and the main features of heat transport from the flow to the wall can be specified by a simple model, assuming a laminar sublayer which exists immediately next to the wall. The heat must pass through this layer before it is transported to the wall by turbulent mixing. The interaction between the laminar sublayer and the turbulent core determines the heat transfer process. By using relationships proposed by Reynolds and Prandtl, it is possible to derive formulas

for heat transfer which require only hydrodynamic information. Generally, the fluid layers near the wall are the main component influencing heat transfer. The velocities in these layers are parallel to the wall while the heat flow is normal to the wall. It is assumed that the gradient in velocity is in the y direction (normal to the wall) only. Thus the heat flux is in the y direction, and the temperature change is mainly in the y direction as well.

The turbulent shear stress may be written as:¹⁶

$$\tau_t = m'(U' - U) \quad (3.42)$$

and the relationship between the heat transfer and shear stress in turbulent flow becomes:¹⁶

$$q_t = \tau_t C_p \frac{t-t'}{U'-U} \quad (3.43)$$

"This relation was first derived by Reynolds in 1874 and is therefore called the Reynolds analogy."¹³ The ratio of the heat transfer to the shear stress has the same relationship in laminar or turbulent flow when $k/\mu = c_p$ or when $c_p\mu/k = P_r = 1$. A fluid having a Prandtl number equal to 1 exhibits the same heat transfer relationships in laminar or in turbulent flow. For fully developed flow in a tube, the free stream values are replaced with the mean velocity, U_m , and the bulk temperature, t_b .

$$Q_w = q_w A = R \frac{c_p}{U_m} (t_b - t_w) \quad (3.44)$$

R is the resistance ($R=\tau_w A$) and Q_w is the heat flow at the wall. Note that R is only valid for Prandtl number very close to 1. "Since most gasses have Prandtl numbers which deviate from 1 only slightly, this equation is very useful in obtaining a first approximation to the heat transfer where the resistance is known."¹³ The resistance in a tube with pressure drop Δp is $R = \Delta p d^2 \pi / 4$ and the volume flowing through the tube cross section is $V = U_m d^2 \pi / 4$. Thus the power needed to maintain the flow is:

$$W = V \Delta p = R U_m \quad (3.45)$$

The ratio of the heat flow to power is an important relationship and demonstrates that the power needed for a certain heat transfer shrinks when the mean velocity, U_m , is decreased. This is given by:

$$\frac{Q}{W} = \frac{c_p}{U_m^2} (t_b - t_n) \quad (3.46)$$

3.6.6 -- TURBULENT FLOW IN A TUBE

In fully developed flow, the boundary layers have met at the tube axis with velocity U_s . It becomes apparent that the heat transfer coefficient described in the last equation should be based on the temperature, t_s , along the axis. However, as stated earlier, the heat transfer coefficient in a tube is based on the bulk temperature, t_b , and the mean velocity, U_m . "This is not quite correct because of the different definitions of t_b and U_m , but the

error introduced in this way is quite small.¹³ Using this information, the final formula for heat transfer to the walls of a tube with turbulent flow is:

$$S_t = \frac{0.0396 R_{ed}^{-\frac{1}{4}}}{1 + 1.7 R_{ed}^{\frac{1}{8}} (P_r - 1) P_r^{\frac{1}{4}}} \quad (3.47)$$

Note that for the heat transfer equation as written, the term on the left hand side is equivalent to $NU_d / (R_{ed} P_r)$ which is the Stanton number (S_t). The shape of the temperature profile for different Prandtl numbers can be derived from these equations. Note that for a fluid with Prandtl number equal to 1, the ratio of the temperature differences is equal to the ratio of velocity differences. As Prandtl number increases, the temperature drop in the laminar sublayer begins to dominate. The convection turbulent heat flow to the wall of a tube of length L is:¹⁷

$$Q = h d \pi L (t_w - t_b) \quad (3.48)$$

The methodologies discussed throughout this section are important for the understanding of the actual flow problems inherent in an ELGG barrel, and are necessary to properly evaluate the data and plots obtained through the MACH2 calculations.

3.7 – RADIATIVE HEAT TRANSFER PROCESSES AND HYDROGEN OPACITY

As discussed previously, there are three types (generally) of heat transfer. These are heat convection, heat conduction and thermal radiation. "If the temperature of a gas is not too high, and the density is not too low, the transfer of heat by thermal radiation is usually negligibly small in comparison with that by conduction and convection."¹⁸ However, we are dealing with very high stagnation temperatures and the densities are relatively high, such that thermal radiation must be considered. This can be seen graphically in the following figure:¹⁸

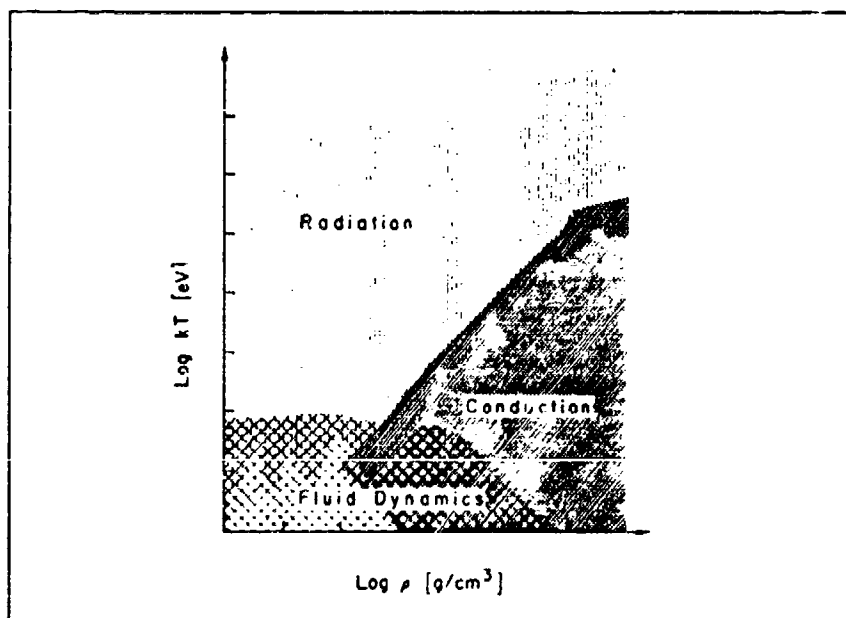


Figure 3 6 Regimes of energy transport

There are three thermal radiation effects on the flow field of a high temperature gas:
1) radiation stresses, 2) radiation energy density, E_R , and 3) heat flux of radiation, Q_R .

Usually, radiation energy density and the radiation pressure are of the same order of magnitude. The following is a definition of the radiation energy density:¹⁹

$$\frac{E_R}{\rho} = \sigma \frac{T^4}{\rho} \quad (3.49)$$

This radiation energy density should be compared with the internal energy, $U_m = c_v T$ of the fluid. Since radiation energy density is proportional to T^4 , while internal energy is proportional to T , a reduction in the temperature by one order of magnitude will result in the radiation energy density becoming three orders of magnitude smaller than that of the internal energy. By comparison with radiative energy density and internal energy, it can be determined when radiation energy density becomes important.

For the radiation equilibrium condition, the radiative flux is:

$$Q_R = \sigma \frac{T^4}{\rho} \quad (3.50)$$

where σ is the Steffan-Boltzmann constant. The heat flux by convection is:

$$Q_V = u c_v T \quad u = \text{the typical flow velocity} \quad (3.51)$$

The radiation flux should be compared to the heat flux by convection. Since Q_R is proportional to T^4 , while Q_V is proportional to T , at high temperatures such as those encountered in the ELGG, Q_R may be of the same order of magnitude or higher than Q_V . If, for example, the density is roughly 1/1000 of air density and temperature is 10,000K

or higher, we should consider the radiation flux. At 100,000K or more, both radiation energy density and radiation flux should be considered.

The thermal radiation may be expressed in terms of a specific intensity, I_ν ,

$$I_\nu = \lim\left(\frac{dE_\nu}{d\sigma d\nu dt d\omega \cos \Theta}\right) \quad (3.52)$$

The amount of radiative energy flowing through an area $\delta\sigma$, in frequency range ν to $\nu + \delta\nu$ in direction of the ray at an angle θ with normal of $\delta\theta$ within solid angle $\delta\omega$ in time interval δt is δE_ν . The total amount of energy radiated over the whole spectrum is:

$$dE = \int \left(\frac{dE_\nu}{d\nu}\right) d\nu = I \cos \Theta d\sigma d\omega dt \quad (3.53)$$

$$I = \int I_\nu d\nu \quad \text{this is the integrated intensity}$$

If the specific intensity, I_ν , is known, the flux of heat energy by thermal radiation, the radiation energy density for the whole spectrum, and the radiation stress tensor can be determined.

At this point, the process to determine the specular absorption coefficient, κ , of radiation is quite difficult and requires either computer simulation or experimentation. Fortunately, this information is available and will be used extensively throughout this thesis. Note that the value of the absorption coefficient determines, among other things, the loss of specific intensity along the ray over a distance in a medium, the optical

thickness, τ , and the heat flux due to radiation. The absorption coefficient is a function of both temperature and density of the medium, as well as the frequency of radiation.

The optical thickness indicates effective length in the absorption of radiation. For a given length ($s - s_0$), if the optical thickness is large, the medium is said to be optically thick. If the optical thickness is small, then we say the medium is optically thin.

For most radiation heat flux considerations, the assumption of Local Thermodynamic Equilibrium, or LTE, will be used. This means that at least locally, the various processes occurring in the fluid have had enough time to relax to an equilibrium state, and it can be said that the particles satisfy the Boltzmann and Maxwell relations. Again, this is an assumption for local conditions only. The system itself can be in a non-equilibrium state. In conjunction with the assumption of LTE, the optical thickness of a medium allows us to choose different ways in handling the thermal radiation equation, which is.¹⁹

$$\text{for LTE} \quad \frac{1}{c} \frac{dI_v}{dt} + \frac{dI_v}{ds} = \rho \kappa'_v (R_v - I_v) \quad (3.54)$$

$$\kappa'_v = \kappa_v [1 - \exp \frac{-hv}{kT}] \quad (3.55)$$

κ'_v is the spectral absorption coefficient corrected for the effects of bound-bound, bound-free, and free-free transitions.

Bound-Bound transitions are simply a radiative change in an atom or molecule from one quantized energy level to another. "Since the energy difference between two quantized energy levels is established by internal molecular structure, the emission and

absorption coefficients for bound-bound transitions are sharply peaked functions of the photon energy $h\nu$. For this reason, bound-bound transitions are said to give rise to emission and absorption lines. In a monatomic gas, such transitions are between electronic states of the atom.¹⁹

Bound-Bound transitions resulting in absorption and emission lines have natural line widths due to the distribution of emitted and absorbed energy over a narrow range of $h\nu$. The natural line width has an associated uncertainty which is further complicated by line broadening due to Doppler broadening and collision broadening. Doppler broadening is the result of thermal motion of the atoms or molecules, and collision broadening results from a perturbation of the radiating atom by encounters with other atoms.

Bound-Free absorption occurs with the interaction of radiation with an atom or molecule causing photoionization or photodissociation of the atom or molecule. The reverse process is called radiative recombination. This results in the removal of an electron from its bound, quantized state by a photon of precisely the correct energy. This ionizes the atom, resulting in a free electron. At this point, the electron can take on any value of kinetic energy, which makes the absorption coefficient for photoionization a continuous non-zero function of photon energy for all values of photon energy that exceed the ionization potential of the atom. (Vincenti and Kruger) The process of photodissociation and radiative recombination is similar.

Free-Free transitions result also in continuous emission and absorption which are both associated with changes in energy of the free electrons in a gas. This process is also

called Bremsstrahlung, and occurs when a free electron interacts with the field of a positive ion.

Getting back to the method of solving the radiative heat flux equation, the idea of optical thickness can be used to simplify the solution process. First, the opacity of the medium needs to be calculated, which will consist of several different species present in the medium. For hydrogen, R. W. Patch has identified seven species which occur at different conditions which contribute significantly to the opacity of the medium. He considered a system from 300K to 40,000K and pressures (relating to densities) from 1 to 1,000 atmospheres. The species he considered were:²⁰

H - hydrogen atoms
H⁺ - protons
e⁻ - free electrons
H₂ - hydrogen molecules
H⁻ - negative hydrogen ions
H₂⁺ - hydrogen diatomic molecular ions
H₃⁺ - hydrogen triatomic molecular ions

By treating the plasma as an ideal gas except for coulomb interactions between free charged particles, considering only singly excited electronic states of H₂, non-degenerate free electrons, and assuming the photon pressure was negligible, among other assumptions, Patch was able to create several tables and figures showing the number densities of the species as a function of temperature and pressure. His work includes fifteen different chemical reactions, takes into account bound-bound, bound-free, and free-free transitions, and corrects for varying pressures and temperatures. This

information led to the calculation of the Planck and Rosseland opacities which are used in the solution process of the radiative heat transfer equation. The data presented by Patch is located in appendix D.

Vincenti and Kruger show that the time derivative of the radiative heat transfer equation can be neglected by considering the characteristic speed and distances within a system to that of the speed of light. They show that for most systems, this ELGG included, the time derivative can be neglected without loss of information. There are two main ways in which the radiative heat transfer equation can be made relatively easy to solve. These are the optically thin, governed by Planck's law, and the optically thick cases, governed by the Rosseland diffusion equation.

The optically thin case assumes that the specific intensity, I_v , is much less than the Planck function, or otherwise known as the equilibrium value $B_v(T)$. When this case is met, the gas is said to be emission dominated. In other words, very little absorption occurs. If this assumption holds true isotropically and for all frequencies, the heat flux will depend only on local conditions and will be equal to the total volumetric rate of spontaneous emission. In this case, the Planck absorption coefficient is used, or more accurately, the Planck mean absorption coefficient, α_p , and it's inverse, the Planck mean free path, λ_p . The Planck function and associated heat flux are as follows:

$$\text{Planck Function: } B_v(T) \equiv I_v^* = \frac{2hv^3/c^2}{e^{hv/kT}-1} \quad (3.56)$$

$$\text{Planck heat flux: } \frac{dq}{dx} = 4\alpha_p \sigma T^4 \quad (3.57)$$

The optically thick case occurs when the specific intensity, I_v , is of the same order of magnitude as the Planck function, or otherwise known as the equilibrium value $B_v(T)$. In this case, the medium is considered to be optically thick, and is absorption dominated. Vincenti & Kruger demonstrate that in the case of optically thick medium, isotropic radiation, and for the case that all frequencies are accounted for, the following Rosseland diffusion approximation can be obtained:¹⁹

$$Q_i^R = -\frac{16*\sigma*T^3}{3*\alpha_R} \frac{\partial T}{\partial x_i} \quad (3.58)$$

where α_R is the Rosseland mean absorption coefficient, and it's inverse is the Rosseland mean free path.

At this point, it is important to be able to understand which regime of operation, Rosseland diffusion or Planck would be expected to dominate in the ELGG barrel section. The following is an excerpt of simulations accomplished using Mathcad and shows that the Rosseland diffusion approximation for the temperatures and pressures considered is not a valid assumption. The medium, in this case hydrogen, turned out to be optically thin, so the Planck method should be expected to be the dominant player in order to calculate the heat transfer. However, model development will be conducted using both methods for comparison purposes to the results obtained from MACH2. The results of these calculations are in appendices C and E. The following is the basic methodology used to run the Mathcad simulations presented in the appendix:

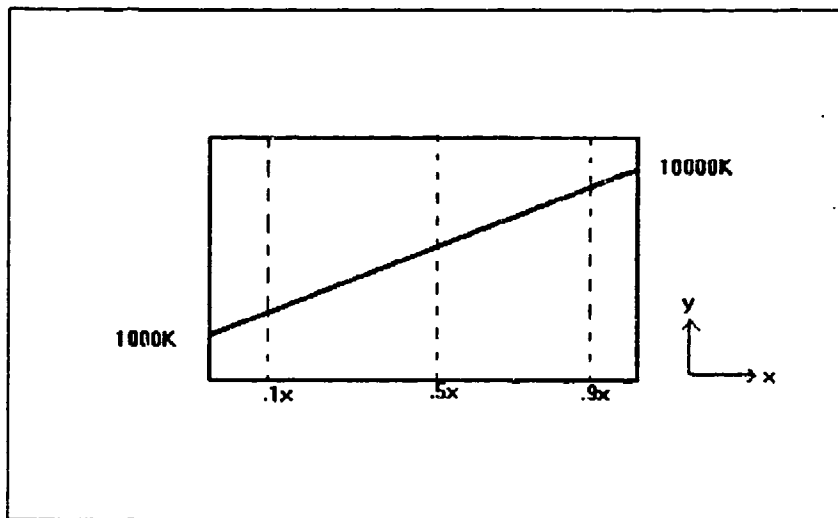


Figure 3.7 Test case for Rosseland and Planck evaluations

In this figure, Δ , is the increment considered along the x axis. The scale size of the system that considered is 10 millimeters, thus $.1\Delta$ would be 1 mm, etc... The temperature gradient, assumed to be linear, turned out to be 900K/mm. The following is a graph calculated with Mathcad which shows the Rosseland and Pianck mean free paths at 1,000 and 100 atmospheres. Note that the Rosseland mean free path is larger than that of the Planck mean free path, suggesting that the radiation coming out of the working fluid may be flux limited, and that the Rosseland approximation may not be a valid choice for the conditions present in the barrel region of the ELGG.

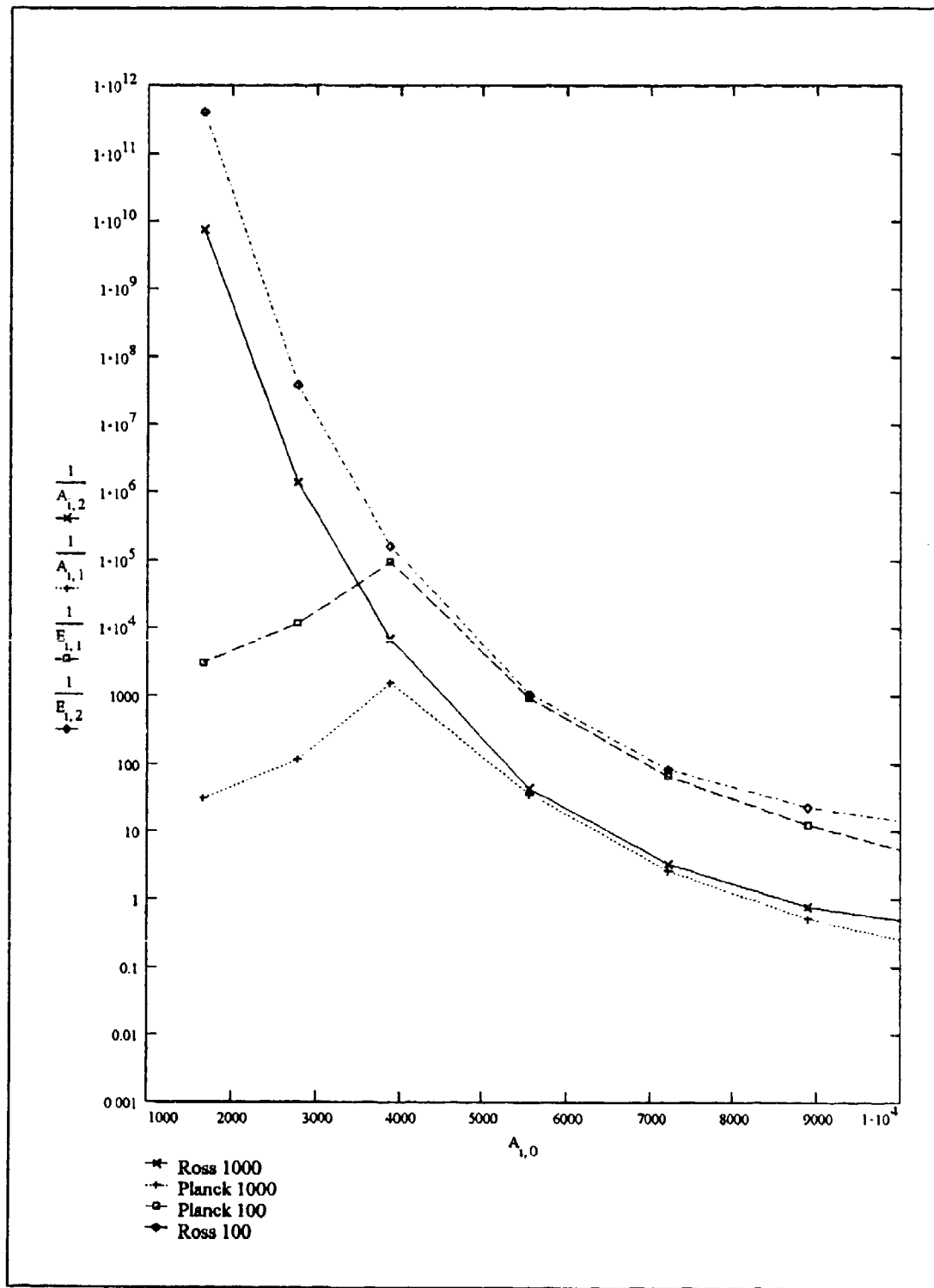


Figure 3.8 Results of Mathcad Rosseland and Planck mean free path versus temperature calculations (1,000K to 10,000K)

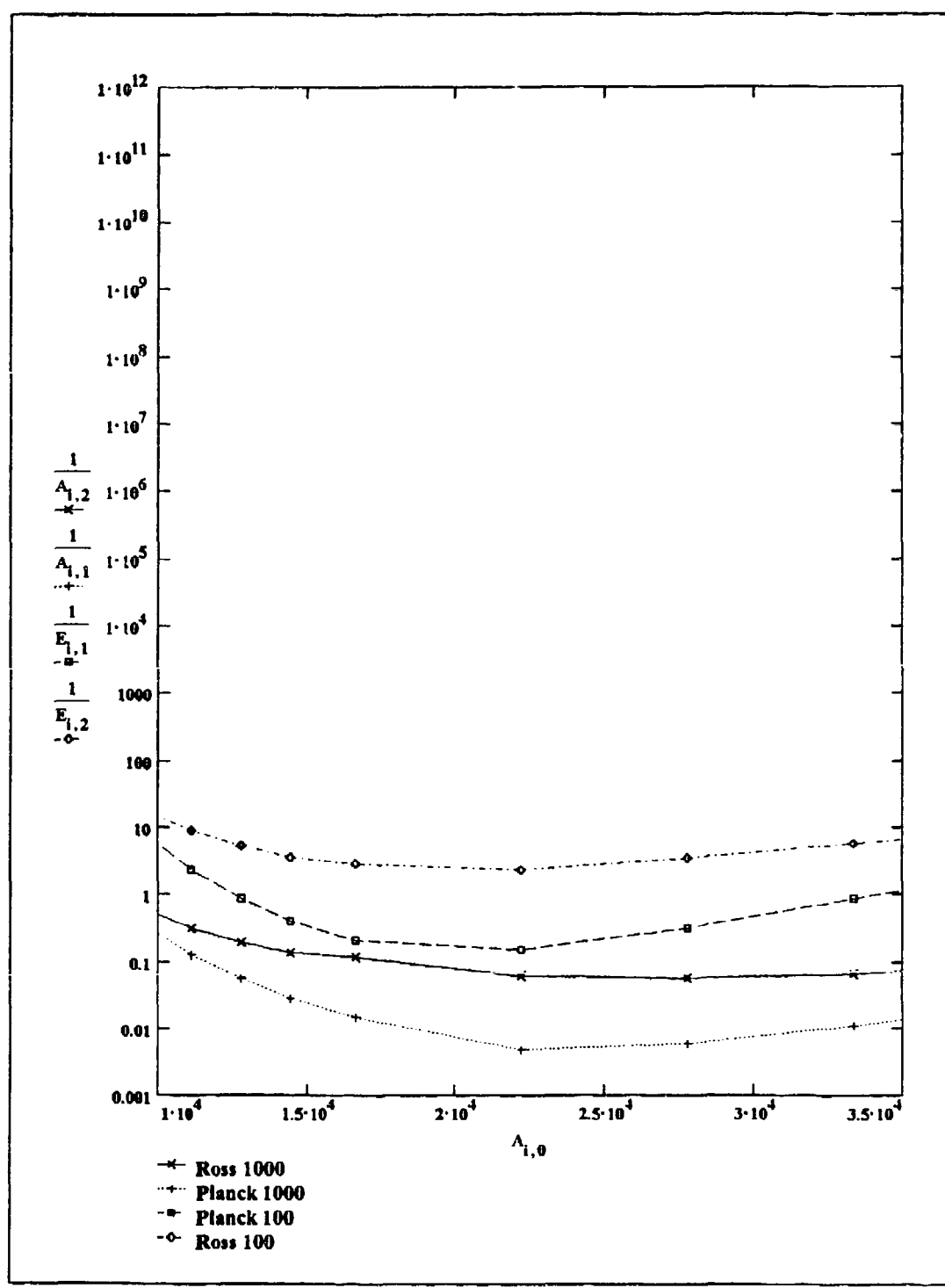


Figure 3.9 Results of Mathcad Rosseland and Planck mean free path verses temperature calculations (10,000K to 35,000K)

3.8 -- MACH2 OPERATION AND TEST

"MACH2 is a 2 1/2 dimensional MHD computer simulation tool for problems in complex geometry's"⁹⁴ This code uses the technique of domain decomposition with the use of logically rectangular blocks and uses an arbitrary Lagrangian-Eulerian hydrodynamic algorithms. This program was written by the combined efforts of several military and civilian scientists at the Phillips Laboratories at Kirtland AFB, New Mexico.

MACH2 utilizes an input deck, labeled im2, for problem identification and to inform the MACH2 code which set of equations to use. For example, it is possible to have the code numerically solve the flow problems within the barrel region of the ELGG with viscous effects "turned off", and have radiation effects "turned on". This greatly helps in the analysis of the dynamics of the system, and allows for selective studies of various flow parameters.

MACH2 affords a great deal of flexibility in designing a particular problem, and has a wide variety of output data. In order to test the code and verify its proper operation, an im2 was setup which had all effects "turned off", and the code was run to calculate the exit conditions of the ELGG. After 33,000 cycles using a time step of 1.0 e-8 seconds, the code reached a steady state solution. The total duration of the flow through the 1 meter long, 30 mm inner diameter tube was found to be 2.9891 e-03 seconds. The exit conditions predicted by MACH2 reached steady state operation and had exactly the same values as the inlet conditions. Samples of the im2 and output data run for this test are included in appendix K. Due to limitations in the availability of hydrogen data within the

MACH2 code itself, this test, and subsequent runs will use argon as the working fluid.

Although argon has vastly different thermal and physical characteristics from hydrogen, the trends and observations made with the hydrogen models discussed in this thesis will be applicable to the results obtained with MACH2.

The test results of the MACH2 coding show that the code is working correctly and is providing data which should be reliable. It was important to run this test for two reasons. The first is the need for MACH2 to be tested at various different geometry's and conditions, and the second was to foster familiarity with the code, the im2, and the output produced.

CHAPTER IV

ANALYSIS OF HEAT TRANSFER

4.1 - DETERMINATION OF DEGREE OF IONIZATION AND WORKING FLUID COMPOSITION

In order to ensure the applicability of the models developed in this thesis, it is prudent to consider how the working fluid is affected by the conditions it will encounter within the ELGG barrel region. The degree of ionization and the species created by these conditions are important because these effects greatly affect the way in which the working fluid behaves and what order of magnitude can be expected for heat change. The ionization of the working fluid essentially robs some of the flow energy within the fluid and if the degree of ionization is high, less flow energy will be available for projectile acceleration. Additionally, recombination effects, if significant, will change the flow energy as well.

Ionization is a process which removes an electron from an atom, leaving the atom with a net positive charge. The first ionization potential, V_i (measured in eV), of the atom is the energy required to completely remove an outer electron from its normal state in a neutral atom to a distance beyond the sphere of influence of the nucleus.

In a plasma, the temperature is high, and the ionization is essentially due to thermal ionization. Ionization by thermal collision will eventually result in a Maxwellian velocity

distribution and involves an energy transfer from the fast moving, energetic electrons and the heavy particles. The degree in which the electron temperature decreases depends on the rate of recombination, transfer of energy to vibrational, rotational, and translational energy states, and radiation effects. It also depends on the individual species, the volume and the initial temperature of the electrons, ions and neutrals. Additionally, it depends on the physical boundaries of the system. By considering dissociation, ionization, and recombination processes separately, it is possible to get an idea of what is happening in this system and develop expressions which allow a first approximation.

The ionization level and conductivity are primarily determined by electron temperature rather than the heavy particle temperature. This state is present in the inlet region of the ELGG due to the use of arc heating of the working fluid. According to Jahn, there appears to be some justification for computing the ionization level from a Saha equation, using the electron temperature. Additionally, Rosa states that the use of the equilibrium constant for calculation of species is justified because it is simply a relation between the forward and reverse rate constants and therefore holds for non-equilibrium conditions as well.

Using the Saha equation discussed in section 3.1, the following graphs and data were calculated at stagnation temperatures ranging from 1,000K to 35,000K and at stagnation pressures ranging from 100 to 1,000 atmospheres. The range of these temperatures and pressures are expected to be present within the barrel region of the ELGG.

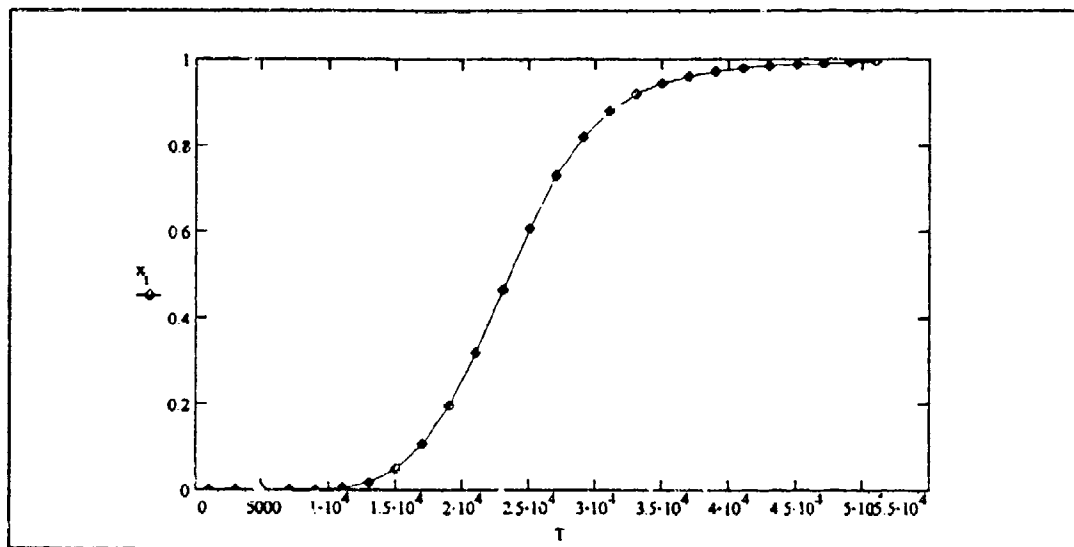


Figure 4.1 Ionization at 100 atm

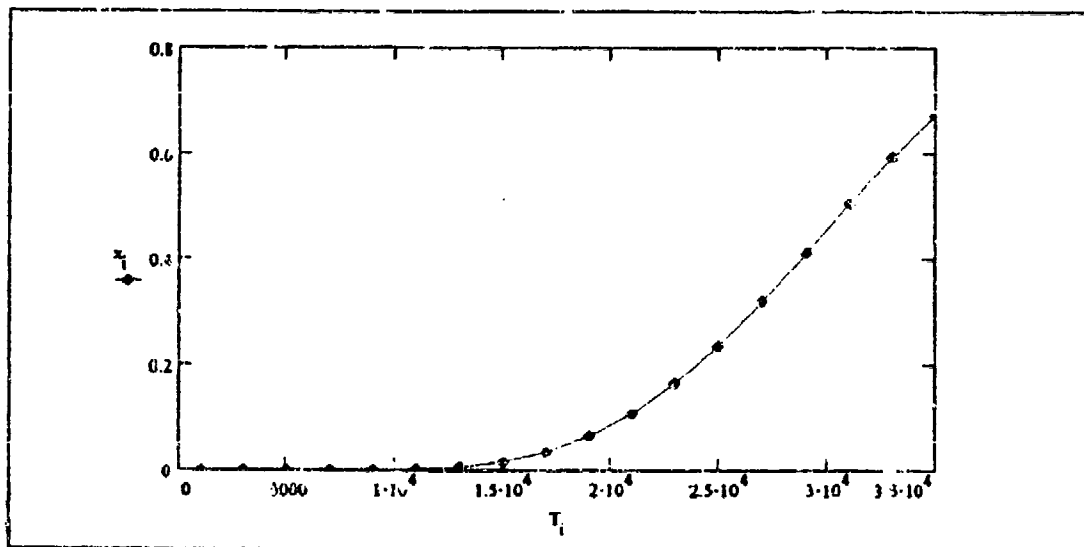


Figure 4.2 Ionization at 1,000 atm

From these charts and the data contained in appendix A, it is clear that ionization within the barrel section of the EGG will not be an important consideration

until the inlet temperature exceeds approximately 20,000K at 1,000 atmospheres. The trends of these charts show that as the temperature increases, the ionization increases as well, but with increased pressure, the ionization decreases. At the extremes of the conditions which can be expected within the ELGG barrel region, the ionization rate at inlet stagnation temperatures of 35,000K and pressures of 1,000 atmospheres is approximately 50 percent of the working fluid composition.

These results are confirmed by considering the species number densities provided by R. W. Patch and included in appendix D. From this data, it can be seen that the number density of electrons and ions are 9.291×10^{25} at a pressure of 1,000 atmospheres and 30,000K. By comparison, the number density at these conditions for H is 7.020×10^{25} . From this empirical data, the hydrogen is nearly 70 percent ionized, and this supports the results obtained by the Saha equation.

As the working fluid travels through the barrel region, the loss of heat energy due to the transport processes and viscous effects will cause chemical relaxation towards molecular hydrogen. To determine the chemical relaxation rate, it must be understood that all chemical processes take place by molecular collisions or radiative interactions.⁹⁵ For purposes of this discussion, radiative interactions will be neglected and collision processes are assumed to dominate. According to Anderson, nearly 200,000 collisions are required for either dissociation of the molecule, or molecular recombination to occur.⁹⁵ Obviously this takes a finite amount of time, during which non-equilibrium effects are present. Non-equilibrium can be defined as the effects of finite reaction

processes which require a definite amount of time in order to react to a rapid change in conditions in which a gas is subjected.

The time required for relaxation to occur is governed by rate constants. When the working fluid is heated by the arc prior to the barrel inlet, a certain percentage of the reaction will be in the form of dissociation. In general, molecular dissociation energies are equal to or less than the ionization energies of the constituent atoms. Due to the very high energies and electron temperatures involved, it will be assumed that regardless of whether or not a system is in equilibrium, the rate at which a reaction proceeds in the forward direction is equal to the rate in the reverse direction at a given temperature.¹⁹ This assumes that other non-equilibrium effects do not affect the rate of reactions.¹⁹ Therefore, the forward and reverse reaction rates can be related via the equilibrium constant:

To determine whether or not the chemical processes are frozen, in equilibrium, or non-equilibrium in the barrel section, the chemical rate of recombination-dissociation must be compared to the characteristic time the plasma takes to traverse the length of the barrel. If the recombination rate is less than the characteristic transit time of the working fluid, the flow is said to be frozen.

In addition to chemical relaxation, internal modes of energy also seek out equilibrium conditions. Although chemical reactions require somewhere around 200,000 collisions in order to reach a new equilibrium state, vibrational energy is exchanged and equilibrium attained in approximately an order of magnitude less, typically around 20,000 collisions.⁹³

Vibrational energy is quantized into different specific energy levels, and it is through collisions that a change from one energy level to another is accomplished. If the system consists only of harmonic oscillators at equilibrium, a Boltzman distribution will exist, assuming constant temperature. During the time the distribution of particles is not described by the Boltzman equation, the system is in a non-equilibrium state.

When a particle moves from one energy level to another, it undergoes a transition which requires collisions to occur. The transition probability is governed by the collisional frequency, Z, and the number of particles in the system, N. The following are used to determine the collisional frequency:

$$Z = n\pi d^2 \sqrt{\frac{8kT}{\pi M}} \quad (4.1)$$

$$M = \frac{m_A m_B}{(m_A + m_B)} \text{ (reduced mass)} \quad (4.2)$$

$$\lambda = \frac{1}{\sqrt{2\pi d^2 n}} \text{ (mean free path)} \quad (4.3)$$

$$\sigma = \pi d^2 \text{ (collision cross section)} \quad (4.4)$$

The transfer of energy through collisions from vibrational to translational energy creates a temperature rise in the system. While vibrational energy is experiencing the molecular collisions, the working fluid is in a non-equilibrium state and energy is "locked" inside the vibrational energy levels, thus some of the energy of the fluid is not available

for projectile motion. According to Anderson, the vibrational relaxation time is a function of both temperature and pressure. This comes from the fact that the transition probability and the collision frequency are also functions of pressure (an indication of how probable a collision will be) and temperature (indicating the relative kinetic energy of the particles).

The following is a table of calculated relaxation times for both chemical reactions (recombination) and vibrational energy.

Table 4.1 Calculation of relaxation times at various velocities, temperatures and constant pressure of 1000 atm (*data from Brown⁹²)

initial velocity	initial temp	chemical dist (meters)	vibrational dist (meters)	collisions/meter	collision freq "Z"	collision area (meters) ²
500	11,605	4.216x10 ⁻⁵	5.157x10 ⁻⁶	4.848x10 ⁹	2.424x10 ¹²	9.749x10 ⁻¹⁰
4,500	11,605	3.713x10 ⁻⁴	4.641x10 ⁻⁵	5.386x10 ⁸	2.424x10 ¹²	9.749x10 ⁻¹⁰
13,000	11,605	001	1.341x10 ⁻⁴	1.864x10 ⁷	2.424x10 ¹²	9.749x10 ⁻¹⁰
500	23,000	7.314x10 ⁻⁷	9.142x10 ⁻⁸	2.735x10 ¹¹	1.367x10 ¹⁴	8.173x10 ⁻¹⁰
4,500	23,000	6.582x10 ⁻⁶	8.228x10 ⁻⁷	2.735x10 ¹¹	1.367x10 ¹⁴	8.178x10 ⁻¹⁰
13,000	23,000	1.9026x10 ⁻⁵	2.377x10 ⁻⁶	2.052x10 ¹⁰	1.367x10 ¹⁴	8.178x10 ⁻¹⁰
500	34,000	5.551x10 ⁻⁷	6.938x10 ⁻⁸	3.603x10 ¹¹	1.802x10 ¹⁴	7.271x10 ⁻¹⁰
4,500	34,000	4.996x10 ⁻⁶	6.244x10 ⁻⁷	3.603x10 ¹¹	1.802x10 ¹⁴	7.271x10 ⁻¹⁰
13,000	34,000	1.443x10 ⁻⁵	1.804x10 ⁻⁶	3.603x10 ¹¹	1.802x10 ¹⁴	7.271x10 ⁻¹⁰

Considering the results of the calculations for both the chemical and vibrational relaxation times, it is clear that even the slowest chemical relaxation time occurring at an inlet temperature of 1 eV and velocity of 13,000 m/sec, the flow is able to reach equilibrium within .033 diameters. This suggests that non-equilibrium will not be a factor in the barrel region, and that the particles can be considered in a Boltzman distribution throughout the length of the barrel. Vibrational modes are also in equilibrium. Additionally, frozen flow losses are negligible for the entire operating range of inlet temperatures. As the flow progresses, the electron and heavy particle temperatures should rapidly achieve equilibrium, and associated with this, a rapid loss of ionization will result, leaving the working fluid composed of only molecular hydrogen and atomic hydrogen at the exit of the barrel. The effects of recombination will serve to increase the amount of energy within the working fluid, tending to counter the effects of transport losses, thus providing more energy for the purpose of projectile motion.

The following figure demonstrates the species number densities within the ELGG barrel region and corroborates the findings of the above calculations. At the inlet stagnation temperature and pressure of 30,000K and 1,000 atmospheres, figure 4.4 suggests that the working fluid is mainly composed of ionized atomic hydrogen, with molecular hydrogen making up only a fraction of the remainder of the fluid. Thus it can be assumed that the working fluid is completely dissociated, and the number of free electrons is of the same order of magnitude as that of atomic hydrogen. Note that the stagnation temperature and pressure in the inlet region of the barrel rapidly decreases as the effects of conduction, radiation and viscous effects deplete the energy from the fluid.

This causes a rapid recombination of atomic hydrogen, H, into molecular hydrogen, H₂. Patch describes the number density of H decreasing from 6.757×10^{26} at 10,000K to 8.97×10^{25} at 4,000K while H₂ increases from 5.695×10^{25} at 10,000K to 1.745×10^{27} at 4,000K. Temperature drops of this magnitude typically can be expected to occur within the first 10 diameters into the barrel region, which equates to approximately 3.34×10^{-5} seconds at an inlet velocity of 3,000 m/sec. The following graph from Patch demonstrates the number densities of species at 1,000 atmospheres.

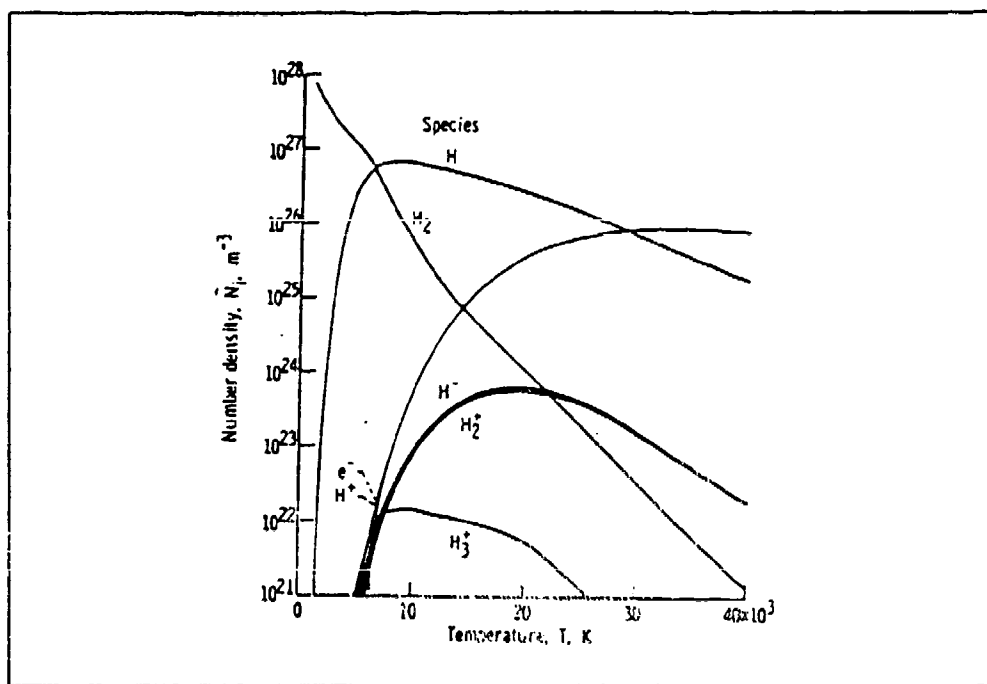


Figure 4.3 Number densities of Hydrogen at 1,000 atm

From this discussion and the results of the Saha equation and data provided by Patch, the use of the molecular hydrogen and the various thermodynamic and opacity properties associated with H₂ within the models developed is justifiable, with only small variances at

inlet temperatures of up to 10,000K and pressures of 1,000 atmospheres. The working fluid within the barrel region of the ELGG for these conditions can best be described as a weakly ionized plasma at best, and is actually a high temperature flow of slightly dissociated gas with rapid recombination within the first few diameters into the pipe. However, at inlet stagnation temperatures in excess of 10,000K, the dissociation begins to dominate, and the thermodynamic properties of the working fluid begin to experience rapid fluctuations. Fortunately, by using the empirical data from Patch, the change in species is included in the thermodynamic data used for the heat transfer analysis within this thesis. This also applies to the increasing ionization of the working fluid as inlet temperatures exceed approximately 20,000K.

From experimental data gathered by Zube, the translational relaxation occurs so quickly that non-equilibrium in this energy mode can be observed to be negligible for the regions of interest in the ELGG. Consider the following table:

Table 4.2 Translational Relaxation times

Process	relaxation time (seconds)
electron self relaxation	10^{-11} to 10^{-10}
hydrogen-hydrogen kinetic relaxation	10^{-9}
electron-proton kinetic relaxation	10^{-8}

From this information, and the fluid velocities expected at the inlet of the ELGG barrel, the slowest translational relaxation takes approximately .0005 diameters to reach

equilibrium. This demonstrates that the translational energy is in equilibrium immediately past the inlet, and confirms the assumption that translational non-equilibrium can be neglected. This holds true for rotational non-equilibrium as well.

4.2 – CONDUCTIVE HEAT TRANSFER ANALYSIS

In the development of the conduction one dimensional model for the ELGG barrel region, the assumptions of a calorically perfect, inviscid gas with steady flow have been used. From the discussions of the species number densities and the degree of ionization, these assumptions are acceptable for development of trends and general conductive heat transfer calculations. These results will give insight into the processes taking place as well as data in which to validate the MACH2 coding and operation for problems of this kind.

As discussed, conduction occurs in two main ways. Conduction acts internally, which tends to transfer heat energy within the fluid itself, and by contact between the fluid and the walls of the barrel. Internal conduction along the flow direction has been assumed to be negligible compared to the conduction to the walls .

To begin the discussion of the effects of conduction only, neglecting viscous effects, radiation, and convection for the moment, a set of data for conduction has been computed beginning with inlet stagnation temperatures ranging from 8,000K to 34,000K (.68 eV to 2.93 eV) and pressures from 850 to 1,150 atmospheres. By using the tabulated data on the thermal conductivity of hydrogen throughout a wide range of

temperatures and pressures, the following graph has been compiled which shows the heat transfer per unit mass at various temperatures and pressures.

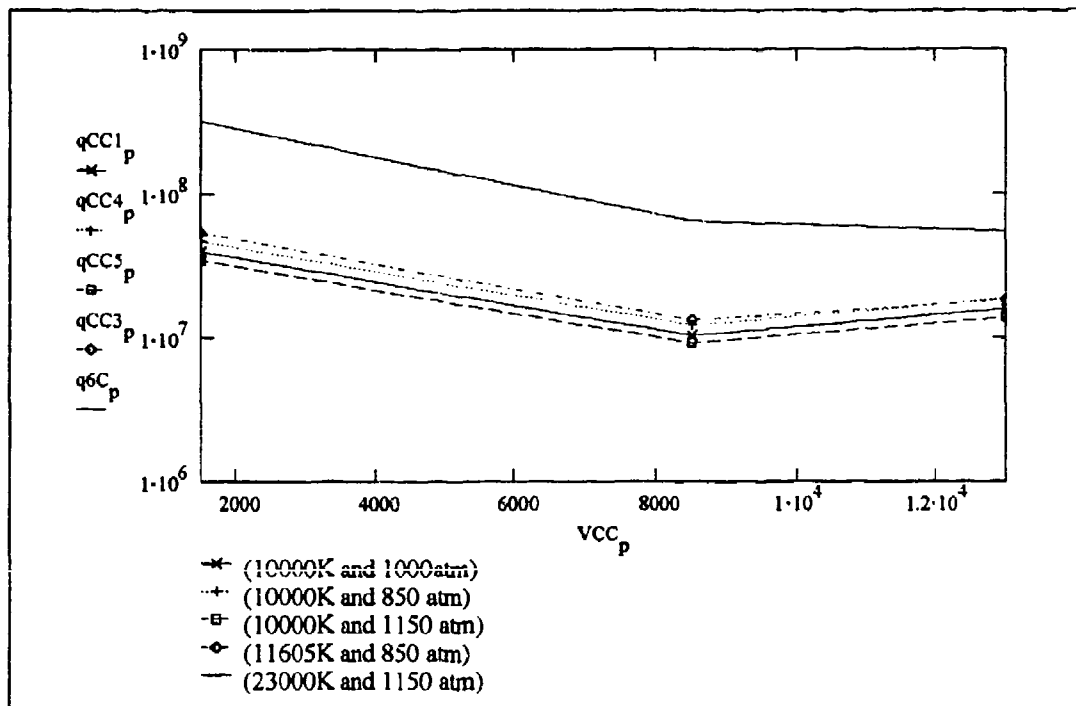


Figure 4.4 Heat transfer per unit mass for conduction only

This graph, and the associated data contained in appendix F, indicate several key findings about the conduction within the barrel of the ELGG. The first is the effect of velocity on the heat transfer. For this model, the effects of velocity changes is noticed for a variety of conflicting reasons. The duration of time the fluid remains in the barrel region is an important consideration. Conduction is highly dependent on the physical contact between the fluid and the walls, and by changing the duration that this occurs is reflected in the heat transfer. Velocity also affects the static temperatures and pressures

and these effects are felt by conduction through the amount of mass present within the flow and the temperature gradients created between the walls, assumed to be at a constant 300K, and the fluid. Finally, the change in the temperature and pressure serves to change the thermal conductivity, which correspondingly changes the rate of heat transfer.

The figure graphically depicts these various effects, and the following trends are noted. First, if the inlet temperature is held fixed, and the inlet pressure (both are stagnation) is varied, the heat transfer actually decreases with increasing pressures. This can be explained by considering the conduction heat flow equation. The heat flow is given in terms of Joules/Kg, which equates the heat flow to the unit mass. As pressure increases, the amount of mass in the fluid increases. This effect causes the heat flow per unit mass to decrease, which is what the chart depicts. What this means for the ELGG, is that for an increase in base pressure, there will be a higher mass flow rate (i.e. a point), and with it, more heat should be expected to be conducted to the barrel walls.

However, it can be seen that by holding the inlet pressure constant, but increasing the temperature, the conduction heat transfer per unit mass increases. This is explained by the fact that higher temperature gradients are experienced by the flow, and correspondingly, higher conduction heat transfer will result. Additionally, with increasing temperature at the range of constant pressures to be expected in the ELGG, the thermal conductivity increases, also increasing the amount of heat transfer that should be observed.

Considering the range of heat transfer based on inlet conditions, it is apparent that a wide range of values can be expected. The following table is a section of the data calculated and included in the appendices. It illustrates the heat transfer and percent of inlet power remaining for various inlet conditions.

Table 4.3 Conduction data for heat transfer and percent power available at exit

inlet velocity	inlet temperature	inlet pressure	exit pressure	heat transfer	% power at exit
1,500	10,000	1,000	1,003	-3.956x10 ⁷	72.09
13,000	10,000	1,000	2,260	-1.588x10 ⁷	88.8
1,500	23,000	1,000	1,011	-3.125x10 ⁸	40.14
13,000	23,000	1,000	1,435	-5.501x10 ⁷	83.13
1,500	11,605	1,000	1,008	-5.432x10 ⁷	67.53
13,000	11,605	1,000	1,930	-1.818x10 ⁷	88.96
1,500	10,000	850	857.6	-4.654x10 ⁷	67.16
13,000	10,000	850	2,402	-1.868x10 ⁷	86.82
1,500	10,000	1,150	1,158	-3.44x10 ⁷	75.73
13,000	10,000	1,150	2,288	-1.381x10 ⁷	90.08

From this table, it is evident that conduction effects are most pronounced at low inlet velocities and high inlet temperatures. The power remaining at the exit is highly

dependent on the velocity, as can be seen. The highest velocities correspond the shortest duration of conduction within the barrel itself.

4.3 – ANALYSIS OF VISCOUS EFFECTS

Viscous or frictional effects on a fluid flowing through a pipe has been examined with a one dimensional calorically perfect model and the results follow in this section. As mentioned, viscous effects tend to drive the inlet Mach number toward unity, thus the possibility of choked flow is present whenever viscosity is taken into account. Also note that the effects of viscous action are opposite to those of the transport processes and this difference will be explored. The results in this section are for viscous effects only.

In order to address the effect of friction on the flow of gases down the barrel region of the ELGG, the choice of friction factor must be discussed. There are analytical expressions for the calculation of friction factors for laminar flow in a pipe, but there is not a definitive expression for turbulent flow. As previously discussed, friction factor in turbulent flow is a function of Reynolds number, Mach number and the ratio L/D. The ratio L/D for the ELGG discussed in this thesis turns out to be 33.3, which according to Keenan and Neumann is within acceptable limits for supersonic flow. Additionally, the range of Reynolds numbers are between those discussed for Keenan and Neumann, which is suggestive that their research and conclusions are applicable here.

The following are tables of results based on numerical simulations ran using the procedures detailed in the third chapter. These tables show the impacts of various

friction factors, inlet stagnation temperatures and pressures at a specific inlet velocity on the viscous effects. The method of evaluation, and the full table of calculations and results is located in the appendices.

Table 4.4 Viscous effects with varying input data and friction factors with constant velocity of 4,500 m/sec

friction factor	inlet temp	inlet press	exit press	theo length	press ratio
3.0×10^{-3}	10,000	1,000	988.83	37.11	98.89
3.0×10^{-3}	10,000	850	840.59	37.112	98.89
3.0×10^{-3}	10,000	1,150	1,137	37.11	98.87
3.0×10^{-3}	8,000	1,000	986.1	28.43	98.61
3.0×10^{-3}	11,605	1,000	990.48	44.14	99.05
2.0×10^{-3}	10,000	1,000	992.62	55.67	99.26
4.0×10^{-3}	10,000	1,000	985.2	61.48	98.52

Table 4.5 Viscous effects with varying input data and friction factors with constant velocity of 13,000 m/sec

friction factor	inlet temp	inlet press	exit press	theo length	press ratio
3.0×10^{-3}	10,000	1,000	280.65	1.27	28.06
3.0×10^{-3}	10,000	850	238.67	1.27	28.08
3.0×10^{-3}	10,000	1,150	323.07	1.27	28.09
3.0×10^{-3}	8,000	1,000	96.01	1.63	9.6
3.0×10^{-3}	11,605	1,000	402.54	1.04	40.25
2.0×10^{-3}	10,000	1,000	358.91	1.9	35.89
4.0×10^{-3}	10,000	1,000	183.78	1.04	18.38

The data used to determine the viscosity of the working fluid was obtained from Patch and from INSPI and is included in appendix D. This data takes into account the differing species due to the various temperatures and pressures inherent in the barrel region of the ELGG.

From the data tables, and the information included in the appendices, it is clear that the friction factor, as well as the inlet conditions largely effect the flow characteristics. Additionally, the effects of the theoretical length are apparent. First, note that at low inlet velocities, the effect of pressure changes is nearly negligible on the viscous losses. However, inlet stagnation temperature changes has a more pronounced effect since the temperature directly effects the Mach number. At the relatively low inlet velocity of 1,500 m/sec, the Mach number ranges from .18 to .22. Stagnation losses in this environment would be expected to be minimal, as is borne out by table 4.2.

In addition, the impact of changing the friction factor can be seen in this table as well. Recall that the effect of friction is to drive the inlet mach number towards unity. As the friction factor increases, more frictional effects are noticed by the flow, and the higher the stagnation losses. Hence by going from a friction factor of .003 to .004, there is a corresponding drop in the stagnation pressure at the exit. The results of the changing friction factor are clearly evident in the preceding tables.

The changing of the initial conditions and friction factors are even more dramatic at the higher speeds indicated in table 4.3. This is to be expected since the shear stress at the wall is a function of flow velocity and the Reynolds number. Note again that inlet pressure is not really a factor due to the relatively small density changes, but inlet

temperature dramatically changes the flow characteristics. As temperature increases, the Mach number drops, the Reynolds number increases and the shear stress at the wall decreases, thus explaining the increase in the stagnation pressure ratio at the exit. In effect, higher temperatures tend to decrease the frictional effects, at least in the realm of the ELGG operation studied. The following figures graphically demonstrate the effects of changing inlet conditions at constant friction factors, and constant inlet conditions at different friction factors.

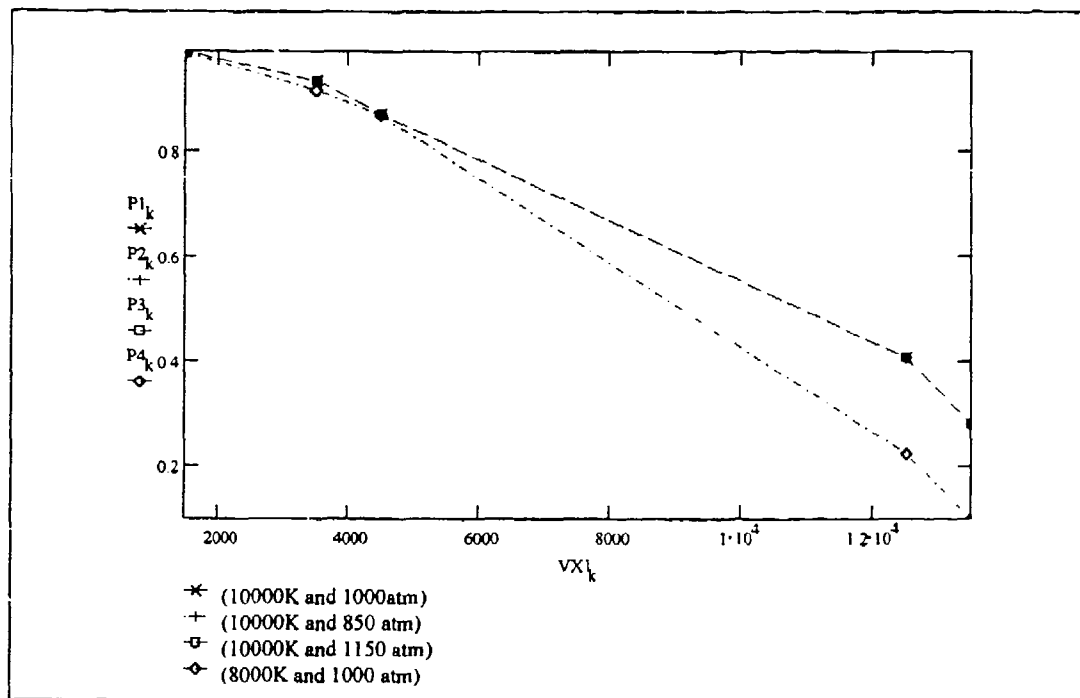


Figure 4.5 Ratio of stagnation pressures verses velocity with a friction factor of .003

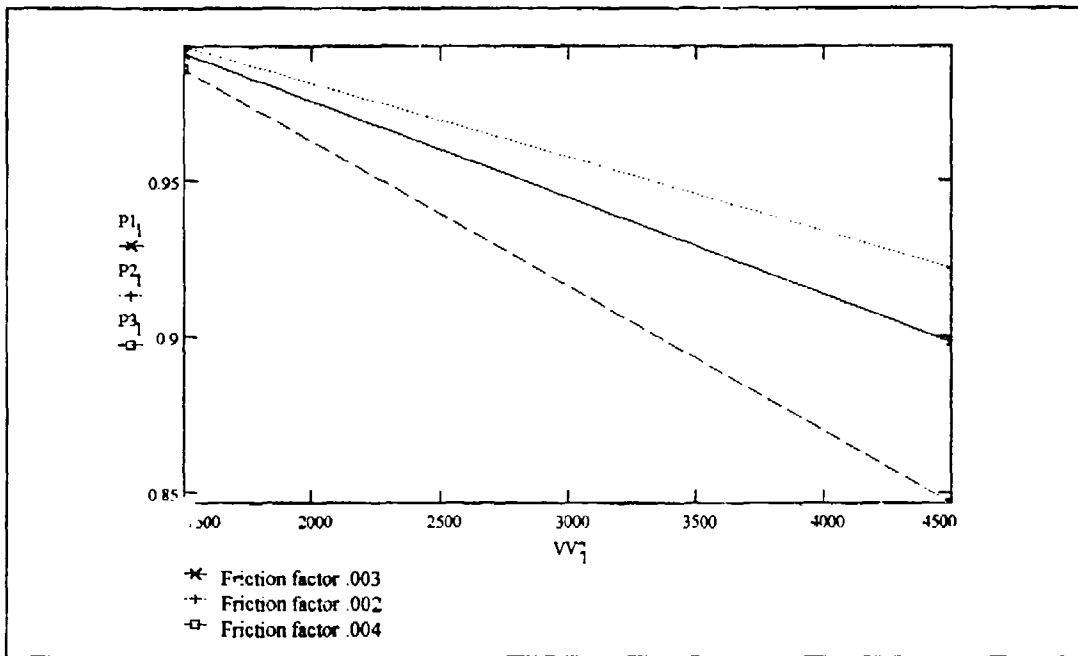


Figure 4.6 Ratio of stagnation pressures verses velocity at different friction factors

As discussed in the model development earlier, frictional effects tend to drive the Mach number towards unity, thus bringing the distinct possibility of choked flow. By looking at the data in the previous tables, and appendices, it is apparent that theoretical length changes not only due to changes in frictional factor, but also by inlet conditions. Again, figure 4.5 demonstrates that pressure changes at the inlet have negligible effect on the theoretical length, but temperature changes have a dramatic effect. This is due to the strong influence Mach number has on the calculation of the theoretical length. For the cases where temperature was at 10,000K and a friction factor of .003, the entire range of inlet velocities from 4,500 m/sec to 12,500 m/sec are not acceptable due to choking in the pipe. With an inlet temperature of 8,000K, this range dropped to include velocities as

low as 4,050 m/sec and as the temperature rose to 2.5 eV, velocities needed to be higher than 20,500 m/sec in order to preclude choking. These inlet conditions must be avoided.

It is highly likely that in the actual barrel of the ELGG, the specific heats will not remain constant, and that their ratio will change. This effect on the theoretical length of the tube has been calculated , and the following trends were discovered. As the ratio of specific heats decreases, the theoretical length tends to increase at the same Mach numbers. Thus, a decreasing γ is actually beneficial in terms of helping to prevent choking of the flow. The opposite is true for an increase in γ . This data is located in the appendices, and in section 3.4.

From the results of this analysis, it will be important to compare the effects of radiation, conduction, and convection within the range of inlet conditions which prevent choked flow.

4.4 -- ANALYSIS OF CONVECTION

Convection is determined in the ELGG by the pressure differentials resulting in forced flow within the gun barrel. As discussed, the flow entering the barrel forms boundary layers which grow to meet at the tube axis. However, the large values of Reynolds numbers (on the order of 10^6) precludes boundary layer growth analysis since fully developed conditions persist immediately past the tube inlet. According to the work of Siegel, Piacesi, and Bixler, "this conclusion is justified and the turbulent boundary layer completely fills the barrel throughout its length." ²⁰ Additionally, in his studies of gun

barrel dynamics, "Williams assumed the flow to be fully developed turbulent flow immediately because of the large Reynolds numbers attained by the driver gas almost immediately."²¹

With this in mind, the thermal starting region was found to begin immediately at the entrance region of the barrel as well, and both the fluid boundary layer and the thermal boundary layers extend to the axis of the tube. Thus the downstream velocity profile does not change from that at the inlet. The following table represents flow at inlet conditions of 10,000K and 1,000 atmospheres at various inlet velocities. The full range of data is included in the appendices.

Table 4.6 Effect of friction factor on convection heat transfer to barrel walls

friction factor	inlet velocity	inlet temperature	inlet pressure	exit pressure	heat transfer "q" to walls	% power	Press Ratio
3.0×10^{-3}	1,500	10,000	1,000	1,004	-2.139×10^7	84.83	1004×10^{-3}
3.0×10^{-3}	4,500	10,000	1,000	1,028	-1.581×10^7	88.85	1028×10^{-3}
3.0×10^{-3}	13,500	10,000	1,000	1,503	-7.83×10^6	94.47	1503×10^{-3}
2.0×10^{-3}	1,500	10,000	1,000	1,004	-1.39×10^7	84.83	1004×10^{-3}
2.0×10^{-3}	4,500	10,000	1,000	1,028	-1.581×10^7	88.85	1028×10^{-3}
2.0×10^{-3}	13,500	10,000	1,000	1,503	-7.83×10^6	94.47	1503×10^{-3}
4.0×10^{-3}	1,500	10,000	1,000	1,004	-2.139×10^7	84.83	1004×10^{-3}
4.0×10^{-3}	4,500	10,000	1,000	1,028	-1.581×10^7	88.85	1028×10^{-3}
4.0×10^{-3}	13,500	10,000	1,000	1,503	-7.83×10^6	94.47	1503×10^{-3}

The first interesting thing to note from the data presented in the table is that, other than limiting the range of inlet conditions necessary to avoid choked flow as discussed for viscous effects, the friction factor does not impact the convection results. This is due to the fact that the flow is immediately fully developed because of the large Reynolds numbers involved, and boundary layer effects are not important in this regime of operation since the entire flow is essentially contained in the boundary layer.

What does dramatically impact the amount of heat loss due to convection is the inlet temperature and velocity. Pressure again, as for viscous effects, does not play a key role. Consider the following table containing calculated data from the convection model.

Table 4.7 Effect on convection heat transfer to walls using various inlet conditions

inlet velocity	inlet temp	inlet press	exit press	heat trans	% power	press ratio
1,500	10,000	1,000	1,004	-2.139x10 ⁷	84.83	1004x10 ⁻³
1,500	10,000	850	853.65	-2.17x10 ⁷	84.69	1043x10 ⁻⁴
1,500	10,000	1,150	1,155	-2.114x10 ⁷	85.08	1043x10 ⁻⁴
1,500	8,000	1,000	1,005	-1.552x10 ⁷	86.31	1005x10 ⁻³
1,500	11,605	1,000	1,004	-2.633x10 ⁷	84.01	1004x10 ⁻³
13,500	10,000	1,000	1,503	-7.83x10 ⁶	94.47	1503x10 ⁻³

As can be seen, inlet stagnation pressure has a minimal effect on changes in exit stagnation pressure and on the amount of heat per unit mass transferred by convection.

Pressure only has an effect by changing the density, which in turn is the only mechanism pressure has which can influence the heat transfer by convection.

Temperature, however, has a large effect on the heat transfer by convection.

Temperature is a main component in the determination of the heat transfer, and in fact the heat transfer is directly proportional to temperature changes. Velocity plays two key roles in the heat transfer by convection. First, by the fact that higher velocities simply reduce the transit time of the fluid through the tube, less time is allowed for the convection heat transfer to the barrel wall's to take place. This limits the amount of heat lost and explains the larger percentage of inlet power remaining at the exit for higher velocities. Secondly, the velocity directly impacts the Reynolds number and Stanton number. These two factors, along with the Prandtl number dramatically effects the heat transfer coefficient.

In order for the Reynolds analogy assumptions to be valid, the Prandtl number should be close to 1.0, as previously mentioned in chapter 3.6. For the entire range of data considered, the Prandtl number ranged from no lower than .929 and to no higher than 1.098. This represents approximately a 9 percent variation from the optimum of 1.0, but is well within the acceptable limits set forth by Eckert.¹³ The following table illustrates the results of calculations at various inlet stagnation temperatures and pressures and inlet velocities.

Table 4.8 Convection parameters at varying inlet conditions

inlet velocity	inlet temp	inlet press	Reynolds #	Prandtl #	Stanton #	Coeff of frict
1,500	10,000	1,000	1.273x10 ⁴	1006x10 ⁻³	1x10 ⁻³	2x10 ⁻³
4,500	10,000	1,000	3.251x10 ⁴	1006x10 ⁻³	.931x10 ⁻³	2x10 ⁻³
13,500	10,000	1,000	9.48x10 ³	1006x10 ⁻³	1x10 ⁻³	3x10 ⁻³
1,500	10,000	850	1.082x10 ⁴	1098x10 ⁻³	1x10 ⁻³	2x10 ⁻³
4,500	10,000	850	2.763x10 ⁴	1098x10 ⁻³	.989x10 ⁻³	2x10 ⁻³
13,500	10,000	850	8.061x10 ³	1098x10 ⁻³	1x10 ⁻³	2x10 ⁻³
1,500	10,000	1,150	1.464x10 ⁴	929x10 ⁻³	1x10 ⁻³	2x10 ⁻³
4,500	10,000	1,150	3.739x10 ⁴	929x10 ⁻³	.959x10 ⁻³	2x10 ⁻³
13,500	10,000	1,150	1.091x10 ⁴	929x10 ⁻³	1x10 ⁻³	3x10 ⁻³
1,500	8,000	1,000	1.812x10 ⁴	1006x10 ⁻³	1x10 ⁻³	2x10 ⁻³
4,050	8,000	1,000	4.173x10 ⁴	1006x10 ⁻³	.896x10 ⁻³	2x10 ⁻³
13,500	8,000	1,000	3.154x10 ³	1006x10 ⁻³	2x10 ⁻³	3x10 ⁻³
1,500	11,605	1,000	1.044x10 ⁴	994x10 ⁻³	1x10 ⁻³	2x10 ⁻³
4,500	11,605	1,000	2.258x10 ⁴	994x10 ⁻³	.976x10 ⁻³	2x10 ⁻³
13,500	11,605	1,000	1.333x10 ⁴	994x10 ⁻³	1x10 ⁻³	2x10 ⁻³

From this data and the relationships of pressure, temperature and flow velocity, we can consider the amount of heat transfer due to convection. The following graph illustrates the heat flow per unit mass for convection at various inlet velocities. Note from this graphical analysis that the heat transfer by convection is only affected appreciably by temperature and velocity changes, and pressure changes are negligible.

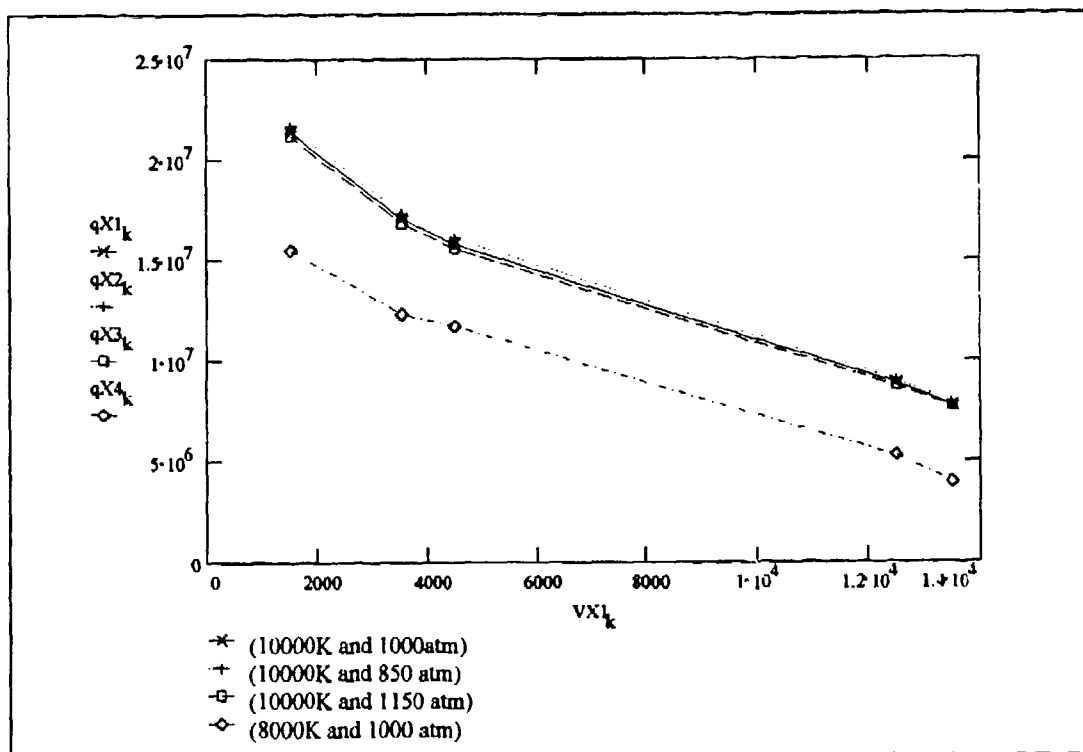


Figure 4.7 Heat transfer per unit mass for convection at a friction factor of .003

4.5 ANALYSIS OF RADIATION

Radiation is the transport of energy out of the system mainly by virtue of the temperature within the fluid. However, how the thermal energy is transferred depends on the properties of the fluid, most notably the opacity. To determine the optical depth of the working fluid, the models described in section 3.7 are used. This methodology initially indicated that at 10,000K and 100 atmospheres, the mean free path for the working fluid based on Rosseland emission is approximately .45 to .55 meters as opposed to Planck mean free paths of approximately .2 to .3 meters. This would suggest that the

radiation coming from the fluid may be flux limited, or in other words, is limited by the equilibrium specific intensity or Planck function.

However, this data has been shown to not completely describe the system studied in this thesis. The following figures show the calculation of the heat transfer per unit mass for Rosseland and Plank radiation.

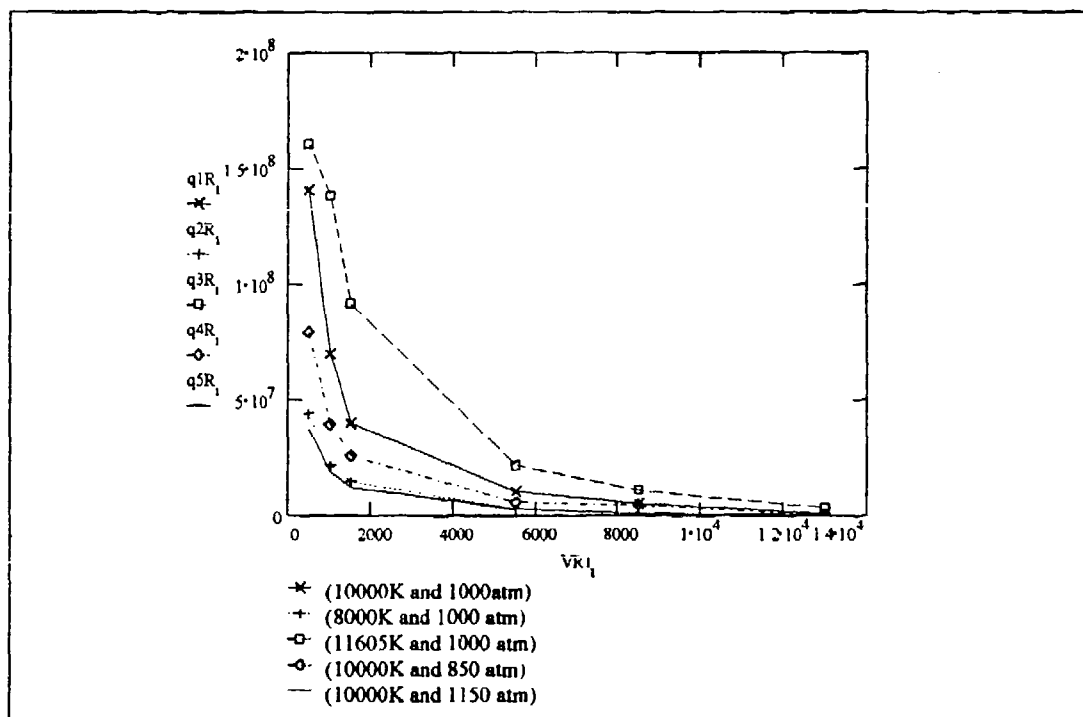


Figure 4.8 Rosseland radiation heat transfer per unit mass

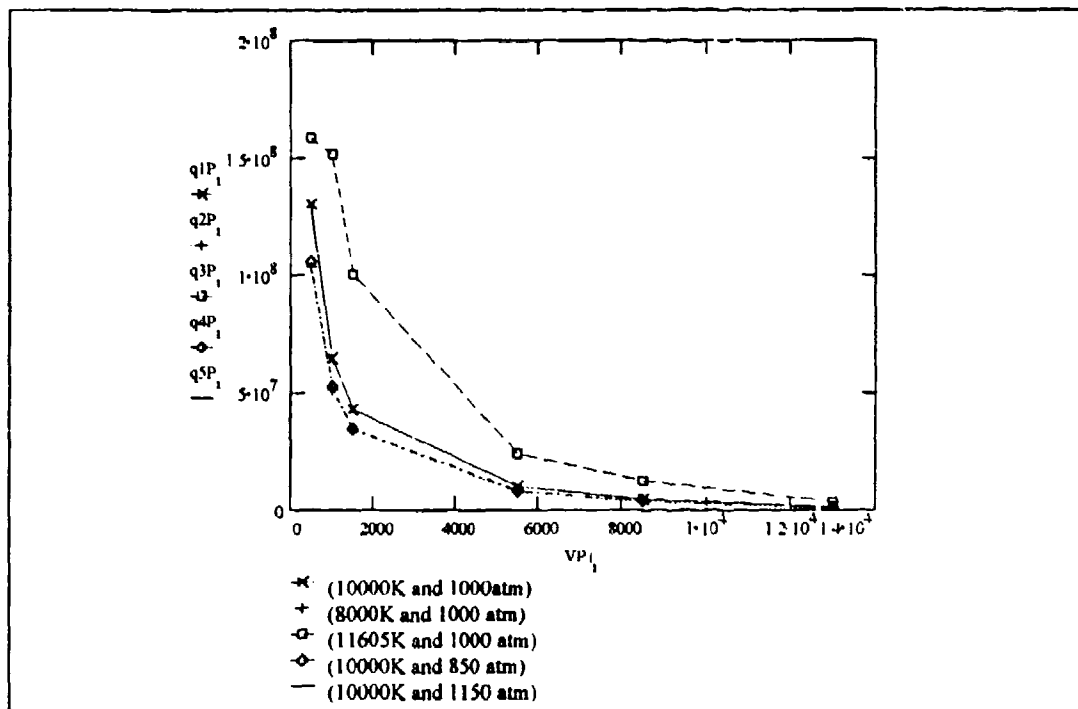


Figure 4.9 Planck radiation heat transfer per unit mass

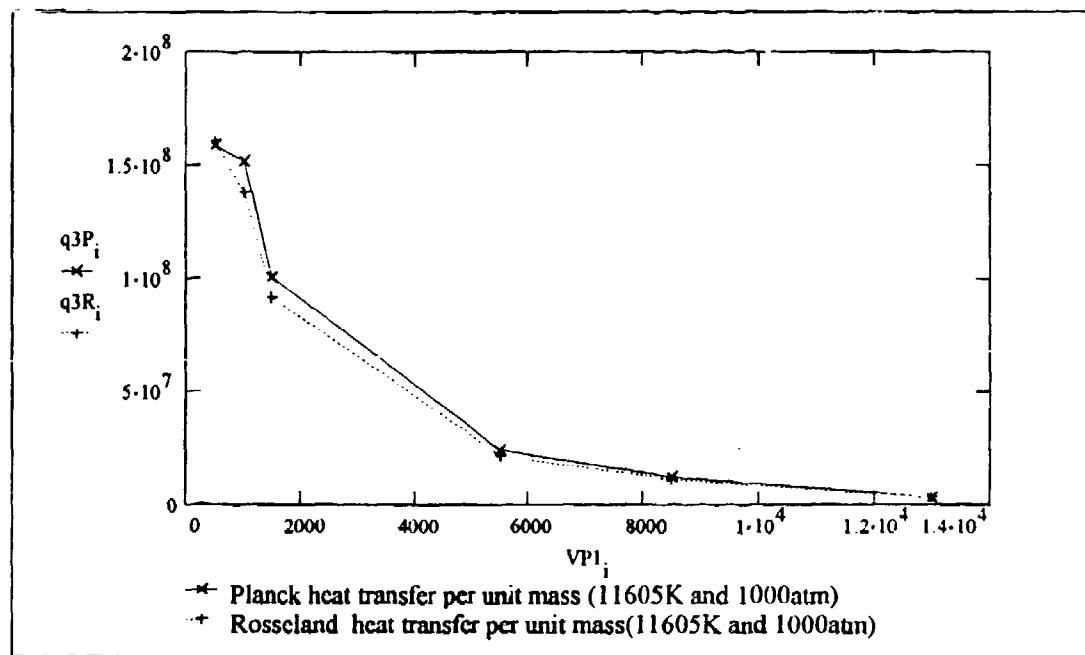


Figure 4.10 Comparison between Planck and Rosseland radiation heat transfer at 1,000 atm and 11,605K

As it can be seen from these graphs, at various points either method is usable, with some points flux limited by Planck radiation and others absorption limited by Rosseland radiation. However, by looking at conditions of 23,000K and 1,000 atmospheres, it is clearly seen that Rosseland diffusion is appropriate for the model of radiation heat loss. This effect becomes more pronounced as temperature increases. At nearly 3 eV and 1,000 atmospheres, the Rosseland diffusion heat transfer is 3 orders of magnitude less than Planck, suggesting a highly absorption dominated working fluid. As pressure drops, this was also found to be the case. It seems that since both Rosseland and Planck have similar mean free paths down to approximately 5,000K, the methodology to use is Rosseland diffusion, and not Planck as previously expected . This would tend to indicate that the ELGG system studied is mainly absorption dominated throughout its operating range rather than emission dominated.

The difference between the initial results and those determined by the models developed in sections 3.5 and 3.7, is that initially purely blackbody radiation, σT^4 , was assumed to be sufficient for Planck calculations, but this is not completely true. As pointed out in section 3.7, there should have been included in the preliminary thesis work the factor $4\alpha_p$, which makes the difference and accounts for the Planck mean absorption coefficient.

The variation in radiation heat transfer over velocity changes is explained by the fact that higher flow speeds decreases the working fluid transition time through the tube, thus limiting the time for the fluid to radiate energy. This is similar to the effects encountered in the convection and conduction results as well.

As discussed in section 3.7, the radiation energy density can be computed and compared to the convection heat flux and the internal energy to determine when radiation should be considered. The radiation energy density initially found in the tube can be calculated from the inlet conditions. It should be noted that as the temperature changes with the flow down the tube, this radiation energy density drops as the fourth power of the temperature, thus radiation will rapidly become negligible towards the end of the barrel region. The combined effects of radiation, convection and conduction serve to force the flow temperature down.

The radiation energy density for 10,000K and 1,000 atmospheres inlet conditions with inlet velocity 3,500 m/sec is found to be 5.67×10^7 Watts/meter whereas the internal energy is 1.005×10^8 Watts/meter, the convection heat flux is approximately 1.75×10^7 , and the conduction heat flux is approximately 3.05×10^7 Watts/meter. Clearly the effects of thermal radiation is of the same order of magnitude as that of conduction and convection, and must be included in heat transfer studies. The assumptions used in models used by other researchers, namely Siegel, Stephenson, and the Weapons Laboratory at Rock Island, that radiation is not a factor is incorrect and by avoiding the inclusion of radiation effects must raise questions as to the accuracy of their results.

4.6 – COMPARATIVE ANALYSIS

In this section, the various transport mechanisms and the viscous effects will be compared and determination of the regimes of operation where these heat loss processes

dominate will be made. The regimes of operation show where these mechanisms are of equal order of magnitudes, and trends discovered from the one dimensional models will be discussed in order to fully analyze the MACH2 results. The power remaining in the working fluid is examined as is the ratio of exit to inlet stagnation pressures. Internal energy changes associated with the various heat loss mechanisms will also be looked at.

It has been mentioned that the cooling effects of conduction, radiation, and convection on the working fluid tend to drive the Mach number away from unity, thus avoiding the prospects of choked flow, shockwave development and the corresponding loss in efficiency and the inevitable "correction" of the flow inlet conditions. However, viscous effects act to drive the Mach number towards unity, suggesting that there may be a trade off of effects.

Since all these processes are, in reality, closely coupled together, it is not possible to analytically describe all these effects simultaneously. However, the data presented up to this point can give some understanding of what can be expected for the flow of a high temperature working fluid down the barrel of the ELGG.

Consider the ratio of stagnation pressures from the exit to the inlet. This is an indication of the overall effects each of the dissipative modes has on the fluid. For conduction, it has been determined that at inlet velocities below approximately Mach .5, the ratio of stagnation pressures remains nearly constant for inlet pressures of 1,000 atmospheres, and temperatures up to 1.8 eV. Above this temperature range, the ratio increases slightly, from 1.003 at 1 eV to 1.07 at 2.92 eV. This shows, in effect, that the temperature at constant pressure of 1,000 atmospheres has negligible effect on

conduction. This was also determined to hold true for pressure ranges from 850 atmospheres to 1,150 atmospheres.

As the velocity was increased beyond Mach .5, the results changed, showing a high degree of variation in the stagnation pressure ratio with both temperature and pressure. The change from low to high velocity ranges is manifested in the duration of time the fluid remains in the ELGG barrel region, and the variations noted indicate the dependence of the thermal conductivity to both temperature and pressure. According to data provided by INSPI, both temperature increases and pressure decreases show marked increases in the thermal conductivity of the hydrogen working fluid.

For radiation, it has been computed that the velocity changes do not have the large variations in stagnation pressure ratios exhibited by conduction, and that changing pressure has little effect on the ratio as well. There was nearly a linear correspondence to increasing temperature and increasing pressure ratio. It is interesting to note that both the Rosseland and Planck radiation data indicated pressure ratios which were to within 1% of each other, although the heat transfer was far greater for Planck.

Viscous effects tended to decrease the exit stagnation pressures, whereas all the other heat loss mechanisms tended to increase the exit stagnation pressure. This is consistent with the particular models used, and dramatically shows the difference between heat transport mechanisms and viscous effects. Viscous effects showed little change based on temperature or pressure variations, but were dramatically affected by velocity changes. This is consistent with expectations since viscous effects are driven by gradients in velocity throughout the flow region, and higher velocities tend to create large velocity

gradients, most notably near the tube walls. Pressure ratios as low as .0926 were calculated at speeds in excess of Mach 3.2 at a temperature of 8,000K and pressure of 1,000 atmospheres.

Convection showed similar results as conduction, but the pressure ratios were never as large as those found in conduction. Convection pressure ratios were negligibly affected by pressure variations, but were strongly affected by inlet temperature increases and flow velocity. Pressure ratios ranged from 1.806 at 8,000K, 1,000 atmospheres and flow velocity of 13,000 m/sec, to 1.310 at 34,000K, 1,000 atmospheres and 13,000 m/sec.

Although it cannot simply be a matter of looking at these results and combining the information to predict the final outcome, it is possible to note that increases in stagnation pressure ratios are associated with increased heat dissipation from the working fluid, and that viscous effects tend to decrease this ratio. As a first approximation, it is noted that as the inlet temperature of the working increases, regardless of the pressure at the inlet (within the scope of this thesis) the combined increase of the pressure ratio due to conduction, radiation, and convection are practically offset by the decrease caused by viscous dissipation. However, as the inlet velocity increases to well over Mach 1.0, the situation changes, and it can be expected that viscous effects will tend to dominate over the other three. Again, this is only a first approximation, and recall that the effects of radiation, convection and conduction were calculated using one dimensional, steady state, inviscid models. The calculations from the MACH2 code will be able to simultaneously solve these together, and a better representation of the actual system should be obtained.

In addition to the stagnation pressure ratio, the heat transfer for convection, conduction and radiation can be compared, and regimes of influence determined. Consider conduction heat transfer data obtained from calculations made using the one dimensional model developed in chapter 3.5. This data demonstrates that as the velocity increases at any temperature and pressure combination, the heat transfer decreases, due mainly to the reduced transit time of the working fluid. Generally, the trends indicate that at a constant pressure of 1,000 atmospheres, and velocity ranges from 500 m/sec to 13,000 m/sec, the following range of heat transfer is obtained:

Table 4.9 Conductive heat transfer data

Inlet temperature (K)	Range of heat transfer calculated (J/kg)
8,000	7.464×10^7 to 1.816×10^7
10,000	1.17×10^8 to 7.83×10^6
23,000	3.125×10^8 to 5.501×10^7
34,000	1.444×10^8 to 1.066×10^8

Under the same conditions mentioned above, the Rosseland and Planck heat transfer ranges were determined and are shown in table 4.10. Table 4.11 shows the data for convection using the same conditions as conduction and radiation.

Table 4.10 Radiative heat transfer data

Inlet temperature (K)	Rosseland heat transfer (J/kg)	Planck heat transfer (J/kg)
8,000	4.421×10^7 to 1.786×10^5	1.034×10^8 to 4.717×10^5
10,000	1.403×10^8 to 1.252×10^6	1.303×10^8 to 1.219×10^6
23,000	2.120×10^7 to 1.412×10^6	8.244×10^{10} to 5.521×10^9
34,000	1.605×10^8 to 1.287×10^6	2.508×10^{11} to 2.017×10^9

Table 4.11 Convection heat transfer data

Inlet temperature (K)	Range of heat transfer calculated (J/kg)
8,000	1.522×10^7 to 4.007×10^6
10,000	2.139×10^7 to 7.83×10^6
23,000	8.924×10^7 to 4.428×10^7
34,000	1.419×10^7 to 7.748×10^6

From the above three tables, it is now possible to discuss regimes of influence for these heat transport processes. To do this, the regimes for which data was obtained will be outlined using constant inlet pressure of 1,000 atmospheres.

For temperature regions below 10,000K, conduction dominates the flow at higher inlet velocities, but near 10,000K, both conduction and radiation are noted to be nearly equal in magnitude. Convection tends to maintain at a level of heat transfer which is an order of magnitude less than conduction. It is also apparent that convection is more

important in this regime than either Rosseland or Planck radiation when velocities in excess of Mach .8 are concerned. This region is characterized by inlet temperatures less than 1 eV, heavy conduction throughout the barrel region, and radiation effects rapidly diminished as the flow progresses throughout the barrel.

For flow in regimes of operation between 1 eV and 2 eV, the flow has nearly equal magnitudes of conduction, convection and Rosseland radiation, although the Planck radiation model shows several orders of magnitude higher heat transfer. This was discussed in section 4.7, and from this point, the working fluid is absorption dominated, thus limiting the amount of radiation seen at the walls. Thus Rosseland diffusion approximations should more adequately model the fluid in this regime of operation, and the data for Rosseland radiation will be used exclusively. The effects of velocity in this regime are not as apparent as in the below 1 eV regime, and due to the combined effects of all three heat transfer processes, the radiation will decrease due to the temperature drop associated with the heat loss. This reduction in radiation due to the temperature loss will rapidly shift the radiation component of heat transfer to the regime discussed previously due to the dependence of T^4 . Additionally, the effect of heat loss is to increase the flow velocity, thus further reducing the radiation expected. The corresponding increase in velocity as the fluid progresses will keep the conduction and convection heat loss within the same order of magnitude.

The final regime studied is that from 2 eV to 3 eV. In this region, Rosseland radiation dominates at inlet velocities below Mach .7, and conduction is seen to be a strong heat transfer mechanism. Both conduction and radiation are an order of magnitude greater

than convection at low velocities, and at high inlet velocities, radiation and convection are of the same order of magnitude. Again, the temperature decreases associated with heat loss will tend to rapidly diminish the radiative heat transfer, but radiation should remain a large contributing factor throughout a significant portion of the barrel length. The following three figures graphically illustrate the flow regimes discussed:

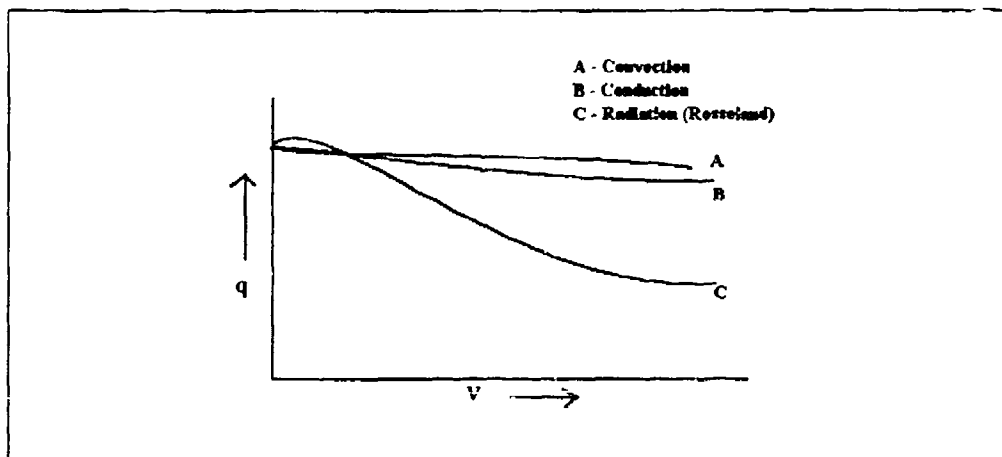


Figure 4.11 Representation of transport processes in the operating regime of less than 1 eV (1,000 atm)

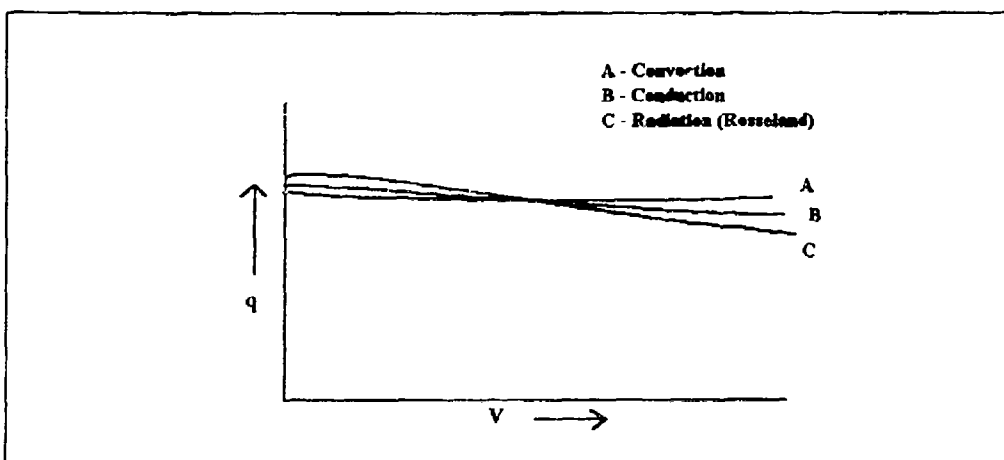


Figure 4.12 Representation of transport processes in the operating regime from 1 eV to 2 eV (1,000 atm)

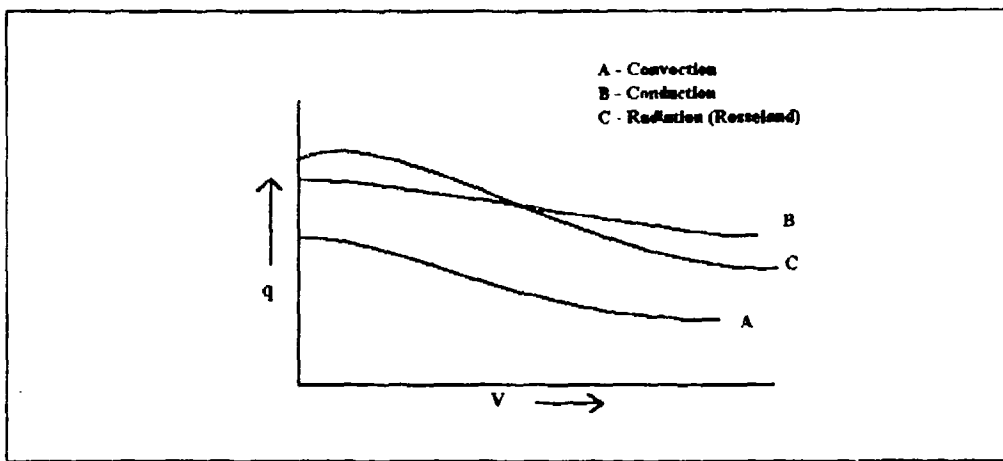


Figure 4.13 Representation of transport processes in the operating regime from 2 eV to 3 eV (1,000 atm)

From this analysis, it is apparent that conduction will play a significant role in the flow of the working fluid in the barrel region of the ELGG. Convection also plays a major role, but is only significant at high inlet velocities. Radiation has been shown to be absorption dominated throughout the operating region, dominating at temperatures in excess of 2 eV, and rapidly diminishing as distance through the barrel increases.

To complete the flow regime analysis, the problem of choked flow caused by viscous effects in addition to these heat transfer processes must be included. As noted previously, the viscous effects will limit the inlet flow velocities based on the formation of a normal shock in the tube. At this point, the flow has reached the maximum mass flow rate, and no further increase can be tolerated. From figure 3.3 and table J.1, it was determined that inlet velocities must be below Mach .63 or above Mach 2.36 with a friction factor of .003 in order to prevent choking of the flow. Using the equation of continuity (equation 3.19), the maximum mass flow rate is determined to be 6.596 kg/sec, with an inlet cross

sectional area of $7.069 \times 10^{-4} \text{ m}^2$, interior surface area of $.094 \text{ m}^2$ and interior barrel volume of $7.069 \times 10^{-4} \text{ m}^3$. The ELGG Barrel length is 1.0 meters.

This changes slightly the flow regimes discussed in that much of the flow detailed cannot actually be expected to be seen in the ELGG barrel. Since the viscous effects limit inlet velocities to below Mach .63, the low speed discussion remains valid. However, since only inlet speeds in excess of Mach 2.36 are allowed, it can be expected that convection will be a significant heat transfer process if supersonic flow within the barrel is required. This will also tend to decrease the radiation heat loss and conduction due to the decreased working fluid transit time through the barrel.

The power remaining at the exit of the ELGG barrel is an indicator of the ability for the working fluid to accelerate a projectile. From the results discussed in sections 4.1 through 4.5, it was determined that the conditions favoring the largest percentage of power remaining were high temperature and high velocities. This can be seen in tables 4.3, 4.6, and G.1. This works out well since the Mach numbers will be much higher than the choking Mach number of 2.36. At inlet speeds of 13,000 m/sec, the percentage of power remaining at the exit for each of the transport processes can be compared. Conduction shows a dependence on pressure, ranging from a low of 86.82% at 10,000K and 850 atmospheres, to 90.08% at 10,000K and 1,150 atmospheres. At constant pressure of 1,000 atmospheres, the range is from 83.98% at 8,000K to 88.96% at 11,605K, and then dropping off to 77.88% at 34,000K. Rosseland radiation shows no pressure dependence, and the percentage ranges from 97.3% to 99.7%, hence the high speed tending to limit the amount of radiation losses due to low transit times. Finally,

convection does not exhibit pressure dependencies, but shows a range from 83.92% at 34,000K to a high of 96.47% at 8,000K. Thus convection is again shown to be more effective at higher temperatures and velocities. These results also show that conduction remains a major contributor throughout the range of operating conditions of the ELGG.

As the flow progresses, the decreasing temperature can act to change the γ of the fluid which will also affect the limiting Mach numbers. According to figure D.4, however, generally the decreasing temperature at a nearly constant pressure of 1,000 atmospheres will tend to decrease the γ which is actually beneficial, since a lower γ has been shown to decrease the limiting Mach number.

A final point for discussion, and an important finding, is the effect recombination has on the overall energy of the working fluid. When the working fluid is heated by the electric arc, a substantial portion of the fluid may be ionized. From figure 4.2, it was shown that this could be as high as 50 percent at 3 eV. In addition to the amount the working fluid is ionized, it was shown that it is nearly completely dissociated into atomic hydrogen at temperatures as low as 1 eV. Considering the dramatic decrease in stagnation temperature at the exit, it is necessary to consider the energy liberated by the recombination of positively charged atomic hydrogen and the free electrons. It was shown that the working fluid is not frozen as it progresses down the barrel, and in fact the relaxation rates are sufficient for equilibrium to be reached at every point during the time the fluid travels through the barrel. Because of this, and the fact that the fluid remains substantially atomic hydrogen down to approximately 10,000K, the following recombination reaction can be assumed to be dominant.



The energy of ionization is given as 1.31×10^3 KJ/mol for this process. Using the assumption that the recombination brings the electron to the ground state, and data on electron number densities provided by Patch⁷⁸, the table 4.12 was produced which demonstrates the liberated energy which may be expected by this reaction. Calculations have shown that stagnation temperatures at low inlet velocities may drop to or below 5,200K. Higher velocities and temperatures may not have such a large change, but will retain orders of magnitudes similar to those shown in figure 4.12. Below 5,200K, the electrons are nearly 100% recombined and molecular hydrogen begins to dominate the working fluid

Table 4.12 Energy liberated during recombination (1,000 atm)

Initial velocity	Inject stagnation temperature	Inlet stagnation pressure	Exit static temperature	number density change (e^-)	Energy released by recomb (J)
1,500	10,000	1,000	7,169	5.37×10^{23}	8.257×10^2
8,500	10,000	1,000	6,119	1.29×10^{22}	1.984×10^4
13,000	10,000	1,000	2,404	4.55×10^{17}	6.997×10^4
1,500	23,000	1,000	954	5.437×10^{23}	8.361×10^4
8,500	23,000	1,000	17,330	1.968×10^{23}	3.026×10^4
13,000	23,000	1,000	10,506	4.713×10^{23}	7.247×10^3
8,500	34,000	1,000	22,920	5.971×10^{23}	8.913×10^4
13,000	34,000	1,000	13,470	3.756×10^{23}	5.776×10^4

This information is very important when compared to the magnitudes of energy loss for each of the transport processes. In order to facilitate direct comparisons, the following table of energy loss for each of the transport processes at various initial conditions was produced.

Table 4.13 Transport energy loss at 1,000 atm (* 4500 m/sec for convection)

Initial velocity (m/sec)	Inlet stagnation temperature (K)	Mass flow (kg/sec)	Rosseland energy loss (J)	Planck energy loss (J)	Conduction energy loss (J)	Convection energy loss (J)
1,500	10,000	2.56	6.856x10 ⁴	7.319x10 ⁴	6.74x10 ⁴	3.65x10 ⁴
1,500	23,000	1.12	1.587x10 ⁴	6.171x10 ⁷	2.339x10 ⁵	6.679x10 ⁴
1,500	34,000	0.63	6.780x10 ⁴	1.061x10 ⁸	No Data	6.296x10 ³
5500*	10,000	7.26	1.410x10 ⁴	5.665x10 ⁴	1.649x10 ⁴	1.837x10 ⁴
8,500	23,000	4.83	1.770x10 ⁵	6.914x10 ⁸	3.682x10 ⁴	3.01x10 ⁴
8,500	34,000	2.72	8.041x10 ²	1.257x10 ⁷	4.614x10 ⁴	2.89x10 ³

Note that the energy liberated by recombination plays little part in the flow characteristics and heat transfer at low initial temperatures. However, as the static temperature exceeds approximately 15,000K, the energy from recombination approaches that of the energy lost through the transport processes. This is especially apparent at higher velocities since the transport processes are limited by the duration of time the fluid remains in the barrel. Note further that between 2 eV and 3 eV, the energy liberated is of

equal or greater magnitude than that from all the transport processes combined. From previous discussions, Planck radiation is not considered.

What this shows is that as the temperature increases into the 2 eV to 3 eV range, energy is made available for projectile motion by recombination of the free electrons with ionized atomic hydrogen. This is a significant finding, and provides strong support for the use of high temperature plasmas as working fluids for the purpose of projectile motion. Table 4.14 illustrates the hydrogen specific internal energy as well as the degree of ionization and dissociation. From this data, it is obvious that for hydrogen, ionization energy makes up a significant portion of the internal energy at 2 to 3 eV, and contributes to the working fluid's ability to provide for projectile motion. This effect is negligible for lower inlet stagnation temperatures, at 1,000 atmospheres. Dissociation energy is made available to the working fluid only during the recombination of atomic hydrogen into molecular hydrogen, but only at temperatures below 10,000K. At higher inlet temperatures, the recombination was found to be negligible, and hence added little to the working fluid internal energy.

Table 4.14 Hydrogen internal energy data (8,500 m/sec, 1,000 atm)

inlet stag temp (K.)	inlet sie (J/Kg)	exit sie (J/Kg)	inlet static temp (K)	exit static temp (K)	inlet degree of ionization	exit degree of ionization	inlet degree of dissoc	exit degree of dissoc
10,000	4.41×10^7	2.926×10^7	7,451	6,119	3.659×10^{-5}	1.857×10^{-4}	0.71	0.39
23,000	5.43×10^7	1.078×10^7	20,450	17,330	.135	.0872	fully	fully
34,000	4.63×10^7	9.54×10^7	31,450	22,920	.5263	.172	fully	fully

CHAPTER 5

ANALYSIS OF MACH2 COMPUTATIONS

Several full model computations were conducted with the MACH2 code, first isolating each process for verification of proper operating conditions, and then running full model simulations with all effects on simultaneously. It should be noted that these computations were performed with argon due to the limitations faced in getting hydrogen properties properly coded into the program. Nevertheless, the previous ground work and results are applicable for trend analysis and can provide methods for verifying the results obtained from MACH2.

The computations completed used a calculation mesh of 10 icells (x direction) and 10 jcells (y direction) with inlet conditions of stagnation temperature ranging from 10,000K to 24,000K, static densities from 1.858 kg/m³ to 43.163 kg/m³, and velocities of Mach .5 and 3.5. These inlet Mach numbers were chosen based on the theoretical length analysis in chapter 3 to preclude choked flow conditions within the barrel region. The computations were conducted with both Planck and Rosseland radiation parameters and included the effects of viscosity, conduction, and chemical reactions.

MACH2 generates data in two main ways, numerical data and plots, both of which were used for this analysis. A sample set of data is included in appendix L. Two cases are presented, both using Planck radiation with inlet Mach numbers of 3.5, one at 10,000K and the other at 23,000K. Table 5.1 presents a small portion of the overall data generated for five separate cases.

Table 5.1 Full model results for MACH2 computations (average)

Rad Model	Inlet stag temp (K)	Inlet Mach #	Stag Enthalpy change	Ratio of stag pressures	# diameters for developed flow	Exit Mach #
Planck	10,000	5.0×10^4	-1.818×10^6	1.73	5.04×10^{-1}	3.38×10^{-1}
Roseland	23,000	3.5	$+3.681 \times 10^5$	0.57	5.10×10^{-1}	2.60×10^{-1}
Planck	23,000	3.5	$+1.652 \times 10^5$	0.78	5.10×10^{-1}	3.09×10^{-1}
Planck	10,000	3.5	-4.772×10^6	1.01	3.67×10^{-1}	2.92×10^{-1}
Roseland	10,000	3.5	-4.435×10^6	0.83	3.67×10^{-1}	2.54×10^{-1}

For computations at inlet stagnation temperatures of 10,000K, the flow develops a low temperature region near the wall with the lowest velocity in this region as well. This increases gradually for both quantities towards the axis, leaving the density at the highest values near the wall. The flow field demonstrates small scale velocity magnitudes directed slightly towards the wall with a fan wave expansion at the exit. The flow shows that boundary layers grow rapidly to fully developed flow within .504 diameters of the barrel inlet. Figure 5.1 illustrates this data. Note that the proportion indicated is misleading. The barrel is 1.0 meters long and has radius .015 meters from the center line.

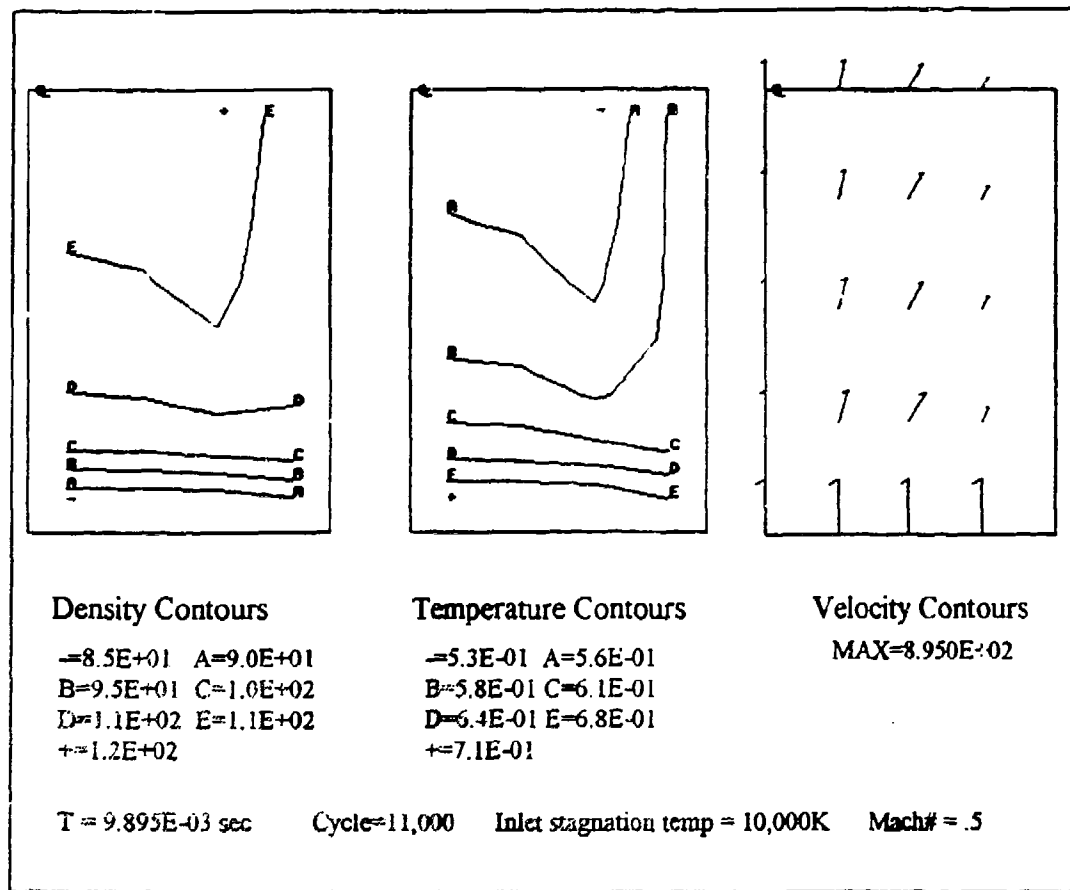


Figure 5.1 Full model computations

It is interesting to note that density is largest near the wall and barrel exit, suggesting that the effective tube radius is reduced in the flow direction due to density variations. This is supported by velocity data showing highest velocity near the axis and trailing off gradually to within 2 cells of the wall, then a rapid velocity decrease occurs. According to data from the Mach2 runs, axis velocities of 5.044×10^2 m/sec decreasing to 4.263×10^2 m/sec within 2 cells of the wall are present, with a sudden drop to 2.006×10^2 m/sec at the wall interface.

Due to the low inlet flow speed, sound wave transit times are three times greater, on average, than the working fluid transit time down the length of the barrel. This explains the near uniform pressure contours throughout the barrel region, and suggests that the flow has plenty of time to communicate changing conditions throughout the flow. This holds true for the barrel length as well as from the tube walls to the tube axis.

Viscous dissipation was found to not be a strong factor in this flow due to the low inlet velocities, as well as the low inlet temperature. Chemical recombination of the working fluid appears to play no significant role in this operation regime as well. Finally, as predicted by the trends discussed in chapter 4, there is a stagnation pressure increase at the exit, and the Mach number drops. This indicates a direct correspondence to the one dimensional model developed in chapter 3. (see table 5.1 for data)

As the Mach number at the inlet increases to 3.5 with the same inlet stagnation temperature of 10,000K, the situation changes markedly. There is a high temperature region created near the barrel walls over the entire length. In this region, velocity is at the lowest value and density is also at the lowest value. This is in direct contrast to the subsonic results previously discussed. A region of high density (6.8 kg/m^3 verses 1.3 kg/m^3) persists near the tube axis. Vorticity is initially widespread throughout the interior of the barrel, but by 10,895 cycles, it is no longer a factor, suggesting that the flow has become fully developed. This is clearly seen in the plots located in appendix L.

Considering the two radiation models employed in the calculations, Planck radiation results in a higher enthalpy loss than the Rosseland model, suggesting that the flow may be absorption dominated, much the same way that the hydrogen working fluid was found

to be. The change in enthalpy is much higher for both models at this higher inlet velocity.

The flow shows an average exit Mach number of 2.54 for the Rosseland case and 2.92 for the Planck case. This demonstrates that the choice of Mach 3.5 was an effective measure in avoiding choked flow. However, the Mach number decreases are not as severe as predicted, mainly due to viscous dissipation in the working fluid near the walls.

Since the fluid is supersonic throughout the barrel, the pressure waves cannot keep up with the flow, and non-uniform pressure variations were demonstrated. This effect was present in the axial direction, but was not severe in the radial direction due to the small tube radius and relatively short wave transition time in the radial direction.

At inlet conditions of Mach 3.5 and stagnation temperature of 23,000K, the effects noted for the supersonic flow at the lower temperature are present, but show much higher magnitudes. The temperature band near the wall has higher temperatures and is thinner than that demonstrated at 10,000K. Boundary layer growth is very rapid (less than 8.95×10^{-4} sec) in the flow direction.

The supersonic flows do not show the density region near the exit acting to reduce the tube radius as demonstrated for subsonic flow. In all cases the temperature, density, and pressure approach towards steady state values as time progresses, and rapid turbulent boundary layer development resulted in fully developed flow within one diameter into the barrel region. Once this occurred, the velocity profile did approach a uniform distribution with strong changes near the wall. This is also in accord to general trends predicted by the one dimensional models in chapter 3 and analyzed in chapter 4.

For argon, the degree of ionization is very low ($<< 1\%$) for most regimes studied, due mainly to the high inlet stagnation pressure of 1,000 atmospheres, and the high ionization energy for argon. However, at 2 eV and inlet Mach number of 0.5, argon is 30.86% ionized, and this energy may be recovered for projectile motion. Considering table 5.2, except for the high temperature, low inlet velocity case, there is a low degree of ionization, making recombination energy negligible. The argon is apparently a weakly ionized plasma at 1,000 atmospheres at temperatures below 2 eV and at high velocities.

Table 5.2 Argon internal energy data (1,000 atm)

inlet Mach #	inlet stag temp (K)	inlet sic (J/Kg)	exit sic (J/Kg)	static inlet temp (K)	static exit temp (K)	inlet deg of ionizaiton	exit deg of ionization	type rad
3.5	10,000	8.901×10^5	1.138×10^6	1,964.73	2,756.19	$<<1\%$	$<<1\%$	Planck
3.5	10,000	8.901×10^5	1.373×10^6	1,961.25	3,509.35	$<<1\%$	$<<1\%$	Ross
3.5	23,000	1.684×10^6	2.105×10^6	4,502.74	6,12628	$<<1\%$	$<<1\%$	Ross
0.5	10,000	3.152×10^6	2.115×10^6	9,186.52	6,136.72	1%	$<<1\%$	Planck
3.5	23,000	1.684×10^6	1.885×10^6	4,502.74	5,146.82	$<<1\%$	$<<1\%$	Planck
0.5	23,000	2.146×10^7	2.155×10^6	21,237.15	6,013.71	30.86%	$<<1\%$	Planck

It is apparent that the MACH2 program is an important tool in the study of ELGG barrel regions and shows results following the general trends of simpler models. The development of high temperature bands near the walls is not predicted by the models developed in chapter 3, which is a consequence of the more sophisticated techniques employed in the programming of MACH2.

CHAPTER VI

CONCLUSION

This thesis has considered the thermal characteristics and heat transfer within an ELGG barrel section. The ELGG examined consisted of a 1.0 meter barrel with .03 meter diameter separated from an arc chamber or convergent-divergent expansion nozzle by a diaphragm designed to burst at a specific pressure. The regimes of operation studied were inlet stagnation temperatures from 8,000K to 34,000K, inlet stagnation pressures from 850 atmospheres to 1,150 atmospheres, and inlet velocities from 500 m/sec to 16,000 m/sec. These operating parameters are far in excess of those encountered in typical artillery applications, and this thesis represents the first in-depth discussion designed to specifically address the heat transfer mechanisms within an ELGG barrel section for these conditions.

The heat loss processes discussed were thermal conduction from the working fluid to the surrounding barrel walls, forced convection within the fluid due to the highly energetic working fluid plasma entering the barrel, and both Planck and Rosseland radiation losses from the working fluid to the barrel walls. Viscous effects were also considered, as was the chemical recombination effects at high flow temperatures,

pressures and velocities. In order to study these processes, several one dimensional, steady state models were constructed with the assumption of a calorically perfect working fluid.

Hydrogen gas was selected as the working fluid for the ELGG due to the high natural sound speed and low molecular weight of 2.016×10^3 kg/kmol. Additionally, hydrogen has a high ionization potential which was presumed prior to the beginning of this thesis to aid in the energy transferred to the projectile by allowing the fluid to travel farther down the barrel before losing energy due to transport processes.

This assumption was proven to be correct when inlet stagnation temperatures exceeded 20,000K and at velocities greater than 8,500 m/sec when 1,000 atmospheres was used as the stagnation inlet pressure. At these conditions, it was determined that the energy liberated by the recombination of the electrons and the ionized hydrogen atoms could offset or even exceed, in some circumstances, the losses due to conduction, convection and radiation. The working fluid was found to be ionized to as much as 50 percent at inlet stagnation conditions of 30,000K and 1,000 atmospheres.

The possibilities of non-equilibrium of the working fluid were detailed, and it was found that due to the high densities associated with the inlet conditions mentioned previously, as well as the fast relaxation rates, the working fluid was able to reach equilibrium conditions throughout the barrel region. Frozen flow losses were shown to be negligible as well.

The determination was made that the working fluid remains absorption dominated throughout the barrel region, suggesting that the Rosseland diffusion model accurately

predicts the radiation losses as opposed to the Planck methodology. This finding showed that only when temperatures drop to approximately 1 eV does Planck radiation begin to be applicable, but at this point, the radiation losses became insignificant.

Three distinct regions of operation within the ELGG barrel section were determined where various transport processes dominated. In the region of operation with inlet conditions of 1,000 atmospheres and temperatures up to 1 eV, conduction dominated the system, with radiation limited to a short duration due to the rapidly dropping temperature of the flow. Convection tended to play a significant role in this region only at higher inlet velocities.

The second region of operation extended from 1 eV to 2 eV, and calculations demonstrated that all three transport processes are of nearly equal magnitude in this domain. Radiation is able to play a more significant role due to the dependence on T^4 , but it still tended to drop in importance as the flow progressed, whereas conduction and convection remained significant throughout the barrel.

In the third region, radiation dominates, with conduction contributing a significant amount of heat loss as well. Convection remains at an order of magnitude less than conduction and radiation in this region. It was determined that conduction is the consistent heat loss mechanism throughout all three regions, while convection tends to have the largest effects at higher velocities.

Viscous effects were determined to be present at all phases of the flow through the barrel, and the main effect was to cause choking of the flow. However, development of a theoretical length model which is designed to identify operation regions which prevent

choking of the flow was developed. It was determined that the conditions for choking the flow were determined by the friction factor, the ratio of specific heats of the working fluid, the inlet Mach number, and the length of the barrel itself.

The applicability of the computer code MACH2 was tested for use with ELGG barrel sections, and data obtained from MACH2 was analyzed with trends and data developed in this thesis. Due to limitations in the coding of MACH2, hydrogen data was unavailable, and argon was used as the working fluid. Despite this difficulty, trends determined in the hydrogen models and analysis provided important guidelines in the understanding of the calculations produced by MACH2.

The results of MACH2 computations show that at supersonic flow conditions within the ELGG barrel, a band of high temperature forms near the walls, suggesting that viscous effects produce heating of the fluid, and this effect is seen in the decrease in enthalpy loss at the exit. Subsonic regions showed a region of high density forming at the wall/exit interface, which tended to actually reduce the exit area of the flow, and in effect, acted as a sort of nozzle. Velocity data produced in each of the computational runs was able to verify this effect. Supersonic flows, however, did not show this region of higher density, mainly due to the high temperature band along the walls.

All flows, however, were shown to develop small scale directed flow from the axis to the walls, and a fan type expansion at the wall/exit interface. The strength of this directed flow was determined to be directly dependent on the inlet Mach number and stagnation temperature. Additionally, flow temperature, pressure, and density tended towards some steady state condition as time and computational cycles progressed.

MACH2 proved to be a useful, if complicated, tool in the study of the ELGG thermal characteristics, and provided insights into actual system operation which would otherwise be prohibitively difficult, if not impossible. The ability to study transport processes either separately or simultaneously is an important part of the code, and aids greatly to its flexibility.

Comparing the results from both hydrogen and argon chemical reactions (tables 4.14 and 5.2), it became apparent that argon makes a poor choice for a propellant in an ELGG. Hydrogen at temperatures from 2 to 3 eV is able to provide significant energy to the working fluid in the recombination process of free electrons and ionized atomic hydrogen. This liberated energy is thus available for the process of projectile motion, and allows the energy to be "transported" through the barrel without being lost as conduction or radiation energy. The high ionization potential of argon compared to hydrogen (15.81 eV to 13.527 eV), combined with the high pressures in the ELGG, prevents this from occurring except at inlet temperatures in excess of 2 eV and low Mach numbers.

The results of this thesis show that the ELGG is a plausible idea which can take advantage of high energy plasmas for the purpose of projectile motion. The determination of regimes of transport dominance is essential to the future production of ELGG devices, as is the finding that chemical recombination can be an effective way to minimize transport losses at high temperatures using hydrogen as the working fluid. Finally, by carefully tailoring the inlet flow conditions, supersonic flow can be maintained throughout the barrel region, significantly enhancing the possibilities of very high speed projectile motion.

APPENDIX A

Degree of Hydrogen Ionization Calculations

These calculations were performed with the use of MATHCAD 4.0. The methodology utilizes the Saha equation with hydrogen temperatures from 1,000K to 35,000K and pressures of 100, 1,000, and 10,000 atmospheres. Also included in this appendix is a graph showing the ionization potential lowering as a function of temperature.

(This appendix is referenced by chapter 3.1, page 23 and chapter 4.1, page 65)

Calculation of Degree of Ionization for Hydrogen (Saha Equation)

$u_1 = 1$ Partition function for ionized hydrogen

$u_0 = 2$ Partition function for ground state hydrogen

$\chi_h = 2.178 \cdot 10^{-18}$ joule ionization energy of hydrogen

$P_{\text{gas}} = 1.01325 \cdot 10^8 \frac{\text{newton}}{\text{m}^2}$ Gas pressure at 1000 atmospheres

$m_e = 9.11 \cdot 10^{-31}$ kg Rest Mass of electron

$k = 1.38 \cdot 10^{-23} \frac{\text{joule}}{\text{K}}$ Planck's Constant

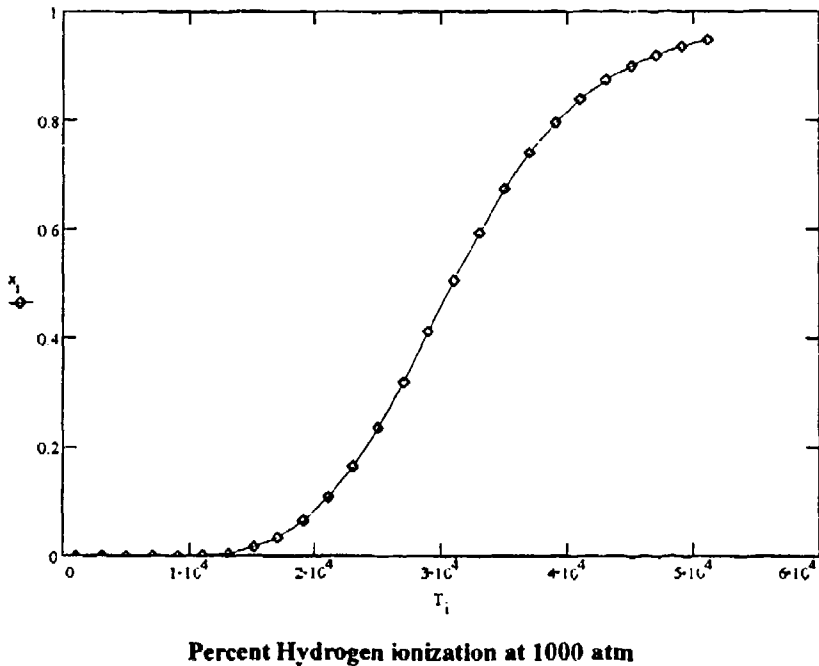
$h = 6.63 \cdot 10^{-34}$ joule sec Boltzman Constant

Calculate the degree of ionization from temperatures of 1000 K to 50000 K

$i = 0, 2..50$

$T_i = 1000 \text{ K} + i \cdot 1000 \text{ K}$

$$Q_i = \left(\frac{u_1}{u_0} \right) \cdot \left(\frac{2}{P_{\text{gas}}} \right) \cdot \frac{(2 \cdot \pi \cdot m_e)^{\frac{3}{2}}}{h^3} \cdot \left(k \cdot T_i \right)^{\frac{5}{2}} \cdot \left(e^{-\frac{1}{k \cdot T_i}} \right) \quad x_i = \sqrt{\frac{Q_i}{1 + Q_i}}$$



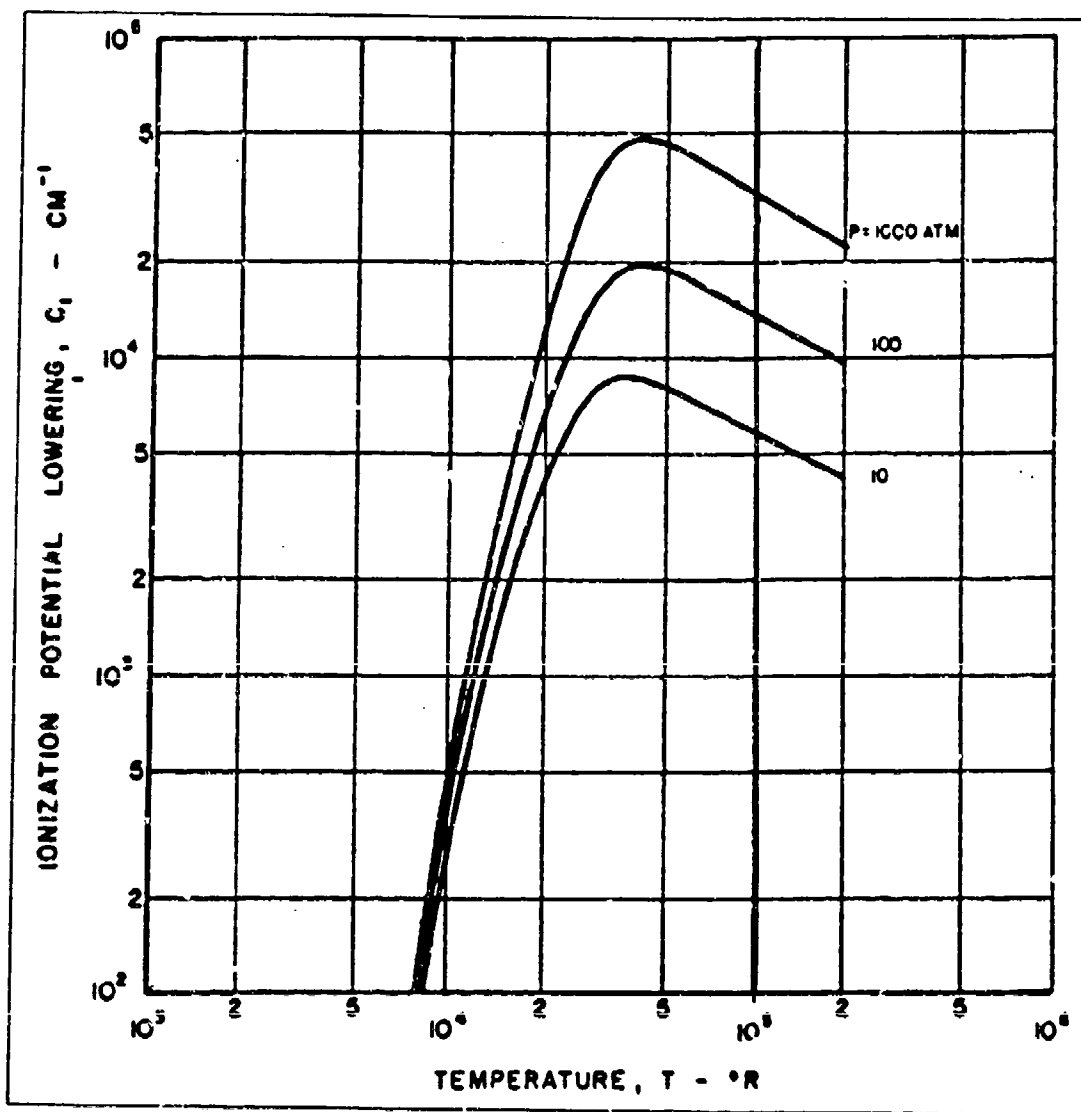


Figure A.1 Ionization potential lowering as a function of temperature (Rankine)

APPENDIX B

SESAME Plots

This information is obtained from the Los Alamos New Opacity Library and SESAME Opacity Data.

(This appendix is utilized for chapter 3.7, page 52 and chapter 4.5, page 89

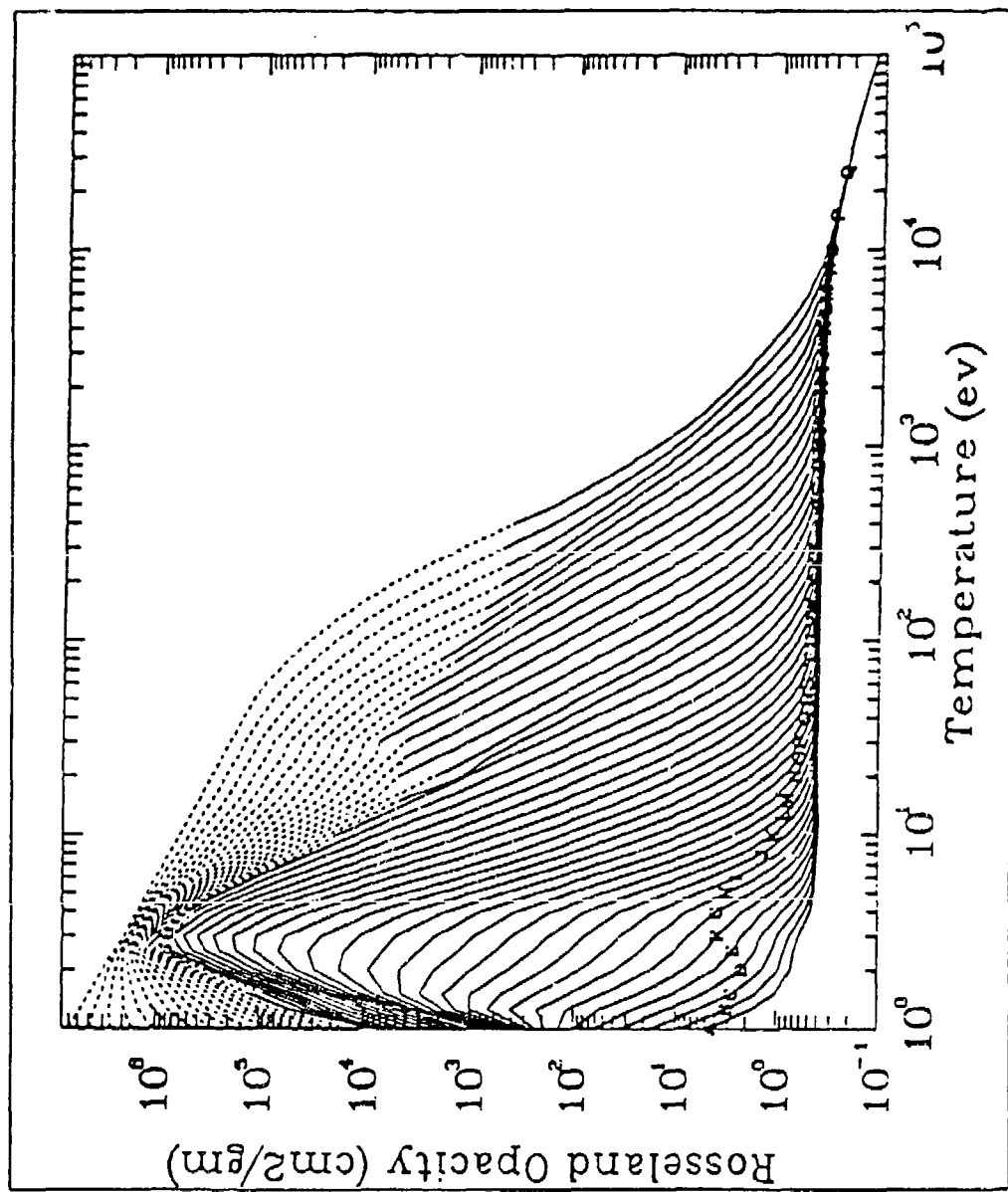


Figure B.1 SESAME Rosseland opacity for hydrogen

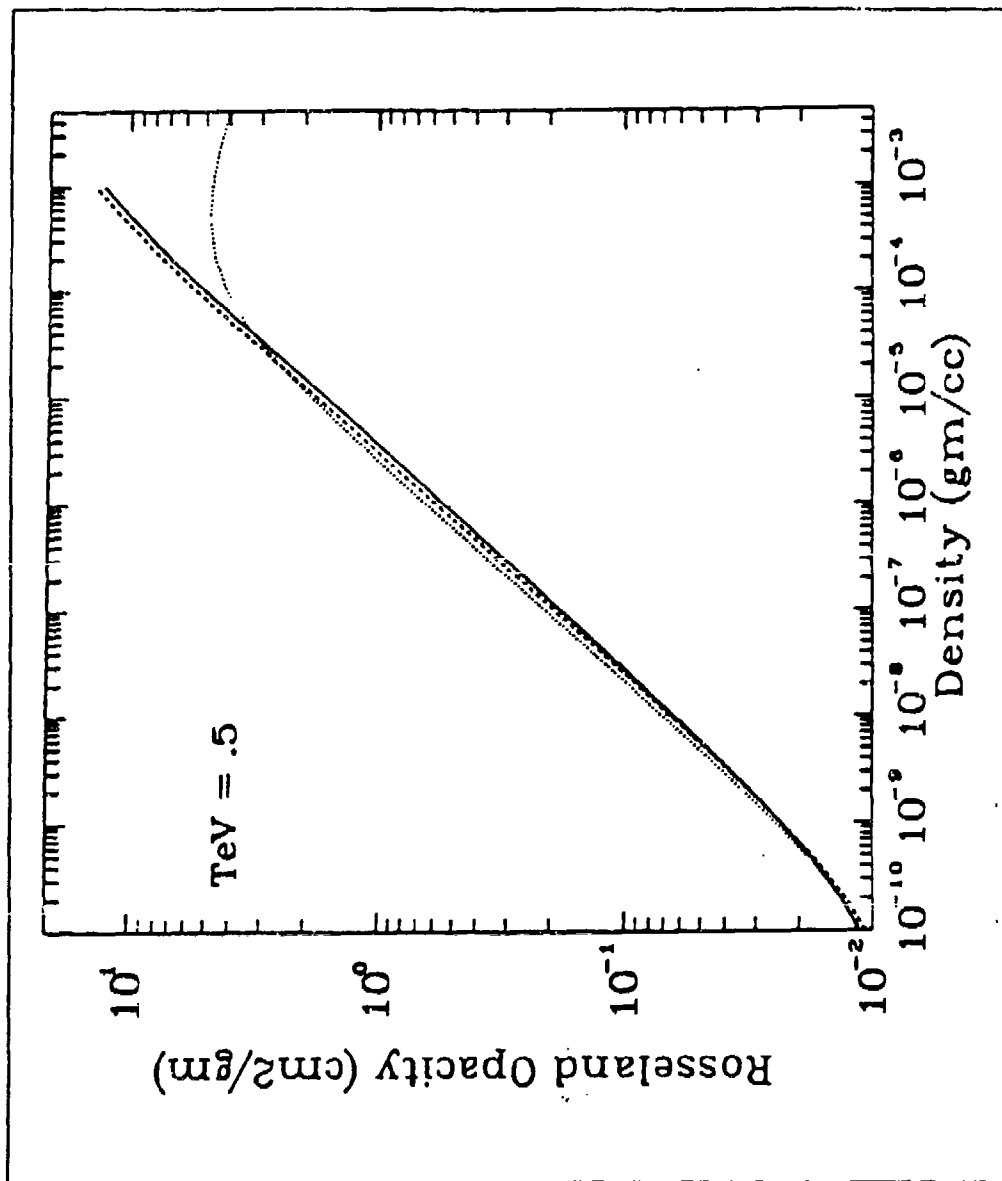


Figure B.2 SESAME opacity comparison for hydrogen

APPENDIX C

Opacity and Blackbody Radiation Plots

These plots were created with MATHCAD 4.0 using data provided by N. L. Krascella and R. W. Patch. Other Plots courtesy of NASA-Langley.

(This appendix is referenced by chapter 3.7, page 52, and chapter 4.5, page 89)

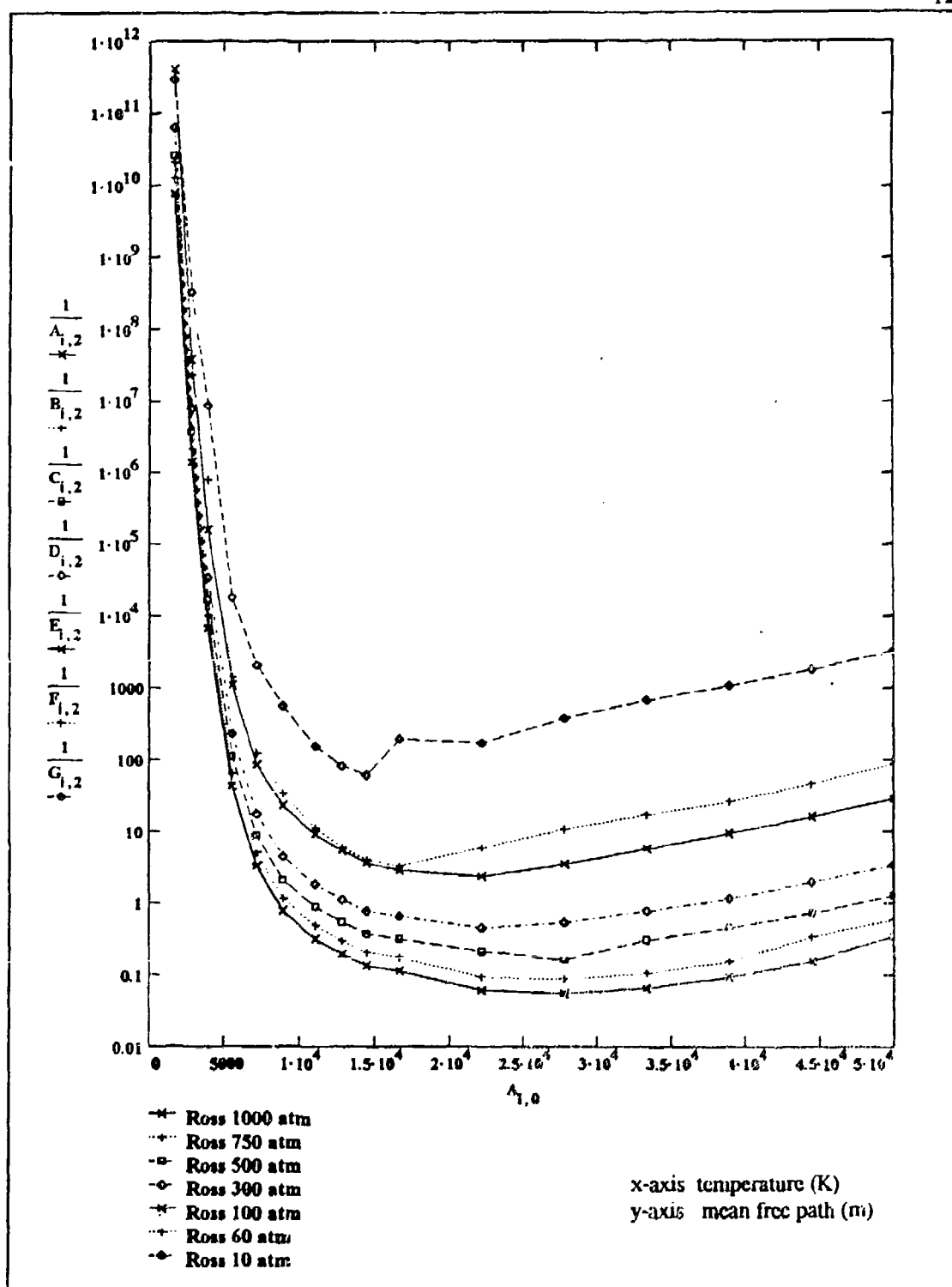


Figure C.1 Hydrogen rosseland mean free path based on data by Patch⁷⁸

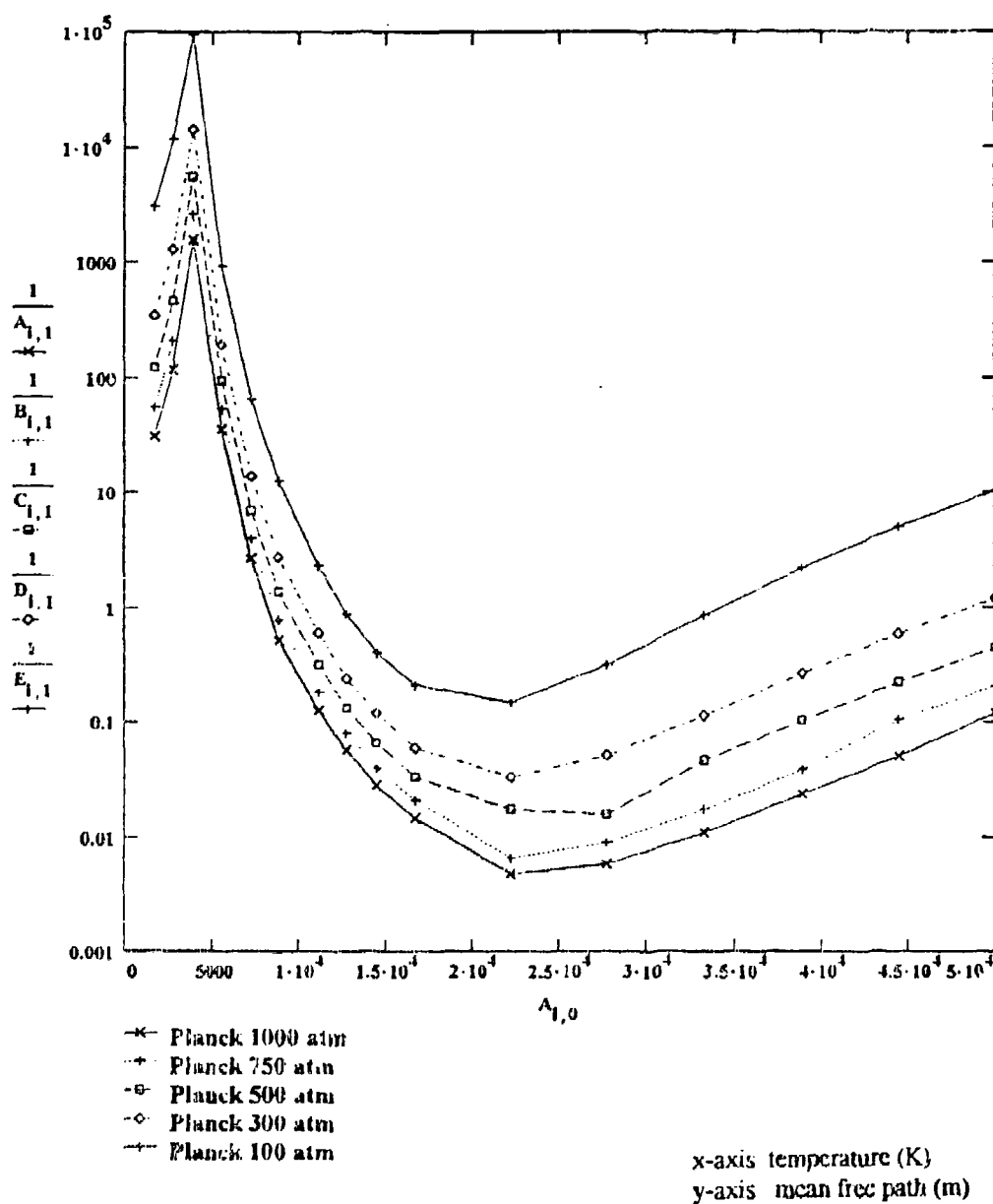


Figure C.2 Hydrogen planck mean free path based on data by Patch⁷

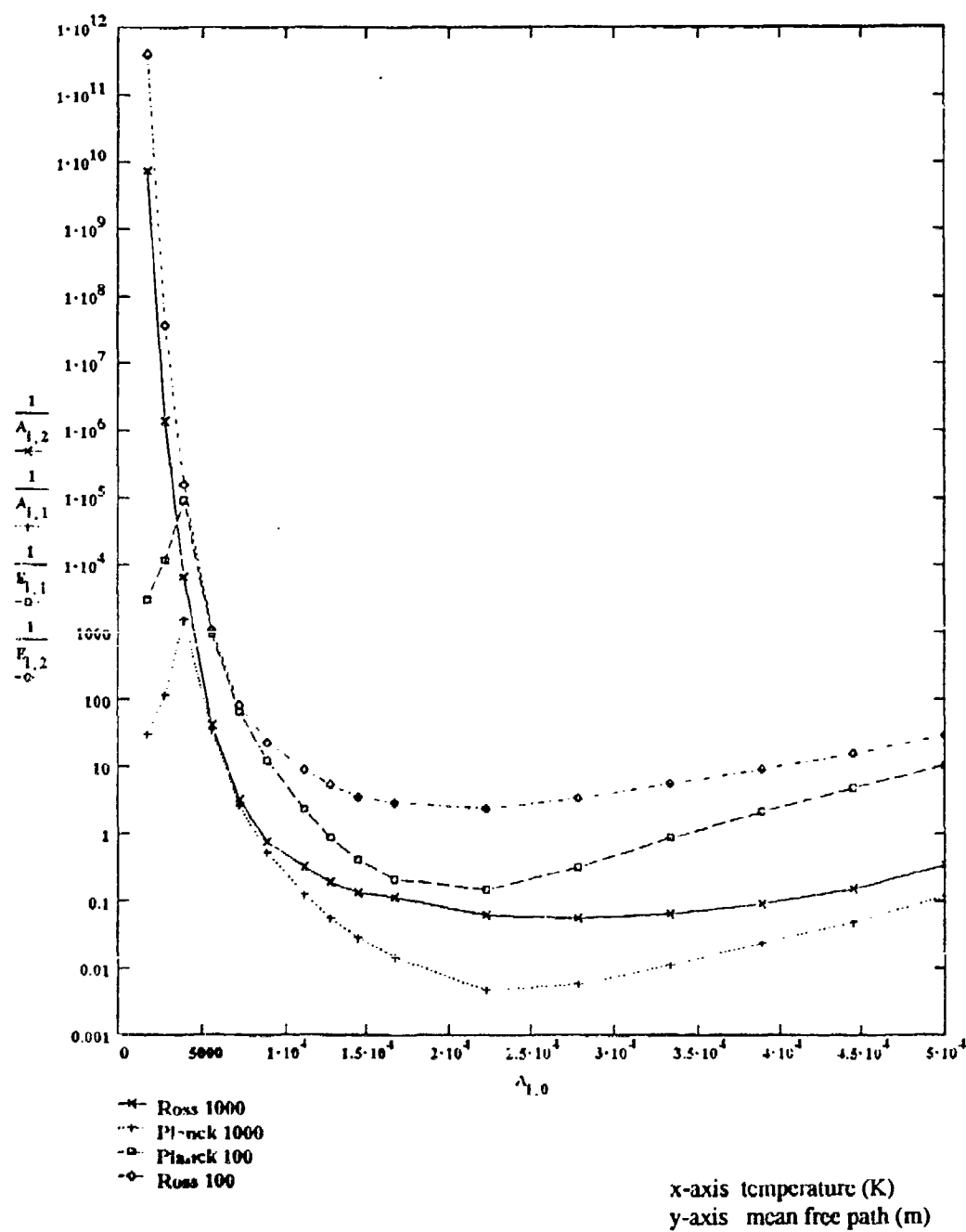
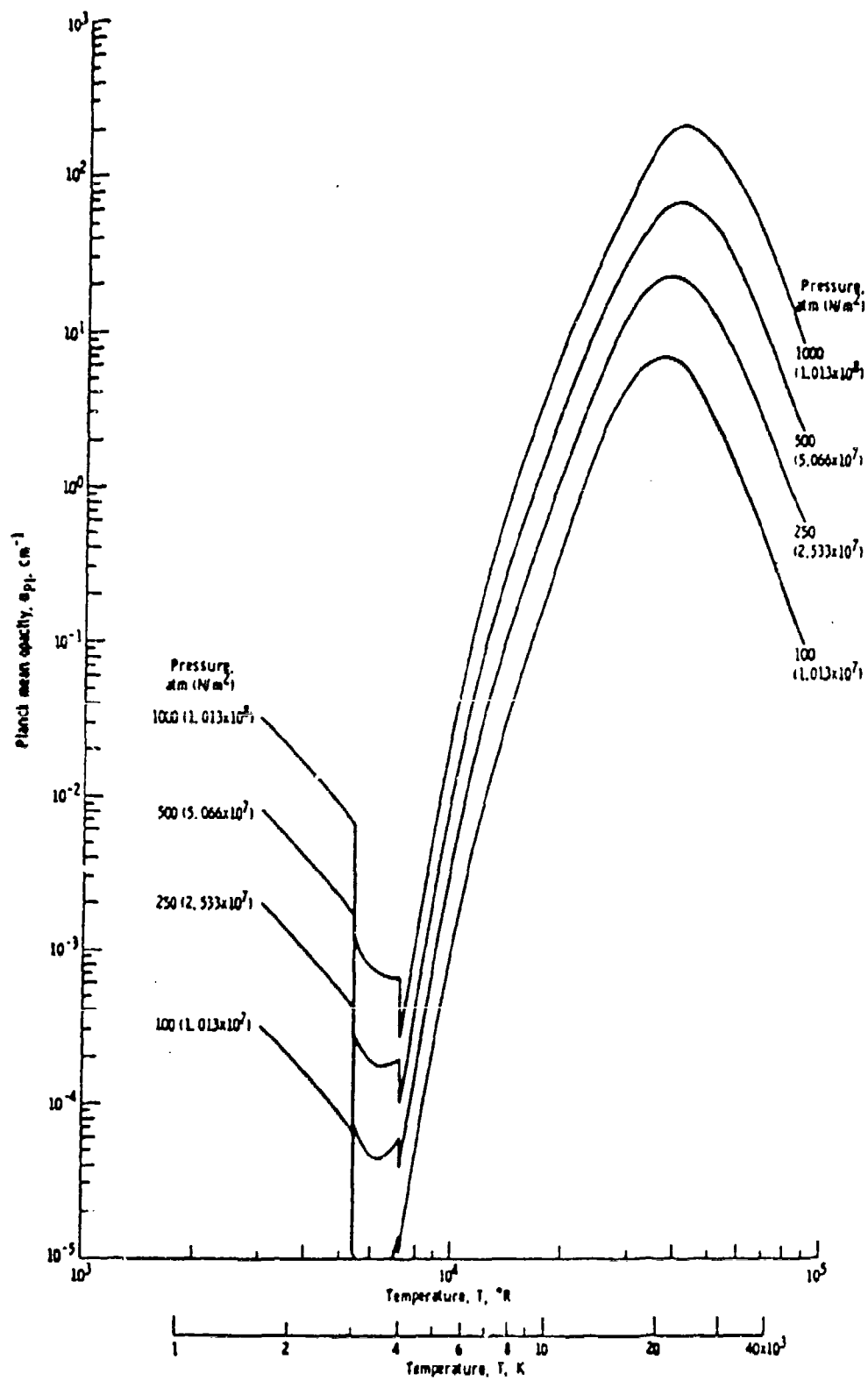


Figure C.3 Comparison of hydrogen mean free paths based on data by Patch⁷⁸ (Data at 1,000 and 100 atmospheres)

Figure C.4 Planck mean opacity for hydrogen⁷

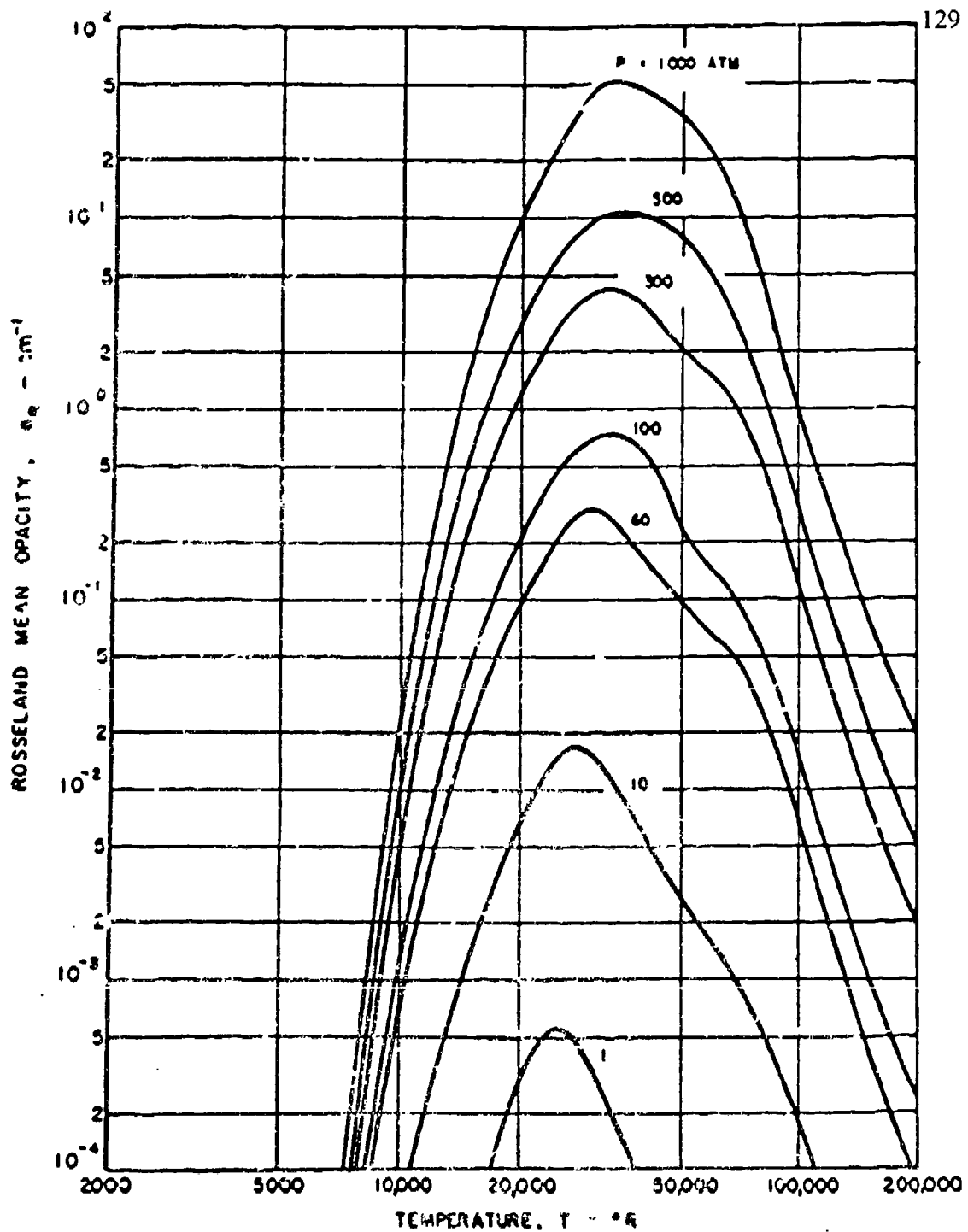


Figure C.5 Rosseland mean opacity for hydrogen⁷⁸

APPENDIX D

Hydrogen Composition and Data

Hydrogen species composition and number density plots. Plots are for hydrogen number densities at pressures of 10 to 1,000 atmospheres and temperatures from 300K to 40,000K. Species included are H_2 , H_2^+ , H, H^+ , e^- , H^- , H_3^+ , H_2^+ , and H^+ . Data obtained from Patch⁷⁸ and INSPI.

(This appendix is referenced by chapter 2.2, page 17, chapter 3.1, page 23, chapter 4.1, page 65, chapter 4.6, page 93 and chapter 6, page 113)

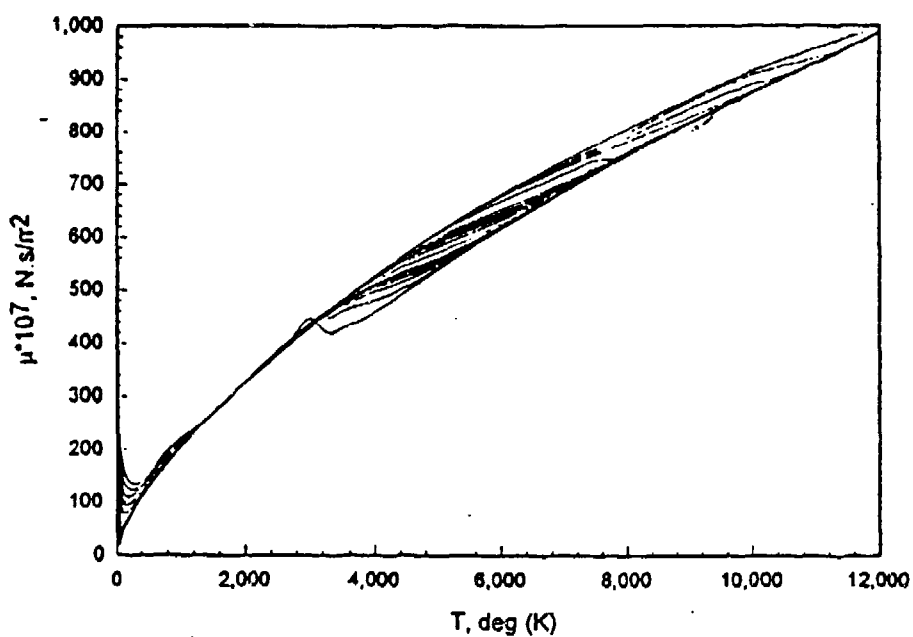


Figure D.1 Hydrogen Viscosity as a function of temperature

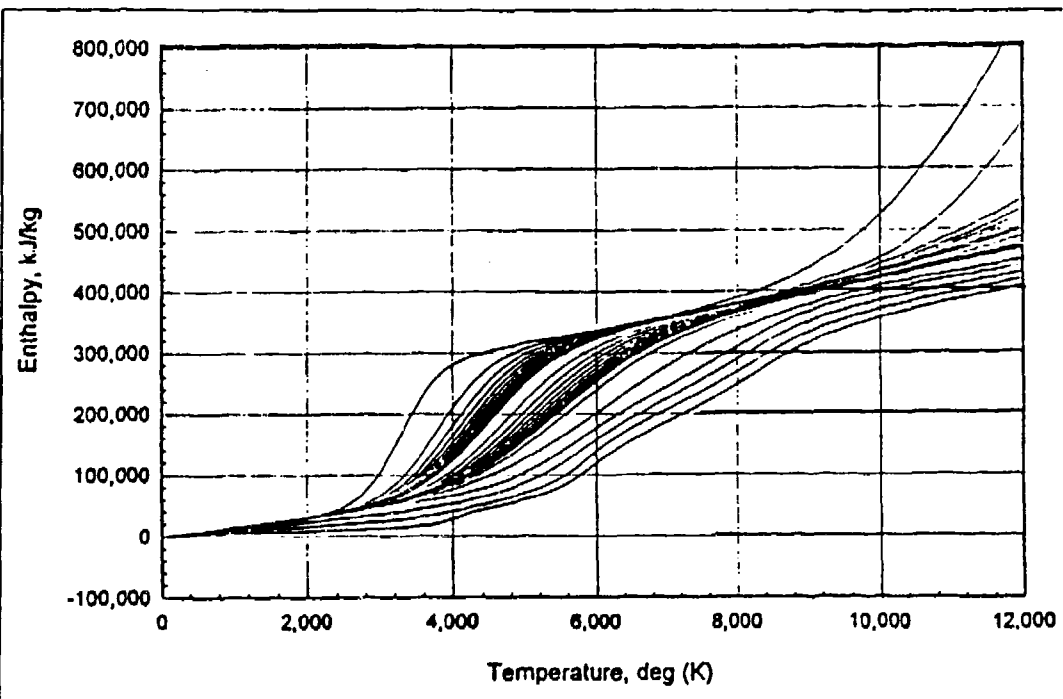


Figure D.2 Hydrogen enthalpy as a function of temperature

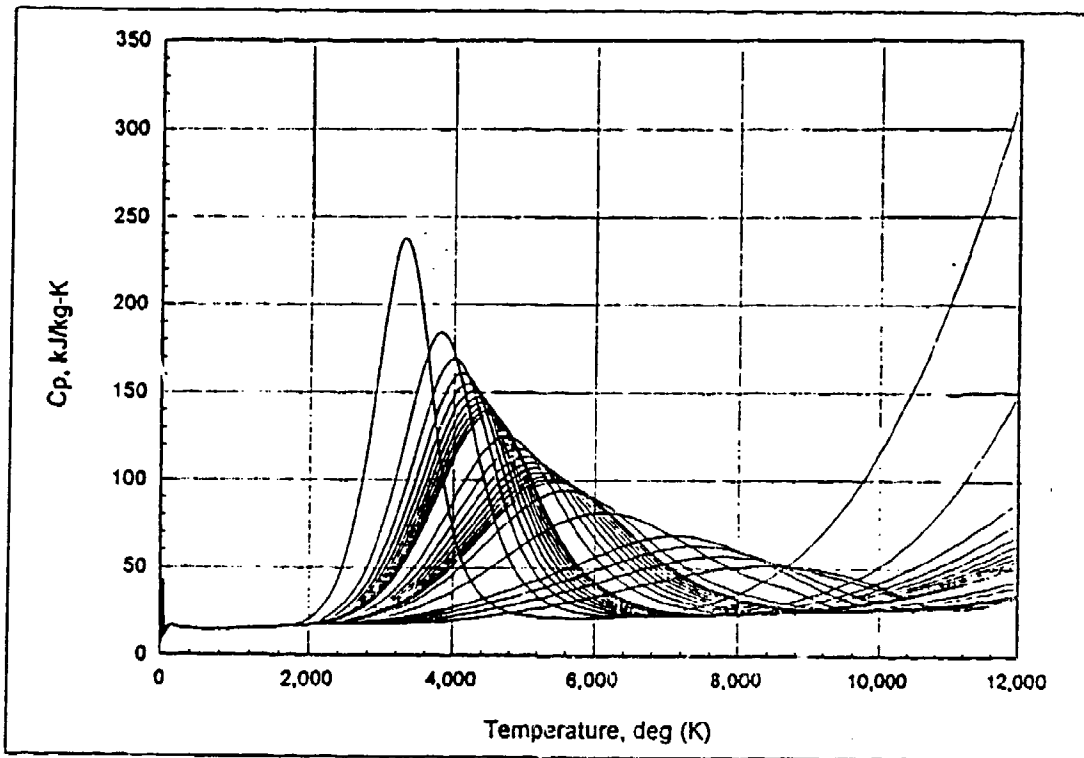


Figure D.3 Hydrogen specific heats as a function of temperature

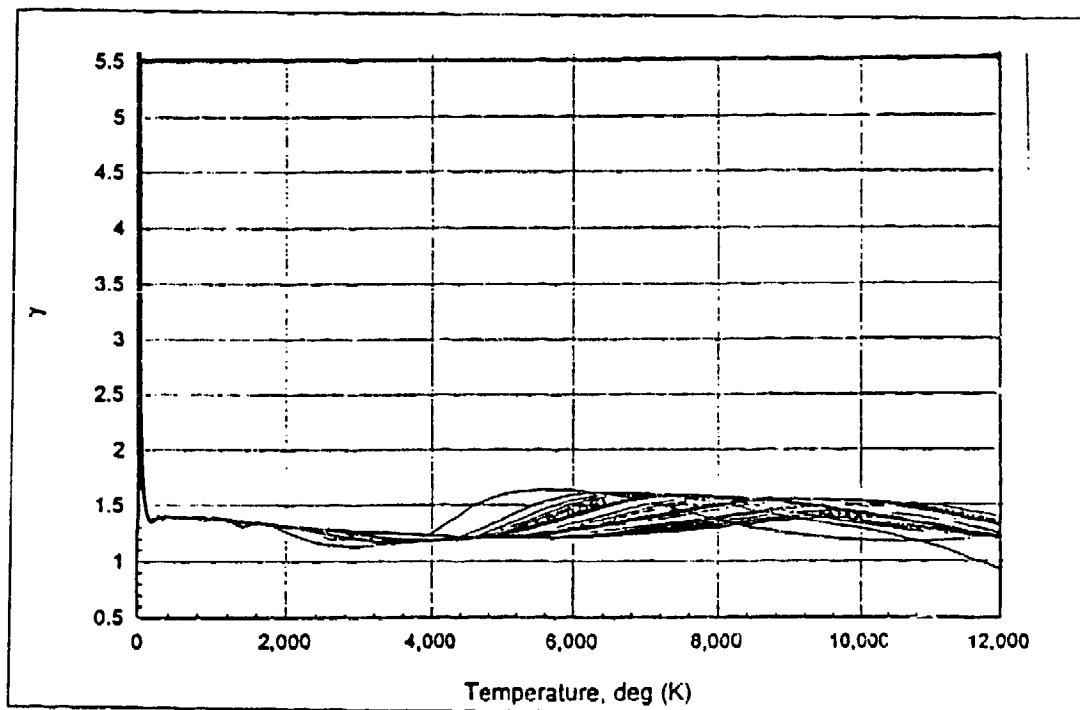


Figure D.4 Hydrogen γ as a function of temperature

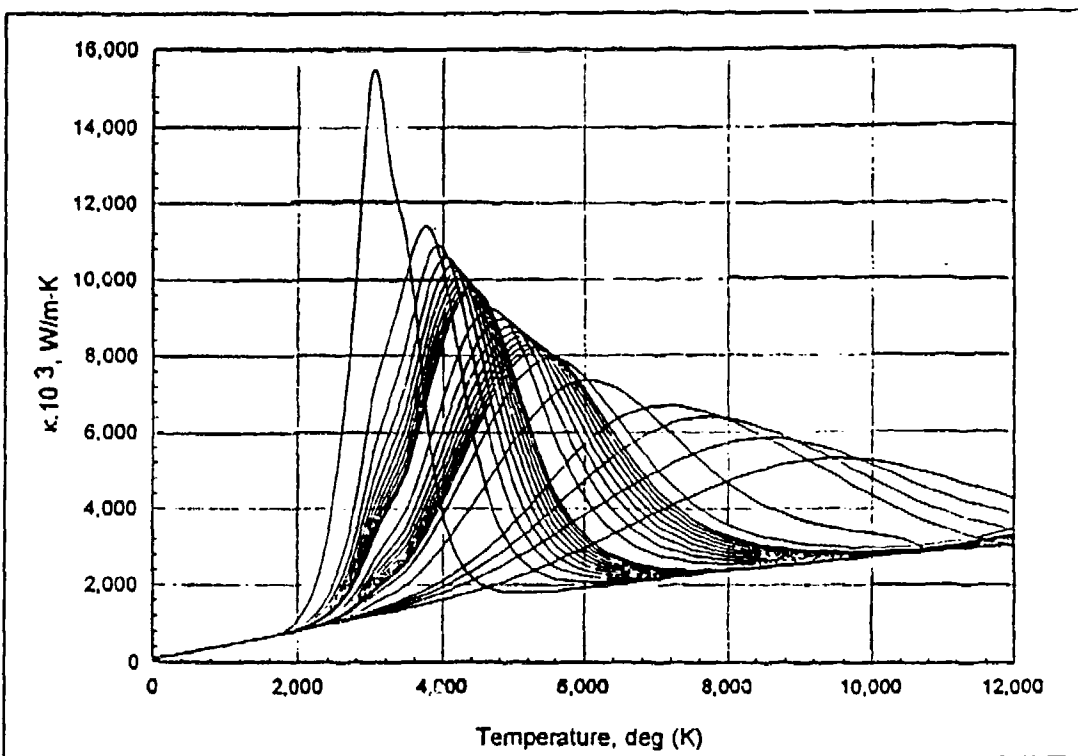


Figure D.5 Hydrogen thermal conductivity as a function of temperature

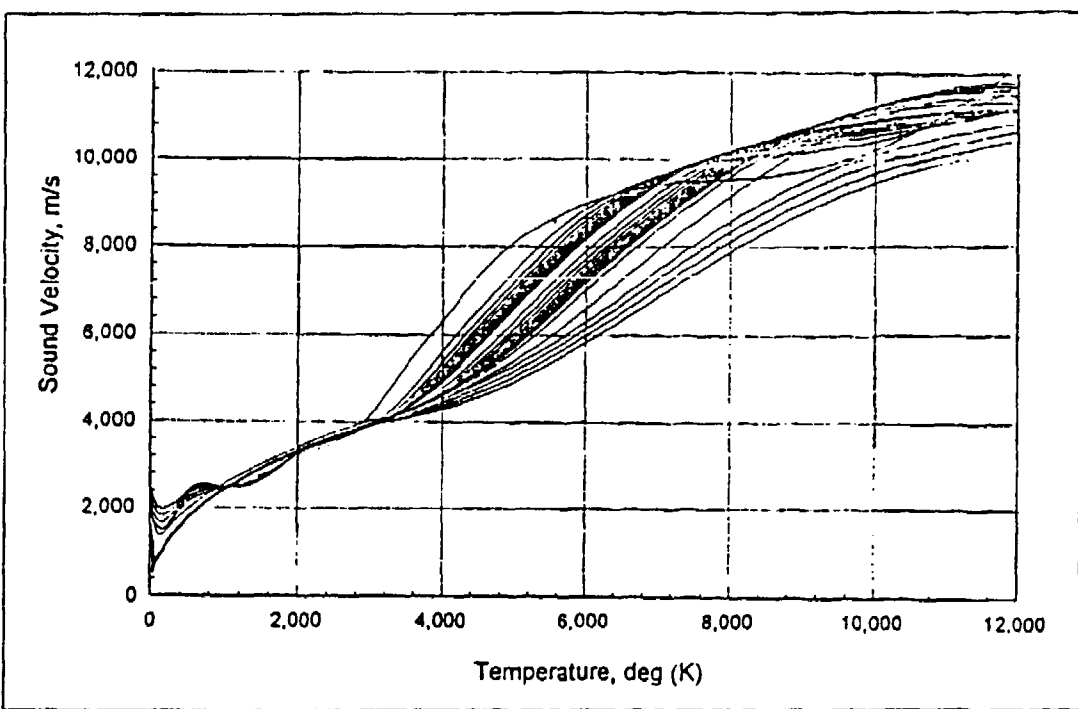


Figure D.6 Hydrogen sound velocity as a function of temperature

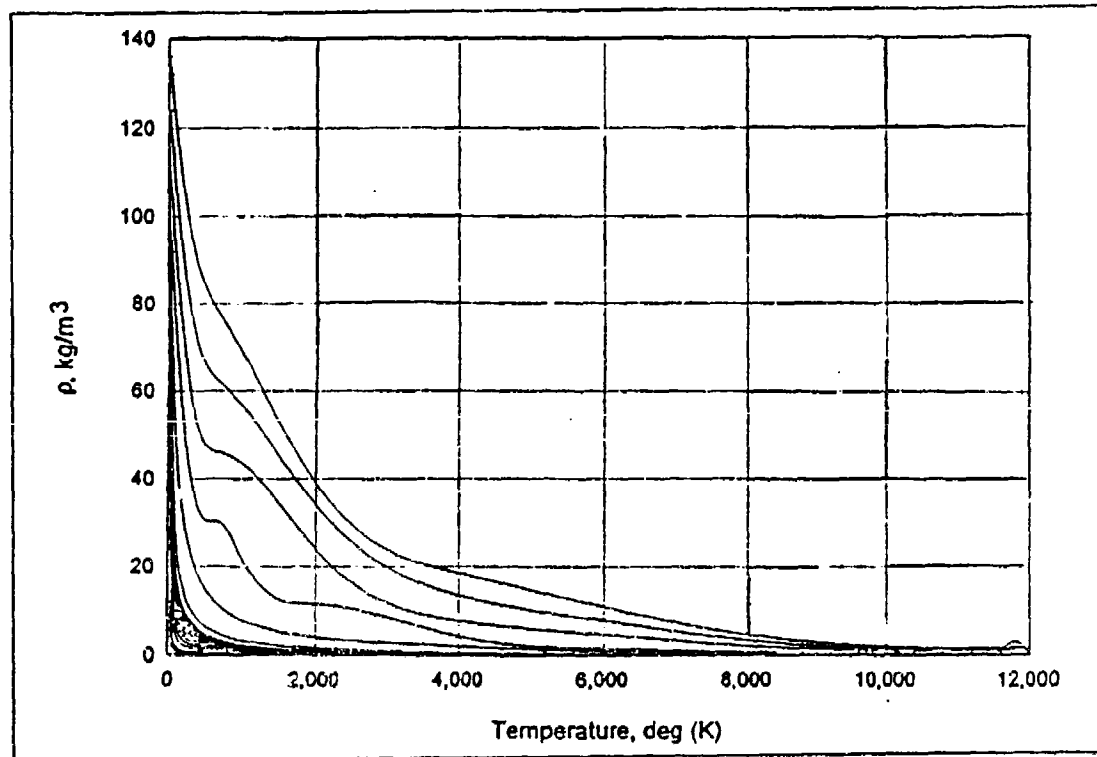


Figure D.7 Hydrogen density as a function of temperature

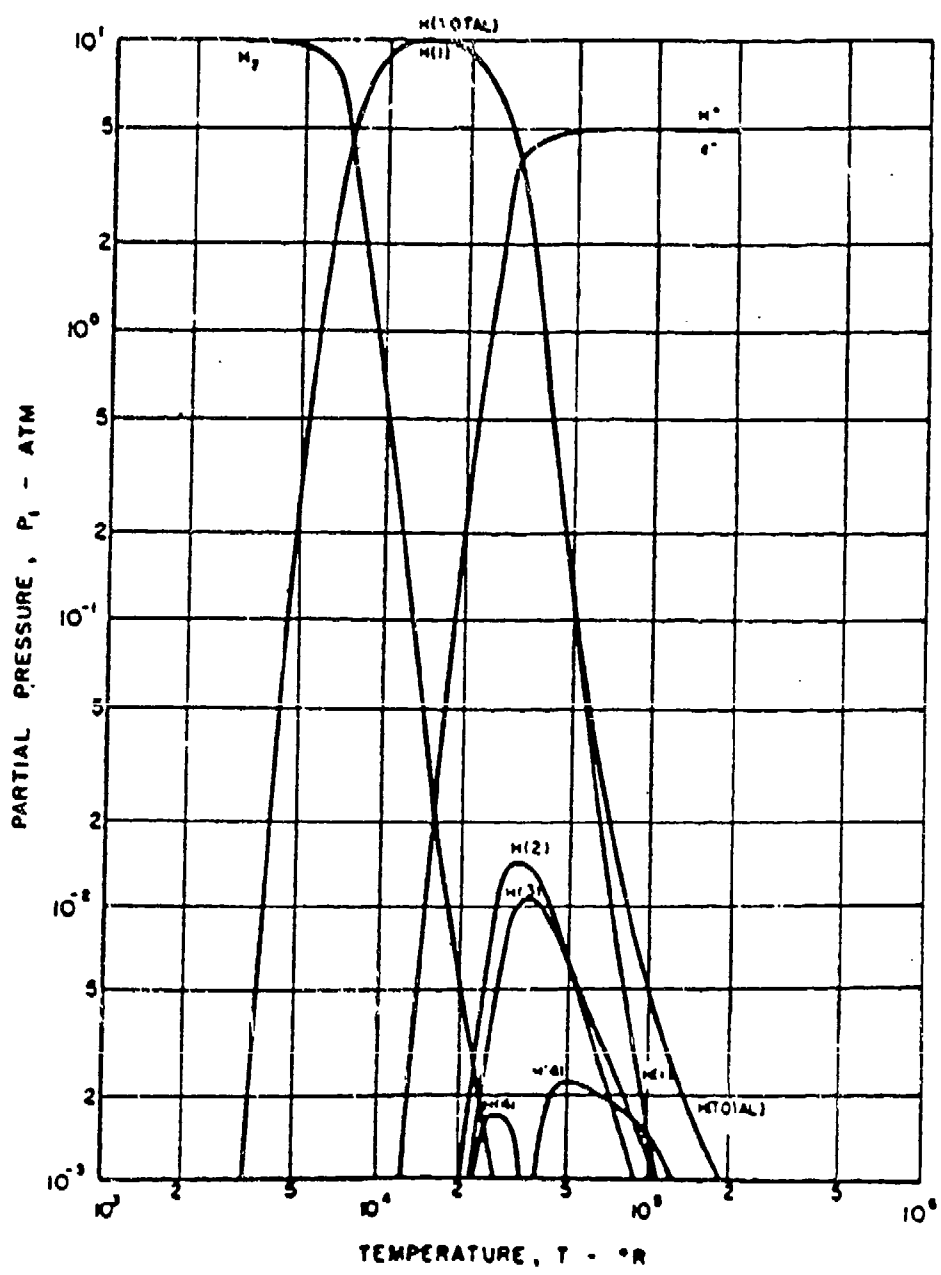


Figure D.8 Hydrogen composition at 10 atmospheres

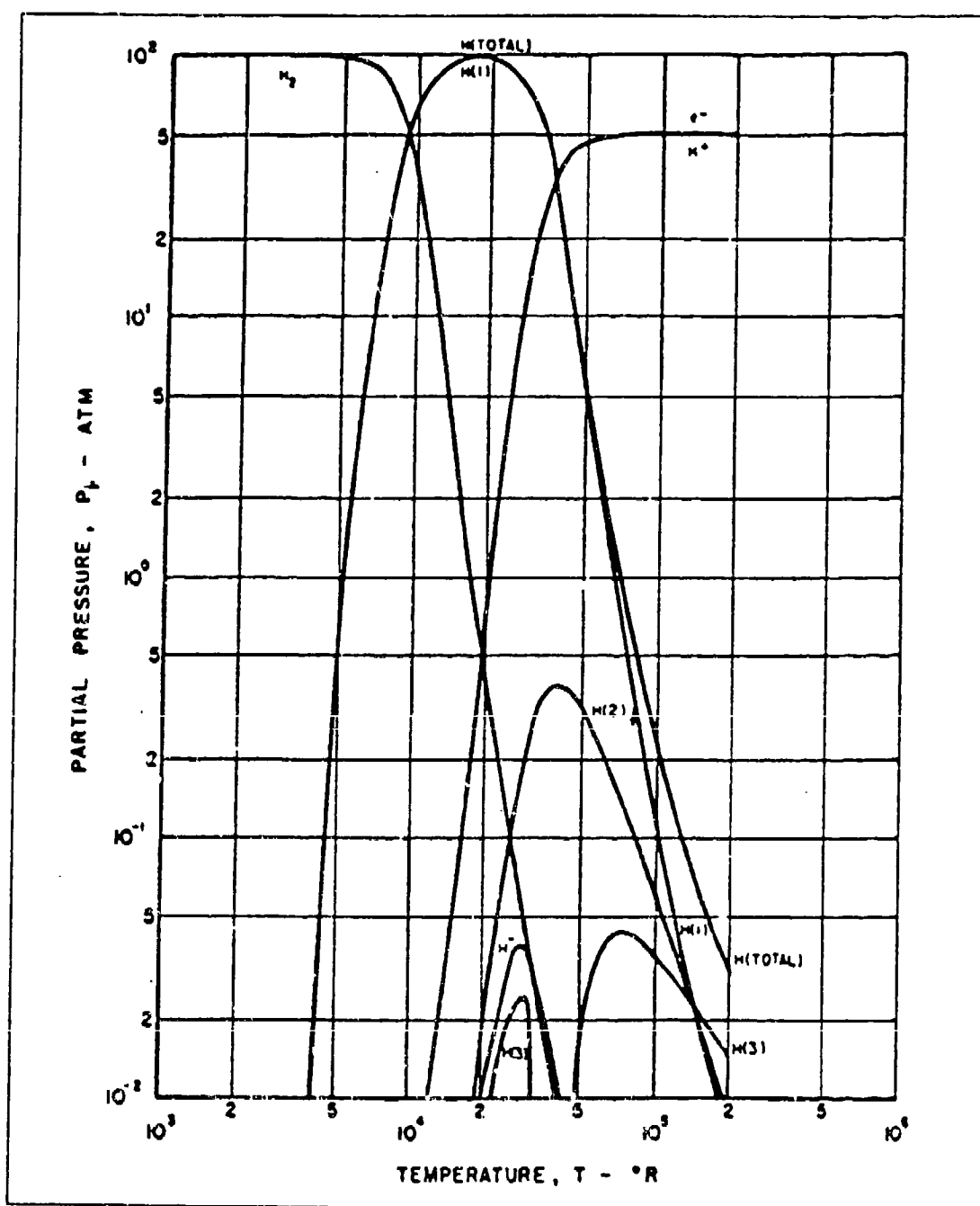


Figure D.9 Hydrogen composition at 100 atmospheres

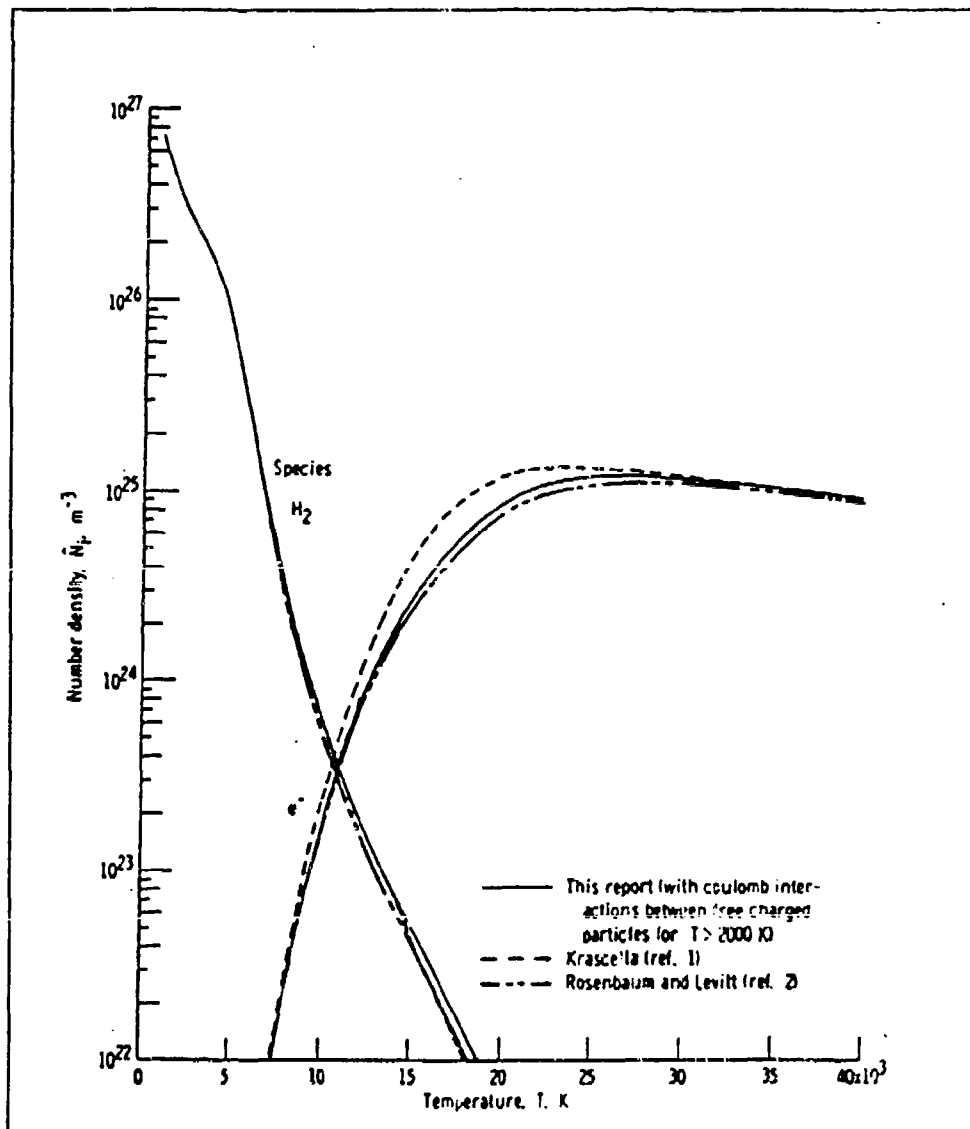


Figure D.10 Hydrogen species number densities at 100 atmospheres

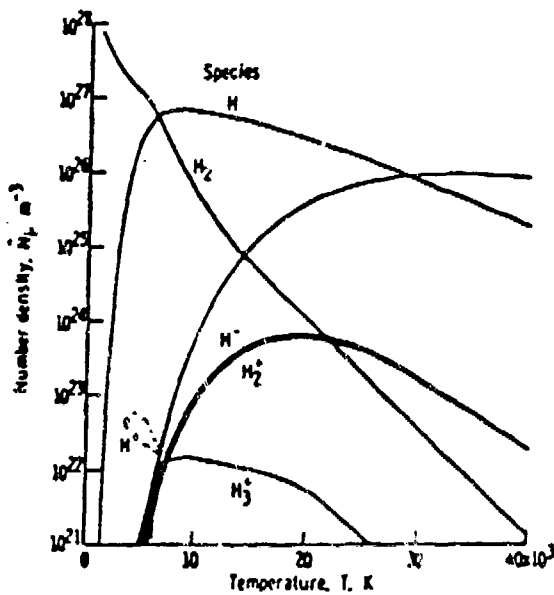


Figure D.11 Hydrogen number densities at 1,000 atmospheres

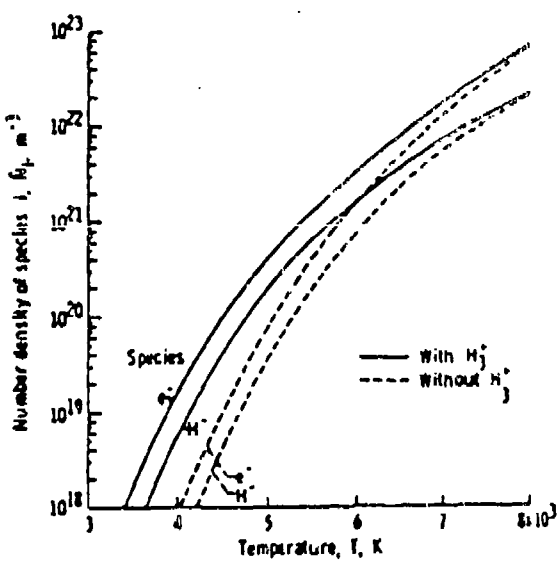


Figure D.12 Calculated number densities of hydrogen at 1,000 atm

APPENDIX E

Rosseland Diffusion Approximation Calculations

These calculations are performed on MATHCAD 4.0. Data is for hydrogen gas at 10, 100, 500, and 1,000 atmospheres and temperatures from 1,000K to 10,000K. Graphs are comparisons with Rosseland results and Blackbody radiative flux predictions.

(This appendix is referenced in chapter 3.7, page 52)

Calculation of the Radiative heat transfer using Rosseland Diffusion Approximation at 1000 atmospheres. Data for Rosseland opacities is from Krascelia and Patch.

$$k = 0, 1..6 \quad i = 0, 1..10 \quad l = 0, 1..9$$

From Patch: $TF_k = KB_k =$

1667	0.1316 10 ⁻⁰⁹
2778	0.7163 10 ⁻⁰⁶
3889	0.1471 10 ⁻⁰³
5556	0.2371 10 ⁻⁰¹
7222	0.3011 10 ⁻⁰⁰
8889	0.1313 10 ⁰¹
11111	0.3176 10 ⁰¹

TE is the temp at which KB, i.e.
Rosseland opacity is calculated

Define:

$\sigma_{\text{sigma}} = 5.67 \cdot 10^{-08}$ The Steffan-Boltzmann constant

$D_i = 0.01 + 1.0 \cdot i$ This is the distance along the X-axis

$DT = 900$ This is the assumed linear temperature gradient

$\Delta x_i = D_{i+1} - D_i$ This is the increment along the X-axis

$T_i = 1000 + (DT \cdot D_i)$ This is the temperatures along the X-axis

Interpolate from given data the Rosseland opacity at specified temperature.

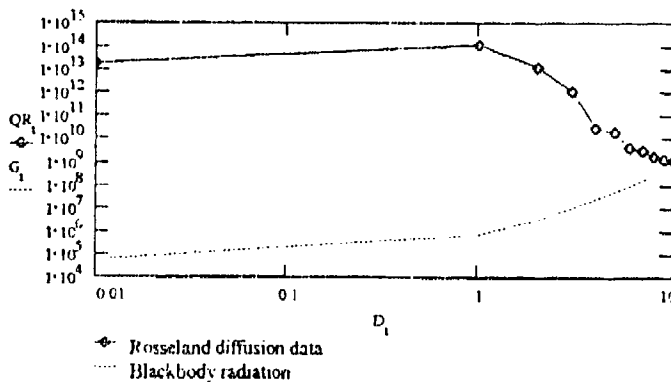
$$\alpha_{R_i} = \text{interpol}(TE, KB, T_i) \quad \alpha_{R_0} = \alpha_{R_1}$$

Calculate the radiative heat transfer using procedure in Vincenti & Kruger.

$$QR_i = \frac{16 \cdot \sigma_{\text{sigma}} (T_i)^3}{(3 \cdot \alpha_{R_i} \cdot 100)} \left(\frac{T_{i+1} - T_i}{\Delta x_i} \right) 1000$$

$$G_i = \sigma_{\text{sigma}} (T_i)^4$$

This calculates the value of the blackbody radiation flux at each temperature region within the system.



Radiative Heat Transfer to a wall at 1000 atmospheres. QR is in units of
Watts/meter², G is in Watts/meter², and D is the distance in millimeters.

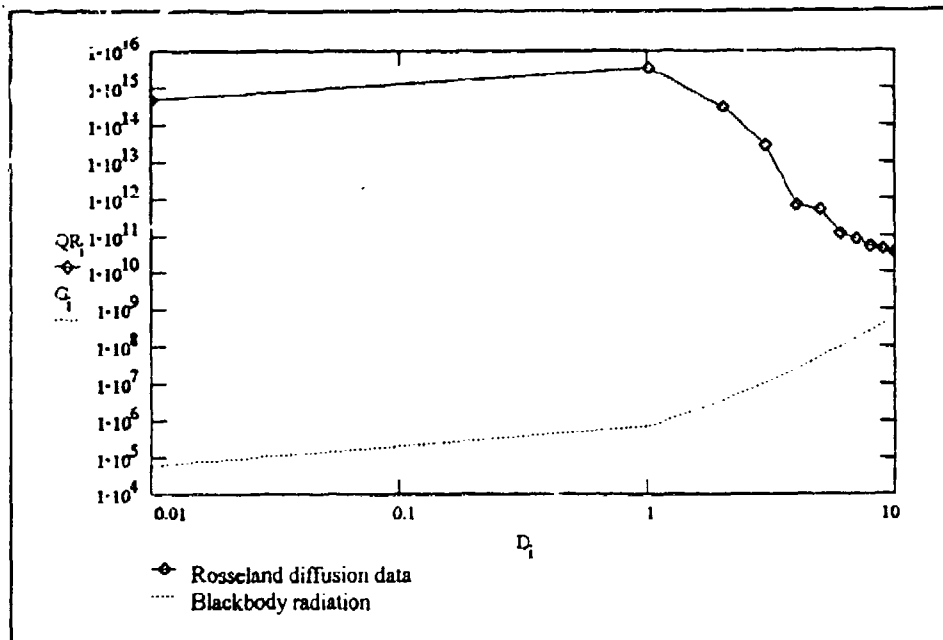


Figure E.1 Radiative heat transfer to wall at 100 atmospheres. QR is in units of Watts/meter², G is in Watts/meter², and D is in millimeters.

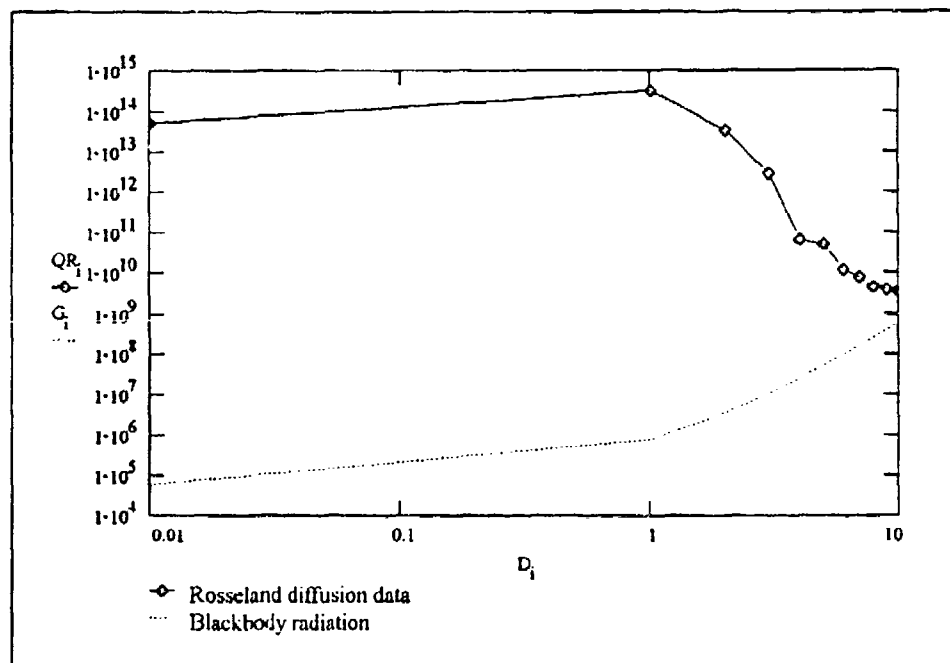


Figure E.2 Radiative heat transfer to wall at 500 atmospheres. QR is in units of Watts/meter², G is in Watts/meter², and D is in millimeters.

APPENDIX F

Calculation results for conduction model

This data is produced with Mathcad 4.0. This appendix contains one sample case data and computed tabular data.

Variables used:

Molwt - molecular weight	R - gas constant
γ - ratio of specific heats	k - thermal conductivity
μ - viscosity	T_{01} - inlet stagnation temp
P_{01} - inlet stagnation press	V_1 - inlet velocity
ρ_{01} - inlet stagnation density	a_{∞} - stagnation sound speed
a_1 - inlet sound speed	M_1 - inlet Mach number
T_1 - inlet static temp	P_1 - inlet static press
time - transit time	mass - mass of working fluid
ρ_1 - initial density	q - heat transfer per unit mass
P_01P_1 - ratio of press	$T_{01}T_1$ - ratio of temps
Red - Reynolds number	Le - Laminar entrance length
h_{10} - inlet enthalpy	

(variables with a 2 in them indicate exit conditions)

(this appendix is referenced by chapter 3.5, page 37, chapter 3.6, page 39, chapter 4.2, page 75, and chapter 4.6, page 93)

One-Dimensional, compressible inviscid flow with heat extraction based on conduction for calorically perfect hydrogen gas

Initial Gas Properties

$$\begin{aligned} M_{in} &= 2.01 \times 10^4 & R &= 4121.735 & \gamma &= 1.41 \\ C_p &= \frac{T_R}{(T - 1)} & k &= 2.01 & \Delta h &= 8.32 \cdot 10^3 \end{aligned}$$

Tube Data

$$r = 0.5 \quad L = 1.0 \quad V_{in} = \pi r^2 L \quad A_{in} = \pi r^2$$

$$A_{out} = \sqrt{\frac{\pi}{4}} \pi r_{out}^2$$

$$T_{in} = 10000 \quad \theta_{in} = 1150 \quad V_1 = 50.00 \quad \rho_{in} = \frac{p_1 (0.0123 \cdot 10^3)}{R T_{in}}$$

$$a_1 = (\gamma - 1) \left[\frac{A_{in}^2}{A_{out}^2} \right]^{1/(gamma - 1)} \cdot \frac{V_1}{A_{in}}$$

$$T_1 = \frac{(T_{in})}{\left(\frac{r_{in}}{r}\right)^{2/(gamma - 1)}} \quad p_1 = \frac{p_{in}}{\left(\frac{r_{in}}{r}\right)^{2/(gamma - 1)}}$$

$$m_{out} = \frac{L}{V_1} \cdot m_{in} \cdot \left[\frac{p_1 (0.0123 \cdot 10^3) \cdot V_{out}}{R T_1} \right] \quad \rho_1 = \frac{p_1 (0.0123 \cdot 10^3)}{R T_1}$$

Heat Flow Calculation

$$q = \left[\frac{k \cdot A_{out} (T_1 - 400 \text{ K})}{d_{out} L} \right]^4 \cdot \frac{4}{3}$$

Calculation

$$\begin{aligned} p_{out} &= p_1 \cdot \left(\frac{r_{in}}{r_{out}} \right)^{2/(gamma - 1)} & T_{out} &= T_1 + \frac{1}{2} \cdot \frac{1}{k} \cdot \frac{q}{\rho_1} \\ p_{out} &= p_1 \cdot \left(\frac{r_{in}}{r_{out}} \right)^{2/(gamma - 1)} & & \end{aligned}$$

$$\begin{aligned} T_{in} &= T_{out} \\ T_{out} &= \frac{p_1}{C_p} \end{aligned}$$

$$\text{PIPE} = \frac{1 + \gamma}{(1 + \gamma M_1^2)^2} \quad T_{Turb} = M_1^2 \left(\frac{1 + \gamma}{1 + \gamma M_1^2} \right)^2 \quad \rho_{PIPE} = \frac{1}{M_1^2 \left(\frac{1 + \gamma}{1 + \gamma M_1^2} \right)^2}$$

$$\text{PIPE} = \frac{1 + \gamma}{(1 + \gamma M_1^2)^2} \left[\frac{2 + (T - 1) M_1^2}{\gamma + 1} \right]^{-1} \quad T_{Turb} = \frac{\left(\frac{1 + \gamma M_1^2}{\gamma + 1} \right)^2}{\left(\frac{1 + \gamma M_1^2}{\gamma + 1} \right)^2} \left[2 + (\gamma - 1) M_1^2 \right]$$

$$M_2 = 0.345 \quad \rho_{PIPE} = \frac{(1 + \gamma) M_1^2}{(1 + \gamma M_2^2)} \left[2 + (\gamma - 1) M_2^2 \right]$$

$$M_2 = M_1 \quad \rho_{PIPE} = \frac{(1 + \gamma) M_1^2}{(1 + \gamma M_2^2)}$$

$$P_{Turb} = \frac{1 + \gamma}{(1 + \gamma M_2^2)^2} \left[2 + (\gamma - 1) M_2^2 \right]$$

$$P_{Turb} = \frac{1 + \gamma}{(1 + \gamma M_2^2)^2} \left[\frac{2 + (T - 1) M_2^2}{\gamma + 1} \right]^{-1} \quad T_{Turb} = M_2^2 \left(\frac{1 + \gamma}{1 + \gamma M_2^2} \right)^2$$

$$P_{Turb} = \frac{1 + \gamma}{(1 + \gamma M_2^2)^2} \left[\frac{2 + (T - 1) M_2^2}{\gamma + 1} \right]^{-1} \quad P_2 = P_{Turb} \left(\frac{1}{\rho_1 \rho_{PIPE}} \right) p_1 \quad T_2 = T_{Turb} \left(\frac{1}{T_1 T_{in}} \right) T_1$$

$$P_{Turb} = \frac{1 + \gamma}{(1 + \gamma M_2^2)^2} \left[\frac{2 + (T - 1) M_2^2}{\gamma + 1} \right]^{-1} \quad P_2 = P_{Turb} \left(\frac{1}{\rho_1 \rho_{PIPE}} \right) p_1 \quad T_2 = T_{Turb} \left(\frac{1}{T_1 T_{in}} \right) T_1$$

$$P_{Turb} = \frac{p_1 (0.0123 \cdot 10^3)}{R T_2} \quad P_{out} = \frac{P_{Turb}}{\rho_{PIPE}} \quad P_{out} = P_{Turb} \rho_{PIPE} \quad P_2 = P_{Turb} \rho_1 p_1 p_{out}$$

$$x_2 = \sqrt{R \cdot T_2} \quad T_2 = M_2 \cdot x_2$$

Calculate inlet Reynolds number, entrance length, and turbulent boundary layer thickness at 1 meter airfoil.

$$Re_d = \frac{V_1 (2 \pi r_1) \rho_1}{\mu_{in}} \quad L_e = 2.88 \cdot 10^4 \cdot Re_d^{1/4} \quad j = 1.2 \cdot 10$$

$$D_{out} = j \cdot l \quad \frac{D_{out}}{Re_d} = \frac{0.13 \text{ D}_{out}}{l} \quad Re_d^4$$

Calculate Power in flow.

$$h_{10} = \frac{V_1^2}{2} \cdot C_p T_1 \quad h_{20} = \frac{V_2^2}{2} \cdot C_p T_2 \quad P_{out} = p_1 V_1 A_{in} h_{10} \quad P_{out} = p_2 V_2 A_{in} h_{20}$$

Calculate power available at exit (present).

$$\frac{P_{out}}{P_{out, present}} = 100$$

$$\begin{aligned} \text{Calculate change in entropy (present).} \\ \text{Calculate the change in internal energy (present).} \\ \Delta E = \frac{(p_1 \cdot p_2) \cdot (10^3)^2}{2} \left(\frac{1}{p_1} - \frac{1}{p_2} \right) \end{aligned}$$

Hydrogen (Colorically perfect) Conduction only model

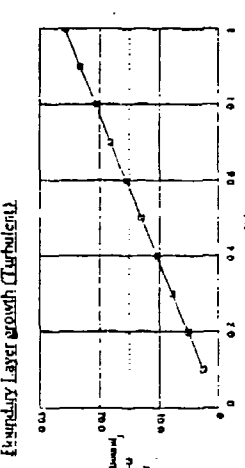
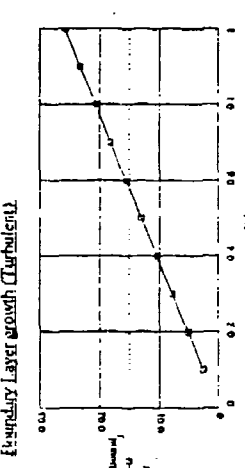
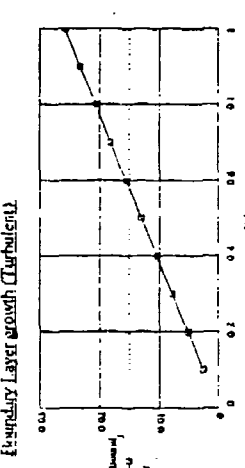
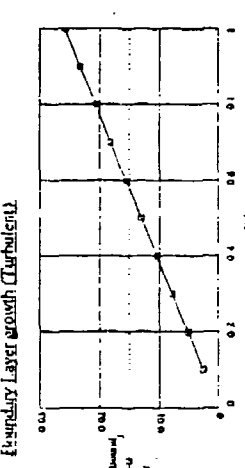
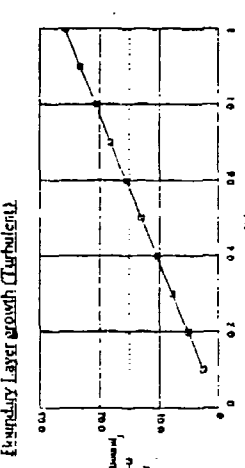
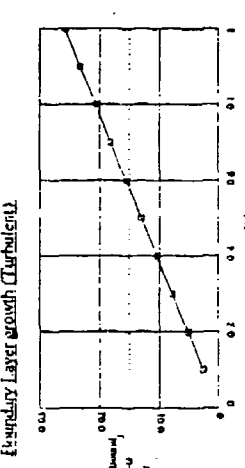
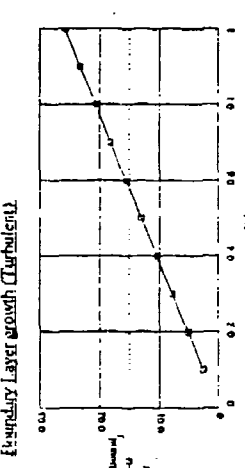
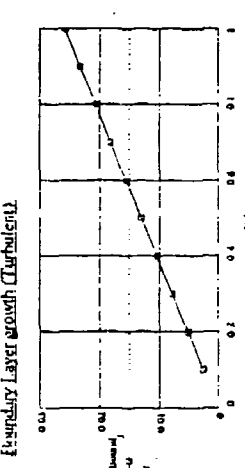
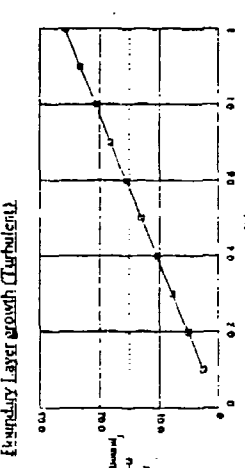
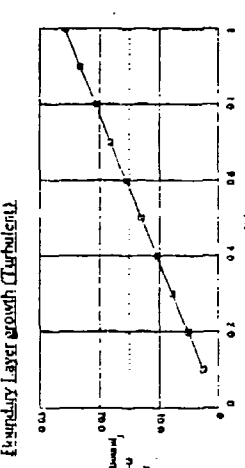
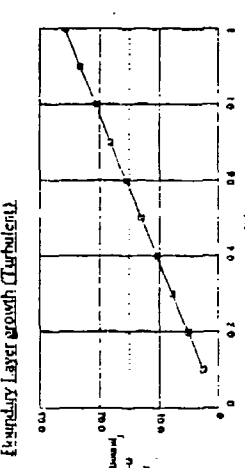
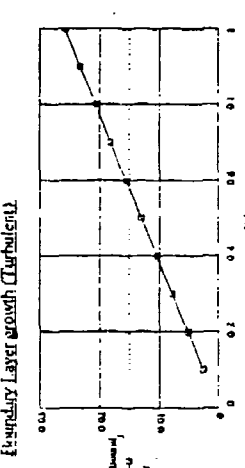
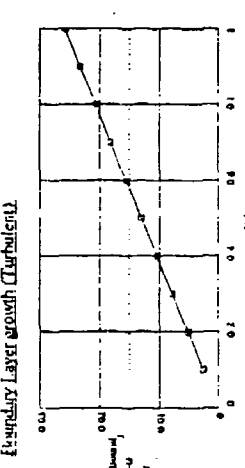
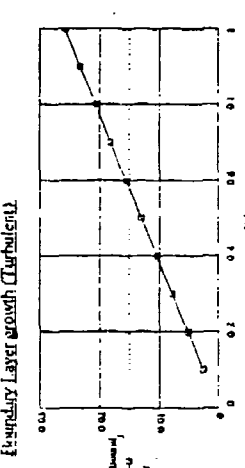
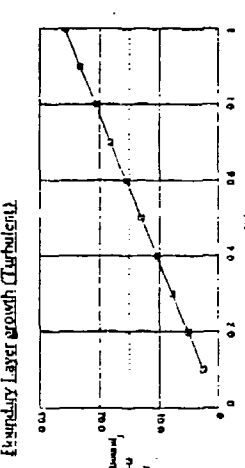
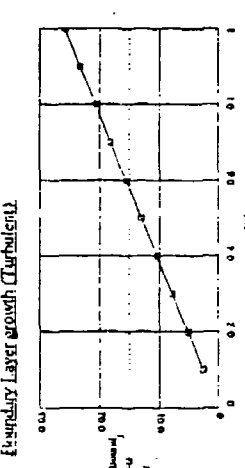
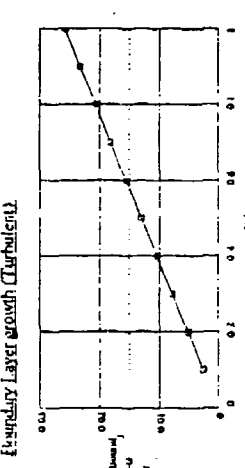
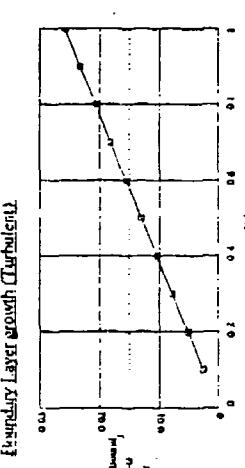
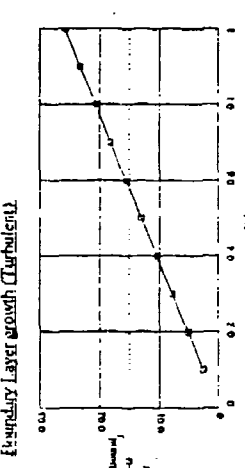
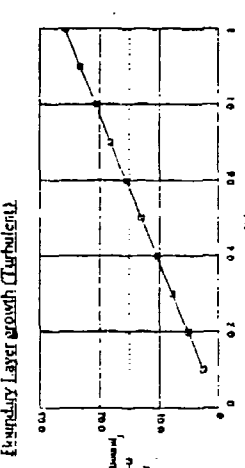
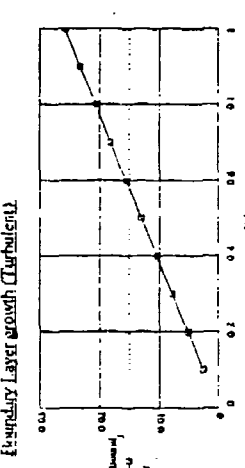
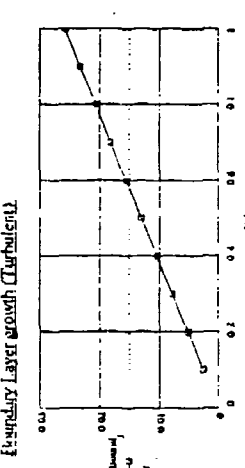
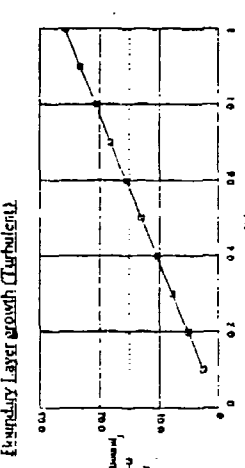
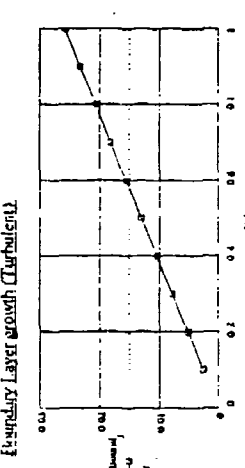
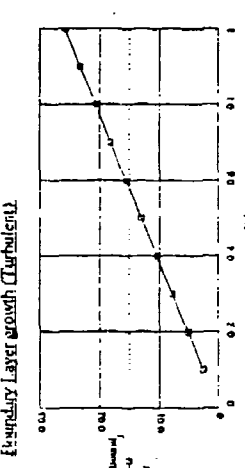
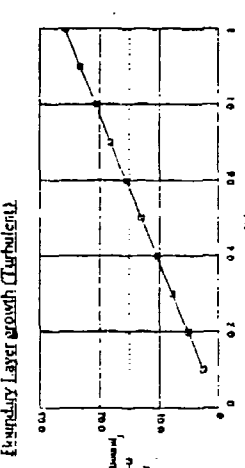
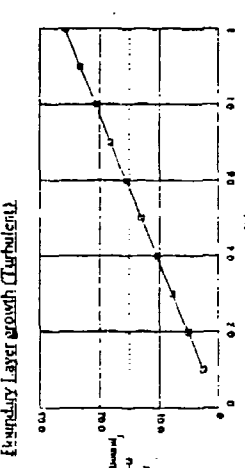
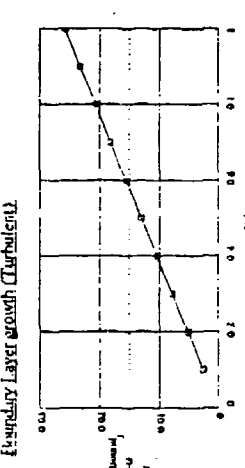
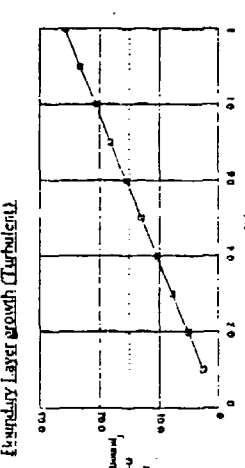
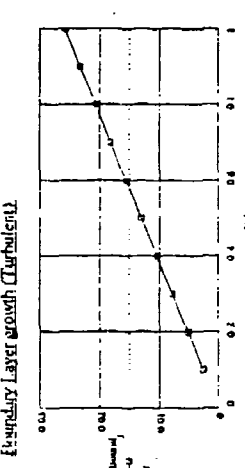
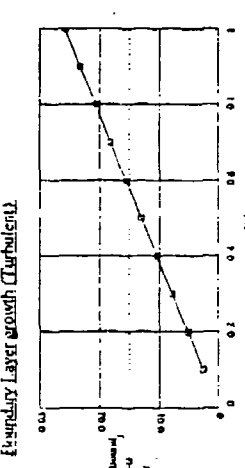
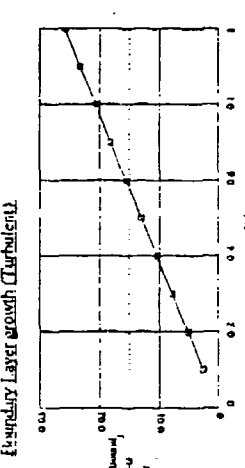
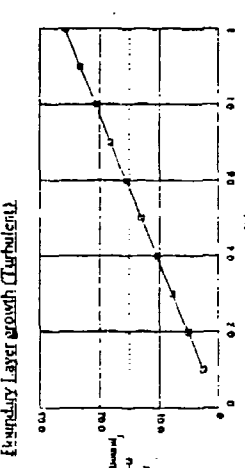
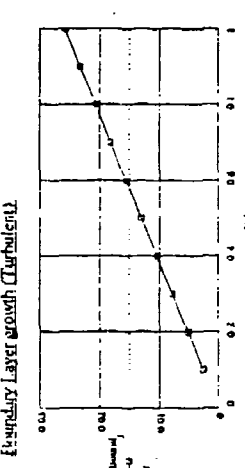
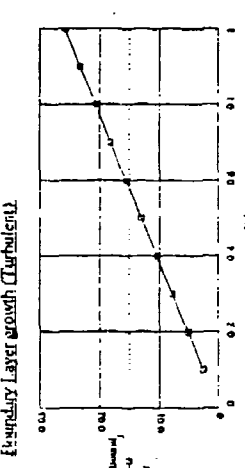
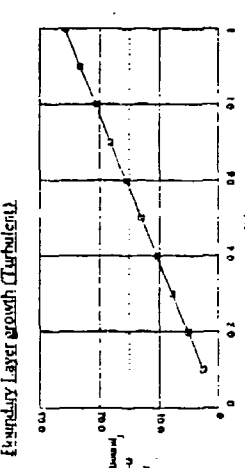
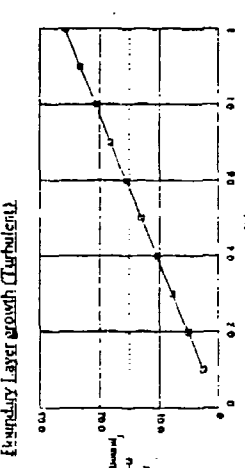
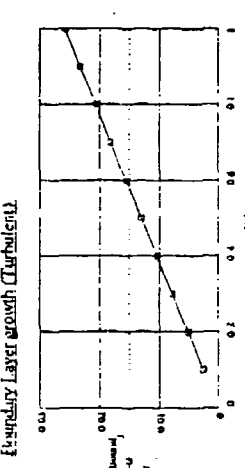
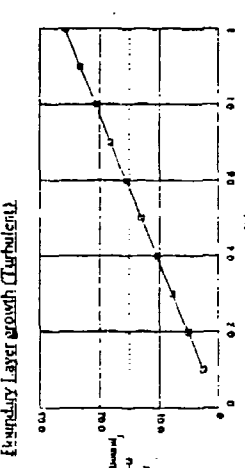
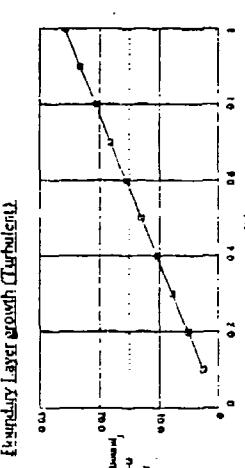
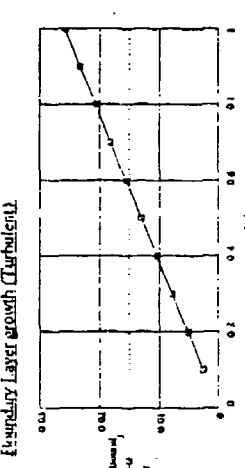
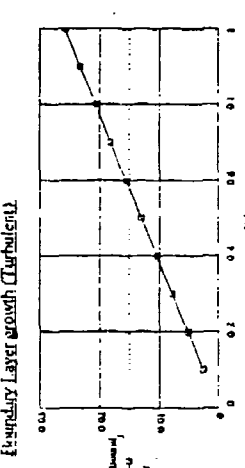
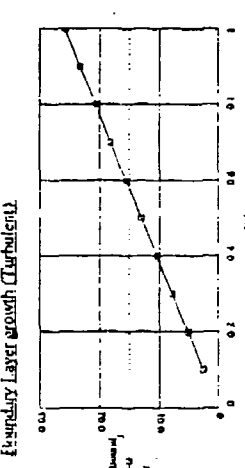
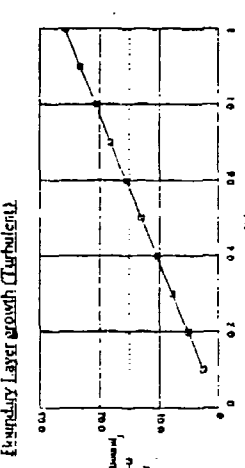
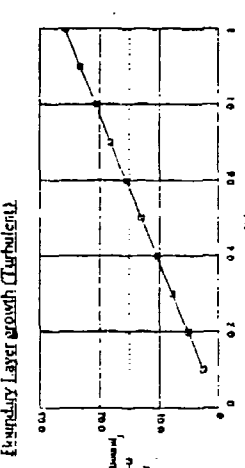
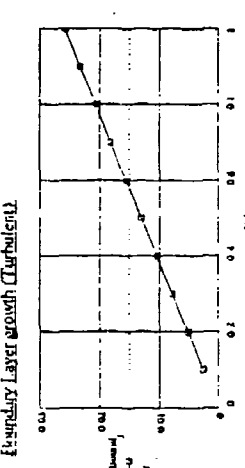
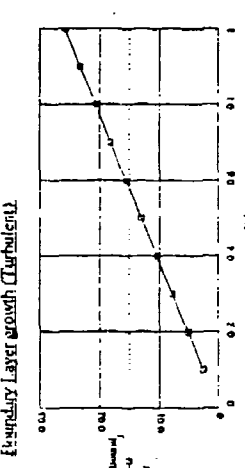
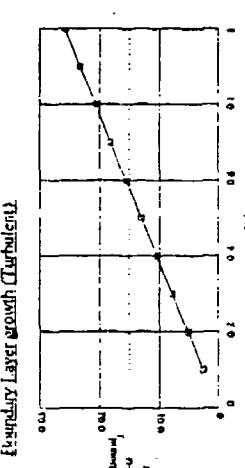
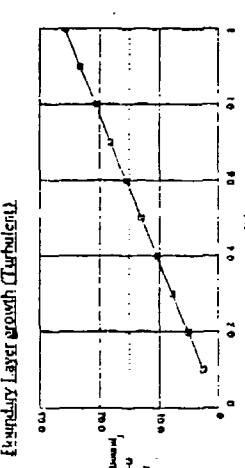
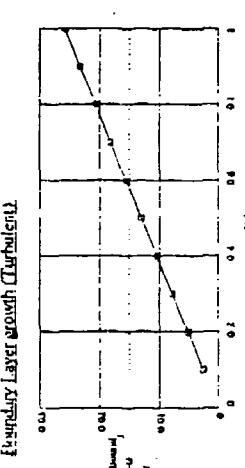
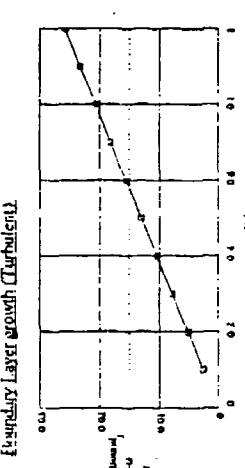
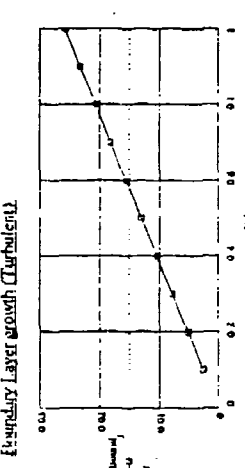
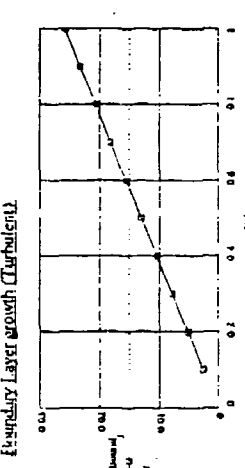
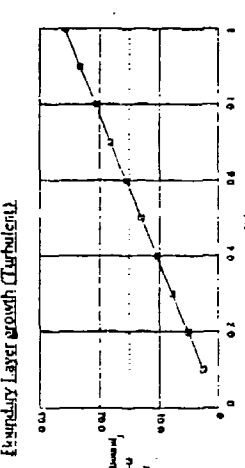
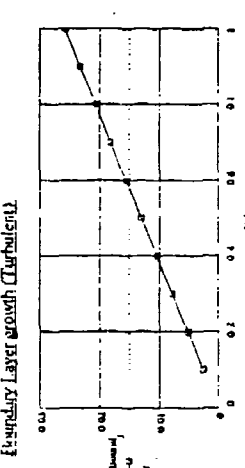
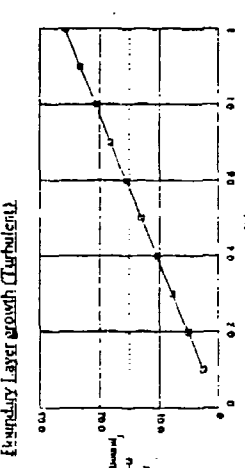
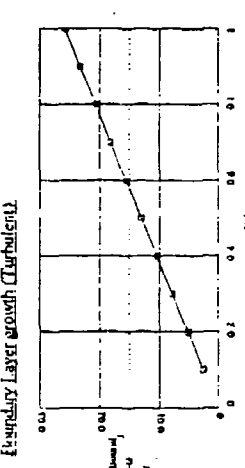
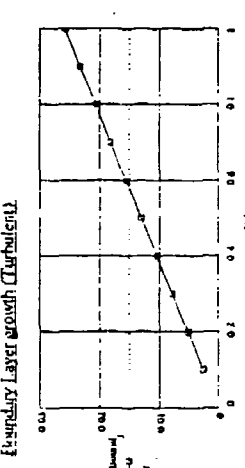
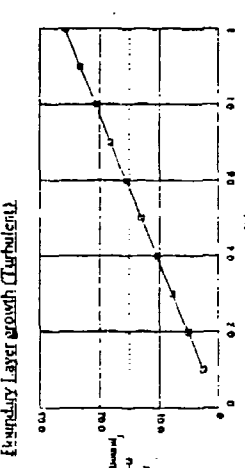
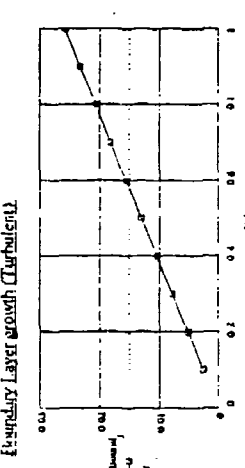
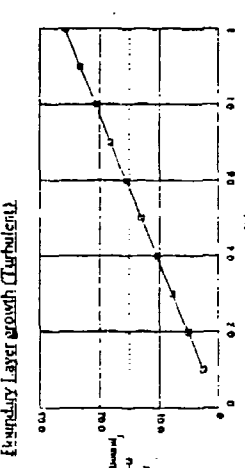
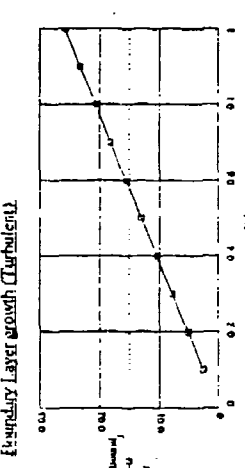
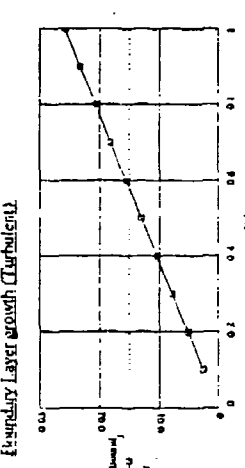
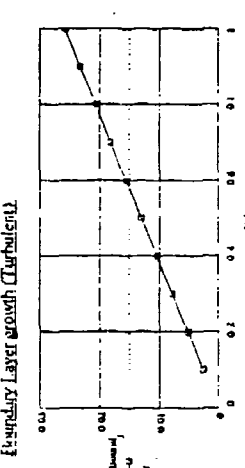
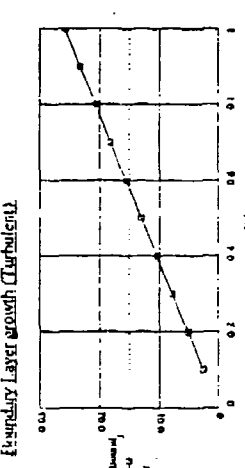
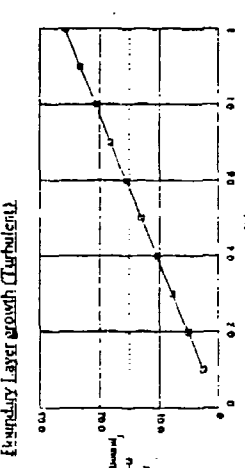
<u>Gas Data:</u>		$\gamma = 1.41$	$k = 2.81 \cdot 10^{-3}$	$K_{Nu} = 8.32 \cdot 10^{-3}$
$R_e = 0.002016$		$C_p = 1.07375 \cdot 10^4$		
$R = 4.122 \cdot 10^3$				
<u>Tubes Data:</u>				
$r = 0.015$	$L = 1$	$V_{Volume} = 7.069 \cdot 10^{-4}$	$A_{Area} = 0.004$	$h_{Coef} = 0.002$
<u>Inlet Flow Calculation:</u>				
$\dot{m} = 1.022 \cdot 10^{-6}$				
<u>Inlet Conditions:</u>				
$V_1 = 500$		$V_2 = 1.18 \cdot 10^3$		
$P_1 = 2.811$		$P_2 = 10.16$		
$T_1 = 5951 \cdot 10^3$		$T_2 = 2.786 \cdot 10^3$		
$M_1 = 0.0065$		$M_2 = 0.0345$		
$F_1 = 1.147 \cdot 10^3$		$F_2 = 1.152 \cdot 10^3$		
$s_1 = 7.62 \cdot 10^3$		$s_2 = 4.924 \cdot 10^3$		
$T_{inj} = 1 \cdot 10^6$		$T_{01} = 2.792 \cdot 10^3$		
$P_{inj} = 1.15 \cdot 10^3$		$P_{02} = 1.155 \cdot 10^3$		
<u>Power Calculations:</u>				
<u>Inlet Power</u>	$P_{inlet} = 1.884 \cdot 10^{10}$			
<u>Outlet Power</u>	$P_{outlet} = 5.252 \cdot 10^9$			
		Percent = 27.87		
<u>Change in internal energy (specific):</u>				
$\Delta E_{inj} = 2.981 \cdot 10^7$		$\Delta E_{out} = -8.988$		
<u>Change in entropy (specific):</u>				
$\Delta S_{inj} = 4.98$				
<u>Friction factor and distance length:</u>				
$Keq = 4.967 \cdot 10^3$		$Le = 4.21$		
<u>Boundary Layer growth (Turbulent):</u>				
				
				
				
				
				
				
				
				
				
				
				
				
				
				
				
				
				
				
				
				
				
				
				
				
				
				
				
				
				
				
				
				
				
				
				
				
				
				
				
				
				
				
				
				
				
				
				
				
				
				
				
				
				
				
				
				
				
				
				
				
				
				
				
				
				
				
<img alt="Graph showing boundary layer thickness (delta) versus dimensionless distance (x/Le). The curve starts at (0,0) and increases towards a plateau. A horizontal dashed line represents the outer flow condition. The y-axis ranges from 0.00 to 0.02, and the x-axis ranges from				

Table F.1 Mathcad conduction data

Conduction Data:								
$VC_1 =$	$TOC_1 =$	$POC_1 =$	$PO2C_1 =$	$PCC_1 =$	$MIC_1 =$	$M2C_1 =$	$q1C_1 =$	
500	10000	1000	1003	17.09	.066	.027	$1.175 \cdot 10^3$	
1000	10000	1000	1005	58.04	.131	.0995	$5.897 \cdot 10^2$	
1500	10000	1000	1008	72.087	.198	.165	$3.956 \cdot 10^2$	
5500	10000	1000	1032	91.18	.763	.644	$1.250 \cdot 10^7$	
8500	10000	1000	1119	92.64	1.292	1.583	$1.043 \cdot 10^6$	
13000	10000	1000	2260	88.797	2.683	3.625	$1.588 \cdot 10^7$	
$VC_2 =$	$TOC_2 =$	$POC_2 =$	$PO2C_2 =$	$PCC_2 =$	$MIC_2 =$	$M2C_2 =$	$q2C_2 =$	
500	8000	1000	1002	34.154	.073	.0427	$7.464 \cdot 10^2$	
1000	8000	1000	1005	66.933	.147	.119	$3.749 \cdot 10^2$	
1500	8000	1000	1008	77.788	.221	.192	$2.519 \cdot 10^2$	
5500	8000	1000	1032	92.703	.866	.706	$8.275 \cdot 10^6$	
8500	8000	1000	1137	93.407	1.51	1.76	$7.474 \cdot 10^6$	
13000	8000	1000	1324	83.981	3.777	12.26	$1.816 \cdot 10^2$	
$VC_3 =$	$TOC_3 =$	$POC_3 =$	$PO2C_3 =$	$PCC_3 =$	$MIC_3 =$	$M2C_3 =$	$q3C_3 =$	
500	11605	1000	1003	3.407	.001	.0112	$1.589 \cdot 10^3$	
1000	11605	1000	1005	51.566	.122	.087	$7.97 \cdot 10^2$	
1500	11605	1000	1008	67.527	.183	.148	$5.342 \cdot 10^2$	
5500	11605	1000	1032	89.995	.703	.599	$1.653 \cdot 10^7$	
8500	11605	1000	1116	91.951	1.172	1.522	$1.324 \cdot 10^6$	
13000	11605	1000	1930	88.955	2.461	3.23	$1.818 \cdot 10^2$	
$VC_4 =$	$TOC_4 =$	$POC_4 =$	$PO2C_4 =$	$PCC_4 =$	$MIC_4 =$	$M2C_4 =$	$q4C_4 =$	
500	10000	850	852.5	2.478	.010	.043	$1.382 \cdot 10^3$	
1000	10000	850	855.0	51.057	.131	.093	$6.938 \cdot 10^2$	
1500	10000	850	857.6	67.162	.198	.159	$4.654 \cdot 10^2$	
5500	10000	850	381.7	89.623	.763	.629	$1.471 \cdot 10^6$	
8500	10000	850	975.88	91.344	1.292	1.634	$1.227 \cdot 10^6$	
13000	10000	850	2402	86.818	2.683	3.887	$1.868 \cdot 10^7$	
$VC_5 =$	$TOC_5 =$	$POC_5 =$	$PO2C_5 =$	$PCC_5 =$	$MIC_5 =$	$M2C_5 =$	$q5C_5 =$	
500	10000	1150	1153	27.87	.066	.035	$1.022 \cdot 10^3$	
1000	10000	1150	1155	63.835	.131	.104	$5.128 \cdot 10^2$	
1500	10000	1150	1158	75.728	.198	.169	$3.44 \cdot 10^2$	
5500	10000	1150	1183	92.331	.763	.657	$1.087 \cdot 10^6$	
8500	10000	1150	1264	93.603	1.292	1.545	$9.069 \cdot 10^5$	
13000	10000	1150	2388	90.078	2.683	3.477	$1.381 \cdot 10^7$	

Table F.2 Mathcad conduction data

VC_6	TOC_6	POC_6	$PO2C_6$	PCC_6	MIC_6	$M2C_6$	q_6C
1500	23000	1000	1011	40.138	.13	.0259	$3.125 \cdot 10^8$
8500	23000	1000	1068	80.102	.78	.554	$6.487 \cdot 10^7$
13000	23000	1000	1435	83.131	1.306	2.002	$5.501 \cdot 10^7$

VC_7	TOC_7	POC_7	$PO2C_7$	PCC_7	MIC_7	$M2C_7$	q_7C
8500	34000	1000	1070	70.047	.629	.438	$1.444 \cdot 10^8$
13000	34000	1000	1662	76.923	1.018	2.143	$1.112 \cdot 10^8$
16000	34000	1000	1796	77.877	1.328	2.309	$1.066 \cdot 10^8$

APPENDIX G

Calculation results for radiation models

This data was produced with Mathcad 4.0. This appendix contains sample case data and computed tabular data for Rosseland diffusion and Planck radiation models.

Variables used:

Molwt - molecular weight	R - gas constant
γ - ratio of specific heats	k - thermal conductivity
μ - viscosity	T_{01} - inlet stagnation temp
P_{01} - inlet stagnation press	V_1 - inlet velocity
ρ_{01} - inlet stagnation density	a_{∞} - stagnation sound speed
a_1 - inlet sound speed	M_1 - inlet Mach number
T_1 - inlet static temp	P_1 - inlet static press
time - transit time	mass - mass of working fluid
ρ_1 - initial density	q - heat transfer per unit mass
P_01P_1 - ratio of press	T_01T_1 - ratio of temps
Red - Reynolds number	Le - Laminar entrance length
h_{10} - inlet enthalpy	

(variables with a 2 in them indicate exit conditions)

(This appendix is referenced by chapter 3.7, page 52, chapter 4.5, page 89 and chapter 4.6, page 95)

Hydrogen (Calorically perfect) Rosseland Diffusion Radiation only model

Gas Data

$\text{Molar} = 0.00316$ $\gamma = 1.41$
 $K = 4.12 \cdot 10^3$ $C_p = 41747.5 \cdot 10^3$

Tubes Data

$r = 0.01$; $L = 1$; $V_{turbine} = 7.669 \cdot 10^{-4}$
 Heat Flux Coefficient:
 $q = 1.756 \cdot 10^7$

Inlet Condition:

$V_1 = 500$

$P_1 = 2.421$

$T_1 = 9.94 \cdot 10^3$

$H_1 = 0.666$

$P_1 = 1.17 \cdot 10^3$

$A_1 = 1.62 \cdot 10^4$

$T_{01} = 1 \cdot 10^3$

$P_{01} = 1.15 \cdot 10^3$

Power of steamline

Inlet Power $P_{inlet} = 1.931 \cdot 10^{10}$

Outlet Power $P_{outlet} = 1.334 \cdot 10^{10}$

Outlet conditions:

$V_2 = 366.661$

$P_2 = 3.445$

$T_2 = 7.33 \cdot 10^3$

$H_2 = 0.5616$

$P_2 = 1.14 \cdot 10^3$

$A_2 = 6.532 \cdot 10^4$

$T_{02} = 7.35 \cdot 10^3$

$P_{02} = 1.15 \cdot 10^3$

External Power Resumption

$P_{ext,out} = 7.472$

Changes in internal entropy (specific)

$\Delta s_{inlet} = 1.07 \cdot 10^3$

Changes in entropy (specific)

$\Delta s_{outlet} = -3.314$

Karman number and width of stream

$K_d = 4.56 \cdot 10^3$ $l_d = 1.26$

Knudsen Layer growth (Turbulent)

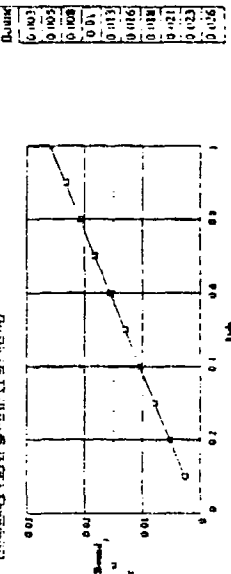


Table G.1 Mathcad rosseland radiation data

Rosseland Radiation Data							
VR1 _i =	TOR1 _i =	POR1 _i =	PO2R1 _i =	PCR1 _i =	M1R1 _i =	M2R1 _i =	q1R _i =
300	10000	1000	1003	1.056	.066	.007	$1.403 \cdot 10^8$
1000	10000	1000	1006	50.735	.131	.093	$6.983 \cdot 10^7$
1500	10000	1000	1009	67.388	.128	.159	$4.023 \cdot 10^7$
5500	10000	1000	1028	92.475	.763	.658	$1.067 \cdot 10^7$
8500	10000	1000	1050	96.356	1.292	1.44	$5.164 \cdot 10^6$
13000	10000	1000	1047	99.117	2.683	2.737	$1.252 \cdot 10^6$
VR2 _i =	TOR2 _i =	POR2 _i =	PO2R2 _i =	PCR2 _i =	M1R2 _i =	M2R2 _i =	q2R _i =
500	8000	1000	1001	61.009	.073	.057	$4.421 \cdot 10^7$
1000	8000	1000	1003	80.607	.147	.132	$2.199 \cdot 10^7$
1500	8000	1000	1004	87.187	.221	.205	$1.453 \cdot 10^7$
5500	8000	1000	1014	97.177	.666	.784	$3.201 \cdot 10^6$
8500	8000	1000	1021	98.761	1.51	1.56	$1.405 \cdot 10^6$
13000	8000	1000	1016	99.645	3.777	3.795	$1.786 \cdot 10^5$
VR3 _i =	TOR3 _i =	POR3 _i =	PO2R3 _i =	PCR3 _i =	M1R3 _i =	M2R3 _i =	q3R _i =
300	11605	1000	1007	1.012	.11	.014	$1.604 \cdot 10^8$
1000	11605	1000	1009	15.239	.123	.047	$1.383 \cdot 10^8$
1500	11605	1000	1013	43.836	.184	.119	$9.155 \cdot 10^7$
5500	11605	1000	1041	86.734	.706	.576	$2.163 \cdot 10^7$
8500	11605	1000	1092	93.274	1.178	1.47	$1.096 \cdot 10^7$
13000	11605	1000	1083	97.967	2.291	2.391	$3.316 \cdot 10^6$
VR4 _i =	TOR4 _i =	POR4 _i =	PO2R4 _i =	PCR4 _i =	M1R4 _i =	M2R4 _i =	q4R _i =
500	10000	850	851.4	44.125	.066	.043	$7.926 \cdot 10^7$
1000	10000	850	852.8	72.16	.131	.111	$3.946 \cdot 10^7$
1500	10000	850	854.3	81.573	.198	.177	$2.612 \cdot 10^7$
5500	10000	850	863.9	95.748	.763	.697	$6.028 \cdot 10^6$
8500	10000	850	864.7	96.67	1.292	.796	$4.72 \cdot 10^6$
13000	10000	850	865.6	99.64	2.683	2.705	$7.075 \cdot 10^5$
VR5 _i =	TOR5 _i =	POR5 _i =	PO2R5 _i =	PCR5 _i =	M1R5 _i =	M2R5 _i =	q5R _i =
300	10000	1150	1151	73.473	.066	.056	$3.756 \cdot 10^8$
1000	10000	1150	1152	86.04	.131	.122	$1.87 \cdot 10^8$
1500	10000	1150	1153	81.61	.198	.188	$1.238 \cdot 10^8$
5500	10000	1150	1159	97.986	.763	.729	$2.856 \cdot 10^6$
8500	10000	1150	1164	99.024	1.292	1.353	$1.383 \cdot 10^6$
13000	10000	1150	1164	99.766	2.683	2.697	$3.353 \cdot 10^5$

One-Dimensional, compressible, inviscid flow with heat extraction based on Planck Radiation for calorically perfect hydrogen gas

Initial Gas Properties

$$M_{in} = 2.0136 \cdot 10^3 \quad R = 4121.735 \quad \gamma = 1.41 \quad M_{in} = 4.63 \cdot 10^4$$

$$C_p = \frac{7 \cdot R}{(\gamma - 1)} \quad \sigma = 1.67 \cdot 10^{-8} \quad dP = 8.52 \cdot 10^4$$

Take Data

$$r = 0.15 \quad L = 1.0 \quad V_{01} = r \cdot \pi \cdot r^2 \cdot L \quad A_{ext} = r \cdot 2 \cdot \pi \cdot L$$

Inlet Conditions:

$$\frac{T_{01}}{T_{01} + 10000} = \frac{p_{01}}{p_{01} + 1150} = \frac{V_{01}}{V_{01} + 13000.00} = \frac{\rho_{01}}{\rho_{01} + \frac{p_{01}(1.01335 \cdot 10^4)}{R \cdot T_{01}}} = \frac{A_{ext}}{A_{ext} + \frac{V_{01}}{2}}$$

$$\frac{T_{01}}{T_{01} + \frac{(r-1)}{2} \cdot k_{H2}} = \frac{p_{01}}{p_{01} + \frac{p_{01}(1.01335 \cdot 10^4) \cdot V_{01}}{R \cdot T_{01}}} = \frac{1}{1 + \frac{r-1}{2} \cdot \frac{1}{M_{in}}}$$

$$time \cdot \frac{L}{V_0} = \frac{p_{01}(1.01335 \cdot 10^4) \cdot V_{01}}{R \cdot T_{01}} = \frac{p_{01}(1.01335 \cdot 10^4)}{R \cdot T_{01}}$$

Heat Flow Calculation

$$q = \left(1 + \sigma \cdot T_{01}^4 \cdot \frac{Area \cdot \Delta T}{mass} \right)$$

Calculations:

$$p_{01} \cdot \left(1 + \frac{r-1}{2} \cdot \frac{1}{M_{in}} \right)^{\frac{1}{(r-1)}} = T_{01} \cdot T_{01} \cdot 1 + \frac{r-1}{2} \cdot \frac{1}{M_{in}} = p_{01} \cdot p_{01} \cdot P_{01}$$

$$p_{01} \cdot \left(1 + \frac{r-1}{2} \cdot \frac{1}{M_{in}} \right)^{\frac{1}{(r-1)}} = T_{01} \cdot T_{01} \cdot T_{01} \cdot \frac{q}{C_p} = T_{01} \cdot q \cdot T_{01}$$

$$p_{01} \cdot \left(\frac{1+r}{2} \cdot \frac{1}{M_{in}} \right)^{\frac{1}{(r-1)}} = T_{01} \cdot T_{01} \cdot M_{in}^2 \cdot \left(\frac{1+r}{2} \cdot \frac{1}{M_{in}} \right)^2 = p_{01} \cdot \frac{1}{M_{in}} \cdot \left(\frac{1+r}{2} \cdot \frac{1}{M_{in}} \right)^2$$

$$p_{01} \cdot \left(\frac{1+r}{2} \cdot \frac{1}{M_{in}} \right)^{\frac{1}{(r-1)}} = T_{01} \cdot T_{01} \cdot \frac{2 \cdot (r-1) \cdot M_{in}^2}{r+1} = T_{01} \cdot T_{01} \cdot \left[\frac{2 \cdot (r-1) \cdot M_{in}^2}{(r+1) \cdot M_{in}^2} \right] \cdot [2 \cdot (r-1) \cdot M_{in}^2]$$

$$T_{01} \cdot T_{01} = \frac{2 \cdot (r-1) \cdot M_{in}^2}{(r+1) \cdot M_{in}^2} \cdot T_{01} \cdot T_{01}$$

$$M_{in} = 2.0136 \cdot 10^3 \quad R = 4121.735 \quad \gamma = 1.41 \quad M_{in} = 4.63 \cdot 10^4$$

Calculate the change in internal energy (specific):

$$\Delta E_S = \frac{(P_1 + P_2)(1.01335 \cdot 10^4)}{2} \cdot \left(\frac{1}{p_1} - \frac{1}{p_2} \right)$$

Calculate initial Reynolds number, Entrance length, and Turbulent boundary layer thickness M_1 , Laminar interval.

$$Re = \frac{V_0 \cdot L}{\nu_0} \quad L = 1.00 \cdot 10^{-4} \cdot Re^{0.75} \quad j = 1, 2, \dots, 10$$

$$Dek = j - 1 \quad Bound = \frac{1}{Re^k}$$

Calculate Power in flow:

$$M_{in} \cdot \frac{V_0^3}{2} \cdot C_p \cdot T_{01} = M_{in} \cdot \frac{V_0^3}{2} \cdot C_p \cdot T_{01}$$

$$Power = p_2 \cdot V_2 \cdot Area / 20$$

Calculate power available at exit (percent):

$$Percent = \frac{Power}{Power_{exit}} \cdot 100$$

Calculate change in entropy (specific):

$$\Delta S_S = \frac{(P_1 + P_2)(1.01335 \cdot 10^4)}{2} \cdot \left(\frac{1}{p_1} - \frac{1}{p_2} \right)$$

Hydrogen (Calorically perfect) Planck Radiation only model

Gas Data

Molar = 0.002016 $\gamma = 1.41$ $K_{\text{B}} = 8.63 \cdot 10^{-5}$
 $R = 4.12 \cdot 10^3$ $C_p = 14134.75 \cdot 10^4$

Tube Data

$r = 0.015$ $L = 1$ $V_{\text{Volume}} = 7.069 \cdot 10^{-4}$ $A_{\text{Area}} = 0.051$ $l_{\text{Tube}} = 7.292 \cdot 10^{-3}$

Heat Flux Calculation:

$$Q = 1.712 \cdot 10^6$$

Power Calculations:

$$\text{Inlet Power} = P_{\text{inlet}} = 1.179 \cdot 10^{10}$$

$$\text{Outlet Power} = P_{\text{outlet}} = 9.333 \cdot 10^9$$

$$\text{Power Remaining:}$$

$$P_{\text{Remaining}} = 991.45$$

Inlet Conditions:

$V_1 = 1 \cdot 10^4$
 $\rho_1 = 0.31$
 $T_1 = 409 \cdot 10^3$
 $s_1 = 2.583$
 $P_1 = 50.98$
 $a_1 = 4.845 \cdot 10^3$
 $T_{01} = 1 \cdot 10^4$
 $P_{01} = 3.15 \cdot 10^3$

Outlet Conditions:

$V_2 = 1.304 \cdot 10^4$
 $\rho_2 = 0.369$
 $T_2 = 3.913 \cdot 10^3$
 $s_2 = 2.7355$
 $P_2 = 49.121$
 $a_2 = 4.768 \cdot 10^3$
 $T_{02} = 9.914 \cdot 10^3$
 $P_{02} = 1.201 \cdot 10^3$

Change in Internal Energy (specific)

$$\Delta E = -4.51 \cdot 10^4$$

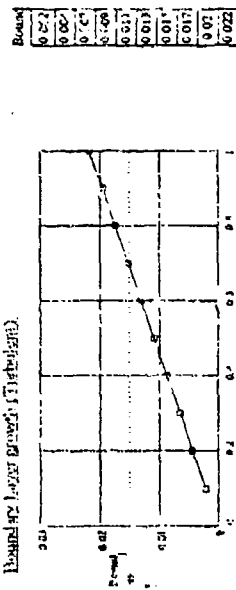
Change in Entropy (specific)

$$\Delta S = -153 \text{ J/K}$$

Reynolds number and entrance length:

$$Re = 1.4 \cdot 10^4 \quad L_e = 1.092$$

Blended 1/2 Layer Eddy (Turbulent)



Boundary Layer Thickness is 1 mm
 Tube radius Co. length is 0.15 m.s.e.

Table G.2 Mathcad planck radiation data

Planck Radiation Data:							
VP1 _i =	TOP1 _i =	POP1 _i =	PO2P1 _i =	PCP1 _i =	M1P1 _i =	M2P1 _i =	q1P _i =
500	10000	1000	1003	8.11	.066	.019	$1.303 \cdot 10^3$
1000	10000	1000	1006	54.24	.131	.096	$6.488 \cdot 10^-1$
1500	10000	1000	1008	69.69	.198	.162	$4.295 \cdot 10^-1$
5500	10000	1000	1026	92.98	.763	.664	$9.945 \cdot 10^6$
8500	10000	1000	1047	96.58	1.292	1.431	$4.849 \cdot 10^6$
13000	10000	1000	1046	99.14	2.683	2.736	$1.219 \cdot 10^9$
VP2 _i =	TOP2 _i =	POP2 _i =	PO2P2 _i =	PCP2 _i =	M1P2 _i =	M2P2 _i =	q2P _i =
500	8000	1000	1003	8.78	.073	.0216	$1.034 \cdot 10^3$
1000	8000	1000	1007	54.63	.147	.107	$5.145 \cdot 10^-1$
1500	8000	1000	1010	70.02	.221	.181	$3.400 \cdot 10^-1$
5500	8000	1000	1030	93.36	.866	.716	$7.533 \cdot 10^5$
8500	8000	1000	1053	97.05	1.51	1.618	$3.349 \cdot 10^6$
13000	8000	1000	1044	99.58	3.777	3.83	$4.717 \cdot 10^5$
VP3 _i =	TOP3 _i =	POP3 _i =	PO2P3 _i =	PCP3 _i =	M1P3 _i =	M2P3 _i =	q3P _i =
500	11605	1000	1005	2.043	.109	.012	$1.589 \cdot 10^3$
1000	11605	1000	1010	7.819	.122	.034	$1.516 \cdot 10^8$
1500	11605	1000	1014	58.905	.183	.111	$1.005 \cdot 10^8$
5500	11605	1000	1044	85.514	.703	.565	$2.383 \cdot 10^7$
8500	11605	1000	1104	92.60	1.172	1.497	$1.217 \cdot 10^-1$
13000	11605	1000	1093	97.688	2.27	2.382	$3.804 \cdot 10^6$
VP4 _i =	TOP4 _i =	POP4 _i =	PO2P4 _i =	PCP4 _i =	M1P4 _i =	M2P4 _i =	q4P _i =
500	10000	850	851.92	25.199	.066	.033	$1.061 \cdot 10^3$
1000	10000	850	853.83	62.707	.131	.103	$5.277 \cdot 10^-1$
1500	10000	850	855.71	75.348	.198	.169	$3.494 \cdot 10^-1$
5500	10000	850	868.36	94.293	.763	.679	$8.09 \cdot 10^5$
8500	10000	850	881.407	97.217	1.292	1.406	$3.944 \cdot 10^6$
13000	10000	850	881.457	99.298	2.683	2.726	$9.913 \cdot 10^5$
VP5 _i =	TOP5 _i =	POP5 _i =	PO2P5 _i =	PCP5 _i =	M1P5 _i =	M2P5 _i =	q5P _i =
500	10000	1150	1153	8.501	.066	.019	$1.296 \cdot 10^3$
1000	10000	1150	1156	54.484	.131	.096	$6.454 \cdot 10^-1$
1500	10000	1150	1159	69.867	.198	.163	$4.273 \cdot 10^-1$
5500	10000	1150	1180	93.021	.763	.664	$9.893 \cdot 10^5$
8500	10000	1150	1203	96.597	1.292	1.430	$4.827 \cdot 10^6$
13000	10000	1150	1202	99.145	2.683	2.736	$1.212 \cdot 10^5$

Table G.3 Mathcad rosseland radiation data

$\text{VR}_6 =$	$\text{TOR}_6 =$	$\text{POR}_6 =$	$\text{PO2R}_6 =$	$\text{PCR}_6 =$	$\text{MIR}_6 =$	$\text{M2R}_6 =$	$q_6 R_p =$
1500	23000	1000	1001	93.89	.13	.125	$2.120 \cdot 10^7$
8500	23000	1000	1004	99.042	.78	.761	$3.126 \cdot 10^6$
13000	23000	1000	1006	99.566	1.376	1.393	$1.412 \cdot 10^6$

$\text{VR}_7 =$	$\text{TOR}_7 =$	$\text{POR}_7 =$	$\text{PO2R}_7 =$	$\text{PCR}_7 =$	$\text{MIR}_7 =$	$\text{M2R}_7 =$	$q_7 R_p =$
1500	34000	1000	1003	66.705	.107	.087	$1.605 \cdot 10^8$
8500	34000	1000	1014	94.782	.629	.583	$2.515 \cdot 10^6$
13000	34000	1000	1026	97.331	1.066	1.243	$1.287 \cdot 10^6$

Table G.4 Mathcad planck radiation data

$\text{VP}_6 =$	$\text{TOP}_6 =$	$\text{POF}_6 =$	$q_6 P_p =$
1500	34.00	1000	$3.244 \cdot 10^{10}$
8500	23.00	1000	$1.218 \cdot 10^{10}$
13000	23.00	1000	$5.211 \cdot 10^9$

$\text{VP}_7 =$	$\text{TOP}_7 =$	$\text{POF}_7 =$	$q_7 P_p =$
1500	34.000	1000	$2.508 \cdot 10^{11}$
8500	34.000	1000	$3.934 \cdot 10^{10}$
13000	34.000	1000	$2.017 \cdot 10^9$

APPENDIX H

Calculation results for viscous effects model

This data was produced with Mathcad 4.0. This appendix contains one sample case data and computed tabular data.

Variables used:

Molwt - molecular weight	R - gas constant
γ - ratio of specific heats	k - thermal conductivity
μ - viscosity	T_{01} - inlet stagnation temp
P_{01} - inlet stagnation press	V_1 - inlet velocity
ρ_{01} - inlet stagnation density	a_{∞} - stagnation sound speed
a_1 - inlet sound speed	M_1 - inlet Mach number
T_1 - inlet static temp	P_1 - inlet static press
time - transit time	mass - mass of working fluid
ρ_i - initial density	$P_{01}P_1$ - ratio of press
$T_{01}T_1$ - ratio of temps	h_{10} - inlet enthalpy
Red - Reynolds number	Le - Laminar entrance length
f - friction factor	LeT - theoretical length

(variables with a 2 in them indicate exit conditions)

(This section is referenced by chapter 3.4, page 31, chapter 4.3, page 79, and chapter 4.6, page 93)

One-Dimensional, compressible, viscous flow for calorically perfect hydrogen gas

Initial Gas Properties:

$$\begin{aligned} \text{Molar } &= 2.0156 \cdot 10^{-3} & R &= 4102.735 & \gamma &= 1.41 \\ C_p &= \frac{\gamma R}{(\gamma - 1)} & k &= 1.12 & M_1 &= 0.52 \cdot 10^{-4} \end{aligned}$$

Tube Data

$$\begin{aligned} r &= 0.15 & L &= 1.0 & \text{Volume} &= \pi r^2 L & A_{T2s} &= \frac{D_{T2s} (1.01325 \cdot 10^5)}{IT_{T2s}} \\ IT_{T1} &= 10000 & P_{T1} &= 1000 & V_1 &= 1500.00 & \rho_{T1} &= \frac{P_{T1} (1.01325 \cdot 10^5)}{RT_{T1}} \end{aligned}$$

$$\Delta u_1 = \sqrt{R/IT_{T1}} \quad \alpha_1 = \sqrt{(\gamma - 1) \left[\frac{M_{11}^2}{(\gamma - 1)} + \frac{V_1^2}{2} \right]} \quad M_{11} = \frac{V_1}{\alpha_1}$$

$$T_1 = \frac{P_{T1}}{1 + \left(\frac{\gamma - 1}{2} \right) M_{11}^2} \quad P_1 = \frac{P_{T1}}{1 + \left(\frac{\gamma - 1}{2} \right) M_{11}^2} \quad t_{\text{time}} = \frac{1}{\sqrt{V_1}}$$

$$\rho_{T1} = \frac{P_1 (1.01325 \cdot 10^5 \cdot \text{Volume})}{R T_1} \quad \rho_1 = \frac{P_1 (1.01325 \cdot 10^5)}{R T_1}$$

$$\text{Calculate initial Reynolds number, fluid entrance length, and friction factor}$$

$$Re_1 = \frac{V_1 D_{T1} \rho_1}{\mu_{\text{gas}}} \quad L_e = 2.38 \cdot 10^{-4} Re_1^{0.5} \quad f = 1.2 \cdot 10$$

$$Re_1 = 1 \quad L_{\text{entrance}} = \frac{2.38 \cdot 10^{-4}}{\mu_{\text{gas}}} \quad f = 1.2 \cdot 10$$

$$\text{Check for friction factor}$$

$$f = 0.03$$

Calculations

$$\begin{aligned} P_{01} P_1 &= \left(1 + \frac{\gamma - 1}{2} M_{11}^2 \right)^{\frac{1}{(\gamma - 1)}} & \tau_{01} T_1 &= 1 + \frac{\gamma - 1}{2} M_{11}^2 & P_{01} &= P_1 P_{01s} \\ \frac{P_{01} P_1}{P_{02} P_2} &= \left(1 + \frac{\gamma - 1}{2} M_{11}^2 \right)^{\frac{1}{(\gamma - 1)}} & \tau_{01} &= \tau_{01} T_1 T_2 & P_{02} &= \frac{P_1 P_{01s}}{(\gamma - 1)^{1/2}} \end{aligned}$$

Calculate change in entropy (specific)

$$\Delta s = -R \ln \left(\frac{P_{02}}{(P_{01})} \right)$$

$$\Delta E = \frac{(P_1 + P_2) \cdot (1.01325 \cdot 10^5)}{2} \cdot \left(\frac{1}{P_{01}} - \frac{1}{P_{02}} \right)$$

Calculate theoretical length:

$$\begin{aligned} L_{cT} &= FL_1 \frac{2r}{4.0f} & T_1 T_{1s} &= \frac{\gamma + 1}{2 + (\gamma - 1) M_1^2} & P_{01} P_{1s} &= \frac{1}{M_1} T_1 T_{1s}^2 \\ P_{01} P_{0s} &= \frac{1}{M_1} \cdot \left(\frac{1}{T_1 T_{1s}} \right)^2 & \rho_1 \rho_{1s} &= \frac{1}{M_1} \left(\frac{1}{T_1 T_{1s}} \right)^2 & FL_2 &= FL_1 \cdot \frac{4 \cdot f \cdot L}{(2 \cdot r)} \\ M_3 &= 1.9987 & M_{12} &= \frac{1 - M_3^2}{\gamma M_3^2} + \frac{\gamma + 1}{2 \cdot \gamma} \ln \left(\frac{(\gamma + 1) M_3^2}{2 + (\gamma - 1) M_3^2} \right) \\ M_2 &= M_3 & P_{02} P_{2s} &= \frac{1}{M_2} \cdot \left(\frac{1}{T_2 T_{2s}} \right)^2 & P_{02} P_{0s} &= \frac{1}{M_2} \left(\frac{1}{T_2 T_{2s}} \right)^2 \\ \tau_{T2s} &= \frac{\gamma + 1}{2 + (\gamma - 1) M_2^2} & P_{02} P_{0s} &= \frac{1}{M_2} \left(\frac{1}{T_2 T_{2s}} \right)^2 & V_2 &= M_{2s} \cdot 2 \\ \rho_{2s} &= \frac{1}{M_2} \left(\frac{1}{T_2 T_{2s}} \right)^2 & P_{02} &= \frac{P_2 (1.01325 \cdot 10^5)}{R \cdot T_2} & & \end{aligned}$$

Hydrogen (Calorically perfect) Viscous effects only model

Gas Data

$\mu_{\text{air}} = 0.002016$ $\gamma = 1.41$ $k = 1.2$ $\text{Nu} = 8.2 \cdot 10^{-4}$
 $R = 4.122 \cdot 10^3$ $C_p = 1.417475 \cdot 10^4$

Tube Data

$r = 0.015$ $L = 1$ $V_{\text{volume}} = 7.069 \cdot 10^{-4}$ $A_{\text{area}} = 0.094$ $L_{\text{tube}} = 6.467 \cdot 10^{-4}$

Inlet Conditions:

$V_1 = 1.5 \cdot 10^3$ $V_2 = 1.517 \cdot 10^3$
 $\rho_1 = 2.411$ $\rho_2 = 2.383$
 $T_1 = 9.921 \cdot 10^3$ $T_2 = 4.919 \cdot 10^3$
 $M_1 = 10.191$ $M_2 = 0.19987$
 $P_1 = 972.569$ $P_2 = 161.574$
 $a_1 = 7.593 \cdot 10^3$ $a_2 = 7.392 \cdot 10^3$
 $P_{01} = 998.926$
 $T_{01} = 1 \cdot 10^3$

Change in internal energy (specific)

$$\Delta E = 4.74 \cdot 10^3$$

Change in enthalpy (specific)

$$\Delta H = 45.896$$

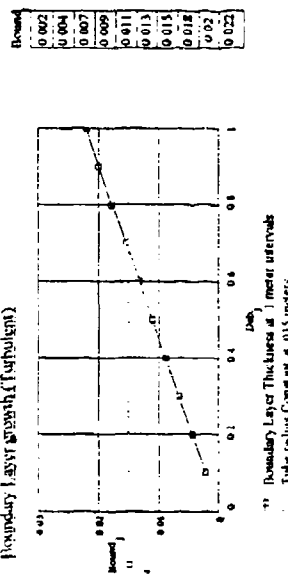
Theoretical length and friction factor

$$L_{\text{theo}} = 37.112$$

$$f = 0.003$$

Reynolds number and laminar skin friction length
 $Re = 1.273 \cdot 10^6$ $L_e = 11.062$

Boundary Layer Strength (Turbulent)



• Boundary Layer Thickness at 1 meter intervals
 - Turbulent Constant @ 0.015 meters

Table H.1 Mathcad viscous data

Viscous Data							
$FF1_k =$	$VV1_k =$	$TOV1_k =$	$P0V1_k =$	$P0V1^2_k =$	$DS1_k =$	$TL1_k =$	
.003	1500	10000	1000	988.926	45.898	37.112	
.003	500	10000	1000	934.18	280.631	3.347	
.003	4500	10000	1000	870.972	569.398	1.098	
.003	12500	10000	1000	406.534	3710	1.034	
.003	13500	10000	1000	280.645	5237	1.269	
$FF2_k =$	$VV2_k =$	$TOV2_k =$	$P0V2_k =$	$P0V2^2_k =$	$DS2_k =$	$TL2_k =$	
.003	1500	10000	850	840.587	45.898	37.112	
.003	3500	10000	850	794.053	280.631	3.347	
.003	4500	10000	850	740.436	569.79	1.098	
.003	12500	10000	850	345.554	3710	1.034	
.003	13500	10000	850	238.07	5235	1.269	
$FF3_k =$	$VV3_k =$	$TOV3_k =$	$P0V3_k =$	$P0V3^2_k =$	$DS3_k =$	$TL3_k =$	
.003	1500	10000	1150	1137	45.839	37.112	
.003	3500	10000	1150	1071	280.631	3.347	
.003	4500	10000	1150	1002	569.79	1.098	
.003	12500	10000	1150	467.515	3710	1.034	
.003	13500	10000	1150	323.073	5233	1.269	
$FF4_k =$	$VV4_k =$	$TOV4_k =$	$P0V4_k =$	$P0V4^2_k =$	$DS4_k =$	$TL4_k =$	
.003	1500	8000	1000	986.101	57.691	28.429	
.003	3500	8000	1000	914.147	369.985	2.142	
.003	4500	8000	1000	868.005	583.465	1.062	
.003	12500	8000	1000	222.356	6197	1.379	
.003	13500	8000	1000	96.011	9658	1.633	
$FF5_{kk} =$	$VV5_{kk} =$	$TOV5_{kk} =$	$P0V5_{kk} =$	$P0V5^2_{kk} =$	$DS5_{kk} =$	$TL5_{kk} =$	
.003	1500	11605	1000	990.475	39.447	44.144	
.003	3500	11605	1000	944.382	235.863	4.379	
.003	4500	11605	1000	898.035	443.277	1.597	
.003	13500	11605	1000	402.539	3751	1.042	
$FF6_k =$	$VV6_k =$	$TOV6_k =$	$P0V6_k =$	$P0V6^2_k =$	$DS6_k =$	$TL6_k =$	
.002	1500	10000	1000	992.616	30.547	55.668	
.002	4500	10000	1000	921.587	336.574	1.647	
.002	13500	10000	1000	358.906	4224	1.904	
$FF7_k =$	$VV7_k =$	$TOV7_k =$	$P0V7_k =$	$P0V7^2_k =$	$DS7_k =$	$TL7_k =$	
.004	1500	10000	1000	985.196	61.475	27.834	
.004	4500	10000	1000	846.315	687.767	1.102	
.004	14500	10000	1000	183.782	6982	1.039	

Table H.2 Mathcad viscous data

FF8 = .003	T0V8 = 23000	P0V82 = 995.249
VV8 = 1500	P0V8 = 1000	TL8 = 94.869
FF9 = .003	T0V9 = 34000	P0V92 = 996.775
VV9 = 1500	P0V9 = 1000	TL9 = 144.41

APPENDIX I

Calculation results for convection model

This data was produced with Mathcad 4.0. This appendix contains one sample case data and computed tabular data.

Variables used:

Molwt - molecular weight	R - gas constant
γ - ratio of specific heats	k - thermal conductivity
μ - viscosity	T_{01} - inlet stagnation temp
P_{01} - inlet stagnation press	V_1 - inlet velocity
ρ_{01} - inlet stagnation density	a_{∞} - stagnation sound speed
a_1 - inlet sound speed	M_1 - inlet Mach number
T_1 - inlet static temp	P_1 - inlet static press
time - transit time	mass - mass of working fluid
ρ_1 - initial density	q - heat transfer per unit mass
$P_{01}P_1$ - ratio of press	$T_{01}T_1$ - ratio of temps
Red - Reynolds number	Le - Laminar entrance length
h_{10} - inlet enthalpy	τ_w - wall shear stress

(variables with a 2 in them indicate exit conditions)

(This appendix is referenced by chapter 3.6, page 39, chapter 4.4, page 84, and chapter 4.6, page 93)

One-Dimensional, compressible, inviscid flow with heat extraction based on Convection for calorically perfect hydrogen gas

Initial Gas Properties

$$\text{Molar } = 2.015 \times 10^3 \quad R = 4121.735 \quad T = 141$$

$$C_p = \frac{7R}{(7-1)} \quad k = 1.2 \quad M_0 = 2.52 \times 10^{-3}$$

Turb Data

$$r = 0.15 \quad L = 10 \quad \text{Volume} = \pi r^2 L \quad Area = \pi r^2 L$$

exit Conditions

$$P_{exit} = P_{inlet} + \frac{1}{2} \left[(y-1) \left(\frac{A_{exit}}{A_{inlet}} - \frac{V_{inlet}^2}{V_{exit}^2} \right) \right] \quad M_{exit} = \frac{P_{inlet}}{P_{exit}} \frac{(y+1)(k-1)}{k-1}$$

$$T_{exit} = \frac{P_{exit}}{1 + \left(\frac{1}{2} \right) M_{exit}^2} \quad P_{exit} = \frac{P_{inlet}}{1 + \left(\frac{1}{2} \right) M_{exit}^2}$$

$$\text{mass} = \frac{L}{V_{exit}} \quad \dot{m}_{exit} = \frac{P_{inlet} (1.01325 \times 10^5 \text{ N/m}^2)}{R \cdot T_{exit}} \left(\frac{1.01325 \times 10^5 \text{ N/m}^2}{R \cdot T_{exit}} \right)^{\frac{1}{k-1}}$$

$$\text{mass} = \frac{L}{V_{exit}} \quad \dot{m}_{exit} = \frac{P_{inlet} (1.01325 \times 10^5 \text{ N/m}^2)}{R \cdot T_{exit}} \left(\frac{1.01325 \times 10^5 \text{ N/m}^2}{R \cdot T_{exit}} \right)^{\frac{1}{k-1}}$$

$$Re_{exit} = \frac{V_{exit} \cdot D_{exit}}{\nu} \quad Le = 2.33 \times 10^4 \cdot Re/(2\pi) \quad j = 1, 2, 10$$

$$f_{exit} = 1 + \frac{24}{Re_{exit}} \cdot \frac{1}{Re_{exit}^{1/4}} \quad f_{exit} = 23 \text{ Darcy}$$

Calculate the Froude number.

Calculate the Sauter number.

$$Pr = \frac{C_p \cdot \mu}{k} \quad Saut = \frac{0.0198 \cdot Re^{1/4}}{1 + 0.7 Re^{0.5} / Pr} \quad j = 1, 2, 10$$

Calculate the heat transfer coefficient.

$$h = St \cdot Pr \cdot Vi \quad St = \frac{k_1}{k_2} \quad \text{Calculate friction factor.}$$

Calculate the coefficient of friction.

$$CF = 2 \left(\frac{h}{(C_p \cdot \rho \cdot V_i)} \right)^{1/4} \quad f = 0.03$$

Heat Flow Calculation

$$Q_{heat} = 0.0154 \cdot \rho \cdot V_i^2 \quad q = \frac{1}{4} \left[\frac{1}{(1.12)} \int_{V_1}^{V_2} h(T) \cdot dV \right] \text{ J/mole}$$

Calculate the change in enthalpy (specific)

$$\Delta h_{S,exit} = \frac{P_{inlet} \cdot (P_{exit} - P_{inlet})}{2} \left(\frac{1.01325 \times 10^5}{\rho_1 \cdot \rho_2} \right)^{1/2} \quad \text{Calculate the change in internal energy (specific)}$$

Percent = $\frac{\text{Power}_{exit} - \text{Power}_{inlet}}{\text{Power}_{inlet}} \cdot 100$

Calculate change in inventory (specific)

$$\Delta m_{exit} = \frac{P_{inlet} \cdot (P_{exit} - P_{inlet})}{2} \left(\frac{1.01325 \times 10^5}{\rho_1 \cdot \rho_2} \right)^{1/2} \quad \text{Calculate Power available at exit (percent)}$$

$$\text{Percent} = \frac{\text{Power}_{exit} - \text{Power}_{inlet}}{\text{Power}_{inlet}} \cdot 100$$

Calculate Power in flow

$$h_{inlet} = \frac{V_i^2}{2} \cdot C_p \cdot T_1 \quad h_{exit} = \frac{V_2^2}{2} \cdot C_p \cdot T_2 \quad \Delta h = \int_{V_1}^{V_2} h(V) dV \quad V_2 = M_2 \cdot A_2$$

Calculate Power available at exit (percent)

$$\text{Percent} = \frac{\text{Power}_{exit} - \text{Power}_{inlet}}{\text{Power}_{inlet}} \cdot 100$$

Calculations

$$P_{inlet} \cdot \left(1 + \frac{7-1}{2} M_0^2 \right)^{1/(y-1)} \quad T_{inlet} \cdot 1 + \frac{7-1}{2} M_0^2$$

$$P_{inlet} \cdot \left(1 + \frac{7-1}{2} M_0^2 \right)^{(y-1)} \quad T_{inlet} \cdot T_{exit}$$

$$P_{inlet} \cdot \left(\frac{1+y}{(1+y) M_0^2} \right)^{1/(y-1)} \quad T_{inlet} \cdot C_p$$

$$P_{inlet} \cdot \left(\frac{1+y}{(1+y) M_0^2} \right)^{1/(y-1)} \quad T_{inlet} \cdot T_{exit}$$

$$P_{inlet} \cdot \left(\frac{1+y}{(1+y) M_0^2} \right)^{1/(y-1)} \quad \rho_1 \cdot \rho_2 \cdot \left(\frac{1+y}{(1+y) M_0^2} \right)^{1/(y-1)} \quad \text{Power}_{exit}$$

$$P_{inlet} \cdot \left(\frac{1+y}{(1+y) M_0^2} \right)^{1/(y-1)} \quad \rho_1 \cdot \rho_2 \cdot \left(\frac{1+y}{(1+y) M_0^2} \right)^{1/(y-1)} \quad \text{Power}_{inlet}$$

$$P_{inlet} \cdot \left(\frac{1+y}{(1+y) M_0^2} \right)^{1/(y-1)} \quad \text{Power}_{exit}$$

$$P_{inlet} \cdot \left(\frac{1+y}{(1+y) M_0^2} \right)^{1/(y-1)} \quad \text{Power}_{inlet}$$

$$P_{inlet} \cdot \left(\frac{1+y}{(1+y) M_0^2} \right)^{1/(y-1)} \quad \text{Power}_{exit}$$

$$P_{inlet} \cdot \left(\frac{1+y}{(1+y) M_0^2} \right)^{1/(y-1)} \quad \text{Power}_{inlet}$$

$$P_{inlet} \cdot \left(\frac{1+y}{(1+y) M_0^2} \right)^{1/(y-1)} \quad \text{Power}_{exit}$$

$$P_{inlet} \cdot \left(\frac{1+y}{(1+y) M_0^2} \right)^{1/(y-1)} \quad \text{Power}_{inlet}$$

$$P_{inlet} \cdot \left(\frac{1+y}{(1+y) M_0^2} \right)^{1/(y-1)} \quad \text{Power}_{exit}$$

$$P_{inlet} \cdot \left(\frac{1+y}{(1+y) M_0^2} \right)^{1/(y-1)} \quad \text{Power}_{inlet}$$

$$P_{inlet} \cdot \left(\frac{1+y}{(1+y) M_0^2} \right)^{1/(y-1)} \quad \text{Power}_{exit}$$

$$P_{inlet} \cdot \left(\frac{1+y}{(1+y) M_0^2} \right)^{1/(y-1)} \quad \text{Power}_{inlet}$$

$$P_{inlet} \cdot \left(\frac{1+y}{(1+y) M_0^2} \right)^{1/(y-1)} \quad \text{Power}_{exit}$$

$$P_{inlet} \cdot \left(\frac{1+y}{(1+y) M_0^2} \right)^{1/(y-1)} \quad \text{Power}_{inlet}$$

$$P_{inlet} \cdot \left(\frac{1+y}{(1+y) M_0^2} \right)^{1/(y-1)} \quad \text{Power}_{exit}$$

$$P_{inlet} \cdot \left(\frac{1+y}{(1+y) M_0^2} \right)^{1/(y-1)} \quad \text{Power}_{inlet}$$

$$P_{inlet} \cdot \left(\frac{1+y}{(1+y) M_0^2} \right)^{1/(y-1)} \quad \text{Power}_{exit}$$

$$P_{inlet} \cdot \left(\frac{1+y}{(1+y) M_0^2} \right)^{1/(y-1)} \quad \text{Power}_{inlet}$$

$$P_{inlet} \cdot \left(\frac{1+y}{(1+y) M_0^2} \right)^{1/(y-1)} \quad \text{Power}_{exit}$$

$$P_{inlet} \cdot \left(\frac{1+y}{(1+y) M_0^2} \right)^{1/(y-1)} \quad \text{Power}_{inlet}$$

$$P_{inlet} \cdot \left(\frac{1+y}{(1+y) M_0^2} \right)^{1/(y-1)} \quad \text{Power}_{exit}$$

$$P_{inlet} \cdot \left(\frac{1+y}{(1+y) M_0^2} \right)^{1/(y-1)} \quad \text{Power}_{inlet}$$

$$P_{inlet} \cdot \left(\frac{1+y}{(1+y) M_0^2} \right)^{1/(y-1)} \quad \text{Power}_{exit}$$

$$P_{inlet} \cdot \left(\frac{1+y}{(1+y) M_0^2} \right)^{1/(y-1)} \quad \text{Power}_{inlet}$$

$$P_{inlet} \cdot \left(\frac{1+y}{(1+y) M_0^2} \right)^{1/(y-1)} \quad \text{Power}_{exit}$$

$$P_{inlet} \cdot \left(\frac{1+y}{(1+y) M_0^2} \right)^{1/(y-1)} \quad \text{Power}_{inlet}$$

$$P_{inlet} \cdot \left(\frac{1+y}{(1+y) M_0^2} \right)^{1/(y-1)} \quad \text{Power}_{exit}$$

$$P_{inlet} \cdot \left(\frac{1+y}{(1+y) M_0^2} \right)^{1/(y-1)} \quad \text{Power}_{inlet}$$

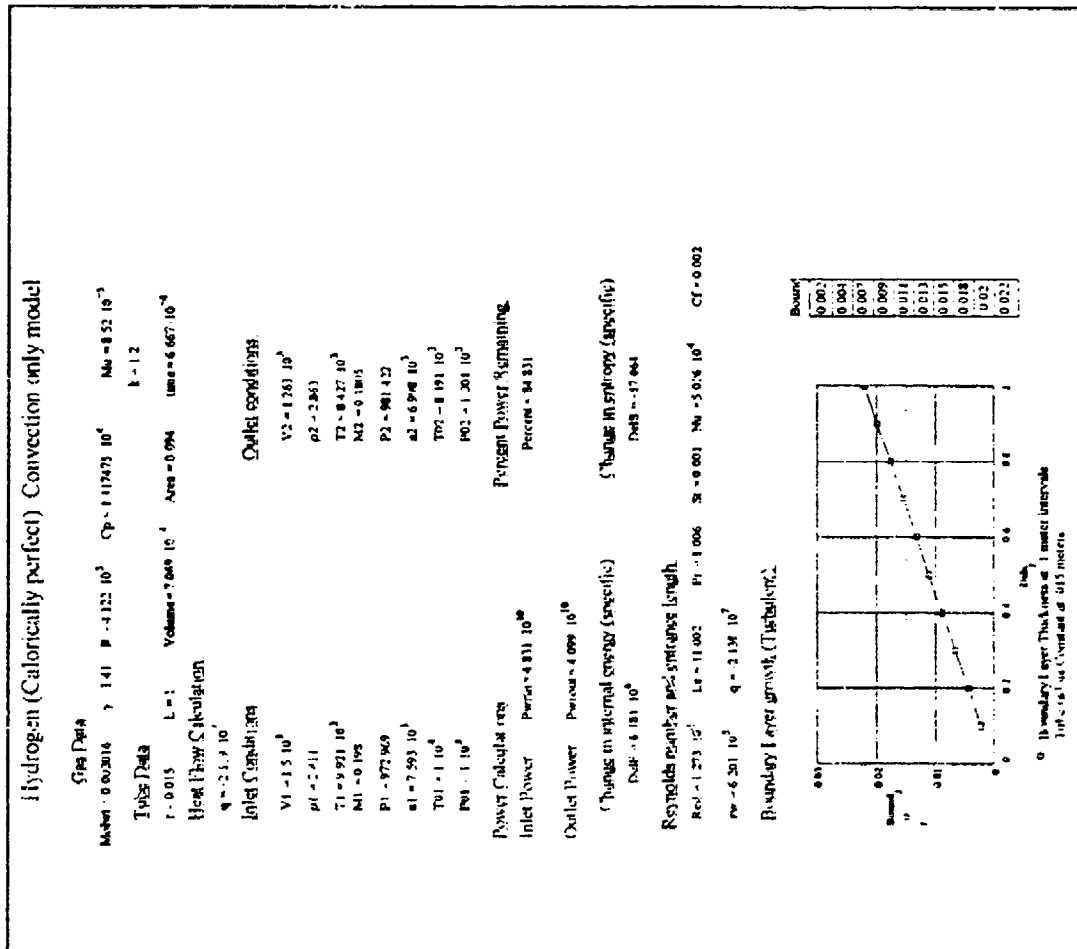


Table I.1 Mathcad convection data

Convection Data						
FFC1 _k	VX1 _k	TOX1 _k	PON1 _k	POX12 _k	PRX1 _k	qX1 _k
.003	1500	10000	1000	1004	84.831	2.139·10 ⁷
.003	3500	10000	1000	1018	87.97	1.705·10 ⁷
.003	4500	10000	1000	1028	88.846	1.581·10 ⁷
.003	12500	10000	1000	1371	93.727	1.605·10 ⁷
.003	13500	10000	1000	1503	94.475	8.892·10 ⁶
						7.83·10 ⁵
FFC2 _k	VX2 _k	TOX2 _k	PON2 _k	POX22 _k	PRX2 _k	qX2 _k
.003	1500	10000	850	853.653	84.689	2.17·10 ⁷
.003	3500	10000	850	865.597	87.769	1.734·10 ⁷
.003	4500	10000	850	873.833	88.652	1.605·10 ⁷
.003	12500	10000	850	1172	93.634	1.605·10 ⁷
.003	13500	10000	850	1286	94.401	9.025·10 ⁶
						7.935·10 ⁵
FFC3 _k	VX3 _k	TOX3 _k	PON3 _k	PON32 _k	PRX3 _k	qX3 _k
.003	1500	10000	1150	1155	85.082	2.114·10 ⁷
.003	3500	10000	1150	1170	88.139	1.681·10 ⁷
.003	4500	10000	1150	1181	89.007	1.558·10 ⁷
.003	12500	10000	1150	1570	93.805	1.558·10 ⁷
.003	13500	10000	1150	1719	94.538	8.751·10 ⁶
						7.741·10 ⁵
FFC4 _k	VX4 _k	TOX4 _k	PON4 _k	PON42 _k	PRX4 _k	qX4 _k
.003	1500	8000	1000	1005	86.313	1.552·10 ⁷
.003	3500	8000	1000	1020	89.139	1.232·10 ⁷
.003	4500	8000	1000	1026	89.615	1.178·10 ⁷
.003	12500	8000	1000	1521	95.314	1.178·10 ⁷
.003	13500	8000	1040	1806	96.468	5.314·10 ⁶
						4.007·10 ⁵
FFC5 _{kk}	VX5 _{kk}	TOX5 _{kk}	PON5 _{kk}	PON52 _{kk}	PRX5 _{kk}	qX5 _{kk}
.003	1500	11605	1000	1004	83.997	2.537·10 ⁷
.003	3500	11605	1000	1017	87.22	2.112·10 ⁷
.003	4500	11605	1000	1025	88.126	1.953·10 ⁷
.003	13500	11605	1000	1399	93.46	1.076·10 ⁷

Table I.2 Mathcad convection data

$FFC6_p =$	$VX6_p =$	$T0X6_p =$	$PuX6_p =$	$P0X62_p =$	$PRX6_p =$	$qX6_p =$
[.003]	[1500]	[23000]	[1000]	[1003]	[72.634]	$8.924 \cdot 10^7$
[.003]	[8500]	[23000]	[1000]	[1057]	[83.739]	$5.301 \cdot 10^7$
[.003]	[13000]	[23000]	[1000]	[1297]	[86.417]	$4.428 \cdot 10^7$
<hr/>						
$FFC6_p =$	$VX6_p =$	$T0X6_p =$	$PuX6_p =$	$P0X62_p =$	$PRX6_p =$	$qX6_p =$
[.003]	[1500]	[34000]	[1000]	[1002]	[69.075]	$1.491 \cdot 10^7$
[.003]	[8500]	[34000]	[1000]	[1047]	[81.226]	$9.048 \cdot 10^6$
[.003]	[13000]	[34000]	[1000]	[1310]	[83.923]	$7.748 \cdot 10^6$

APPENDIX J

Calculation results for barrel theoretical length

This data was produced with Mathcad 4.0.

(This appenoix is referenced by chapter 3.4, page 27, chapter 3.6, page 39, chapter 4.3, page 79, chapter 4.6, page 93, and chapter 5, page 107)

Calculation of Theoretical Length of ELGG Barrel based on friction

Gas data for Hydrogen:

$$\gamma = 1.41$$

Tube data:

$$d = .03 \quad L = 1.0$$

To construct the graph, I will calculate the friction in the barrel for Mach numbers ranging from $M = .5$ to $M = 8$ in steps of .05.

$$\text{MACH} = .5$$

$$i = 0, 1..50$$

$$M_i = \text{MACH} + i \cdot 0.05$$

$$\text{Frict}_i = \frac{1 - (\text{MACH} + i \cdot 0.05)^2}{\gamma \cdot (\text{MACH} + i \cdot 0.05)^2} + \frac{\gamma + 1}{2 \cdot \gamma} \ln \left[\frac{(\gamma + 1) \cdot (\text{MACH} + i \cdot 0.05)^2}{2 + (\gamma - 1) \cdot (\text{MACH} + i \cdot 0.05)^2} \right]$$

Calculate the theoretical length for various friction factors from .001 to .005 in steps sizes of .0005:

$$L_{\max 1_i} = \frac{\text{Frict}_i \cdot d}{4.0 (.001)}$$

$$L_{\max 5_i} = \frac{\text{Frict}_i \cdot d}{4.0 (.003)}$$

$$L_{\max 2_i} = \frac{\text{Frict}_i \cdot d}{4.0 (.0015)}$$

$$L_{\max 6_i} = \frac{\text{Frict}_i \cdot d}{4.0 (.0035)}$$

$$L_{\max 3_i} = \frac{\text{Frict}_i \cdot d}{4.0 (.002)}$$

$$L_{\max 7_i} = \frac{\text{Frict}_i \cdot d}{4.0 (.004)}$$

$$L_{\max 4_i} = \frac{\text{Frict}_i \cdot d}{4.0 (.0025)}$$

$$L_{\max 8_i} = \frac{\text{Frict}_i \cdot d}{4.0 (.0045)}$$

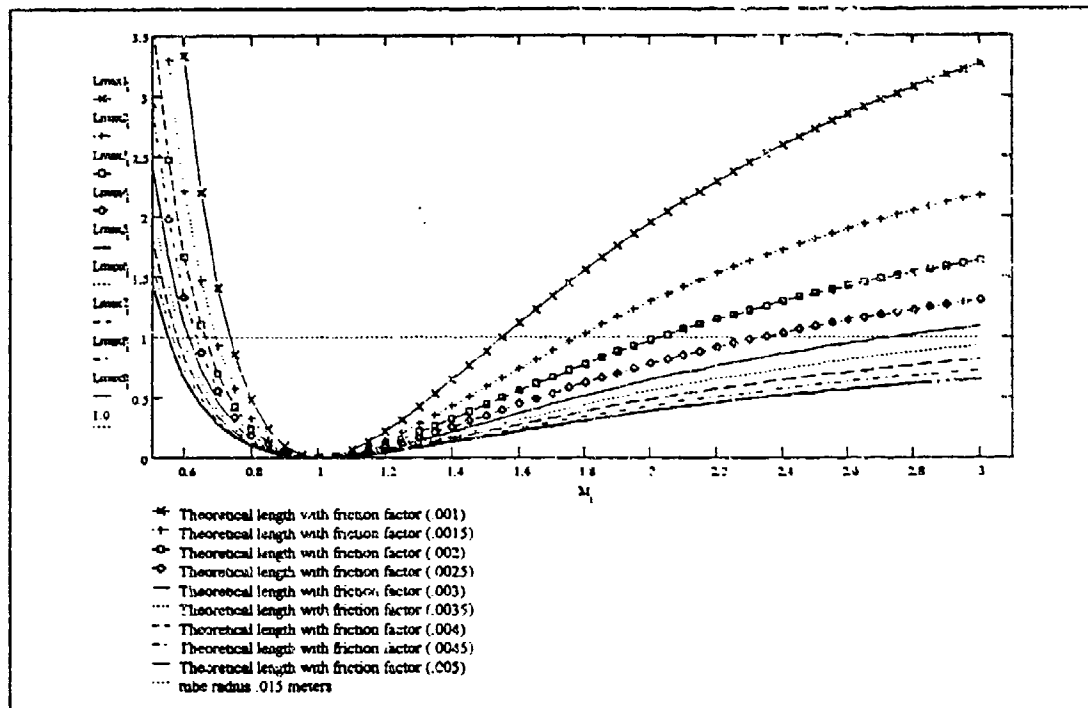


Figure J.3 Theoretical length calculations with γ 1.51 (hydrogen)

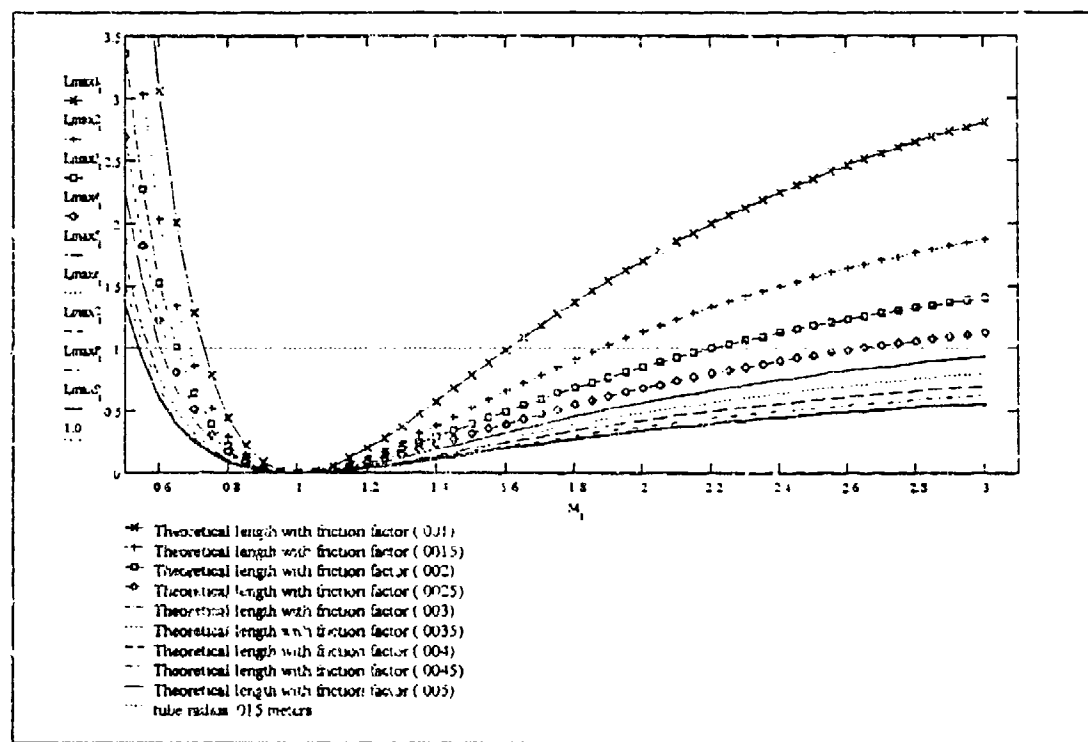


Figure J.4 Theoretical length calculations with γ 1.6. (hydrogen)

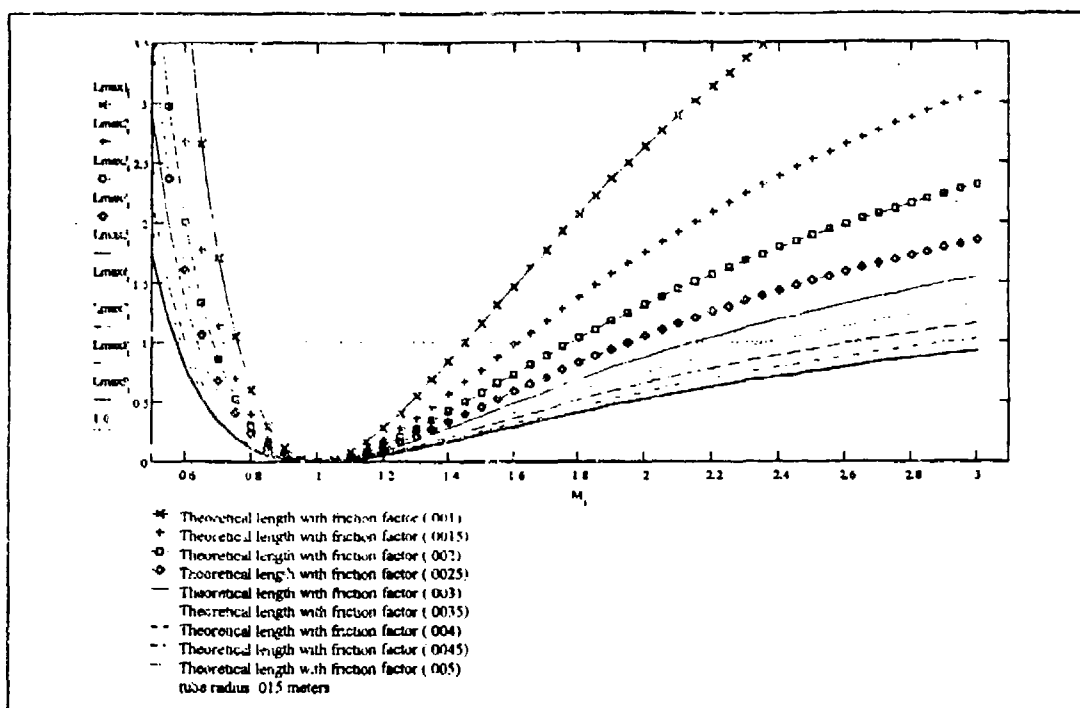


Figure J.1 Theoretical length calculations with γ 1.31 (hydrogen)

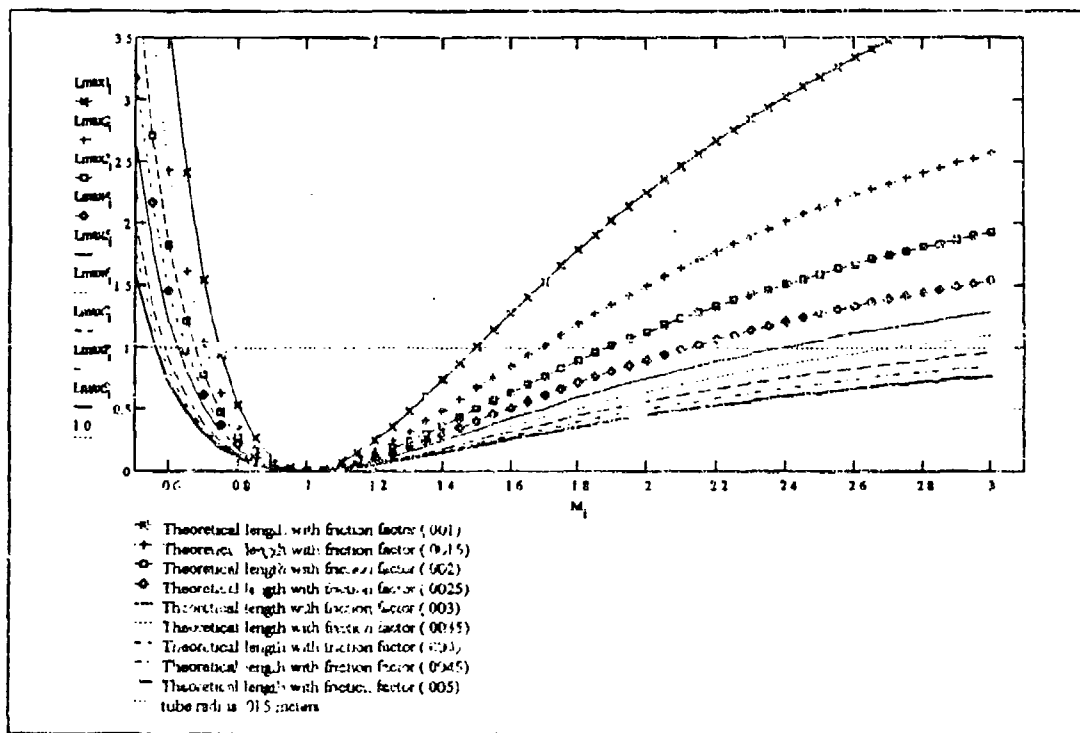


Figure J.2 Theoretical length calculations with γ 1.41 (hydrogen)

Table J.1 Theoretical length calculations from Mathcad

M ₁	L _{max1}	L _{max2}	L _{max3}	L _{max4}	L _{max5}	L _{max6}	L _{max7}	L _{max8}	L _{max9}
0.5	7.947	5.298	3.973	3.179	2.649	2.271	1.987	1.766	1.589
0.55	5.411	3.607	2.705	2.54	1.804	1.546	1.353	1.202	1.082
0.6	3.647	2.431	1.823	1.459	1.216	1.042	0.912	0.81	0.729
0.65	2.411	1.607	1.206	0.964	0.804	0.689	0.603	0.536	0.482
0.7	1.546	1.03	0.773	0.618	0.515	0.442	0.386	0.343	0.309
0.75	0.945	0.63	0.473	0.378	0.315	0.27	0.236	0.21	0.189
0.8	0.537	0.358	0.268	0.215	0.179	0.153	0.134	0.119	0.107
0.85	0.27	0.18	0.135	0.108	0.09	0.077	0.067	0.06	0.054
0.9	0.108	0.072	0.054	0.043	0.036	0.031	0.027	0.024	0.022
0.95	0.024	0.016	0.012	0.01	0.008	0.007	0.006	0.005	0.005
1	0	0	0	0	0	0	0	0	0
1.05	0.02	0.013	0.01	0.008	0.007	0.006	0.005	0.004	0.004
1.1	0.074	0.049	0.037	0.029	0.025	0.021	0.018	0.016	0.015
1.15	0.152	0.101	0.076	0.061	0.051	0.043	0.038	0.034	0.03
1.2	0.249	0.166	0.125	0.1	0.083	0.071	0.062	0.055	0.05
1.25	0.36	0.24	0.18	0.144	0.12	0.103	0.09	0.08	0.072
1.3	0.48	0.32	0.24	0.192	0.16	0.137	0.12	0.107	0.096
1.35	0.607	0.405	0.304	0.243	0.202	0.173	0.152	0.135	0.121
1.4	0.738	0.492	0.369	0.295	0.246	0.211	0.185	0.164	0.148
1.45	0.872	0.581	0.436	0.349	0.291	0.249	0.218	0.194	0.174
1.5	1.007	0.671	0.503	0.403	0.336	0.288	0.252	0.224	0.201
1.55	1.141	0.761	0.571	0.457	0.38	0.326	0.285	0.254	0.228
1.6	1.275	0.85	0.637	0.51	0.425	0.364	0.319	0.283	0.255
1.65	1.407	0.938	0.703	0.563	0.469	0.402	0.352	0.313	0.281
1.7	1.537	1.024	0.768	0.615	0.512	0.439	0.384	0.341	0.307
1.75	1.664	1.109	0.832	0.666	0.555	0.475	0.416	0.37	0.333
1.8	1.788	1.192	0.894	0.715	0.596	0.511	0.447	0.397	0.358
1.85	1.909	1.273	0.955	0.764	0.636	0.546	0.477	0.424	0.382
1.9	2.027	1.351	1.014	0.811	0.676	0.579	0.507	0.45	0.405
1.95	2.142	1.428	1.071	0.857	0.714	0.612	0.535	0.476	0.428
2	2.253	1.502	1.127	0.901	0.751	0.644	0.563	0.501	0.451
2.05	2.361	1.574	1.181	0.944	0.787	0.675	0.59	0.525	0.472
2.1	2.466	1.644	1.233	0.986	0.822	0.704	0.616	0.548	0.493
2.15	2.567	1.711	1.283	1.027	0.856	0.733	0.642	0.57	0.513
2.2	2.665	1.776	1.332	1.066	0.888	0.761	0.666	0.592	0.533
2.25	2.759	1.84	1.38	1.104	0.92	0.788	0.69	0.613	0.552
2.3	2.851	1.901	1.425	1.14	0.95	0.815	0.713	0.634	0.57
2.35	2.939	1.96	1.47	1.176	0.98	0.84	0.735	0.653	0.588
2.4	3.025	2.017	1.512	1.21	1.008	0.864	0.756	0.672	0.605
2.45	3.107	2.072	1.554	1.243	1.036	0.888	0.777	0.691	0.621
2.5	3.187	2.125	1.594	1.275	1.062	0.911	0.797	0.708	0.637
2.55	3.264	2.176	1.632	1.306	1.088	0.933	0.816	0.725	0.653
2.6	3.338	2.226	1.669	1.335	1.113	0.954	0.835	0.742	0.668
2.65	3.41	2.274	1.705	1.364	1.137	0.974	0.853	0.758	0.682
2.7	3.48	2.32	1.74	1.392	1.16	0.994	0.87	0.773	0.696
2.75	3.547	2.364	1.773	1.419	1.182	1.013	0.887	0.788	0.709
2.8	3.611	2.408	1.806	1.445	1.204	1.032	0.903	0.803	0.722
2.85	3.674	2.449	1.837	1.469	1.225	1.05	0.918	0.816	0.735
2.9	3.734	2.489	1.867	1.494	1.245	1.067	0.934	0.83	0.747
2.95	3.792	2.528	1.896	1.517	1.264	1.084	0.948	0.843	0.758

APPENDIX K

MACH2 Test Results

Note: the plots shown illustrate the ELGG barrel section with a length of 1.0 meter, and a width measured from the axis center line to the wall, a distance of .015 meter. The proportions of the plots make it appear that the radius is nearly the same size as the length, which is not true. These plots are for illustration purposes only, and are not drawn to scale. The flow enters from the right and exits to the left of the plots shown.

(This appendix is referenced by chapter 3.8, page 63)

MACH2 test im2

```

Scontrol
twin = 50.0e-4,
ncycwfn = 100000,
dt = 1.0e-6,
dtmax = 9.0e-6,
imres = 9,
theo = 0.5.

eoson = .true.,
tzput = 0,

HydroN = .true.,
courmax = 2.0,
wrelax = 0.25,
itopt = 100,
eps = 1.0e-4,
conserv = 0.0,
rmvoirm = 0.8,
rof = 3.0e-8,
strength = .false.,
! dragfrac = 15.76,
! denyidl = 10,
! thmidif = .true.,
! tztol = 1.0e-3,
! fbdmt = 0.4,
! nthmax = 100,
meshon = .false.,
! nsmooth = 3,
multgrd = .false.,
! mgimax = 100,
! sloconv = 0.75,
! ncorpriv = 3,
! nvccmx = 1,
radiate = .false.,
ciron = .false.,
bdiff = .false.,
magon = .false.,
Send

Sezphys
eosmodig = 'tabular',
ang = 18.0,
swg = 39.94,
graig = 0.66867,
tcnmodig = 'constant',
etc0g = 100.0
posat0g = 3.66e-10,
fromellg = 67.4,
Send

Sezgeom
npres = 4,
pointx(1) = 0.0,
pointx(2) = 15.0e-3,
pointx(3) = 15.0e-3,
pointy(3) = 1.0,
pointx(4) = 0.0,
pointy(4) = 1.0,
nbtk = 1,
corners(1,1) = 4,3,2,1,
Send

Simmesh
name(5) = 'BARREL',
advcl = 0.0,
orthog = 0.0,
nigen = 0,
ntar = 0,
Send

! Block 1
icells(1) = 4,
jcells(1) = 8,
rot(1) = 28,
vi(1) = 0.0,
ui(1) = 0.0,
temp(1) = 0.0345,
gdv(1) = 0.0,
matname(1) = 'ar-mrc',
Send

! Block 1
gndbc(1,1) = 'normalgr',
hydbc(1,1) = 'flowthru',
prob(1,1) = 'continuity',
gndbc(2,1) = 'normalgr',
hydbc(2,1) = 'wall',
velbc(2,1) = 'no slip',
! therm(2,1) = 'conduct',
Send

gndbc(3,1) = 'normalgr',
hydbc(3,1) = 'flowthru',
velbc(3,1) = 'specified',
vflow(3,1) = 3000.0,
flow(3,1) = 0.0345,
roflow(3,1) = .28,
Send

gndbc(4,1) = 'nor.nalgr',
hydbc(4,1) = 'axis',
Send

Soutput
inty = 'edit..20',
ncyc0 = 50,
ncycp = 50,
ptscale = 'expand',
pmargin = 0.1,
ctrst = 1.0e-4,
contyp = 'log',
inbound = .false.,
ivenc = 2,
jvenc = 1,
plot(0) = 'fluid',
plot(4) = 'ion',
plot(14) = 'arker',
Send

```

$T = 1.000E-00$
 Cycle = 1
 Calculation Mesh
 1st X = 0.00E+00
 X INC = 2.00E-03
 1st Y = 0.00E+00
 Y INC = 2.00E-01

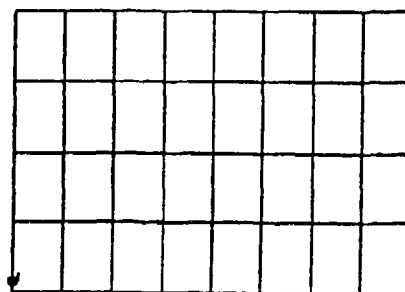


Figure K.1 MACH2 Calculation mesh Cycle 1 ($L=1.0m$ $r=.015m$)

$T = 1.000E-00$
 Cycle = 1
 Velocity
 MAX = 3.000E+03

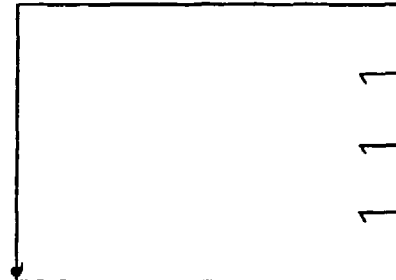


Figure K.2 MACH2 Velocity calculation Cycle 1 ($L=1.0m$ $r=.015m$)

$T = 1.000E-00$
 Cycle = 1
 Density
 $\rho = 2.8E-01$ $A=2.8E-01$
 $B=2.8E-01$ $C=2.8E-01$
 $D=2.8E-01$ $E=2.8E-01$
 $\pm=2.8E-01$

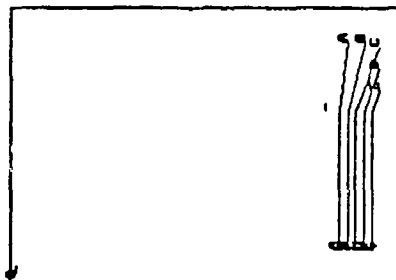


Figure K.3 MACH2 Density calculation Cycle 1 ($L=1.0m$ $r=.015m$)

$T = 1.000E-00$
 Cycle = 1
 Temperature
 $\gamma=3.5E-02$ $A=3.5E-02$
 $B=3.5E-02$ $C=3.5E-02$
 $D=3.5E-02$ $E=3.5E-02$
 $\pm=3.5E-02$

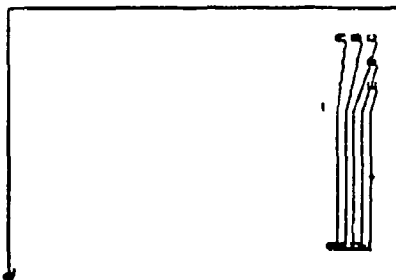


Figure K.4 MACH2 Temperature calculation Cycle 1 ($L=1.0m$ $r=.015m$)

$T = 1.000E-00$
 Cycle = 1
 Pressure
 $-=2.3E+04 \quad A=2.3E+04$
 $B=2.3E+04 \quad C=2.3E+04$
 $D=2.3E+04 \quad E=2.3E+04$
 $+ = 2.3E+04$

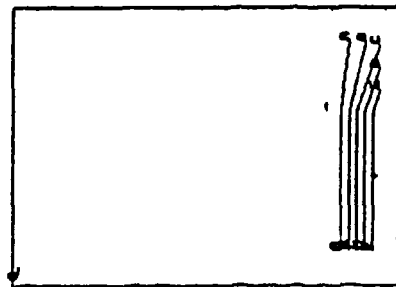


Figure K.5 MACH2 Pressure calculation Cycle 1 ($L=1.0m \ r=.015m$)

$T = 4.495E-04$
 Cycle = 5000
 Velocity
 MAX = 3.000E+03

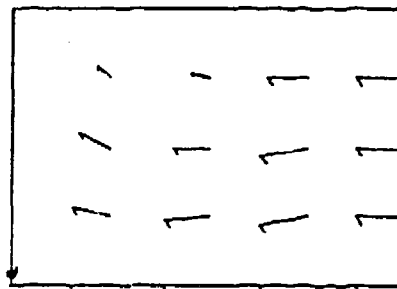


Figure K.6 MACH2 Velocity calculation Cycle 5000 ($L=1.0m \ r=.015m$)

$T = 4.495E-04$
 Cycle = 5000
 Density
 $-=2.5E-01 \quad A=3.2E-01$
 $B=4.0E-01 \quad C=5.1E-01$
 $D=6.4E-01 \quad E=8.1E-01$
 $+ = 1.0E+00$

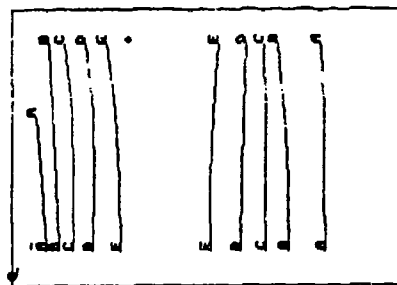


Figure K.7 MACH2 Density calculation Cycle 5000 ($L=1.0m \ r=.015m$)

$T = 4.495E-04$
 Cycle = 5000
 Temperature
 $-=3.4E-02 \quad A=4.1E-02$
 $B=4.9E-02 \quad C=5.9E-02$
 $D=7.1E-02 \quad E=8.6E-02$
 $+ = 1.0E-01$

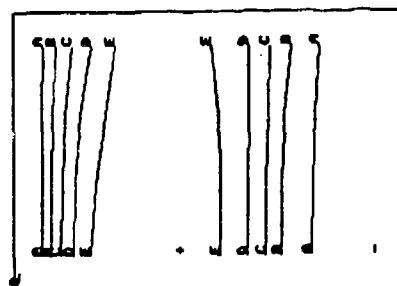


Figure K.8 MACH2 Temperature calculation Cycle 5000 ($L=1.0m \ r=.015m$)

$T = 1.000E-00$
 Cycle = 5000
 Pressure
 $-=2.3E+04 \quad A=3.4E+04$
 $B=5.0E+04 \quad C=7.4E+04$
 $D=1.1E+05 \quad E=1.6E+05$
 $+2.4E+05$

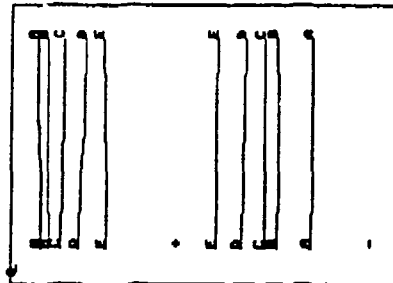


Figure K.9 MACH2 Pressure calculation Cycle 5000 ($L=1.0m \quad r=.015m$)

$T = 2.989E-03$
 Cycle = 33210
 Density
 $-=2.8E-01 \quad A=2.8E-01$
 $B=2.3E-01 \quad C=2.8E-01$
 $D=2.8E-01 \quad E=2.8E-01$
 $+2.8E-01$

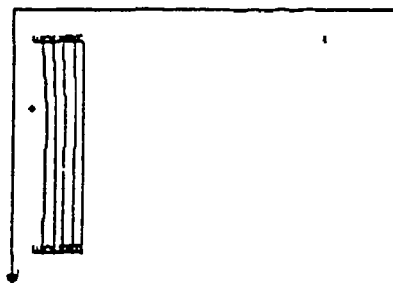


Figure K.10 MACH2 Density calculation Cycle 33210 ($L=1.0m \quad r=.015m$)

$T = 2.898E-03$
 Cycle = 33210
 Temperature
 $-=3.5E-02 \quad A=3.5E-02$
 $B=3.5E-02 \quad C=3.5E-02$
 $D=3.5E-02 \quad E=3.5E-02$
 $+3.5E-02$

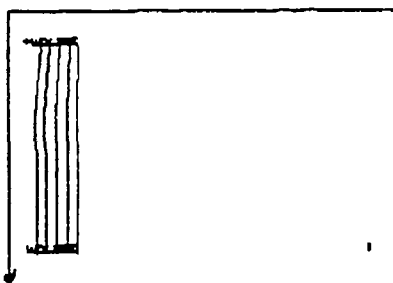


Figure K.11 MACH2 Temperature calculation Cycle 33210 ($L=1.0m \quad r=.015m$)

$T = 2.898E-03$
 Cycle = 33210
 Pressure
 $-=2.3E+04 \quad A=2.3E+04$
 $B=2.3E+04 \quad C=2.3E+04$
 $D=2.3E+04 \quad E=2.3E+04$
 $+2.3E+04$

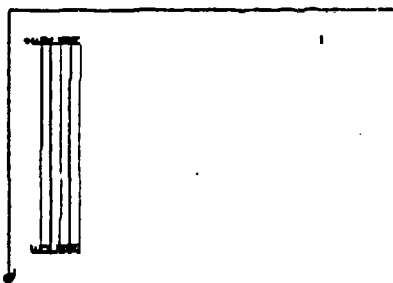


Figure K.12 MACH2 Pressure calculation Cycle 33210 ($L=1.0m \quad r=.015m$)

Figure K.13 MACH2 sample run data

APPENDIX L

MACH2 calculation results and charts

This appendix contains sample runs for two cases utilizing the full effects, with Planck radiation. The im2 used for each case precedes the plots which were produced. The first case is for inlet conditions of stagnation temperature 10,000K, stagnation pressure of 1,000 atmospheres, and inlet Mach number of 3.5. The second case is for inlet stagnation temperature of 23,000K, stagnation pressure of 1,000 atmospheres, and inlet Mach number of 3.5.

Note: the plots shown illustrate the ELGG barrel section with a length of 1.0 meter, and a width measured from the axis center line to the wall, a distance of .015 meter. The proportions of the plots make it appear that the radius is nearly the same size as the length, which is not true. These plots are for illustration purposes only, and are not drawn to scale. The flow enters from the right and exits to the left of the plots shown. Figure L.1 shows the calculation mesh and dimensions, and is representative for both cases

(This appendix is referenced by chapter 5, page 107 and chapter 6, page 113)

MACH2 im2 for full model using planck radiation

Inlet conditions:

$T_0 = 10,000\text{K}$

$V = 2,889 \text{ m/sec}$

$\rho = 4.273 \text{ kg/m}^{**3}$

```

!control
twin = 98.0e-4,
ncycm = 40000,
dt = 1.0e-7,
dmax = 9.0e-7,
imme = 9,
thetB = 0.5,
ecson = .true.,
tsplit = 0,
hydron = .true.,
courmax = 2.0,
wrelax = 0.25,
itopx = 100,
eps = 1.0e-4,
converg = 0.0,
rmvolm = 0.8,
rof = 3.0e-8,
strength = .true.,
dragfrac = 15.78,
denyld = 10,
thmidf = .true.,
toltol < 1.0e-3,
fiderr = 0.4,
ntrmax = 100,
meshon = .false.,
multgrid = .false.,
radiate = .true.,
ciron = .false.,
balff = .false.,
magon = .false.,
Send

!ezgeom
norts = 4
pointx(1) = 0.0,
pointy(1) = 0.0,
pointz(2) = 15.0e-3,
pointx(2) = 0.0,
pointz(3) = 15.0e-3,
pointy(3) = 1.0,
pointz(4) = 0.0,
pointy(4) = 1.0,
nblk = 1,
corners(1,1) = 4,3,2,1,
Send

!simrush
numeq(5) = 'BARREL',
eqv12 = 0.0,
orthog = 0.0,
ncon = 0,
nter = 0,
! Block 1
icells(1) = 10,
jcells(1) = 10
rox(1) = 4.273,
vx(1) = 0.0,
ux(1) = 0.0,
temp(1) = 705,
govt(1) = 0.0,
matname(1) = 'air-mrc',
radmod(1) = 'emission',
opacity(1) = 'opecp',
Send

!ezphys
esmodig = 'tabular',
ang = 18.0,
awg = 39.94
gmtg = 0.00067,
Send

!out
rotfrm(2,1) = 1.66,
gndbc(3,1) = 'normalg',
hydbc(3,1) = 'flowthru',
velbc(3,1) = 'specified',
vflow(3,1) = 2889.0,
tflow(3,1) = 705,
rflow(3,1) = 4.273,
Send

!output
intdy = 'edit5.50',
nycyc = 10000,
ncycp = 1000,
plotscale = 'expand',
pmargin = 0.1,
dtrst = 1.0e-4
contrp = 'log',
inbound = .false.,
irecanc = 2,
jrecanc = 1,
plot(0) = 'flow',
plot(4) = 'hor',
plot(14) = 'dark',
Send

```

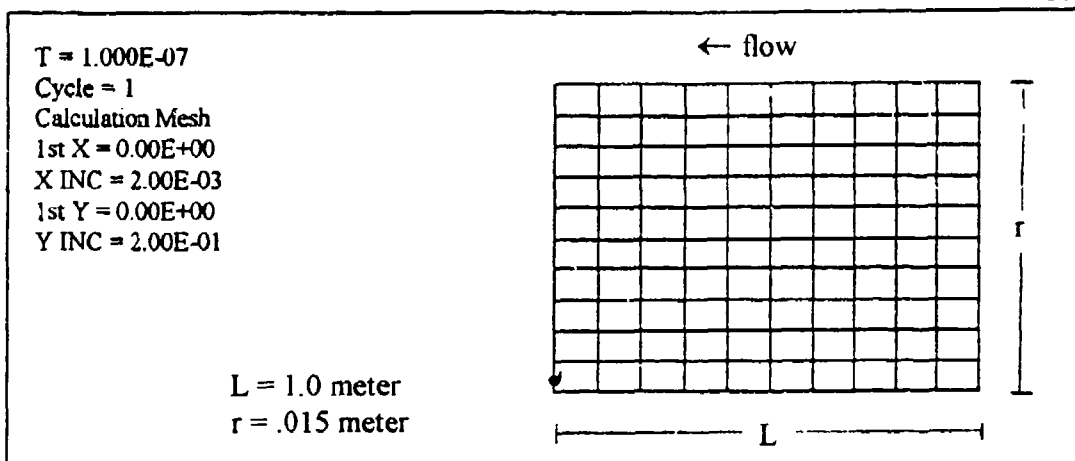
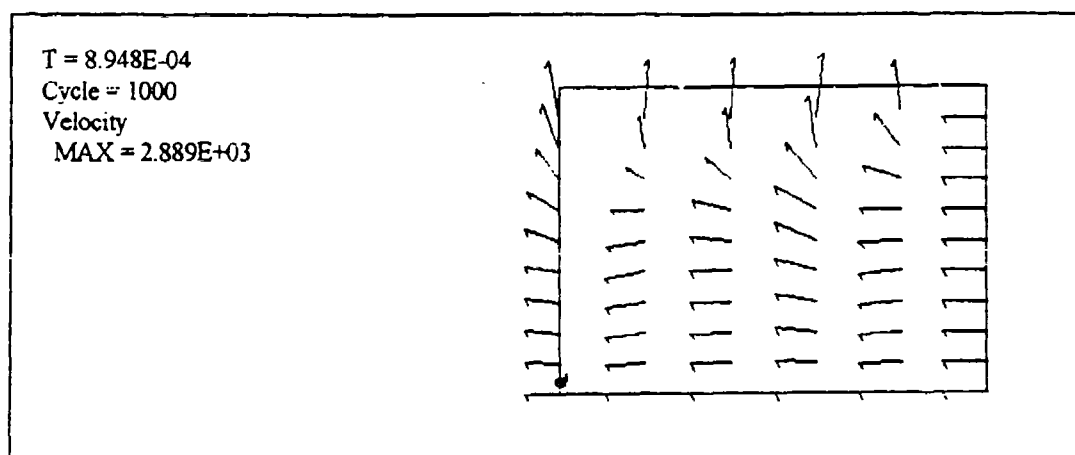
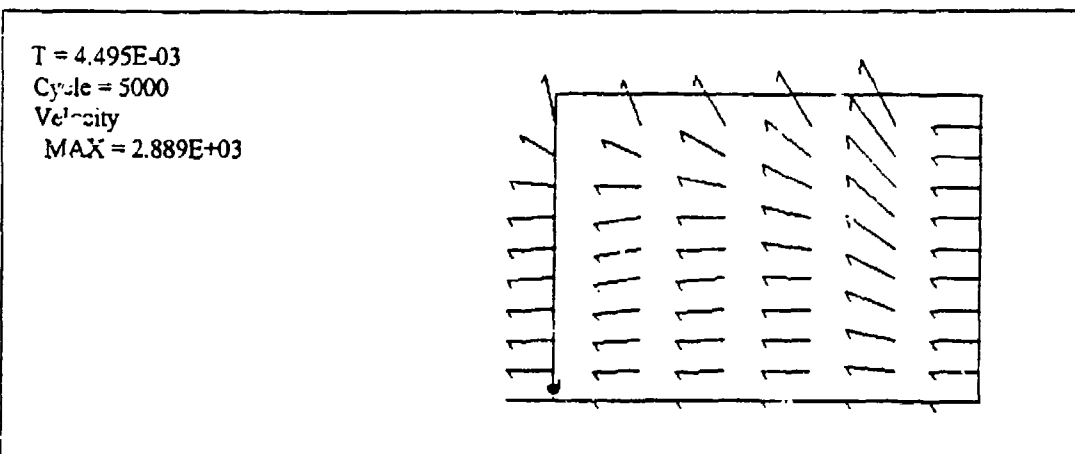


Figure L.1 Calculation mesh for MACH2 calculation (full model)

Figure L.2 MACH2 planck full model velocity Cycle 1000 ($T_o=10,000\text{K}$, $M=3.5$)Figure L.3 MACH2 planck full model velocity Cycle 5000 ($T_o=10,000\text{K}$, $M=3.5$)

$T = 9.800E-03$
 Cycle = 10895
 Velocity
 MAX = 2.889E+03

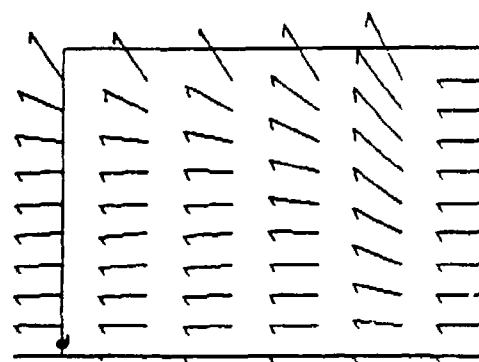


Figure L.4 MACH2 planck full model velocity Cycle 10895 ($T_0=10,000K$, $M=3.5$)

$T = 8.948E-04$
 Cycle = 1000
 ABS Vorticity
 $- = 1.4E+02$ $A=2.9E+05$
 $B=5.8E+05$ $C=8.6E+05$
 $D=1.2E+06$ $E=1.4E+06$
 $+ = 1.7E+06$

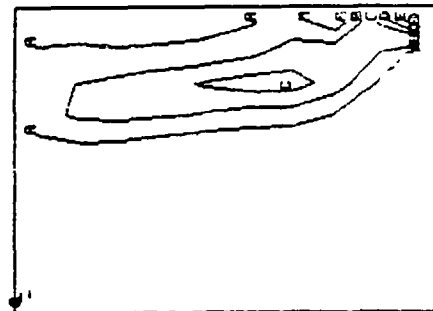


Figure L.5 MACH2 planck full model vorticity Cycle 1000 ($T_0=10,000K$, $M=3.5$)

$T = 4.495E-03$
 Cycle = 5000
 ABS Vorticity
 $- = 1.7E+02$ $A=2.9E+05$
 $B=5.8E+05$ $C=8.7E+05$
 $D=1.2E+06$ $E=1.5E+06$
 $+ = 1.7E+06$

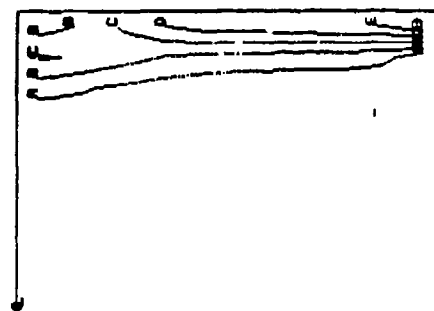


Figure L.6 MACH2 planck full model vorticity Cycle 5000 ($T_0=10,000K$, $M=3.5$)

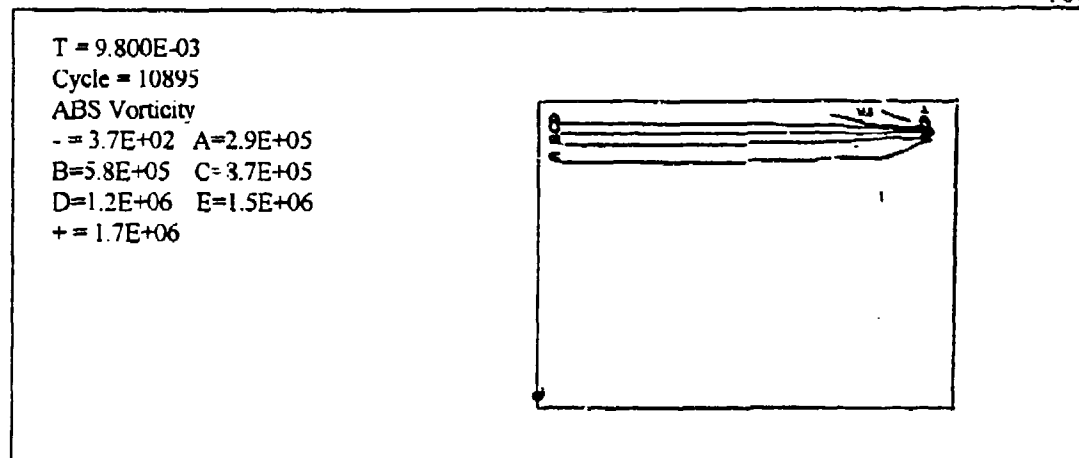


Figure L.7 MACH2 planck full model **vorticity** Cycle 10895 ($T_o=10,000K$, $M=3.5$)

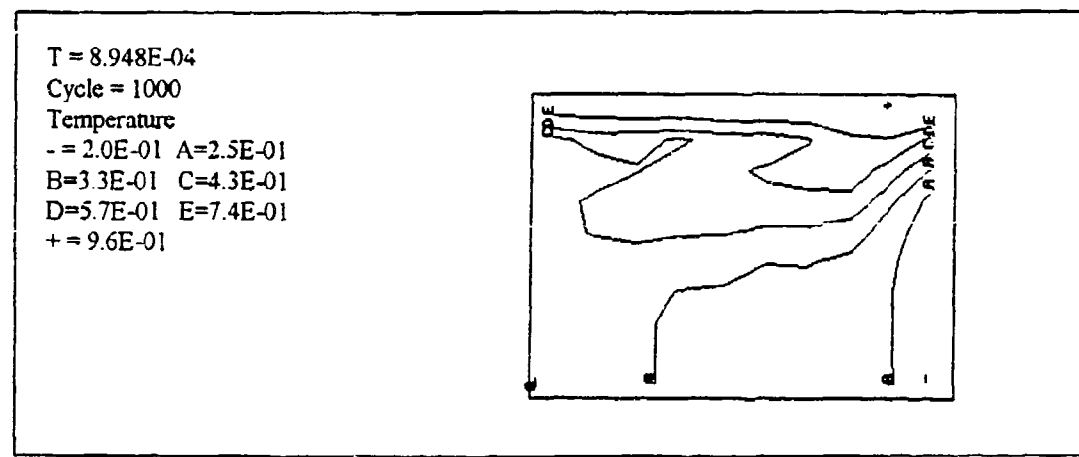


Figure L.8 MACH2 planck full model **temperature** Cycle 1000 ($T_o=10,000K$, $M=3.5$)

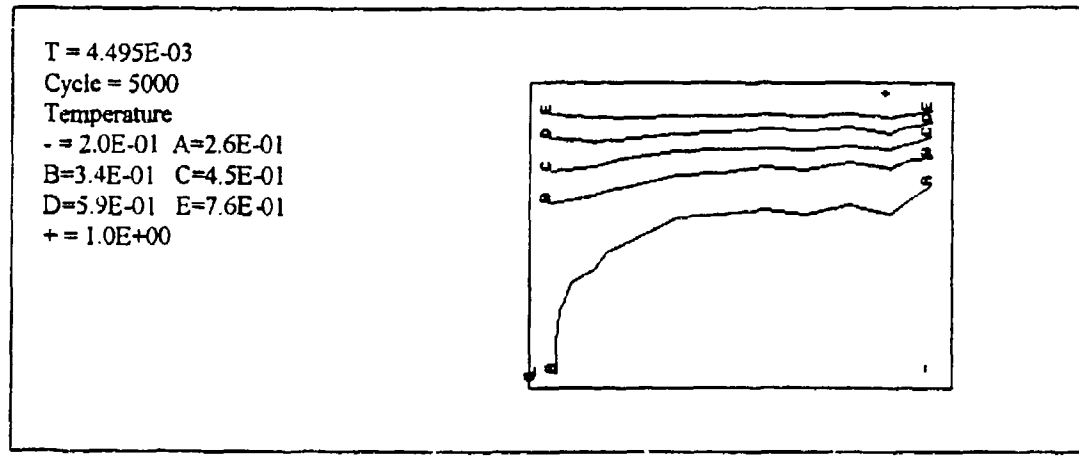


Figure L.9 MACH2 planck full model **temperature** Cycle 5000 ($T_o=10,000K$, $M=3.5$)

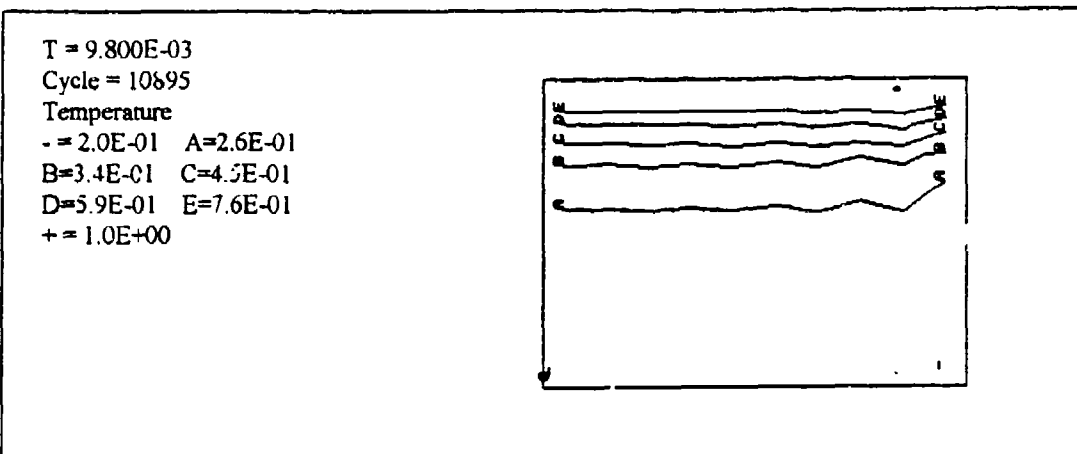


Figure L.10 MACH2 planck full model temperature Cycle 10895 ($T_o=10,000K$, $M=3.5$)

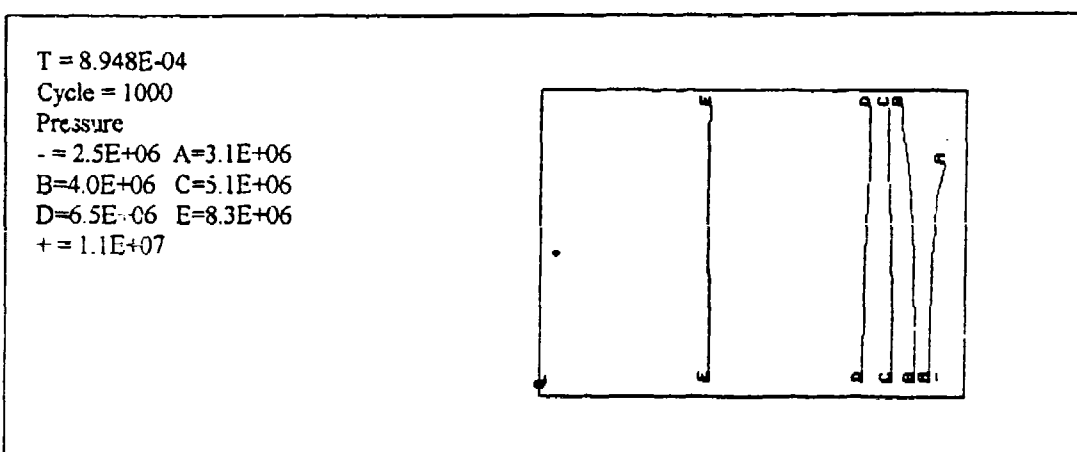


Figure L.11 MACH2 planck full model Pressure Cycle 1000 ($T_o=10,000K$, $M=3.5$)

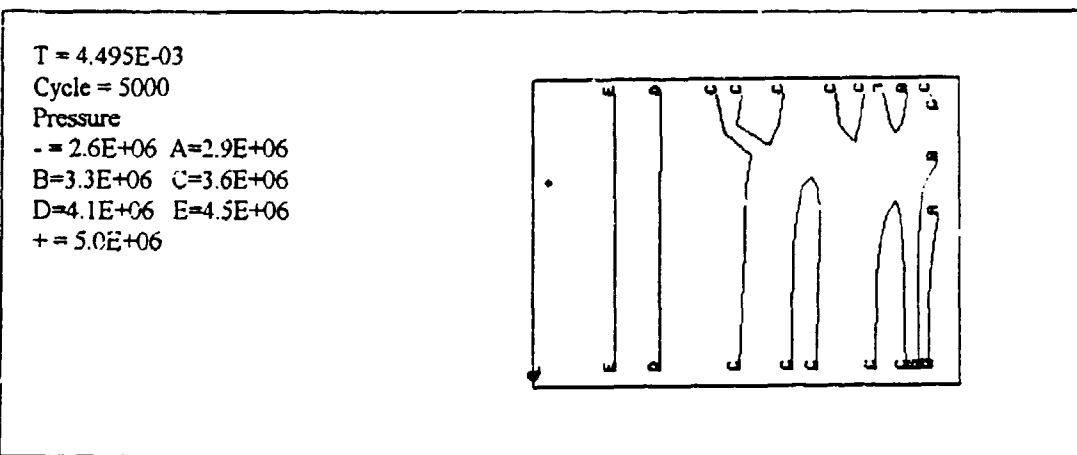


Figure L.12 MACH2 planck full model Pressure Cycle 5000 ($T_o=10,000K$, $M=3.5$)

$T = 9.800E-03$
 Cycle = 10895
 Pressure
 $- = 2.6E+06 \quad A=2.8E+06$
 $B=3.0E+06 \quad C=3.2E+06$
 $D=3.4E+06 \quad E=3.7E+06$
 $+ = 3.9E+06$

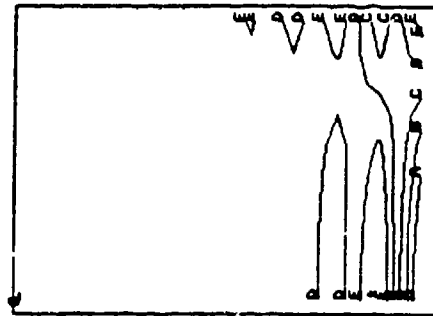


Figure L.13 MACH2 planck full model **pressure** Cycle 10895 ($T_o=10,000K$, $M=3.5$)

$T = 8.948E-04$
 Cycle = 1000
 Density
 $- = 1.3E+00 \quad A=1.7E+00$
 $B=2.3E+00 \quad C=3.1E+00$
 $D=4.2E+00 \quad E=5.8E+00$
 $+ = 7.8E+00$

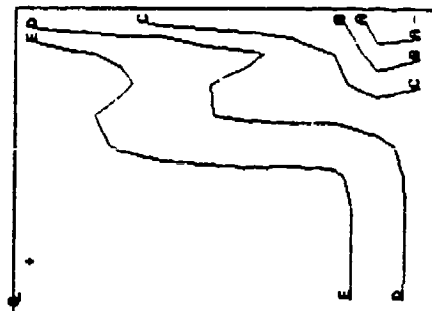


Figure L.14 MACH2 planck full model **density** Cycle 1000 ($T_o=10,000K$, $M=3.5$)

$T = 4.495E-03$
 Cycle = 5000
 Density
 $- = 1.3E+00 \quad A=1.7E+00$
 $B=2.3E+00 \quad C=3.1E+00$
 $D=4.2E+00 \quad E=5.8E+00$
 $+ = 7.8E+00$

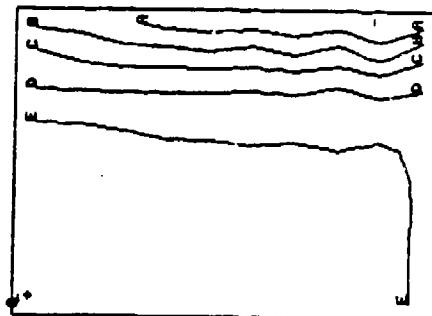


Figure L.15 MACH2 planck full model **density** Cycle 5000 ($T_o=10,000K$, $M=3.5$)

T = 9.800E-03
Cycle = 10895
Density
- = 1.3E+00 A=1.7E+00
B=2.2E+00 C=2.9E+00
D=3.9E+00 E=5.1E+00
+ = 6.8E+00

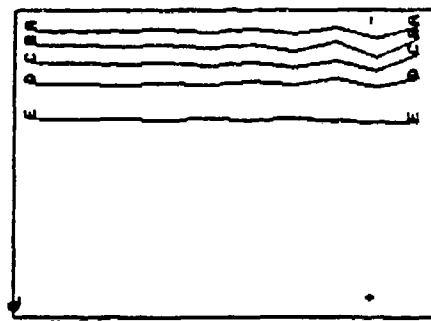


Figure L.16 MACH2 planck full model density Cycle 10895 ($T_o=10,000K$, $M=3.5$)

MACH2 im2 for full model using planck radiation

Inlet conditions:

$T_0 = 23,000\text{K}$

$V = 4,381 \text{ m/sec}$

$\rho = 1.858 \text{ kg/m}^{**3}$

```

Scontrol
twth = 98.0e-4.
ncyowl = 40000.
dt = 1.0e-7.
dtmax = 9.0e-7.
imms = 9.
tstab = 0.5.

coson = true..
lsplit = 0.

hydron = true..
courmax = 2.0.
wrelax = 0.25.
itopt = 100.
eps = 1.0e-4.
conserv = 0.0.
rmvalrm = 0.8.
rlf = 3.0e-8.

strength = true..
dragrec = 15.76.
denyld = 10.

thmidif = true..
tdtol = 1.0e-3.
fbfrm = 0.4.
nchrmmax = 100.

meshon = false..
mugrd = false..
radiate = true..
caron = false..
bdrt = false..
magon = false..
Send

Sezgeom
rptrns = 4.
poinbx(1) = 0.0.
poinby(1) = 0.0.
poinbx(2) = 15.0e-3.
poinby(2) = 0.0.
poinbx(3) = 15.0e-3.
poinby(3) = 1.0.
poinbx(4) = 0.0.
poinby(4) = 1.0.
nbil = 1.
corners(1,1) = 4.3.2.1.
Send

Simmesh
name(5) = 'BARREL'.
equiv = 0.0.
orthog = 0.0.
rpen = 0.
nter = 0.

! Block 1
icells(1) = 10.
jcells(1) = 10.
rcx(1) = 1.858.
vtx(1) = 0.0.
ux(1) = 0.0.
temp(1) = 300.
pdvtx(1) = 0.0
mainame(1) = 'air-mrc'.
radname(1) = 'emission'.
opacity(1) = 'opsec.

Sezphys
semodig = 'tabular'.
ang = 18.0.
avg = 38.94.
gm1g = 0.00007.

prndbc(1,1) = 'normalgr'.
hydbc(1,1) = 'flowin'.
prob(1,1) = 'continut'.

prndbc(2,1) = 'normalgr'.
hydbc(2,1) = 'wall'.
velbc(2,1) = 'no slip'.
thmbc(2,1) = 'conduct'.
tethrm(2,1) = 300.0.

```

T = 8.947E-04
Cycle = 1000
Velocity
MAX = 4.381E+03

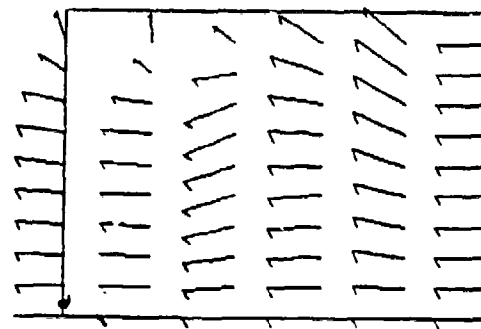


Figure L.17 MACH2 planck full model velocity Cycle 1000 ($T_e=23,000\text{K}$, $M=3.5$)

T = 4.495E-07
Cycle = 5000
Velocity
MAX = 4.381E+03

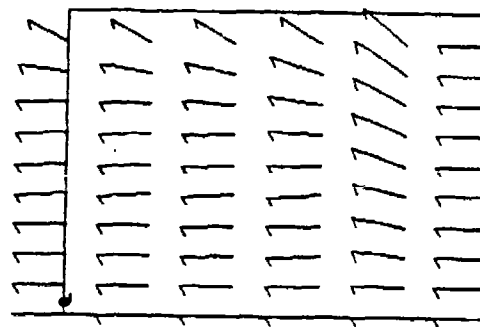


Figure L.18 MACH2 planck full model velocity Cycle 5000 ($T_o=23,000K$, $M=3.5$)

T = 9.800E-03
Cycle = 10895
Velocity
MAX = 4.381E+03

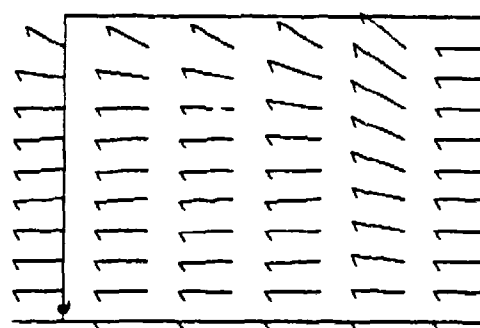


Figure L.19 MACH2 planck full model velocity $C_{s,1} \cdot 10^{-5}$ ($T_e=23,000\text{K}$, $M=3.5$)

$T = 8.947E-04$
 Cycle = 1000
 ABS Vorticity
 $\rightarrow 1.3E+02 A=4.5E+05$
 $B=9.1E+05 C=1.4E+06$
 $D=1.8E+06 E=2.3E+06$
 $\leftarrow 2.7E+06$

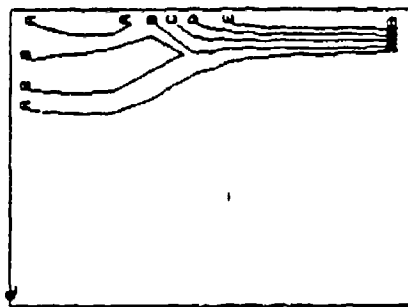


Figure L.20 MACH2 planck full model vorticity Cycle 1000 ($T_o=23,000K, M=3.5$)

$T = 4.495E-03$
 Cycle = 5000
 ABS Vorticity
 $\rightarrow 1.8E+02 A=4.5E+05$
 $B=9.1E+05 C=1.4E+06$
 $D=1.8E+06 E=2.3E+06$
 $\leftarrow 2.7E+06$

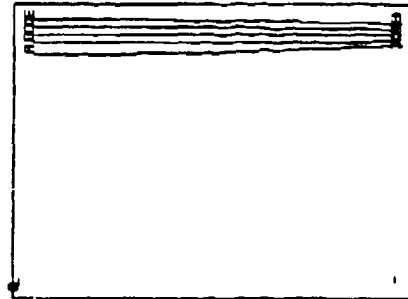


Figure L.21 MACH2 planck full model vorticity Cycle 5000 ($T_o=23,000K, M=3.5$)

$T = 9.800E-03$
 Cycle = 10895
 ABS Vorticity
 $\rightarrow 1.8E+02 A=4.5E+05$
 $B=9.1E+05 C=1.4E+06$
 $D=1.8E+06 E=2.3E+06$
 $\leftarrow 2.7E+06$

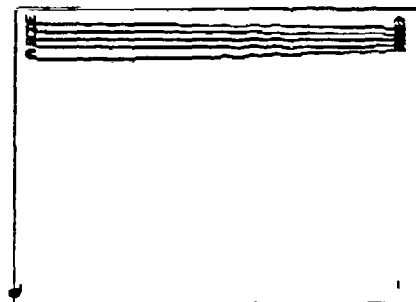


Figure L.22 MACH2 planck full model vorticity Cycle 10895 ($T_o=23,000K, M=3.5$)

$T = 8.947E-04$
 Cycle = 1000
 Temperature
 $\rightarrow 4.2E-01 A=4.9E-01$
 $B=5.7E-01 C=6.6E-01$
 $D=7.7E-01 E=9.0E-01$
 $\leftarrow 1.1E+00$

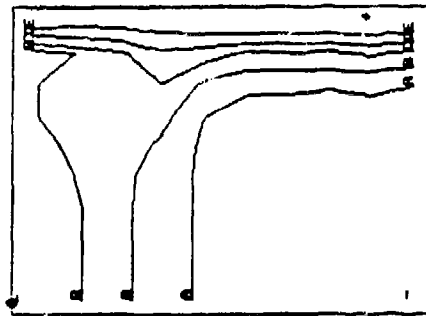


Figure L.23 MACH2 planck full model temperature Cycle 1000 ($T_o=23,000K$, $M=3.5$)

$T = 4.495E-03$
 Cycle = 5000
 Temperature
 $\rightarrow 4.2E-01 A=4.9E-01$
 $B=5.7E-01 C=6.6E-01$
 $D=7.7E-01 E=9.0E-01$
 $\leftarrow 1.1E+00$

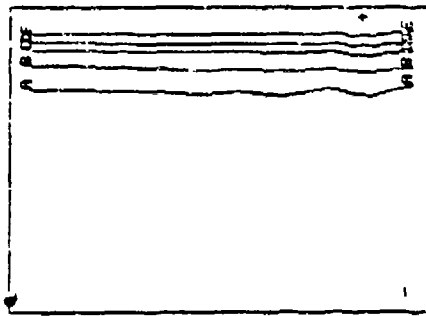


Figure L.24 MACH2 planck full model temperature Cycle 5000 ($T_o=23,000K$, $M=3.5$)

$T = 9.800E-03$
 Cycle = 10895
 Temperature
 $\rightarrow 4.2E-01 A=4.9E-01$
 $B=5.7E-01 C=6.6E-01$
 $D=7.7E-01 E=9.0E-01$
 $\leftarrow 1.1E+00$

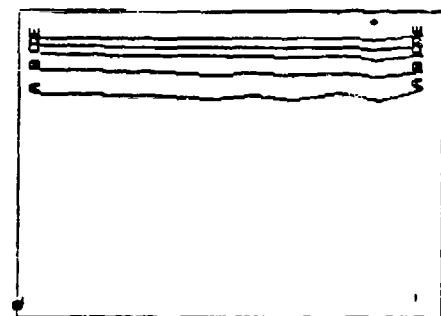


Figure L.25 MACH2 planck full model temperature Cycle 10895 ($T_o=23,000K$, $M=3.5$)

$T = 8.947E-04$
 Cycle = 1000
 Pressure
 $A=2.4E+06$
 $B=2.8E+06$
 $C=3.2E+06$
 $D=3.6E+06$
 $E=4.2E+06$
 $F=4.8E+06$

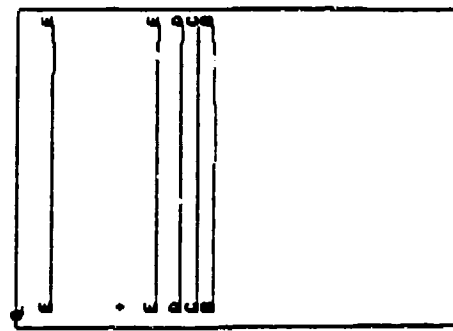


Figure L.26 MACH2 planck full model pressure Cycle 1000 ($T_o=23,000K$, $M=3.5$)

$T = 4.495E-03$
 Cycle = 5000
 Pressure
 $A=2.2E+06$
 $B=2.3E+06$
 $C=2.3E+06$
 $D=2.4E+06$
 $E=2.5E+06$
 $F=2.6E+06$

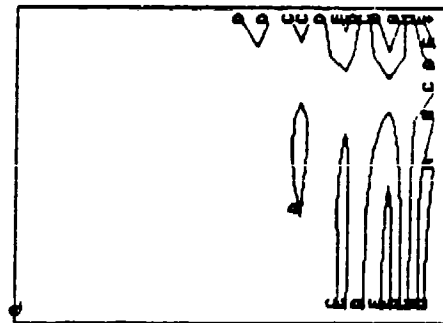


Figure L.27 MACH2 planck full model pressure Cycle 5000 ($T_o=23,000K$, $M=3.5$)

$T = 9.300E-03$
 Cycle = 10895
 Pressure
 $A=2.2E+06$
 $B=2.3E+06$
 $C=2.3E+06$
 $D=2.4E+06$
 $E=2.5E+06$
 $F=2.6E+06$

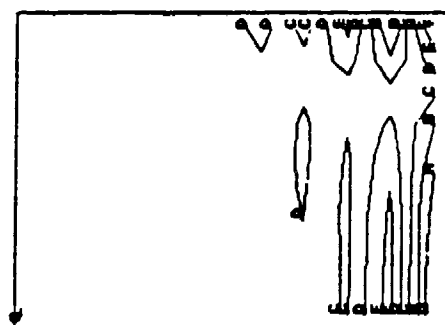


Figure L.28 MACH2 planck full model pressure Cycle 10895 ($T_o=23,000K$, $M=3.5$)

$T = 8.947E-04$
 Cycle = 1000
 Density
 $\rightarrow 8.3E-01 A=1.0E+00$
 $B=1.3E+00 C=1.7E+00$
 $D=2.1E+00 E=2.7E+00$
 $F=-3.4E+00$

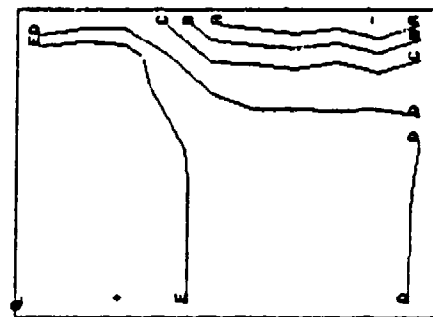


Figure L.29 MACH2 planck full model density Cycle 1000 ($T_o=23,000K$, $M=3.5$)

$T = 4.495E-03$
 Cycle = 5000
 Density
 $\rightarrow 8.2E-01 A=9.8E-01$
 $B=1.2E+00 C=1.4E+00$
 $D=1.6E+00 E=2.0E+00$
 $F=2.3E+00$

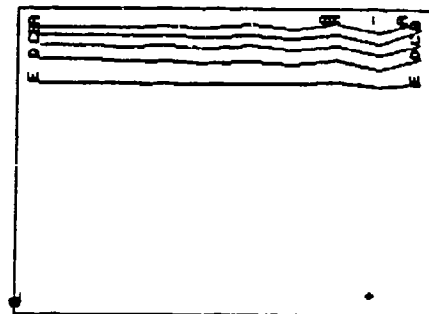


Figure L.30 MACH2 planck full model density Cycle 5000 ($T_o=23,000K$, $M=3.5$)

$T = 9.800E-03$
 Cycle = 10895
 Density
 $\rightarrow 8.2E-01 A=9.8E-01$
 $B=1.2E+00 C=1.4E+00$
 $D=1.6E+00 E=2.0E+00$
 $F=2.3E+00$

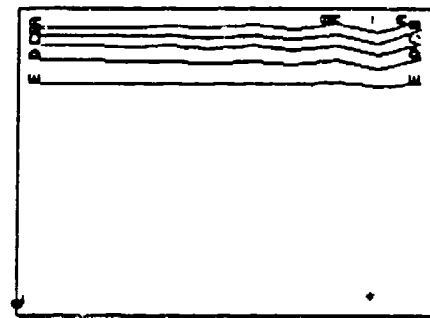


Figure L.31 MACH2 planck full model density Cycle 10895 ($T_o=23,000K$, $M=3.5$)

LIST OF REFERENCES

1. Juhasz, A. A., Jamison, K., White, K., and Wren, G., "Introduction to Electrothermal Gun Propulsion", 26th JANNAF Combustion Subcommittee Meeting, Vol. III, 23-27 October 1989.
2. Rutberg, F. G., "The Branch of All-Union Research Institute for Electrical Machinery", The Branch of VNIIElectromash Leningrad.
3. Tidman, Derek A., and Massey, Dennis W., "Electrothermal Light Gas Gun", IEEE Transactions on Magnetics, Vol. 29, NO. 1, Jan 1993.
4. King, Merril K., "Cycle Analysis Studies of Candidate Formulations for Electrothermal Guns", 26th JANNAF Combustion Subcommittee Meeting, Vol. III, 23-27 October 1989.
5. Chryssomallis, G. S., Marinos, C. D., Ricci, R. S., and Cook, D. C., "Combustion Augmented Plasma Gun", 25th JANNAF Combustion Subcommittee Meeting, Vol. III, October 1988.
6. Bunte, Steven, W., and Beyer, Richard A., "Temperature Measurements of ET Plasmas", 26th JANNAF Combustion Subcommittee Meeting, Vol. III, 23-27 October 1989.
7. Juhasz, Arpad A., "Activities in Electrothermal Gun Propulsion", 26th JANNAF Combustion Subcommittee Meeting, Vol. III, 23-27 October 1989.
8. Oberle, William, "A Feasibility Study of Power Curve - Working Fluid Combinations for Optimal ET Gun Performance", 25th JANNAF Combustion Subcommittee Meeting, Vol. III, October 1988.

9. Turchi, Peter J., "Design of a Gigawatt-Level Quasi-Steady Flow Facility for Advanced Space Exploration Research", AIAA/NASA/OAI Conference on Advanced SEI Technologies, September 4-6, 1991.
10. Kippenhahn, R., and Weigert, A., "Stellar Structure and Evolution", Springer-Verlag Berlin Heidelberg New York, 1990.
11. Anderson, John D., "Modern Compressible Flow, with historical perspective", McGraw-Hill Publishing Co., New York.
12. Cambel, Ali Bulent, and Jennings, Burgess, H., "Gas Dynamics", McGraw-Hill Book Company, New York, 1958.
13. Eckert, E. R. G., "Heat and Mass Transfer", McGraw-Hill Book Company, Inc., New York, 1963.
14. Gully, J. H., Spann, M. L., and Pratap, S. B., "Power Systems for Electrothermal Guns", 26th JANNAF Combustion Subcommittee Meeting, Vol. III, 23-27 October 1989.
15. Bunte, Steven W., and Oberle, William F., "An Analysis of the Thermochemical Performance of Various Working Fluids for an Electrothermal Gun", 25th JANNAF Combustion Subcommittee Meeting, Vol. III, October 1988.
16. Grieg, J. R., Goldstein, S. A., Tidman, D. A., and Massey, D. W., "Principles and Practice of Electrothermal Guns", 25th JANNAF Combustion Subcommittee Meeting, Vol. III, October 1988.
17. Tenenbaum, Samuel B., "Plasma Physics", McGraw-Hill Company, New York, pp. 347-349, 1967.
18. Sturrock, Peter A., "Physics of the Sun, Volume 1: The Solar Interior", D. Reidel Publishing Company, Dordrecht, 1986.
19. Vincenti, Walter G., and Kruger, Charles H., Jr., "Introduction to Physical Gas Dynamics", Robert E. Krieger Publishing Company, Malabar, FL., 1965.
20. Siegel, A. E., Piacesi, R. and Bixler, D. N., "Wall Friction, Heat Transfer and Real-Gas Propellant Effects on High Speed Guns", U. S. Naval Ordnance Laboratory, White Oaks Silver Springs, Maryland.

21. Seigel, Arnold E., Theory of High-Muzzle-Velocity Guns, Progress in Astronautics and Aeronautics, Vol 66, 1979.
22. Loh, W.H.T., Modern Developments in Gas Dynamics, Plenum Press, New York, 1969.
23. Hellund, E. J., The Plasma State, Reinhold Publishing Corp., New York, 1961.
24. Benedict, Robert P., P.E., Fundamentals of Gas Dynamics, John Wiley & Sons, Inc., New York, 1983.
25. Huddlestone, Richard H., and Leonard, Stanley L., Plasma Diagnostic Techniques, Academic Press, New York, 1965.
26. John, James E. A., Gas Dynamics, Allyn and Bacon, Inc., Boston, 1969.
27. Zel'dovich, Ya. B., and Raizer, Yu. P, Physics of Shock Waves and High-Temperature Hydrodynamic Phenomena, edited by Hayes, Wallace D., and Probstein, Ronald F., Academic Press, New York, 1966.
28. Lehr, F. M., Degnan, J.H., Dietz, D., Englert, S. E., Hussey, T. W., Kiuttu, G. F., Messerschmitt, J. M., Mullins, B. W., Outten, C. A., Peterkin, R. E., Roderick, N. F., and Turchi, P. J., Progress in the Formation of a High Density Working Fluid for Solid Liner Implosions, High Energy Plasma Physics Division, Phillips Laboratory, Kirtland A.F.B., NM.
29. Hussey, T. W., Beason, J. D., Bell, D. E., Dietz, D., Douglas, M. R., Marklin, G. F., Peterkin, R. E., Roderick, N. F., and Turchi, P. J., Theoretical Modeling of Pulsed-Power Driven Flux Compression Systems at the Phillips Laboratory, Phillips Laboratory, High Energy Plasma Division, Kirtland A.F.B., NM, 1993.
30. Lehr, F. M., Alaniz, A., Beason, J. D., Carswell, L. C., Degnan, J. H., Crawford, J. F., Englert, S. E., Gahl, J. M., Holmes, T. W., Hussey, T. W., Kiuttu, G. F., Mullins, B. W., Peterkin, R. E., Roderick, N. F., Jr., and Turchi, P. J., Formation of Plasma Working Fluids for Compression by Liner Implosions, Maxwell Laboratories, Inc. Albuquerque, NM, June 2, 1993.
31. Hawke, R. S., Design and Analysis of Isentropic Compression Experiments, Lawrence Livermore Laboratory, University of California, Livermore, CA.
32. Megagauss Physics and Technology, edited by Turchi, Peter J., Plenum Press, New York, 1980.

33. Hewkin, Derrick, and Figura, Edward, "Fundamental Research and Numerical Modeling of the Internal Ballistics of Electrothermal Chemical Guns", IEEE Transactions on Magnetics, Vol. 29, No. 1, Jan 1993.
34. Loeb, A., and Kaplan, Z., "A Theoretical Model for the Physical Process in the Confined high Pressure Discharges of Electrothermal Launchers", IEEE Transactions on Magnetics, Vol. 25, No. 1, Jan 1989.
35. Campo, Antonio, "Development of the Thermal Boundary Layer at the Inlet of a Circular Pipe, and Comparison with Leveque Solution", International Journal of Heat and Fluid Flow, Vol. 11, No. 1., March 1990.
36. Myong, Hyon Kook, "Numerical Investigation of Fully Developed Turbulent Fluid Flow and Heat Transfer in a Square Duct", International Journal of Heat and Fluid Flow, Vol. 12, No. 4, December 1991.
37. Yang, G. and Ebadian, M. A., "Thermal Radiation and Laminar Forced Convection in the Entrance Region of a Pipe with Axial Conduction and Radiation", International Journal of Heat and Fluid Flow, Vol. 12, No. 3, September 1991.
38. Tsai, J. R., and Ozisik, M. N., "Radiation and Laminar Forced Convection of Non-Newtonian Fluid in a Circular Tube", International Journal of Heat and Fluid Flow, Vol. 10, No. 4, December 1989.
39. Chapman, Sydney, and Cowling, T. G., "The Mathematical Theory of Non-Uniform Gases", Cambridge University Press, Cambridge, 1990.
40. Chisholm, D., "The Heat Pipe", Mills & Boon Limited, London, 1971.
41. Fung, Y. C., "A First Course in Continuum Mechanics", Second Edition, Prentice-Hall, Inc. Englewood Cliffs, New Jersey, 1977.
42. Chen, Francis F., "Introductory to Plasma Physics and Controlled Fusion", Second Edition, Volume 1, Plasma Physics, Plenum Press, New York, 1984.
43. Eshbach, Ovid W., and Souders, Mott, "Handbook of Engineering Fundamentals", Third Edition, John Wiley & Sons, New York, 1975
44. Kreith, Frank, and Bohn, Mark S., "Principles of Heat Transfer", Harper Collins Publishers, 1986.
45. Kreyszig, Erwin, "Advanced Engineering Mathematics", Seventh Edition, John Wiley & Sons, Inc., New York, 1993.

46. Gough, P. S., "Numerical Simulation of Electrothermal Gun Interior Ballistics", 27th JANNAF Combustion Subcommittee Meeting, Vol. 1, 5-9 November 1990.
47. Morrison, W. F., Wren, G. P., Oberle, W. F., and Richardson, S. L., "The Application of Lagrange and Pidduck-Kent Gradient Models to Guns using Low Molecular Weight Gasses", 27th JANNAF Combustion Subcommittee Meeting, Vol. 1, 5-9 November 1990.
48. Chen, J. L., Kuo, K. K., and Cheung, F. B., "Theoretical Modeling of the Ballistic Process in an Electrothermal Gun", 27th JANNAF Combustion Subcommittee Meeting, Vol. 1, 5-9 November 1990.
49. Kashiwa, B. A., Padial, N. T., and Butler, T. D., "Toward a Comprehensive for Electrothermal Gun Performance", 27th JANNAF Combustion Subcommittee Meeting, Vol. 1, 5-9 November 1990.
50. "Electromagnetic/Electrothermal Gun Technology Development", Final Report of the Army Science Board (ASB) Panel, Department of the Army, 10 December 1990.
51. Morrison, W. F., Wren, G. P., Oberle, W. F., and Richardson, S. L., "The Application of Lagrange and Pidduck-Kent Gradient Models to Guns Using Low Molecular Weight Gasses", Army Research Laboratory, ARL-TR-48, Feb. 1993.
52. Gough, Paul S., "The XNOVAKTC Code", U. S. Army Laboratory Command, Contractor Report BRL-CR-627, February 1990.
53. Grieg, J. R., Goldstein, S. A., and Massey, D., "Electrothermal Gun Experiments at 20mm and 30 mm", 26th JANNAF Combustion Subcommittee Meeting, Vol. III, 23-27 October 1989.
54. Oberle, W. F., and White, K. J., "A BRL Assessment of the Status of Electrothermal Gun Propulsion", 26th JANNAF Combustion Subcommittee Meeting, Vol. III, 23-27 October 1989.
55. Wren, G. P., and Oberle, W. F., "Theoretical Estimate of Bore Surface Temperature in Electrothermal Guns", 26th JANNAF Combustion Subcommittee Meeting, Vol. III, 23-27 October 1989.
56. Gough, P. S., "Modeling the Effect of Charge Containment on Tube Wall Boundary Layer Development", 26th JANNAF Combustion Subcommittee Meeting, Vol. III, 23-27 October 1989.

57. White, K. J., and Oberle, W. F., "The Effect of Condensed Phase Combustion Products on Ballistic Performance", 26th JANNAF Combustion Subcommittee Meeting, Vol. III, 23-27 October 1989.
58. Gough, P. S., "Influence on Interior Ballistics of Electrothermal Gun of Rate of Mixing of Plasma with Working Fluid", 26th JANNAF Combustion Subcommittee Meeting, Vol. III, 23-27 October 1989.
59. Marinos, C. D., Pfenning, T. M., Dick, W. G., and Chryssomallis, G. S., "X-Ray Radiography Study of the Interaction Between a Plasma Jet and the Working Fluid of a Combustion Augmented Plasma Gun", 26th JANNAF Combustion Subcommittee Meeting, Vol. III, 23-27 October 1989.
60. Oberle, William, and Jamison, Keith, "A System Perspective on Electrothermal Guns", 25th JANNAF Combustion Subcommittee Meeting, Vol. III, October 1988.
61. Magee, Norman H., Jr., "New Opacity Library and SESAME Opacity Data", Los Alamos National Laboratory, Los Alamos, NM, March 30, 1993.
62. "I-4 handbook of Material Properties Data Bases", Vol. Ic: Equations of State, Los Alamos National Laboratory, November 1984.
63. Raznjevic, Kuzman, "Handbook of Thermodynamic Tables and Charts", Hemisphere Publishing Corporation, 1976.
64. Lund, C. M., "XSN LTE Equations", Los Alamos National Laboratory, June 30, 1992.
65. Hendricks, Robert C., Baron Anne K., and Pelier, Ildiko C., "GASP - A Computer Code for Calculating the Thermodynamic and Transport Properties for Ten Fluids: Parahydrogen, Helium, Neon, Methane, Nitrogen, Carbon Monoxide, Oxygen, Fluorine, Argon, and Carbon Dioxide", National Aerodynamics and Space Administration, Washington D. C., February 1975.
66. Gerber, Nathan, and Bundy, Mark L., "Heating of a Tank Gun Barrel: Numerical Study", U. S. Army Laboratory Command, August 1991.
67. Ambrazevicius, A., and Zukauskas, A., Valatkevicius, P., and Kezelis, R., "Plasma Heat Transfer During Turbulent Gas Flow in the Entrance Region of a Circular Tube", AIAA ASME 1974, Thermophysics and Heat Transfer Conference, Boston, Massachusetts, July 15-17, 1974.

68. Bond, John W., Jr., Watson, Kenneth M., and Welch, Jasper A., Jr., "Atomic Theory of Gas Dynamics", Addison, Wesley, Reading Massachusetts, 1965.
69. Allen, C. W., "Astrophysical Quantities", The Athone Press, University of London, 1955.
70. Taylor, Maynard, F., "Correlation of Local Heat-Transfer Coefficients for Single-Phase Turbulent Flow of Hydrogen in Tubes with Temperature Ratios to 23", Lewis Research Center, Cleveland, Ohio, January 1968.
71. Huebner, W. F., Merts, A. L., Magee, N. H., Jr., and Argo, M. F., "Astrophysical Opacity Library", Los Alamos Scientific Laboratory, University of California, August 1977.
72. Gates, D. F., Brown, H. S., and Seigel, A. E., "An Analytic and Experimental Study of the Heat Transfer and Erosion in the NOL Hypervelocity Launcher", AIAA Paper, No. 69-336, April 28-30, 1969.
73. Cambel, Ali Bulent, and Fenn, John B., "Dynamics of Conducting Gasses", Proceedings of the Third Biennial Gas Dynamics Symposium, 1960.
74. Burbidge, Geoffrey, R., Layzer, David, and Phillips, John G., "Annual Review of Astronomy and Astrophysics", Vol 14, Palo Alto, California, 1976.
75. Gentry, Richard A., Martin, Robert E., and Daly, Bart J., "An Eulerian Differencing Method for Unsteady Compressible Flow Problems", Journal of Computational Physics, Vol 1, 87-118, 1966.
76. MATHCAD, Version 4.0, Mathsoft, Inc., 1993
77. Bekefi, G., "Radiation Processes in Plasmas", John Wiley and Sons, Inc., 1966.
78. Patch, R. W., "Absorption Coefficients for Hydrogen", Journal of Quantitative Spectroscopy and Radiative Transfer, Vol. 9, No. 1, pp. 63, 87, Jan 1969.
79. Ohmura, Takashi, and Ohmura, Haruko, "Continuous Absorption due to Free-Free Transitions in Hydrogen", Physics Review, Vol. 121, No. 2, pp. 513-517, Jan 15, 1961.
80. Somerville, W. B., "The Continuous Absorption Coefficient of the Negative Hydrogen Molecular Ion", Astrophysics Journal, Vol. 139, No. 1, pp 192-197, Jan 1 1964.

81. Krascella, N. L., "Tables of the Composition, Opacity, and Thermodynamic Properties of Hydrogen at High Temperatures", NASA SP-3005, 1963.
82. Linskey, Jeffrey L., "On the Pressure-Induced Opacity of Molecular Hydrogen in Late-Type Stars", Astrophysics Journal, Vol. 156, No. 3, pp. 989-1006, Jan 1969.
83. Massey, H. J. W., Ridley, R. O., "Application of Variational Methods to the Theory of the Scattering of Slow Electrons by Hydrogen Molecules", Proceedings of the Physical Society, Vol. 69, No. 6, pp. 659-667, June 1956.
84. Bates, D. R., "Absorption of Radiation by an Atmosphere of H, H⁺, and H₂⁺: a Semi-Classical Treatment", Monthly Notes of the Royal Astronautical Society, Vol. 112, No. 1, pp. 40-44, Jan 1952.
85. Thompson, T. R., "Nonequilibrium Radiation Prediction of Spectral Absorption Coefficients", AIAA, Aerospace Sciences Meeting, New York, January 20-22, 1964.
86. Ozizik, M. Necati, "Radiative Transfer and Interactions with Conduction and Convection", John Wiley and Sons, Inc., 1973.
87. Patch, R. W., "Components of a Hydrogen Plasma Including Minor Species", NASA Technical Note, January 1969.
88. Kamalam, S., and Murty, S. S. R., "Boundary Layer Characteristics with Radiant Energy Transfer under Adverse Pressure Gradient", AIAA 11th Aerospace Sciences Meeting, Washington D. C., January 10-12, 1973.
89. Ragsdale, Robert G., and Einstein, Thomas H., "Two-Dimensional Gray-Gas Radiant Heat Transfer in a Coaxial-Flow Gaseous Reactor", NASA Technical Note, Feb 1964.
90. Robbins, William H., "An Analysis of Thermal Radiation Heat Transfer in a Nuclear-Rocket Nozzle", NASA Technical Note D-586, Jan 1961.
91. Einstein, Thomas H., "Radiant Heat Transfer To Absorbing Gases Enclosed in a Circular Pipe with Conduction, Gas Flow, and Internal Heat Generation", NASA Technical Report R-156, 1963.
92. Brown, Sanborn C., "Basic Data of Plasma Physics", The Technology Press of the Massachusetts Institute of Technology, New York, 1959.

93. Hirsh, Merle N., and Oskam, H. J., "Gaseous Electronics, Vol. 1: Electrical Discharges", Academic Press, New York, 1978.
94. Peterkin, Robert E., Jr., Giancola, Anthony, and Sturtevant, Judy E., "MACH2: A Reference Manual, fifth edition", Phillips Laboratories/WSP, Kirtland AFB, NM, July 1992.
95. Anderson, John D., Jr., "Hypersonic and High Temperature Gas Dynamics", McGraw-Hill Book Company, New York, 1989.

APPENDIX

B. Questionnaire

BACKGROUND INFORMATION

NAME _____ RANK _____

NUMBER OF YEARS MILITARY FLYING (INCLUDE UPT) _____

QUALIFIED AS A CIVILIAN PILOT Y/N IF YES LIST RATING _____

LIST AIRCRAFT FLOWN IN REVERSE CHRONOLOGICAL ORDER

FORMAT: ACFT - YEARS FLOWN - HOURS

EXAMPLE:

F-16 89-92 600HRS A-10 86-89 550HRS T-38 84-85 150HRS T-37 84 75HRS
T-41 83 20HRS

LIST LOW LEVEL TIME (EXCLUDING UPT)

FORMAT: ACFT YEARS FLOWN HOURS

EXAMPLE:

C-130 91-92 40HRS

LIST AIRCRAFT YOU ARE PRESENTLY CURRENT AND QUALIFIED IN

HOURS FLOWN LAST 30 DAYS _____ 60 DAYS _____ 90 DAYS _____

LIST ANY AIRCRAFT IN WHICH YOU HAVE OR PRESENTLY HOLD INSTRUCTOR STATUS

TOTAL FLIGHT TIME CIVILIAN & MILITARY _____

HAVE YOU EVER FLOWN THE MS-1 SIMULATOR? Y/N

IF YES, WHEN AND FOR WHAT PURPOSE?